Numerical Study of the Reactive Flow in a Two-Stream, Coaxial-Jet, Axisymmetric Bluff-Body Combustor

by

Van Luu

B.S., Aerospace Engineering
Iowa State University
(1988)

S.M., Aeronautics and Astronautics
Massachusetts Institute of Technology
(1991)

Submitted to the Department of Mechanical Engineering in Partial Fulfillment of the Requirements for the Degree of

Doctor of Science

at the

Massachusetts Institute of Technology
September 1996

Signature of Author____________________________________
Department of Mechanical Engineering
September 1996

Certified by____________________________________
Ahmed F. Ghoniem
Professor, Mechanical Engineering
Thesis Supervisor

Accepted by____________________________________
Ain A. Sonin
Chairman, Department Graduate Committee

Numerical Study of the Reactive Flow in a Two-Stream, Coaxial-Jet, Axisymmetric Bluff-Body Combustor

by

Van Luu

Submitted to the Department of Mechanical Engineering in Partial Fulfillment of the Requirements for the Degree of Doctor of Science in Mechanical Engineering

Abstract

The axisymmetric *vortex-scalar element* method is used to simulate the reactive flow in a combustor in which a central fuel jet interacts with an annular air stream across a thick bluff body. The vortex method is a Lagrangian scheme in which the vorticity of the flow field is discretized onto a set of finite-area elements with overlapping cores. Convection is simulated by transporting these elements, which are generated within numerical boundary layers, along particle trajectories. Molecular diffusion is modelled by the random walk. Lagrangian elements are also used to transport the species concentration fields in order to maintain the grid-free, self-adaptive nature of the algorithm. The overlap between two scalar elements carrying different species, caused by molecular diffusion, is used to compute mixing and in the fast-chemistry limit, the product formation. In the exothermic reactive-flow calculation, temperature nonhomogeneity is dynamically modelled by volumetric sources.

Simulations reveal that the unsteady dynamics, mixing, and combustion depend strongly on the inlet velocity ratio, the central-jet velocity spectrum, and the enthalpy of reaction. For steady inflow, the complex flow structure in the near-wake region is a dynamically unstable system involving two coexisting and coupled flow instabilities: the central-jet shear layer instability and the outer-stream recirculation region instability. The jet shear layer instability leads to the formation of organized fuel eddies which merge with the air eddies of the outer stream, and a composite burning structure is shed from the recirculation region periodically. This quasi-periodic shedding becomes less vigorous as the velocity of the central jet exceeds that of the annular stream, leading to slower mixing and a longer combustion zone.

The periodic central-jet forcing study shows that a preferred-mode coupling exists between the forced jet and the large-scale structures within the recirculation region. Time-averaged product concentration indicates that the mixing rate enhancement depends on the forcing frequency, as long as the forcing amplitude exceeds a minimum threshold to affect the stability of the jet shear layer.

When the reaction is exothermic, volumetric expansion occurs within the mixing region. As a result, the large-scale eddies become more diffuse, and their rotational rates decrease. Many of the global characteristic flow features observed in the isothermal flow are also present when the reaction is exothermic. However, lower unsteady fluctuation kinetic energy accompanying the reduced vorticity within the eddies somewhat impairs the ability of these large-scale structures to entrain fluid. Thus, large-scale entrainment is significantly decreased and the reaction zone is longer in the exothermic reactive flow.

Thesis Committee:	**Prof. Ahmed F. Ghoniem,**	**Mechanical Engineering,**	**M.I.T. (chairman)**
	Prof. Judson R. Baron,	**Aeronautics and Astronautics,**	**M.I.T.**
	Prof. David A. Gonzales,	**Aeronautics and Astronautics,**	**M.I.T.**
	Prof. James C. Keck,	**Mechanical Engineering,**	**M.I.T.**
	Prof. Ascher H. Shapiro,	**Mechanical Engineering,**	**M.I.T.**

To my uncle, Tai Quach, for providing me with the opportunity to make this possible.

ACKNOWLEDGMENT

I am very grateful to Prof. Ahmed F. Ghoniem for introducing me to the project and for all the invaluable advices and constructive criticisms he has given me in the last five years. I am also very thankful to him for the generous financial support which made it possible for me to pursue my graduate study at M.I.T. I also would like to acknowledge the members on my thesis committee, Prof. Judson R. Baron, Prof. David A. Gonzales, Prof. James C. Keck, and Prof. Ascher H. Shapiro, for their interest and assistance in my research.

Much of the initial work for this project was done by Luis-Filipe Martins and I wish to acknowledge his contribution to this project. I would like to thank all my colleagues in the Reacting Gas Dynamics Laboratory for being good friends and for many enlightening discussions over the years. I also would like to thank Pat Condon for all her help and friendship.

A large number of my friends and the staff members at the (former) McDonnell Douglas Missile Systems Company have directly or indirectly contributed to this endeavor, and I wish to express my sincere appreciation to them. Specifically, I would like to thank my dearest friends, Cliff and Hannah Muilenberg, for providing moral support in times of dire need; my foster parents, Mark and Sylvia Ostroot, for believing in me; and my cousin, Colver Quach, and his family for their understanding. I also would like to thank my friends Naz and Melinda Bedrossian, Martha Brown, Ross Sheckler and his parents, and Rick Boelbey. Special thanks also go to my former supervisors, Gerald Arcangeli, Dan Jaspering, and Fred McCotter, at the (former) McDonnell Douglas Missile Systems Company.

Above all, I am deeply indebted to my uncle, Tai Quach, for providing me with the opportunity to make this possible.

This work was partially supported by the United States Air Force Office of Scientific Research under Grant AFOSR F49620-92-J-0445 and utilized the CRAY-2 and the CRAY Y-MP computer systems at the National Center for Supercomputing Applications, University of Illinois at Urbana-Champaign, and the CRAY C90 computer system at the Pittsburgh Supercomputing Center.

TABLE OF CONTENTS

page

1. INTRODUCTION

2. GOVERNING EQUATIONS FOR TURBULENT REACTIVE FLOWS

3. NUMERICAL SCHEMES

4. ISOTHERMAL REACTIVE-FLOW SIMULATIONS

5. Exothermic Reactive-Flow Simulation

6. Summary, Conclusions, and Suggestions for Future Work

LIST OF FIGURES

1. INTRODUCTION

1.1 BACKGROUND AND MOTIVATION

Nonpremixed turbulent combustion is of fundamental importance and is being utilized in virtually all the modern energy conversion devices found in power generations, manufacturing operations, and propulsion systems. In a nonpremixed combustion system, the reactants are injected as separate streams into the combustion chamber. Thus, mixing of the reactants and the chemical reaction process are required to take place concurrently in the reaction zone. In order to achieve highest efficiency and complete combustion in a given volume, turbulence is usually induced in the reaction zone to promote mixing among the chemical species. As a result, flow fields inside the combustion chambers of nonpremixed combustion systems are usually time-dependent and highly turbulent, involving complex interactions and coupling of fluid mechanic, thermodynamic, and chemical processes. It is well-known that the mixing rate in the reaction zone is usually increased by turbulence, thus, greatly enhancing the overall chemical reaction. On the other hand, the release of thermal energy and concomitant density changes from combustion can significantly affect the flow dynamics and the turbulence level in the flow field. Thus, a thorough understanding of the complex turbulence dynamics within the reaction zone and the flow-combustion interaction are necessary in order to be able to improve the efficiency and to optimize the burning process.

Nonpremixed turbulent reactive flows have been the subject of a large number of experimental, analytical, and numerical studies in the last century [55, 63, 86, 117, 119, 120, 147]. Owing to the complex interaction between the flow and the chemistry, a thorough understanding of nonpremixed turbulent reactive flows requires detailed analyses of the chemical reaction mechanisms, the production and the interaction of the chemical species in the reaction zone, and the flow-combustion interaction. On one hand, the combustion process is greatly influenced by the hydrodynamic field through such effects as strain rate, flame elongation, and curvature; on the other hand, the hydrodynamic field is affected by the combustion process through volumetric expansion and baroclinic vorticity generation. Detailed temporal and spatial distributions of velocity, temperature, and species concentrations are generally required for a complete description of a reactive flow system. However, such detailed information is difficult to obtain from experiments due to the inherent unsteady and fully three-dimensional nature of the flow. As for numerical investigations, despite extensive research effort and all the advances in computational ability in the last twenty years, no realistic solution of the complete governing equations for nonpremixed turbulent reactive flows has yet been achieved, nor is it likely to be, in the foreseeable future. The major difficulty in analyzing nonpremixed turbulent reactive flows numerically comes from the fact that it involves a detailed examination of the convective and diffusive transport processes, coupling with chemical kinetics and heat transfer. The fundamental problem is that these processes occur over length and time scales as large as the confinement and as small as the molecular mixing in a given flow. Unfortunately, in most practical cases of interest, these scales are separated by several orders of magnitude. It is this complex close coupling and feedback between the flow and the chemistry, and the wide range of length and time scales that deter any earnest attempt at solving the complete set of governing equations, and making the development of a sound theory from first principles for these flows next to impossible.

Over the years, theoreticians and numerical researchers have instead devoted much research effort to the development of numerical methods and the construction of turbulence models that can accurately predict the structures of turbulent reactive flows [55]. To treat the complex, unsteady behaviors of turbulent flows, statistical methods have been developed and one of the two main approaches—the moment-equation methods or the probability-density-function (PDF) methods—is generally followed. In the moment-equation approach, averages (usually time-averages) of the relevant physical variables are introduced into the averaged governing equations. However, the procedure leads to a closure problem, introducing more unknown quantities than equations available. This dilemma is generally resolved by introducing *ad hoc* assumptions relating the various unknown quantities to close the system of equations. The main difficulty, however, is in proposing reasonable closure models, and it becomes even more difficult when chemical reactions occur in the flow field. Despite all these problems, moment-equation methods remain popular because they are relatively easy to use and to implement. Most models suggested in the literature can easily be implemented into computer codes developed for solving laminar flows [14]. This allows engineers to economically obtain approximations to various idealized reactive flows for different sets of flow conditions. The numerical results obtained in this way have, in many cases, exhibited relatively good agreements with experimental measurements [23, 24, 69, 77, 86, 106, 123, 137, 138, 139]. Over the years, moment-equation methods have been improved significantly as a result of extensive research, as well as due to their frequent use in many industrial applications. It appears that these methods will remain popular for engineering applications for the foreseeable future.

The second approach, using the probability-density-function methods, relies on the equations of the joint probability functions for the relevant physical variables. The advantage of these methods is due to the fundamental property of the PDF; namely, functions of the scalars, including the mean reaction rate, can be obtained directly from their PDFs. Closure based on the PDF methods has proven very useful in the theoretical description of turbulent flows since the original work of Howthorne *et al.* [66]. The main idea behinds this approximation is to consider the flow quantities as random variables, and the PDFs of these variables are being transported in the solution procedure instead of their finite moments. In flow simulations using PDF methods, the modelled transport equations for the two moments of the scalar fields are solved, and the shapes of the probability distributions are approximated based on the first two moments. In this way, all the higher-order moments required for the equations appeared in closed form. Extensive experiment studies have been conducted to obtain measurements of the PDFs for the scalar quantities for a wide range of flows including jets, wakes, recirculating flows, and mixing layers [54, 86]. Based on these experimental data and the numerical results obtained from simulations using moment-equation methods, researchers have had some success using this approach in obtaining numerical results for some idealized cases which have shown good agreements with experimental measurements. Although results obtained from the PDF approach are encouraging, this approach still cannot account for the complex PDF distributions of the flow which are frequently observed in the mixing zone of practical combustors. Another more systematic way of evaluating PDFs has also been developed in recent years. It involves the obtaining and solving of a transport equation governing the evolution of the PDF, rather than approximating its distribution from its moments. Nevertheless, models are again needed for the closures of certain fluctuation quantities [55]. Details of the different closure models and further discussion on recent progress of the PDF methods for turbulent reactive-flow simulations can be found in [86, 114].

Despite all the advances in developing better and more sophisticated turbulence models over the years, simulations using the two approaches just described can yield satisfactory results only if the flow is dominated by homogeneous turbulence [8, 63]. Unfortunately, the reaction zones of most nonpremixed combustion systems are usually dominated by large-scale turbulent coherent structures [85, 117, 119, 120]. It was pointed out by Libby and Williams that when coherent structures are present in a flow, the accepted theory of turbulence dynamics involving the cascading of large-scale eddies into small dissipative scales must be modified to account for the evolution of the coherent structures which may increase in size, by pairing and merging, in the downstream direction. The existence of coherent structures in a flow implies that unconditional averaging of the flow quantities overlooks and disregards an important physical phenomenon [86]. Currently, no known turbulence closure model has taken into account the contribution of the coherent structures. Thus, in general, it is inappropriate to use the two approaches just described to simulate the reactive flow field in most practical nonpremixed combustion systems.

Recent advancement in supercomputer technologies, especially in the last two decades, have had a major impact on turbulence research. As mentioned earlier, owing to the complex nonlinear interaction between the flow and the chemistry, it is still far from possible to simulate nonpremixed turbulent reactive flows with realistic governing parameters given the current state-of-the-art computational technologies. However, significantly improved efficiency, storage capability, and speed of supercomputers over the last twenty years have made it possible for researchers to solve the appropriate unaveraged transport equations governing turbulent flows over a limited range of flow parameters. Nonetheless, to simulate nonpremixed turbulent reactive flows, modellings are still required and assumptions must also be made concerning other aspects of the simulations in order to make the solution procedure feasible, despite the fact that modelling of certain fundamental properties of the turbulence phenomena is no longer absolutely necessary.[1]

For this research, we would like to select a unique combustor geometry of which the flow

---

[1] One should always keep in mind that this is only true for extremely limited range of Reynolds number.

dynamics encompass as many as possible of the distinctive characteristic flow features in the reaction zones of practical nonpremixed combustion systems, and yet is simple enough to allow us to study the problem numerically by solving the unaveraged governing equations after the application of certain simplified assumptions. The flow of two axisymmetric coaxial jets separated by a thick bluff body is one configuration satisfying this requirement under a restricted range of flow Reynolds number.

The unsteady dynamics of axisymmetric, coaxial-jet, confined bluff-body flow (Figure 1.1a) have commonly been used as a generic model for the studying of turbulent mixing and flow-combustion interactions [85, 117, 119, 120]. This is due to the fact that the wake region downstream of a bluff body is usually dominated by coherent vortical motions, and the unsteady flow dynamics contain many of the complex features which are commonly observed in the flow fields of practical combustors. (See, for example, Davies' experimental study of a D-shaped cylinder [31], Owen and Johnson's circular cylinder experiment [107], and the three-dimensional wake of an ellipsoid study of Perry and Watmuff [112].) Considerable effort has been devoted to the development of numerical models for simulating this type of flows [84]. Unfortunately, the wake region downstream of the bluff body is highly unsteady, three-dimensional, and contains a wide spectrum of length scales when the flow Reynolds number is high. Introducing chemical reaction into the flow further complicated the problem. The excessively large amount of computer time required to simulate the post-transitional, reactive recirculation zone behind a three-dimensional bluff body taking into account in detail of all the fluid-chemistry interactions in the flow renders the numerical approach non-practical. However, it has been confirmed experimentally that although the small-scale fluctuations in post-transitional, axisymmetric bluff-body flows are three-dimensional, the primary flows usually consist of toroidally-shaped large-scale eddies which are quasi axisymmetric, provided that the flow Reynolds number doesn't greatly exceed the critical Reynolds number [84, 85, 119]. It has also been shown that although the small-scale eddies are responsible for the final stage of mixing, the process is initiated by the large-scale structures in the flow since they entrain fluids from the reactant streams into the mixing zone [86, 117, 119, 120]. Thus, understanding the dynamics of axisymmetric, coaxial-jet, confined bluff-body flows is important and is of great interest from both practical and fundamental considerations. Significant research effort has been devoted to the unsteady simulation of reactive bluff-body flow in the last two decades [31, 52, 53, 71, 85, 93, 94, 117, 119, 120]. Results obtained from this extensive effort have shed much new light on the unsteady dynamics of the flow and the overall characteristics of the reactive field in the wake region of the bluff body.

1.2 OBJECTIVES

The primary objective of this work is to study the flow dynamics and the large-scale entrainment and mixing in the near-wake region of a two-stream, coaxial-jet, axisymmetric bluff-body combustor (Figure 1.1). Owing to the fact that most diffusion flames in practical nonpremixed combustion devices are mainly limited by mixing and diffusion of the various chemical species in the flow system [86], the aerodynamic aspects of the flow are emphasized in this research rather than the chemical kinetics or the reaction mechanisms. Specifically, the research will attempt to (1) understand and quantify the evolution, interaction, and the breakdown of the large-scale vortical structures generated at the inner and the outer edges of the bluff body within the recirculation region as a function of different inflow boundary conditions, both steady and time-dependent, and under the assumption of isothermal as well as exothermic reaction; (2) investigate how the large-scale entrainment and mixing are affected by the fluctuation intensity in the flow field and by the inflow boundary conditions; and (3) study the effects of the expansion velocity field on the flow dynamics and quantify the effects of the thermal energy released from combustion on the large-scale entrainment and mixing.

In order to simplify the solution procedure to the point where detailed parametric studies are possible at reasonable computational costs, the axisymmetric-flow assumption will be invoked in all the numerical simulations throughout this research. Admittedly, the axisymmetric-flow assumption is in strong conflict with the fact that all turbulent flows are three-dimensional, especially at the small-scale level. However, the resulting errors, in terms of the large-scale entrainment and mixing in the near-wake region, are expected to be acceptable. This presumption is supported by many experimental and numerical studies on this confined, bluff-body flow configuration [52, 93, 117, 119]. It has long been observed from experimental studies that although the small-scale fluctuations in this confined, buff-body flow configuration are three-dimensional, within a limited range of Reynolds number the primary flow consists of toroidally-shaped large-scale vortical structures which are quasi axisymmetric [85, 119]. Therefore, it is anticipated that the axisymmetric model is able to capture the unsteady dynamics of these large-scale structures and is capable of predicting the initial stage of entrainment in the near-wake region of the bluff body accurately.

1.3 APPROACH AND ORGANIZATION

The Lagrangian *Vortex-Scalar Element Method* is used in this research as the numerical tool to perform the simulations. The vortex method is an adaptive Lagrangian scheme in which the vorticity of the flow field is accurately discretized by a set of finite-area vortex elements with overlapping cores [19, 20]. Lagrangian scalar elements are also used in the simulations to transport the species concentration fields in order to maintain the grid-free, self-adaptive nature of the algorithm [50]. Furthermore, different sets of scalar elements can be used to transport the concentration fields of different species with different diffusivities. Thus, a wide disparity in diffusive length scales can be accommodated naturally without posing any particular difficulty.

The remainder of the dissertation is organized as follows. The general governing equations, the formulation of the analytical model, and the simplified governing equations are presented in Chapter 2. The numerical schemes used in this research are briefly discussed in Chapter 3. Chapter 4 presents results of the isothermal reactive-flow study, and the investigation of the exothermic reactive flow with low heat release will be presented in Chapter 5. A summary of the work performed in this research as well as conclusions and suggestions for future work are discussed in the final chapter.

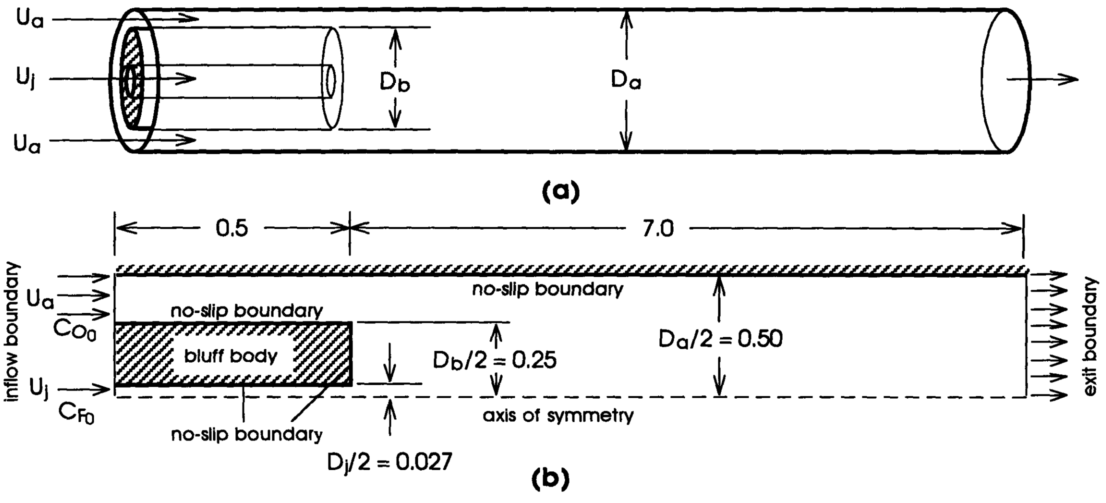

Figure 1.1 Geometry of the two-stream, coaxial-jet, axisymmetric bluff-body combustor used in this research. **(a)** Schematic drawing of the combustor. **(b)** Axisymmetric computational domain. All the dimensions in **(b)** are normalized by the annular diameter (= 0.1 m).

2. GOVERNING EQUATIONS FOR TURBULENT REACTIVE FLOWS

Turbulence is the most common and the most complicated kind of fluid motion in nature. Unfortunately, it is notoriously difficult to predict and peculiarly resistant to mathematical treatment. Chemical reactions occur in a turbulent flow, such as in combustion, increases the difficulties of the problem many folds. Nonetheless, turbulent reactive flows are still described by the conservation equations. Thus, the starting point of simulating turbulent reactive flows should be the conservation equations for mass, species, energy, and momentum for a multi-component, reactive mixture. Since these governing equations provide the necessary frame work for all subsequent discussions, establishment of these equations and their exploitation are critical for the numerical simulation of turbulent reactive flows.

In this chapter, the governing equations for a multi-component, reactive, perfect-gas mixture first will be presented and discussed, followed by the normalization and the application of the low-Mach-number assumption to the equations. Although certain characteristic flow features of real reactive flows can no longer be captured by the equations after the application of the low-Mach-number assumption, the simplified governing equations have the computational advantage that acoustic waves are filtered out, thus relieving the time step size constraint but at the same time, still allowing the flow field to have significant density nonuniformities. Therefore, we are still able to study the effects of the thermal energy released from combustion on the flow dynamics and the large-scale entrainment in the near-wake region using the simplified equations. In Section 2.2, we will obtain the set of approximated equations that is asymptotically valid for small Mach number. The final set of governing equations, describing the unsteady dynamics of a reactive flow of perfect gases in an open axisymmetric flow domain with zero swirl, will be presented in Section 2.3.

A fixed convention on notations will be adopted throughout this dissertation. When we are considering a dimensional quantity, we label the variable with an asterisk. When we are dealing with a dimensionless quantity, no asterisk is used in the variable.

2.1 GOVERNING EQUATIONS FOR A MULTI-COMPONENT REACTIVE GAS MIXTURE

All analyses concerning the dynamics of fluid flows should begin, either directly or indirectly, with the statements of the three fundamental laws. These laws, which are independent of the nature of any particular fluid, are 1) conservation of mass, 2) Newton's second law of motion, and 3) the first law of thermodynamics. Obviously, no process in nature is possible unless the second law of thermodynamics is also satisfied in addition to the conservation equations. The three unknowns which must be obtained simultaneously from the three governing equations are the velocity $\mathbf{u}^*$, the thermodynamic pressure p^*, and the absolute temperature T^*. Since the final forms of the conservation equations usually contain two more thermodynamic variables, the fluid density ρ^* and the specific internal energy of the fluid e^*, as well as the two transport coefficients μ^* and κ^* (the absolute viscosity coefficient and the thermal conductivity of the fluid), additional equations are required to relate these thermodynamic variables and transport coefficients. From classical thermodynamics and the kinetic theory of gases, it is known that if the flow is assumed to be in local thermodynamic equilibrium, then the two thermodynamic variables and the two transport coefficients mentioned above are uniquely determined by the values of p^* and T^*. Thus the complete system of equations is closed by assuming knowledge of four state relations

$$\begin{aligned} \rho^* &= \rho^*(p^*,T^*) \qquad & e^* &= e^*(p^*,T^*) \\ \mu^* &= \mu^*(p^*,T^*) \qquad & \kappa^* &= \kappa^*(p^*,T^*). \end{aligned} \tag{2.1}$$

Finally, in order to specify a given problem uniquely, proper conditions for $\mathbf{u}^*$, p^*, and T^* at the boundaries of the flow domain must be established.

The above discussion applies only to fluid flows of assumed uniform, homogeneous composition (chemical reactions and diffusion of the species are not considered). For a multi-component reactive mixture, the variables in (2.1) are also functions of the mole fraction X_i and we must consider at least two more basic relations, conservation of species and the laws of chemical reaction, plus additional auxiliary relations such as knowledge of the multi-component molecular diffusion coefficient $d_{ij}^* = d_{ij}^*(p^*, T^*)$ [13], chemical equilibrium constants $K_c^* = K_c^*(T^*)$, reaction rates $\dot{r}^* = \dot{r}^*(C_i^*, T^*)$, and the heats of formation H^* of the different species in the reactive mixture. In the following section, we will briefly present the fundamental governing equations for a multi-component, reactive, perfect-gas mixture. These equations supply a complete description of most reactive flow systems under the imposed assumptions when the equations are derived. However, owing to the complexity of these equations and the limitations on current supercomputer technologies, it is not possible to simulate reactive flows using these equations directly. Thus, after the presentation of these equations, additional assumptions will be applied in order to obtain the set of approximate governing equations which is valid for the special flow situations considered in this research. Detailed derivations of the equations presented in this chapter can be found in many standard references [3, 7, 13, 20, 125, 129, 146].

2.1.1 The Continuity and the Species Conservation Equations for a Multi-Component Reactive Gas Mixture

The principle of conservation of mass for species i, when applying to a mixture of N components passing through an infinitesimal, fixed control volume within which species i may be produced or destroyed by chemical reaction at a rate $\dot{r}_i^*$ (mass rate of production of species i per unit volume), yields the following mass conservation equation for the species:[1]

$$\frac{\partial \rho_i^*}{\partial t^*} + \nabla \cdot (\rho_i^* \mathbf{u}^*) = \dot{r}_i^* - \nabla \cdot \rho_i^* (\mathbf{u}_i^* - \mathbf{u}^*) \qquad (i = 1, 2, \ldots, N). \tag{2.2}$$

The first term on the left-hand side of Equation (2.2) represents the time rate of change of the mass (per unit volume) of species i in the control volume, the second term represents the net rate of mass flux (of species i) passing out of the control surfaces per unit volume[2], and $\rho_i^*(\mathbf{u}_i^* - \mathbf{u}^*)$ is the mass flux of the *ith* species relative to the local mass-averaged velocity $\mathbf{u}^*$. In a multi-component reactive mixture of N species, there exists a system of N equations of this kind for the mixture. The summation of these N equations yields the overall continuity equation,

$$\frac{\partial \rho^*}{\partial t^*} + \nabla \cdot (\rho^* \mathbf{u}^*) = 0, \tag{2.3}$$

which is seen to have the same form as that for a pure nonreactive fluid. In Equation (2.3), $\mathbf{u}^*$ and ρ^* are the local mass-averaged velocity and the local mass density of the fluid, respectively. Notice that in order to obtain Equation (2.3), we have made use of the relation

$$\sum_{i=1}^{N} \rho_i^* \mathbf{u}_i^* = \rho^* \mathbf{u}^* \tag{2.4}$$

as well as the law of conservation of mass in the form

$$\sum_{i=1}^{N} \dot{r}_i^* = 0. \tag{2.5}$$

Before proceeding any further, it should be pointed out that since only N-1 of the N mass fractions, $Y_i \equiv \rho_i^*/\rho^*$, in the mixture are independent in any given problem, we can replace any one of the N equations given in (2.2) by the overall continuity equation given in (2.3) for the mixture [13].

---

[1] Pressure diffusion, forced diffusion, and thermal diffusion components of the mass flux vector have been neglected in this equation [13].

[2] ρ_i^* and $\mathbf{u}_i^*$ are the mass density and the velocity with respect to a stationary coordinate system of the i th species, respectively.

The mass conservation equations for the species, as given in Equation (2.2), are fairly general and are not useful for obtaining the concentration profiles when they are being applied in numerical calculations. To make the equations more convenient for computation, Fick's law of diffusion is generally employed and the flux of species due to molecular transport is replaced by the appropriate expression involving the concentration gradients. Carrying out the substitution, the following more restricted diffusion equation for species i in a perfect-gas mixture is obtained [13]

$$\frac{\partial \rho_i^*}{\partial t^*} + \nabla \cdot (\rho_i^* \mathbf{u}^*) = \dot{r}_i^* + \nabla \cdot \left(\frac{C^{*2}}{\rho^*} \sum_{j=1}^{N} M_i^* M_j^* d_{ij}^* \nabla X_i \right) \qquad (i = 1, 2, \ldots, N). \tag{2.6}$$

In Equation (2.6) C^* is the molar density of the mixture, M_i^* and M_j^* are the molecular weights of species i and j, respectively, d_{ij}^* is the multi-component diffusion coefficient (the diffusivity of the pair i-j in a multi-component mixture; in general, d_{ij}^* is not equal to d_{ji}^*), and X_i is the mole fraction of species i in the mixture.[1] For an N-component ideal-gas mixture, the relation is known between the d_{ij}^* (the diffusivity of the pair i-j in a multi-component mixture) and the D_{ij}^* (the diffusivity of the pair i-j in a binary mixture). Since the d_{ij}^* are concentration-dependent, Equation (2.6) is also inconvenient to use in a simulation. It has been shown by Curtiss and Hirschfelder that the concentration gradient ∇X_i can be related to D_{ij}^* by the *Stefan-Maxwell equations* [64]. Moreover, if the mole fraction of species i is small in a mixture, it is possible to define an effective binary diffusivity D_{iM}^*, in analogy of the binary diffusion coefficient, for the diffusion of species i into the mixture. By combining the definition of the effective binary coefficient and the Stefan-Maxwell equations, Curtiss and Hirschfelder had obtained an expression relating D_{ij}^*, the diffusivity of the pair i-j in a binary mixture, and D_{iM}^*, the effective binary diffusion coefficient for the diffusion of species i into the mixture. Detailed discussion and derivation of these equations can be found in [64]. In general, the D_{iM}^* are found to be position-dependent. However, the dependency is quite small under most situations and can usually be neglected.

As will be discussed in Section 2.1.5, a simplified chemical equation of the form $F + \alpha O + \beta D \rightarrow \sigma P + \beta D$ is used in all the simulations for calculating the amount of thermal energy released from combustion, where F, O, D, P represent the fuel, oxidizer, diluent, and products respectively; α and σ are the stoichiometric coefficients, per mole of fuel, of the oxidizer and products, respectively; and β is the total number of moles of diluent per α moles of oxidizer. Since the mole fraction of the diluent used in the simulations is much greater than the mole frac-

---

[1] The expression given in Equation (2.6) is the generalized Fick's law of diffusion for a perfect-gas mixture.

tions of the fuel, oxidizer, or products, the mixture essentially consists of pure inert diluent with traces of the reactants and products. Furthermore, if the mixture is at low density and the total amount of thermal energy released from chemical reaction is small, we can neglect the variation of the fluid density and reduce Equation (2.6) to

$$\frac{\partial \rho_i^*}{\partial t^*} + \mathbf{u}^* \cdot \nabla \rho_i^* = D_{iM}^* \nabla^2 \rho_i^* + \dot{r}_i^* \qquad (i = 1, 2, \ldots, N). \qquad (2.7)$$

It should be pointed out that in arriving at Equation (2.7), we have made the assumption $\nabla \cdot \mathbf{u}^* = 0$ and D_{iM}^* is constant. The condition $\nabla \cdot \mathbf{u}^*$ is identically zero only when the fluid is incompressible. Thus, strictly speaking, the species continuity equation as given in (2.7) is applicable only for an incompressible flow. (Equation (2.7) is generally used for diffusion in dilute liquid solutions at constant temperature and pressure.) However, as a first-order approximation, many combustion problems have been successfully formulated using Equation (2.7) as the species continuity equation [50, 51, 80, 101]. For the sake of simplicity and tractability, we will also assume the species continuity equation can be approximated by Equation (2.7) in this research. However, one should always keep in mind that the underlying assumptions in which Equation (2.7) is arrived, especially in the process of choosing flow parameters for a simulation.

Notice that Equations (2.3) and (2.7) were derived using the *Eulerian approach*. In the alternative *Lagrangian approach*, the changes to the properties of a fluid element are recorded by an observer moving with the fluid element. The transformation of an equation from the Eulerian to the Lagrangian description can easily be accomplished by using the definition of the substantial derivative [3],

$$\frac{D}{Dt^*} = \frac{\partial}{\partial t^*} + \mathbf{u}^* \cdot \nabla . \qquad (2.8)$$

Expanding the divergence term of Equations (2.3) and (2.7) and using Equation (2.8), the continuity and the species conservation equations expressed in terms of the substantial derivative are

$$\frac{D\rho^*}{Dt^*} + \rho^* (\nabla \cdot \mathbf{u}^*) = 0 \qquad (2.8)$$

and

$$\frac{D\rho_i^*}{Dt^*} = D_{iM}^* \nabla^2 \rho_i^* + \dot{r}_i^* \qquad (i = 1, 2, \ldots, N), \qquad (2.9)$$

respectively. When Equation (2.9) is divided by the molecular weight of species i, we get the species continuity equation in terms of the molar concentration C_i^*:

$$\frac{DC_i^*}{Dt^*} = D_{iM}^* \nabla^2 C_i^* + \dot{R}_i^* \qquad (i = 1, 2, \ldots, N) \qquad (2.10)$$

where $\dot{R}_i^*$ is the molar rate of production of species i per unit volume. As discussed earlier, in this study the chemical composition of the flow is assumed to consist of mainly inert diluent with traces of fuel (F), oxidizer (O), and products (P). Thus, only three species conservation equations or two species equations and the overall continuity equation are needed for a simulation. If three species equations are used, we have N = 3 in Equation (2.10) and the index i will imply F, O, or P. In this case, the diffusion coefficients D_{iM}^* are the effective binary diffusion coefficients of these traces of elements diffusing into the mixture consisting mostly of the inert diluent.

2.1.2 THE MOMENTUM EQUATION

Applying Newton's second law to a fluid passing through an infinitesimal, fixed control volume, the following momentum equation is obtained [3]:

$$\frac{\partial(\rho^* \mathbf{u}^*)}{\partial t^*} + \nabla \cdot (\rho^* \mathbf{u}^* \mathbf{u}^*) = \nabla \cdot \Pi_{ij}^*. \tag{2.11}$$

The first term on the left-hand side of the equation represents the time rate of change of momentum per unit volume inside the control volume, and the second term represents the net rate of momentum flux per unit volume passing out of the control volume. Notice that since we are investigating low-speed reactive flows in the absence of electric and magnetic force fields, all body forces have been neglected in the above equation. Applying the following vector identity

$$\nabla \cdot (\rho^* \mathbf{u}^* \mathbf{u}^*) = \rho^* \mathbf{u}^* \cdot \nabla \mathbf{u}^* + \mathbf{u}^* (\nabla \cdot \rho^* \mathbf{u}^*) \tag{2.12}$$

to Equation (2.11) and simplifying the resulting expression using the continuity equation, the momentum equation expressed in terms of the substantial derivative is

$$\rho^* \frac{D\mathbf{u}^*}{Dt^*} = \nabla \cdot \Pi_{ij}^*. \tag{2.13}$$

The term on the right-hand side of Equation (2.13) represents the surface forces per unit volume. The surface forces are those applied by external stresses on the surfaces of the fluid element. These stresses consist of normal and shear stresses and are represented by the stress tensor Π_{ij}^*. Note that the momentum equation, as given in Equation (2.13), is fairly general. It is only when approximate expressions are inserted for the stress tensor that the equation loses its generality. For all gases which can be treated as continuum and certain liquids, it has been observed that the stress at any given point in the flow is linearly dependent on the rate of strain of the fluid. A fluid which behaves in this manner is known as a *Newtonian Fluid*. For a Newtonian fluid, the stress tensor is given by [3]

$$\Pi_{ij}^* = (-p^*)\delta_{ij} + \mu^* \left(\frac{\partial u_i^*}{\partial x_j^*} + \frac{\partial u_j^*}{\partial x_i^*} - \frac{2}{3}\delta_{ij} \frac{\partial u_k^*}{\partial x_k^*} \right) \qquad (i, j, k = 1, 2, 3) \tag{2.14}$$

where δ_{ij} is the Kronecker delta ($\delta_{ij} = 1$ if $i = 1$, and $\delta_{ij} = 0$ if $i \neq j$) and p^* is the static pressure. Note that in expressing the stress tensor in the form of Equation (2.14), Stokes' hypothesis has been implicitly assumed. Thus, the coefficient of bulk viscosity is neglected in the equation and the second coefficient of viscosity $\mu^{*\prime}$ is given by

$$\mu^{*\prime} = \frac{-2}{3}\mu^*. \tag{2.15}$$

For convenience, the stress tensor is usually separated in the following manner

$$\Pi^*_{ij} = -p^*\delta_{ij} + \tau^*_{ij} \tag{2.16}$$

where τ^*_{ij} represents the viscous stress tensor given by

$$\tau^*_{ij} = \mu^*\left(\frac{\partial u_i^*}{\partial x_j^*} + \frac{\partial u_j^*}{\partial x_i^*} - \frac{2}{3}\delta_{ij}\frac{\partial u_k^*}{\partial x_k^*}\right) \qquad (i, j, k = 1, 2, 3). \tag{2.17}$$

By substituting the expression in Equations (2.14-2.17) into (2.13), we obtain the well-known *Navier-Stokes equation:*

$$\rho^*\frac{Du^*}{Dt^*} = -\nabla p^* + \frac{\partial}{\partial x_j^*}\left(\mu^*\frac{\partial u_i^*}{\partial x_j^*} + \frac{\partial u_j^*}{\partial x_i^*} - \frac{2}{3}\delta_{ij}\frac{\partial u_k^*}{\partial x_k^*}\right) = -\nabla p^* + \nabla \cdot \tau^*_{ij}. \tag{2.18}$$

It should be noted that, since body forces have been neglected in the derivation, Equation (2.18) has exactly the same form as the momentum equation for a nonreactive Newtonian fluid. Furthermore, if the flow is either anelastic[1] or incompressible with constant coefficient of viscosity μ^*, Equation (2.18) will reduce to the much simpler form

$$\rho^*\frac{Du^*}{Dt^*} = -\nabla p^* + \mu^*\nabla^2\mathbf{u}^*. \tag{2.19}$$

2.1.3 THE VORTICITY TRANSPORT EQUATION

The momentum equation, as given in Equation (2.18) or (2.19), is expressed in terms of the primitive variables p^*, ρ^*, and $\mathbf{u}^*$. It is well-known that for certain high-Reynolds-number flows it is advantageous to describe the flow field in terms of the spatial distribution of the vorticity Ω^*, where $\Omega^* = \nabla \times \mathbf{u}^*$, rather than in terms of the primitive variables, especially if the flow is barotro-

---

[1] The anelastic-flow assumption removes acoustic phenomena from theoretical consideration, while still allowing an accurate accounting for (1) the buoyancy and inertial effects of variable density, (2) the modification of viscous forces and heat conduction by the variation of transport properties, and (3) the velocity induced by moderately slow expansion or contraction of the particles. Note that the term anelastic applies to the flow, rather than to the fluid [129].

pic[1] [20, 129]. The main reason is that a barotropic flow starts from rest under the influence of conservative body forces, and only those fluid elements that have been subjected to viscous torques ever acquire angular velocity, which is equal to one-half of the vorticity. The rest of the fluid moves in accordance with the relative simple laws of irrotational flow [129]. Moreover, for many real flows the regions where vorticity is other than zero is usually small, even if the flow is not barotropic. This is especially true for flows at high Reynolds numbers. Thus by describing the flow field in terms of the vorticity, it is possible to develop interesting and useful numerical schemes which can be used to analyze the generation of vorticity on a no-slip boundary, and the subsequently motion of the vorticity by convection and diffusion with significant reduction in computational requirements [7, 19, 20]. In this section, we will demonstrate the procedure of applying vector operations on Equation (2.18) in order to obtain the vorticity transport equation.

The divergence and the curl of a vector function of position are fundamental differential operators in vector analysis which yield quantities independent of the coordinate system. The equation describing the transport of vorticity in a flow can be obtained simply by performing vector operations on the momentum equation. Taking the curl of Equation (2.18) we get

$$\nabla \times \frac{D\mathbf{u}^*}{Dt^*} = \nabla \times \left(\frac{-1}{\rho^*}\nabla p^*\right) + \nabla \times \left(\frac{1}{\rho^*}(\nabla \cdot \tau^*_{ij})\right). \tag{2.20}$$

From the following two vector identities

$$\nabla \times (\mathbf{A} \cdot \nabla \mathbf{A}) = -\nabla \times [\mathbf{A} \times (\nabla \times \mathbf{A})] \tag{2.21}$$

$$\nabla \times (\mathbf{A} \times \mathbf{B}) = (\mathbf{B} \cdot \nabla)\mathbf{A} - (\mathbf{A} \cdot \nabla)\mathbf{B} + \mathbf{A}(\nabla \cdot \mathbf{B}) - \mathbf{B}(\nabla \cdot \mathbf{A}) \tag{2.22}$$

we see that the first term in Equation (2.20) can be expressed as

$$\begin{aligned}
\nabla \times \frac{D\mathbf{u}^*}{Dt^*} &= \nabla \times \left[\frac{\partial \mathbf{u}^*}{\partial t^*} + \mathbf{u}^* \cdot \nabla \mathbf{u}^*\right] \\
&= \frac{\partial (\nabla \times \mathbf{u}^*)}{\partial t^*} - \nabla \times [\mathbf{u}^* \times (\nabla \times \mathbf{u}^*)] \\
&= \frac{\partial \Omega^*}{\partial t^*} - \nabla \times [\mathbf{u}^* \times \Omega^*] \\
&= \frac{\partial \Omega^*}{\partial t^*} - [(\Omega^* \cdot \nabla)\mathbf{u}^* - (\mathbf{u}^* \cdot \nabla)\Omega^* + \mathbf{u}^*(\nabla \cdot \Omega^*) - \Omega^*(\nabla \cdot \mathbf{u}^*)].
\end{aligned} \tag{2.23}$$

Since $\nabla \cdot \Omega^* = \nabla \cdot (\nabla \times \mathbf{u}^*) = 0$ for any vector field, Equation (2.23) is reduced to

---

[1] A barotropic flow is one in which surfaces of constant pressure and surfaces of constant density coincide, that is, $\nabla \rho^* \times \nabla p^* = 0$.

$$\nabla \times \frac{D\mathbf{u}^*}{Dt^*} = \frac{\partial \Omega^*}{\partial t^*} + (\mathbf{u}^* \cdot \nabla)\,\Omega^* + \Omega^*(\nabla \cdot \mathbf{u}^*) - (\Omega^* \cdot \nabla)\mathbf{u}^*$$

$$= \left(\frac{D\Omega^*}{Dt^*} + \Omega^*(\nabla \cdot \mathbf{u}^*) - (\Omega^* \cdot \nabla)\mathbf{u}^*\right). \tag{2.24}$$

Next, the first term on the right-hand side of Equation (2.20), $\nabla \times \left(\frac{-1}{\rho^*}\nabla p^*\right)$, can be expanded to give

$$\nabla \times \left(\frac{-1}{\rho^*}\nabla p^*\right) = -\nabla\left(\frac{1}{\rho^*}\right) \times \nabla p^* + \frac{1}{\rho^*}(\nabla \times \nabla p^*)$$

$$= \frac{1}{\rho^{*2}}\nabla \rho^* \times \nabla p^*. \tag{2.25}$$

Note that the second term on the left-hand side in the above equation vanishes because of the fact that $\nabla \times \nabla$ is identically zero. Finally, for the last term in Equation (2.20), $\nabla \times \left(\frac{1}{\rho^*}(\nabla \cdot \tau^*_{ij})\right)$, we have

$$\nabla \times \left(\frac{1}{\rho^*}(\nabla \cdot \tau^*_{ij})\right) = \nabla\left(\frac{1}{\rho^*}\right) \times \nabla \cdot \tau^*_{ij} + \frac{1}{\rho^*}[\nabla \times \nabla \cdot \tau^*_{ij}]$$

$$= \left(\frac{-1}{\rho^{*2}}\right)\nabla \rho^* \times \nabla \cdot \tau^*_{ij} + \frac{1}{\rho^*}[\nabla \times \nabla \cdot \tau^*_{ij}]$$

$$= \frac{1}{\rho^{*2}}[\nabla \cdot \tau^*_{ij} \times \nabla \rho^*] + \frac{1}{\rho^*}[\nabla \times \nabla \cdot \tau^*_{ij}]. \tag{2.26}$$

By substituting Equations (2.24-2.26) into (2.20), we obtain the three-dimensional vorticity transport equation

$$\frac{D\Omega^*}{Dt^*} + \Omega^*(\nabla \cdot \mathbf{u}^*) - \Omega^* \cdot \nabla \mathbf{u}^* = \frac{1}{\rho^{*2}}\nabla \rho^* \times \nabla p^* + \frac{1}{\rho^{*2}}[\nabla \cdot \tau^*_{ij} \times \nabla \rho^*] + \frac{1}{\rho^*}[\nabla \times \nabla \cdot \tau^*_{ij}]. \tag{2.27}$$

An alternative form of Equation (2.27) can be obtained as follows. Since

$$\rho^*\frac{D}{Dt^*}\left(\frac{\Omega^*}{\rho^*}\right) = \rho^*\left[\frac{1}{\rho^*}\frac{D\,\Omega^*}{Dt^*} - \frac{\Omega^*}{\rho^{*2}}\frac{D\rho^*}{Dt^*}\right] = \frac{D\,\Omega^*}{Dt^*} - \frac{\Omega^*}{\rho^*}\frac{D\rho^*}{Dt^*} \tag{2.28}$$

and from the continuity equation we have

$$\frac{D\rho^*}{Dt^*} = -\rho^*(\nabla \cdot \mathbf{u}^*), \tag{2.29}$$

thus, Equation (2.27) can alternatively be expressed as

$$\frac{D}{Dt^*}\left(\frac{\Omega^*}{\rho^*}\right)-\frac{1}{\rho^*}[\Omega^*\cdot\nabla\mathbf{u}^*] = \frac{1}{\rho^{*3}}\nabla\rho^*\times\nabla p^* + \{\frac{1}{\rho^{*3}}[\nabla\cdot\tau^*_{ij}\times\nabla\rho^*]+\frac{1}{\rho^{*2}}[\nabla\times\nabla\cdot\tau^*_{ij}]\}. \quad (2.30)$$

Equation (2.27) or (2.30) is the general vorticity transport equation. Both equations are valid for a three-dimensional flow which does not necessary have to be barotropic. The vorticity transport equation is greatly simplified for an anelastic flow or an incompressible flow with constant density and viscosity coefficient. Under the later assumption, the equation is reduced to

$$\frac{D\Omega^*}{Dt^*}-\Omega^*\cdot\nabla\mathbf{u}^* = \left(\frac{\mu^*}{\rho^*}\nabla^2\Omega^*\right) = (\nu^*\nabla^2\Omega^*) \quad (2.31)$$

where $\nu^* \equiv \mu^*/\rho^*$ is the kinematic viscosity.

2.1.4 THE ENERGY EQUATION

The first law of thermodynamics for a system relates the changes of state experienced by the system to the energy interactions between the system and its surrounding. Consider energy in the forms of heat and work only, the first law of thermodynamics for a system is

$$dE^* = \delta Q^* - \delta W^* \quad (2.32)$$

where δQ^* and δW^* are energy crossing the boundaries of the system in the forms of heat and work, respectively, and E^* is the total energy of the system. For a moving system, such as a flowing fluid element, we assume that only the internal energy and kinetic energy are significant. Thus,

$$E^* = \rho^*\left[e^* + \frac{1}{2}(\mathbf{u}^*\cdot\mathbf{u}^*)\right] \quad (2.33)$$

where e^* is the internal energy of the fluid per unit mass. Similar to the conservation of mass and momentum, applying the first law of thermodynamics to a fluid passing through an infinitesimal, fixed control volume yields the following energy equation

$$\frac{\partial E^*}{\partial t^*}+\nabla\cdot(E^*\mathbf{u}^*) = \dot{Q}^*-\nabla\cdot\mathbf{q}^*+\nabla\cdot(\Pi^*_{ij}\cdot\mathbf{u}^*). \quad (2.34)$$

The first term on the left-hand side of Equation (2.34) represents the time rate of change of total energy per unit volume in the control volume; the second term represents the net rate of total energy per unit volume leaving the control volume through the control surfaces. The first term on the right-hand side of the equation is the rate of heat produced per unit volume inside the control volume, and the second term, $\nabla\cdot\mathbf{q}^*$, is the rate of heat loss by conduction (per unit volume) through the control surfaces. For most gases under normal conditions, the heat transfer is accurately described by Fourier's law of heat conduction. Thus, the heat flux vector $\mathbf{q}^*$ can be expressed as

$$\mathbf{q}^* = -\kappa^* \nabla T^*, \tag{2.35}$$

where κ^* is the coefficient of thermal conductivity and T^* is the absolute temperature. Finally, the last term on the right-hand side of Equation (2.34) represents the work done on the control volume, per unit volume, by the surface forces.

The energy equation can be recasted into a more useful form for numerical calculations as follows. Notice that

$$\rho^* \frac{D(E^*/\rho^*)}{Dt^*} = \rho^* \left[\frac{1}{\rho^*} \frac{DE^*}{Dt^*} - \frac{E^*}{\rho^{*2}} \frac{D\rho^*}{Dt^*} \right], \tag{2.36}$$

and from the continuity equation we have

$$\frac{D\rho^*}{Dt^*} = -\rho^* (\nabla \cdot \mathbf{u}^*). \tag{2.37}$$

Combining Equations (2.36) and (2.37) we see that the left-hand side of Equation (2.36) can also be expressed as

$$\begin{aligned} \rho^* \frac{D(E^*/\rho^*)}{Dt^*} &= \rho^* \left(\frac{1}{\rho^*} \frac{DE^*}{Dt^*} + \frac{E^*}{\rho^*} (\nabla \cdot \mathbf{u}^*) \right) \\ &= \frac{DE^*}{Dt^*} + E^* (\nabla \cdot \mathbf{u}^*) \\ &= \left(\frac{\partial E^*}{\partial t^*} + \mathbf{u}^* \cdot \nabla E^* \right) + E^* (\nabla \cdot \mathbf{u}^*) \\ &= \frac{\partial E^*}{\partial t^*} + \nabla \cdot (E^* \mathbf{u}^*). \end{aligned} \tag{2.38}$$

Therefore,

$$\rho^* \frac{D(E^*/\rho^*)}{Dt^*} = \rho^* \frac{De^*}{Dt^*} + \rho^* \frac{D[(\mathbf{u}^* \cdot \mathbf{u}^*)/2]}{Dt^*} = \frac{\partial E^*}{\partial t^*} + \nabla \cdot (E^* \mathbf{u}^*) \tag{2.39}$$

since $E^* = [e^* + (\mathbf{u}^* \cdot \mathbf{u}^*)/2]\rho^*$ by assumption. Now, forming the scalar dot product of the momentum equation (2.18) and the velocity vector we get

$$\rho^* \frac{D\mathbf{u}^*}{Dt^*} \cdot \mathbf{u}^* = -\nabla p^* \cdot \mathbf{u}^* + (\nabla \cdot \tau_{ij}^*) \cdot \mathbf{u}^*. \tag{2.40}$$

Since

$$\rho^* \frac{D[(\mathbf{u}^* \cdot \mathbf{u}^*)/2]}{Dt^*} = \frac{\rho^*}{2}\left(\frac{Du^{*2}}{Dt^*} + \frac{Dv^{*2}}{Dt^*} + \frac{Dw^{*2}}{Dt^*}\right)$$

$$= \rho^*\left(u^* \frac{Du^*}{Dt^*} + v^* \frac{Dv^*}{Dt^*} + w^* \frac{Dw^*}{Dt^*}\right) \tag{2.41}$$

and

$$\rho^* \frac{D\mathbf{u}^*}{Dt^*} \cdot \mathbf{u}^* = \rho^*\left(u^* \frac{Du^*}{Dt^*} + v^* \frac{Dv^*}{Dt^*} + w^* \frac{Dw^*}{Dt^*}\right), \tag{2.42}$$

therefore, combining Equations (2.39-2.42) we get

$$\rho^* \frac{D(E^*/\rho^*)}{Dt^*} = \rho^* \frac{De^*}{Dt^*} - \nabla p^* \cdot \mathbf{u}^* + (\nabla \cdot \tau_{ij}^*) \cdot \mathbf{u}^*, \tag{2.43}$$

or equivalently as

$$\frac{\partial E^*}{\partial t^*} + \nabla \cdot (E^* \mathbf{u}^*) = \rho^* \frac{De^*}{Dt^*} - \nabla p^* \cdot \mathbf{u}^* + (\nabla \cdot \tau_{ij}^*) \cdot \mathbf{u}^*. \tag{2.44}$$

Substituting the above equation and Fourier's law of heat conduction (2.35) into Equation (2.34) and simplifying the result, we get

$$\rho^* \frac{De^*}{Dt^*} + p^* (\nabla \cdot \mathbf{u}^*) = \dot{Q}^* + \nabla \cdot (\kappa^* \nabla T^*) + [\nabla \cdot (\Pi_{ij}^* \cdot \mathbf{u}^*) - (\nabla \cdot \Pi_{ij}^*) \cdot \mathbf{u}^*]. \tag{2.45}$$

The last group of terms on the right-hand side of Equation (2.45) is known as the dissipation function and is generally given the symbol Φ^*. It represents the heat equivalent of the rate at which mechanical energy is expended in the process of deformation of the fluid due to viscosity. Rewriting Equation (2.45) using the definition of the dissipation function, we get the following form of the energy equation:

$$\rho^* \frac{De^*}{Dt^*} + p^* (\nabla \cdot \mathbf{u}^*) = \dot{Q}^* + \nabla \cdot (\kappa^* \nabla T^*) + \Phi^*. \tag{2.46}$$

The energy equation, as given in (2.46), uses the internal energy of the fluid as the principal variable. Since only low-speed reactive flow of perfect gases will be investigated in this study, the thermal conductivity κ^* can be approximated as constant [13] and the energy equation expressed in terms of the static temperature is the most compact and useful. We can reformulate

Equation (2.46) using the static temperature of the fluid as the principal variable as follows. From the definition of the enthalpy we have

$$h^* \equiv e^* + p^* v^* = e^* + \frac{p^*}{\rho^*} \tag{2.47}$$

where $v^* = 1/\rho^*$ is the specific volume of the fluid. Differentiating the above equation with respect to time, we see that

$$\begin{aligned} \frac{Dh^*}{Dt^*} &= \frac{De^*}{Dt^*} + \frac{D(p^*/\rho^*)}{Dt^*} \\ &= \frac{De^*}{Dt^*} + \left[\frac{\rho^*(Dp^*/Dt^*) - p^*(D\rho^*/Dt^*)}{\rho^{*2}}\right] \\ &= \frac{De^*}{Dt^*} + \frac{1}{\rho^*}\frac{Dp^*}{Dt^*} - \frac{p^*}{\rho^{*2}}\frac{D\rho^*}{Dt^*}. \end{aligned} \tag{2.48}$$

By substituting the continuity equation,

$$\frac{D\rho^*}{Dt^*} = -\rho^*(\nabla \cdot \mathbf{u}^*), \tag{2.49}$$

into Equation (2.48) we get

$$\frac{De^*}{Dt^*} = \frac{Dh^*}{Dt^*} - \frac{1}{\rho^*}\frac{Dp^*}{Dt^*} - \frac{p^*}{\rho^*}(\nabla \cdot \mathbf{u}^*). \tag{2.50}$$

Finally, by substituting the above equation into (2.46) and simplifying the resulting expression, we get the energy equation in terms of the specific enthalpy:

$$\rho^*\frac{Dh^*}{Dt^*} - \frac{Dp^*}{Dt^*} = \dot{Q}^* + \kappa^*\nabla^2 T^* + \Phi^*. \tag{2.51}$$

Notice that in Equation (2.51) the thermal conductivity is assumed to be constant. In general, without specifying the form of the function explicitly, the specific enthalpy can be written as

$$h^* = h^*(p^*, T^*). \tag{2.52}$$

Differentiating the function we get

$$dh^* = \left.\frac{\partial h^*}{\partial T^*}\right|_{p^*} dT^* + \left.\frac{\partial h^*}{\partial p^*}\right|_{T^*} dp^* = \left.\frac{\partial h^*}{\partial T^*}\right|_{p^*} dT^* = \bar{c}_p^* dT^* \tag{2.53}$$

where

$$\left.\frac{\partial h^*}{\partial T^*}\right|_{p^*} \equiv \bar{c}_p^* = \sum_{i=1}^{N} c_{p_i}^* Y_i = \bar{c}_v^* + R^* \tag{2.54}$$

($\bar{c}_p^*$ is the mixture-averaged specific heat at constant pressure). Note that the second equality in Equation (2.53) holds because of the fact that for a perfect gas the internal energy per unit mass e^*, hence h^*, is a function of temperature only. Thus,

$$\left.\frac{\partial h^*}{\partial P^*}\right|_{T^*} = 0 \tag{2.55}$$

identically and

$$\frac{Dh^*}{Dt^*} = \bar{c}_p^* \frac{DT^*}{Dt^*}. \tag{2.56}$$

Substituting Equation (2.56) into (2.51), we obtain the energy equation in terms of the static temperature:

$$\rho^* \frac{DT^*}{Dt^*} - \left(\frac{\gamma - 1}{\gamma R^*}\right) \frac{Dp^*}{Dt^*} = \left(\frac{\gamma - 1}{\gamma R^*}\right) [\, H^* \dot{r}_F^* + \kappa^* \nabla^2 T^* + \Phi^*]. \tag{2.57}$$

In Equation (2.57) $\gamma = \bar{c}_p^* / \bar{c}_v^*$ is the ratio of the specific heats, $\dot{Q}^* \equiv H^* \dot{r}_F^*$ where H^* is the heat of reaction per unit fuel burned and $\dot{r}_F^*$ is the time rate of fuel consumption per unit volume,[1] and $R^* \equiv \tilde{R}^*/\overline{W}^*$ is the gas constant where $\tilde{R}^*$ is the universal gas constant and

$$\overline{W}^* = \frac{1}{\sum_{i=1}^{N} (Y_i / W_i^*)} \tag{2.58}$$

is the mixture-averaged molecular weight of the working fluid (Y_i and W_i^* are the mass fraction and the molecular weight of species i, respectively).

2.1.5 THE CHEMICAL EQUATION

In practical combustion devices, fuels are normally burned with air. Dry air is a mixture of gases that has a representative composition by volume of 20.95% oxygen, 78.09% nitrogen, 0.93% argon, and traces amount of carbon dioxide, neon, helium, methane, and other gases [61]. In a combustion process, oxygen is the main reactive component of air. It is usually sufficient to

---

[1] Note that $\dot{r}_F^*$ is the mass rate of fuel consumption per unit volume, which is differ from $\dot{R}_F^*$, the molar rate of fuel consumption per unit volume, by a factor of $1/W_F^*$.

assume air as consisting of 21% oxygen and 79% inert gases taken as nitrogen (commonly know as atmospheric nitrogen). For the purpose of computations, we can assume that there are approximately 3.773 moles of atmospheric nitrogen for each mole of oxygen.

In combustion, it is possible to oxidize a hydrocarbon fuel completely if sufficient amount of air is provided. The carbon in the fuel then will be converted to carbon dioxide and the hydrogen will be converted to water. The nitrogen in the air is generally not affected significantly by the combustion if the products of reaction are at relatively low temperature. In that case, the nitrogen serves as a diluent and the overall single-step, irreversible reaction equation for a general hydrocarbon fuel of average molecular composition C_aH_b with air is [61]

$$C_aH_b + \left(a + \frac{b}{4}\right)\left(O_2 + 3.773N_2\right) \rightarrow aCO_2 + \frac{b}{2}H_2O + 3.773\left(a + \frac{b}{4}\right)N_2 . \qquad (2.59)$$

Notice that Equation (2.59) only relates the elemental composition of the reactant and product species for complete reaction, it does not indicate the process by which combustion proceeds, which is much more complex. Nonetheless, the use of Equation (2.59) in reactive flow simulations is usually sufficient and can be justified when there is a slow rate-determining step in the combustion process, which is clearly the case in the present study.

As mentioned in the Introduction, the main emphasis of this research is on the aerodynamic aspects of the flow, rather than the chemical kinetics or the reaction mechanisms. The main reason for including a chemical equation in the simulations is for calculating the thermal energy released from combustion. Thus, it is unnecessary for us to consider the fuel and air compositions in detail, and the following generic chemical equation can instead be used in the simulations:

$$F + \alpha O + \beta D \rightarrow \sigma P + \beta D \qquad (2.60)$$

where F, O, D, P represent the fuel, oxidizer, diluent, and products, respectively; α, and σ are the stoichiometric coefficients, *per mole of fuel*, of the oxidizer and products, respectively; and β is the total number of moles of diluent per α moles of oxidizer.[1] Using Equation (2.60) in numerical simulations, the effects of the thermal energy released from chemical reaction on the flow dynamics can conveniently be investigated without having to worry about the complex details of the chemical species and the reaction mechanisms.

---

1. Note that in all the simulations performed in this research, the mole fraction of the diluent is always much greater than the mole fractions of the reactants and the products.

2.2 NONDIMENSIONAL FORM OF THE GOVERNING EQUATIONS AND THE LOW-MACH-NUMBER APPROXIMATION

The governing equations for a multi-component, reactive, perfect-gas mixture have been presented in the last section. For convenience, the final forms of the equations, in terms of the primitive variables, are summarized in Table 2.1 below[1]

Continuity

$$\frac{D\rho^*}{Dt^*} + \rho^* \left(\nabla \cdot \mathbf{u}^*\right) = 0 \tag{2.61}$$

Species conservation

$$\frac{DC_i^*}{Dt^*} = D_{iM}^* \nabla^2 C_i^* - \dot{R}_i^* \qquad (i = F, O) \tag{2.62}$$

Momentum

$$\rho^* \frac{Du^*}{Dt^*} = -\nabla p^* + \nabla \cdot \tau_{ij}^* \tag{2.63}$$

Energy

$$\rho^* \frac{DT^*}{Dt^*} - \left(\frac{\gamma - 1}{\gamma R^*}\right) \frac{Dp^*}{Dt^*} = \left(\frac{\gamma - 1}{\gamma R^*}\right) \left[H^* \dot{r}_F^* + \kappa^* \nabla^2 T^* + \Phi^* \right] \tag{2.64}$$

Equation of state

$$p^* = \rho^* R^* T^* \tag{2.65}$$

Reaction

$$F + \alpha O + \beta D \rightarrow \sigma P + \beta D \tag{2.66}$$

Table 2.1 General governing equations for a multi-component, reactive, perfect-gas mixture.

It should be pointed out that the governing equations as given in Table 2.1, although somewhat general, are strictly valid only under the imposed assumptions when these equations were derived. In general, for numerical computations, it is more convenient if all the governing equations are nondimensional. The main advantage of nondimensionalizing the governing equations is that the characteristic parameters of the flow such as Reynolds number, Mach number, Prandtl number, etc., can be altered independently and their effects on the flow field be investigated separately. Furthermore, by normalizing the equations, it is possible to perform *order-of-magni-*

---

[1] Note the we have neglected the species equation for the diluent and the products. Since the diluent is assumed to be nonreactive, the purpose for including it in the chemical equation is for diluting the reactants and to act as a heat sink when the reaction is exothermic. Thus, the species conservation equation for the diluent is $DC_D^*/Dt^* = 0$ since $D_{DM}^* = D_{DD}^* = 0$ and $\dot{R}_D^* = 0$. As for the products, since only N-1 of the N mass fractions in the mixture are independent in any given problem, we can use either N species equations or N-1 species equations plus the overall continuity equation. In this case, we have chosen the later.

tude analysis on individual term in the equations and to discard terms that are identically zero or physically negligible in order to obtain simpler equations for the special situation under consideration. Many nondimensionalizing procedures are possible by selecting the appropriate reference quantities. To carry out the normalization procedure, let's introduce some dimensionless variables:

$$r = \frac{r^*}{D_a^*} \qquad u = \frac{u^*}{U_a^*} \qquad t = \frac{t^* U_a^*}{D_a^*} \qquad \mu = \frac{\mu^*}{\mu_r^*} \qquad \rho = \frac{\rho^*}{\rho_r^*}$$

$$T = \frac{T^*}{T_r^*} \qquad p = \frac{p^*}{\rho_r^* R^* T_r^*} \qquad C_i = \frac{C_i^*}{C_{F_o}^*} \qquad H = \frac{H^*}{\bar{c}_p^* T_r^*}$$

where p_r^*, T_r^*, ρ_r^*, μ_r^*, κ_r^*, $\bar{c}_p^*$ are the reference pressure, temperature, density, dynamic viscosity coefficient, thermal conductivity, and specific heat at constant pressure taken at the appropriate reference condition; U_a^*, D_a^* are the magnitude of the annular inflow velocity and the diameter of the combustor, respectively. A straightforward substitution of the above dimensionless variables into the equations and simplifying the results, the following nondimensional governing equations are obtained

Continuity	$\frac{D\rho}{Dt} + \rho(\nabla \cdot \mathbf{u}) = 0$		(2.67)
Species conservation	$\frac{DC_i}{Dt} = \frac{1}{PeLe}\nabla^2 C_i - A_F\dot{w}$	$(i = F, O)$	(2.68)
Momentum	$(\gamma M^2)\rho\frac{D\mathbf{u}}{Dt} = -\nabla p + \left(\frac{\gamma M^2}{Re_{D_a}}\right)(\nabla \cdot \tau_{ij})$		(2.69)
Energy	$\rho\frac{DT}{Dt} - \left(\frac{\gamma-1}{\gamma}\right)\frac{Dp}{Dt} = HA_F\dot{w} + \frac{1}{Pe}\nabla^2 T + \frac{(\gamma-1)M^2}{Re_{D_a}}\Phi$		(2.70)
Equation of state	$p = \rho T$		(2.71)
Reaction	$F + \alpha O + \beta D \rightarrow \sigma P + \beta D$		(2.72)

Table 2.2 Dimensionless governing equations for a multi-component, reactive, perfect-gas mixture.

The dimensionless parameters appearing in these equations are the Lewis number, $Le = Pr/Sc$, where $Pr = (\bar{c}_p^* \mu^*)/\kappa^*$ is the Prandtl number and $Sc = \mu^*/D_{iM}^*$ is the Schmidt number, the Reynolds number based on the combustor diameter, $Re_{D_a} = (\rho_r^* U_a^* D_a^*)/\mu_r^*$, the Peclet number, $Pe = Re_{D_a} Pr$, the Mach number $M = U_a^*/\sqrt{\gamma R^* T_r^*}$, and the rate of product formation per unit time, $A_F \dot{w}$, where A_F is the frequency factor.

The normalized governing equations, as presented in Table 2.2, are valid for a flow of reactive, perfect-gas mixture at arbitrary Mach number. This set of equations contains highly nonlinear coupling of the vorticity, entropy, and acoustic modes, a fact that can be established by analyzing the linearized equations [34, 88]. Detailed numerical solutions using this set of equations are prohibitively expensive, if possible, due to the existence of a wide range of length and time scales associated with the evolution of the flow described by these equations. Furthermore, the existence of high-frequency acoustic waves in the flow places a severe restriction on the size of the time step that can be used to integrate the governing equations. Thus, it is advantageous to filter out the influences of the acoustic mode from the equations if possible. It is well-known that for flows where the convective flow time scales are large with respect to the pressure wave propagation, that is, the Mach number is small compared to unity, and the length scales relevant to the convective dynamics are either compatible or significantly larger than those relevant to the propagation of the pressure wave, the acoustic mode is generally concentrated in a frequency band which is much higher than the other two modes. In the asymptotic limit as the Mach number approaches zero, the energy in the acoustic waves is negligibly small compared with both the energy of the fluid convection velocity and the thermodynamic internal energy [92]. Consequently, it is possible to apply the regular perturbation techniques to the governing equations in order to obtain a set of approximate equations that is asymptotically valid for small Mach number. Although certain physical features of real reactive flows will not be able to be captured by the simplified governing equations, we are still able to study in detail of the effects of heat release on the large-scale structure, the mixing field, and the vorticity dynamics of the reactive flows with the simplified governing equations.

Starting with the nondimensional equations presented in Table 2.2, the set of approximate governing equations can be obtained by performing asymptotic expansions on the gas dynamic variables in terms of a small perturbation parameter η, where $\eta \equiv \gamma M^2$ [143]. Let ζ denotes any nondimensional gas dynamics variables p, T, ρ, or **u** and assume that for small but finite η, all the variables can be expanded in terms of a perturbation series in the form

$$\zeta(\mathbf{x},t) = \zeta_0(\mathbf{x},t) + \eta\zeta_1(\mathbf{x},t) + \eta^2\zeta_2(\mathbf{x},t) + \ldots \tag{2.73}$$

A straightforward substitution of these expansions into the conservation equations and collecting all the terms in the equations which are independent of η, we get the following set of zeroth-order equations:

Continuity	$\frac{D\rho_0}{Dt} + \rho_0(\nabla \cdot \mathbf{u}_0) = 0$		(2.74)
Species conservation	$\frac{DC_{i0}}{Dt} = \frac{1}{PeLe}\nabla^2 C_{i0} - A_F\dot{w}$	$(i = F, O)$	(2.75)
Momentum	$\nabla p_0 = 0$		(2.76)
Energy	$\rho_0\frac{DT_0}{Dt} - \left(\frac{\gamma - 1}{\gamma}\right)\frac{Dp_0}{Dt} = HA_F\dot{w} + \frac{1}{Pe}\nabla^2 T_0$		(2.77)
Equation of state	$p_0 = \rho_0 T_0$		(2.78)

Table 2.3 Governing equations for a reactive, perfect-gas mixture with the low-Mach-number assumption and constant thermodynamic pressure p_0.

Notice that the momentum equation has been reduced to a description of the spatial variation of the thermodynamic pressure p_0 from the small-parameter expansion procedure. This is due to the fact that although the thermodynamic pressure p_0 is small enough to have no significant influence on the variation of density or temperature under the low-Mach-number assumption, it is of the same order of magnitude as the acceleration of the fluid elements. Thus, it cannot be neglected in the momentum equation [129]. In order to obtain an equation for the complete description of the velocity field, the first-order momentum equation in the expansion must be retained. The equation is given by

$$\rho_0\frac{D\mathbf{u}_0}{Dt} = -\nabla p_1 + \left(\frac{1}{Re_{D_a}}\right)(\nabla \cdot \tau_{ij_0}). \tag{2.79}$$

As discussed in Section 2.1.3, it is advantageous to describe the flow field in terms of the spatial distribution of the vorticity field for high-Reynolds-number flows. Applying the same vector operations to the simplified momentum equation (2.79), we obtain the corresponding zeroth-order vorticity transport equation

$$\frac{D\Omega_0}{Dt} + \Omega_0(\nabla \cdot \mathbf{u}_0) - \Omega_0 \cdot \nabla\mathbf{u}_0 = \frac{1}{\rho_0^2}\nabla\rho_0 \times \nabla p_1 + \left(\frac{1}{Re_{D_a}}\right)\left\{\frac{1}{\rho_0^2}[\nabla \cdot \tau_{ij_0} \times \nabla\rho_0] + \frac{1}{\rho_0}[\nabla \times \nabla \cdot \tau_{ij_0}]\right\}. \tag{2.80}$$

It should be note that all the dependent variables in the approximate equations appeared only to the zeroth-order except the pressure, for which both p_0 and p_1 appeared in the equations. The distinction between the two pressures is essential both from a theoretical point of view and in the numerical solution procedure. As mentioned above, the zeroth-order pressure, p_0, is commonly known as the thermodynamic pressure. The second component of the pressure, p_1, appeared in the η–component of the expansion of the momentum equation, is generally referred to as the hydrodynamic pressure. It is generated in the flow field to balance the changes in momentum and does not participate directly in the thermodynamic processes. The zeroth-order momentum equation $\nabla p_0 = 0$ simply states the fact that, under the low-Mach-number assumption, the largest component of the pressure in the flow field p_0 is uniform in space but may vary with time due to the addition of thermal energy. Essentially, it means that the speed of sound is infinitely fast compared with the convection speed of the fluid so that disturbances in the thermodynamic pressure caused by combustion are felt instantaneously throughout the whole flow field. For an open flow domain, such as the one used in this research, the thermal energy released from exothermic reaction alters primarily the fluid temperature and density. The temporal and spatial variations of p_0 is usually small due to the low level of thermal energy released from the combustion process [93, 101, 128]. For the sake of simplicity, we will assume p_0 is approximately constant. In that case, the second term on the left-hand side of Equation (2.77) is identically zero.

Before proceeding any further, we should emphasize that in order for the low-Mach-number approximation to remain valid, the rate of thermal energy production $H A_f \dot{w}$ must be restricted. This can easily be seen from the energy equation. If this condition is not met, significantly large local expansion velocity will be generated from the combustion and the low-Mach-number assumption will cease to be valid. The above approximate equations, obtained from the low-Mach-number assumption, are summarized in Table 2.4 (with the momentum equation replaced by the vorticity transport equation). For clarity, all the subscript "o" on the gas dynamic variables have been removed except for the pressure term, which we retain to distinguish the difference between p_0 and p_1. Notice that the set of approximate equations, as presented in Table 2.4, has the computational advantage that acoustic waves are filtered out, thus relieving the time step size constraint but at the same time, still allowing the flow field to have significant density nonuniformities.

Continuity

$$\frac{D\rho}{Dt} + \rho\,(\nabla \cdot \mathbf{u}) = 0 \tag{2.81}$$

Species conservation

$$\frac{DC_i}{Dt} = \frac{1}{PeLe}\nabla^2 C_i - A_F\dot{w} \qquad (i = F, O) \tag{2.82}$$

Vorticity transport

$$\frac{D\Omega}{Dt} + \Omega\,(\nabla \cdot \mathbf{u}) - \Omega \cdot \nabla \mathbf{u} = \frac{1}{\rho^2}\nabla\rho \times \nabla p_1 + \left(\frac{1}{Re_{D_a}}\right)\left\{\frac{1}{\rho^2}[\nabla \cdot \tau_{ij} \times \nabla\rho] + \frac{1}{\rho}[\nabla \times \nabla \cdot \tau_{ij}]\right\} \tag{2.83}$$

Energy

$$\rho\frac{DT}{Dt} = \frac{1}{Pe}\nabla^2 T + H A_F \dot{w} \tag{2.84}$$

Equation of state

$$p_0 = \rho T = \text{constant} \tag{2.85}$$

Reaction

$$F + \alpha O + \beta D \rightarrow \sigma P + \beta D \tag{2.86}$$

Table 2.4 Governing equations for a reactive, perfect-gas mixture with the low-Mach-number assumption and constant thermodynamic pressure p_0.

2.3 GOVERNING EQUATIONS FOR AN AXISYMMETRIC FLOW DOMAIN EXPRESSED IN TERMS OF VORTICITY AND STREAM FUNCTION

The governing equations given in Table 2.4 provide a complete description of a three-dimensional, reactive, perfect-gas mixture of three species under the assumptions of low Mach number and constant thermodynamic pressure p_0. As discussed in Chapter 1, the focus of this research is on the investigation of the dynamics of the quasi-axisymmetric, large-scale flow structures and the large-scale entrainment and mixing in the near-wake region of a confined, axisymmetric bluff-body combustor. The study will be carried out in the context of an axisymmetric flow with zero swirl. Under this assumption, the motion of the fluid in any longitudinal plane passing through the axis of symmetry is identical, and the variations of all flow properties in the azimuthal coordinate direction, $\partial/\partial\theta$, are zero (θ is the azimuthal coordinate in a cylindrical polar coordinate system). Thus, the equations given in Table 2.4 can further be simplified considerably with the additional assumption. Furthermore, the numerical scheme used in this research is the *vortex-scalar element method*, which is a Lagrangian scheme employing vorticity-stream function formulation. Therefore, in this section we will reformulate the governing equations given in Table 2.4 using vorticity and stream function as the primary variables and to apply the additional assumptions in order to obtain the final set of equations used in the simulations of this research.

As shown by Majda and Sethian [92], for reactive-flow calculations using the vortex method, a more convenient form of the continuity equation can be obtained by combining Equations (2.81) and (2.85). First by differentiating Equation (2.85) we get

$$\frac{Dp_0}{Dt} = \frac{D\rho}{Dt}T + \rho\frac{DT}{Dt} = 0 \tag{2.87}$$

since p_0 is assumed constant in this study. Substituting Equation (2.87) into the overall continuity equation, the following equation is obtained:

$$\nabla \cdot \mathbf{u} = \frac{1}{T}\frac{DT}{Dt}. \tag{2.88}$$

Equation (2.88) describes the hydrodynamics-combustion interaction in terms of the volumetric expansion produced by the release of thermal energy from chemical reaction. The second part of the dynamical role of combustion, baroclinic vorticity generation due to the variable density field, is captured by the vorticity transport equation (2.83). For an axisymmetric flow with zero swirl, only one component of the vorticity vector has non-zero value and this component has a unit vector in the azimuthal coordinate direction: $\Omega = (\zeta, \omega, \xi) = (0, \omega, 0)$. Thus, the vorticity transport equation can significantly be simplified. Specifically, the third term on the left-hand side of Equation (2.83) is equal to

$$\Omega \cdot \nabla \mathbf{u} = \left[\zeta\left(\frac{\partial}{\partial r}\right) + \omega\left(\frac{1}{r}\frac{\partial}{\partial \theta}\right) + \xi\left(\frac{\partial}{\partial z}\right)\right]\mathbf{u}. \tag{2.89}$$

Since $\mathbf{u} = (v, w, u)$, thus

$$\Omega \cdot \nabla \mathbf{u} = \zeta\left[\frac{\partial v}{\partial r}\mathbf{e}_r + v\frac{\partial \mathbf{e}_r}{\partial r} + \frac{\partial w}{\partial r}\mathbf{e}_\theta + w\frac{\partial \mathbf{e}_\theta}{\partial r} + \frac{\partial u}{\partial r}\mathbf{e}_z + u\frac{\partial \mathbf{e}_z}{\partial r}\right] +$$

$$\frac{\omega}{r}\left[\frac{\partial v}{\partial \theta}\mathbf{e}_r + v\frac{\partial \mathbf{e}_r}{\partial \theta} + \frac{\partial w}{\partial \theta}\mathbf{e}_\theta + w\frac{\partial \mathbf{e}_\theta}{\partial \theta} + \frac{\partial u}{\partial \theta}\mathbf{e}_z + u\frac{\partial \mathbf{e}_z}{\partial \theta}\right] +$$

$$\xi\left[\frac{\partial v}{\partial z}\mathbf{e}_r + v\frac{\partial \mathbf{e}_r}{\partial z} + \frac{\partial w}{\partial z}\mathbf{e}_\theta + w\frac{\partial \mathbf{e}_\theta}{\partial z} + \frac{\partial u}{\partial z}\mathbf{e}_z + u\frac{\partial \mathbf{e}_z}{\partial z}\right]. \qquad (2.90)$$

Note that since ζ, ξ, w, and $\partial/\partial\theta$ are all equal to zero, hence, $\Omega \cdot \nabla \mathbf{u} = 0$ for an axisymmetric flow with zero swirl, and the vorticity transport equation becomes

$$\frac{D\omega}{Dt} + \omega(\nabla \cdot \mathbf{u}) = \frac{1}{\rho^2}\nabla\rho \times \nabla p_1 + \left(\frac{1}{Re_{D_a}}\right)\left\{\frac{1}{\rho^2}[\nabla \cdot \tau_{ij} \times \nabla\rho] + \frac{1}{\rho}[\nabla \times \nabla \cdot \tau_{ij}]\right\}. \qquad (2.91)$$

Again, for an anelastic flow or an incompressible flow with constant coefficient of viscosity, we can further reduce the vorticity transport equation to

$$\frac{D\omega}{Dt} = \frac{1}{\rho^2}\nabla\rho \times \nabla p_1 + \left(\frac{1}{Re_{D_a}}\right)\nabla^2\omega. \qquad (2.92)$$

The two modes of hydrodynamics-combustion interactions, volumetric expansion and vorticity generation, can be analyzed separately using the Helmholz-Hodge Decomposition Theorem [20]. The theorem states that any vector field $\mathbf{s}$ on a domain D can be uniquely decomposed in the form

$$\mathbf{s} = \mathbf{x} + \nabla\phi \qquad (2.93)$$

where $\mathbf{x}$ and $\nabla\phi$ represent a divergence-free and an irrotational vector field, respectively. From classical hydrodynamics, it is known that the instantaneous relative motion of the fluid in a small neighborhood of any point in the flow field is a combination of (1) an isotropic expansion such that the rate of increase of volume of a material element, per unit volume, is ε ($\nabla \cdot \mathbf{u} = \varepsilon$), (2) a pure straining motion without change of volume of the fluid element, and (3) a rigid-body rotation with an angular velocity equal to one-half of Ω. Denoting these three quantitatively different vector fields by $\mathbf{u}_\varepsilon$, $\mathbf{u}_\varphi$, and $\mathbf{u}_\omega$, respectively, the total velocity field $\mathbf{u}$ can be synthesized using these three vector fields as

$$\mathbf{u} = \mathbf{u}_\varepsilon + \mathbf{u}_\varphi + \mathbf{u}_\omega. \qquad (2.94)$$

Notice that the three vector fields used to synthesize $\mathbf{u}$ have the following general properties

$$\nabla \cdot \mathbf{u}_\varepsilon = \varepsilon, \qquad \nabla \times \mathbf{u}_\varepsilon = 0 \qquad \text{(irrotational)} \qquad (2.95)$$

$$\nabla \cdot \mathbf{u}_\varphi = 0, \qquad \nabla \times \mathbf{u}_\varphi = 0 \qquad \text{(solenoidal and irrotational)} \tag{2.96}$$

$$\nabla \cdot \mathbf{u}_\omega = 0, \qquad \nabla \times \mathbf{u}_\omega = \Omega \qquad \text{(solenoidal and rotational)} \tag{2.97}$$

where ε and Ω are the local divergence and curl of **u**, respectively. $\mathbf{u}_\omega$ is generally known as the *velocity induced by vorticity* and $\mathbf{u}_\varepsilon$ is known as the *velocity induced by divergence*. It should be pointed out that the two velocity fields $\mathbf{u}_\varepsilon$ and $\mathbf{u}_\omega$ are generally defined in an infinite domain and contain no information about the boundaries of the flow domain. In particular, the flow field represents by $(\mathbf{u}_\omega + \mathbf{u}_\varepsilon)$ would pass through a solid wall of the enclosure, and would have vanishingly small velocity at points which are sufficiently far away from the region containing the dilation and the vorticity. To correct this problem, $\mathbf{u}_\varphi$ is prescribed on the boundaries of the flow domain; it provides the required corrections to have the $(\mathbf{u}_\omega + \mathbf{u}_\varepsilon)$ velocity field to conform to a specified normal velocity at the domain boundaries. That is, for the boundaries of the flow domain ∂D we have

$$\mathbf{u}_\varphi \cdot \mathbf{n} = (\mathbf{u} \cdot \mathbf{n}) - (\mathbf{u}_\varepsilon + \mathbf{u}_\omega) \cdot \mathbf{n} \tag{2.98}$$

where **n** is the unit normal on a boundary of the enclosure and $\mathbf{u} \cdot \mathbf{n}$ is the prescribed velocity on that boundary. For a fixed, solid-wall boundary, $\mathbf{u} \cdot \mathbf{n} = 0$ and the boundary condition becomes

$$\mathbf{u}_\varphi \cdot \mathbf{n} = -(\mathbf{u}_\varepsilon + \mathbf{u}_\omega) \cdot \mathbf{n}. \tag{2.99}$$

As discussed earlier, since both $\mathbf{u}_\varphi$ and $\mathbf{u}_\varepsilon$ are irrotational, an irrotational vector field $\mathbf{v} = \mathbf{u}_\varphi + \mathbf{u}_\varepsilon$ can be defined. In addition, there exists a velocity potential φ such that $\mathbf{v} = \nabla\varphi$. Moreover, the equation governing the velocity potential can be obtained by substituting the total velocity, $\mathbf{u} = \mathbf{u}_\omega + \mathbf{u}_\varphi + \mathbf{u}_\varepsilon = \mathbf{u}_\omega + \mathbf{v} = \mathbf{u}_\omega + \nabla\varphi$, into Equation (2.88)

$$\nabla \cdot \mathbf{u} = \nabla \cdot (\mathbf{u}_\omega + \nabla\varphi) = (\nabla \cdot \mathbf{u}_\omega) + \nabla^2\varphi = \frac{1}{T}\frac{DT}{Dt}. \tag{2.100}$$

Since $\mathbf{u}_\omega$ is solenoidal by construction (that is, $\nabla \cdot \mathbf{u}_\omega = 0$) and $\nabla \cdot (\nabla\varphi) = \nabla \cdot (\mathbf{u}_\varepsilon + \mathbf{u}_\varphi) = \nabla \cdot \mathbf{u}_\varepsilon = \varepsilon$, Equation (2.100) is reduced to

$$\nabla \cdot \mathbf{u} = \nabla^2\varphi = \frac{1}{T}\frac{DT}{Dt} = \varepsilon, \tag{2.101}$$

which is the classical Poisson equation with a source term $\varepsilon = \frac{1}{T}\frac{DT}{Dt}$ on the right-hand side of the equation. Notice that by using the velocity potential, the computational effort is reduced considerably by transforming the problem from one with two independent variables (the two components of the potential velocity) to a problem with only one unknown function φ.

Consider next the vector field $\mathbf{u}_\omega$. Since $\mathbf{u}_\omega$ has zero divergence but whose rotation is not zero, a velocity potential cannot be defined for $\mathbf{u}_\omega$. However, for axisymmetric flow there exists a function known as the *Stokes stream function*. This function can be defined for a rotational flow field which can used to relate the velocity components v and u [81]. Furthermore, it is also possible to derive a governing equation relating the stream function to the vorticity in the flow domain. As shown by Lamb [81], a stream function ψ can be defined for an axisymmetric flow such that

$$\rho v = \frac{-1}{r}\frac{\partial \psi}{\partial z}, \qquad \rho u = \frac{1}{r}\frac{\partial \psi}{\partial r}. \tag{2.102}$$

Since the relationships between v, u and the derivatives of the stream function are based on the principle of conservation of mass, the continuity equation is automatically satisfied by the stream function. Now, taking the cross product of the total velocity $\mathbf{u}$ we get

$$\nabla \times \mathbf{u} = \nabla \times (\mathbf{u}_\varepsilon + \mathbf{u}_\varphi + \mathbf{u}_\omega) = \nabla \times (\mathbf{u}_\varepsilon + \mathbf{u}_\varphi) + \nabla \times \mathbf{u}_\omega. \tag{2.103}$$

Because $(\mathbf{u}_\varepsilon + \mathbf{u}_\varphi)$ is irrotational, therefore, $\nabla \times (\mathbf{u}_\varepsilon + \mathbf{u}_\varphi) = 0$ and we have

$$\nabla \times \mathbf{u} = \nabla \times \mathbf{u}_\omega = \omega \tag{2.104}$$

since $\nabla \times \mathbf{u}_\omega = \Omega = (0, \omega, 0)$. If the flow is anelastic or incompressible with constant density, we can combine Equations (2.102) and (2.104) to obtain a Poisson equation relating the stream function and the vorticity:

$$\nabla^2 \psi = -\omega. \tag{2.105}$$

The final set of governing equations for an axisymmetric flow domain, arrived at the low-Mach-number assumption with constant thermodynamic pressure, is presented in Table 2.5. These equations will be used throughout this research. The numerical schemes use in this research will be developed in the next chapter.

$$\mathbf{u} = (\mathbf{u}_\varepsilon + \mathbf{u}_\varphi) + \mathbf{u}_\omega = \mathbf{v} + \mathbf{u}_\omega \tag{2.106}$$

$$\mathbf{v} = \nabla\varphi \tag{2.107}$$

$$\nabla^2\varphi = \frac{1}{T}\frac{DT}{Dt} = \varepsilon \tag{2.108}$$

$$\mathbf{u}_\omega = \nabla\psi \tag{2.109}$$

$$\nabla^2\psi = -\omega \tag{2.110}$$

$$\frac{D\omega}{Dt} + \omega(\nabla\cdot\mathbf{u}) = \frac{1}{\rho^2}\nabla\rho\times\nabla p_1 + \left(\frac{1}{Re_{D_a}}\right)\left\{\frac{1}{\rho^2}[\nabla\cdot\tau_{ij}\times\nabla\rho] + \frac{1}{\rho}[\nabla\times\nabla\cdot\tau_{ij}]\right\} \tag{2.111}$$

$$\rho\frac{DT}{Dt} = \frac{1}{Pe}\nabla^2 T + HA_F\dot{w} \tag{2.112}$$

$$\frac{DC_i}{Dt} = \frac{1}{PeLe}\nabla^2 C_i - A_F\dot{w} \qquad (i = F, O) \tag{2.113}$$

$$F + \alpha O + \beta D \rightarrow \sigma P + \beta D \tag{2.114}$$

$$p_0 = \rho_T = \text{constant} \tag{2.115}$$

where

$$\mathbf{r} = (r,z) \tag{2.116}$$

$$\nabla = \left(\frac{\partial}{\partial r}\right)\mathbf{e}_r + \left(\frac{\partial}{\partial z}\right)\mathbf{e}_z \tag{2.117}$$

and

$$\nabla^2 = \frac{1}{r}\frac{\partial}{\partial r}\left(r\frac{\partial}{\partial r}\right) + \frac{\partial^2}{\partial z^2}. \tag{2.118}$$

Table 2.5 Axisymmetric governing equations for a three-component, reactive, perfect-gas mixture with the low-Mach-number assumption and constant thermodynamic pressure.

3. NUMERICAL SCHEMES

Numerical analysis of post-transitional flow has traditionally been carried out using finite difference discretization of the averaged Navier-Stokes equations, supplemented by eddy-viscosity turbulence closure (see the discussion in the Introduction). Results obtained from these simulations have proven that this approach is able to quantitatively capture most of the mean flow features. However, its success at predicting the fluctuating scalar quantities, such as the unsteady temperature or the product concentration field, has been limited [22, 40]. It is speculated that the correct prediction of the mean flow properties, such as the velocity, is due to the fact that over most of the flow domain the inertia terms in the governing equations dominated over the fluctuation terms. Correct evaluation of the fluctuating flow properties, on the other hand, is critically dependent upon and limited by the effectiveness of the turbulence model employed in the simulation. It is well-known that a simulation employing the time-averaged Navier-Stokes equations is adequate for an engineering problem where the flow is dominated by homogeneous turbulence; however, the approach is inappropriate for a flow which is dominated by large-scale coherent structures. It was pointed out by Libby and Williams that when coherent structures are present in a flow, the usual picture of turbulence dynamics involving the cascading of large-scale eddies into smaller dissipative scales must be modified to account for the evolution of the coherent structures which may increase in size, by pairing and merging, in the downstream direction [86]. The existence of coherent structures in a flow implies that an unconditional average overlooks and disregards this important physical phenomenon. Currently, no known turbulence closure model has taken into account the contribution of the coherent structures. Thus, a closure model optimized for a given type of flows is usually not adequate for predicting the behaviors of the flow in other configurations. Furthermore, if most of the interesting turbulence dynamics of a flow is modeled a priori, the outcome of the numerical computations based on these turbulence models cannot substantially advance our understanding of turbulent flows. Since the Navier-Stokes equations describe flows in both the laminar and turbulent regimes, a better way to investigate post-transitional flows numerically is to solve the Navier-Stokes equations directly without employing any of the conventional averaging procedure and closure models. Such an approach, in comparison with calculations using turbulence models, has the advantage that modelling of the physics is kept to a minimum, and most of the turbulence dynamics can be recovered directly from the computational results. Thus the results can further be used to understand many important mechanisms of turbulent transport and their direct coupling with chemical kinetics in turbulent reactive flows.

Owing to the presence of the bluff body and the confinement, confined bluff-body flows always carry vorticity. Moreover, the vortical structures being generated in the flow field can often grow to the same size as the enclosure of the flow [93]. Thus, from the above discussion, it is clear that conventional numerical schemes with eddy-viscosity turbulence closures are unsuitable as the numerical tools for this research. It has been suggested and demonstrated that this class of confined, axisymmetric bluff-body flows can best be analyzed in terms of the semi-deterministic vortical structures since their dynamics are relatively insensitive to the small-scale turbulence [43, 44, 93]. Therefore, the axisymmetric *vortex-scalar element method*, a Lagrangian numerical scheme employing finite-area vortex and scalar ring elements to discretize the vorticity and the scalar field, respectively, is proposed to be used as the numerical tool for this research.

The axisymmetric vortex-scalar element method is an extension of the two-dimensional vortex method developed by Chorin for solving high-Reynolds-number nonreactive flows [19, 20]. The method has been used successfully by Ghoniem *et al.* for obtaining numerical solutions to the unsteady Navier-Stokes equations at relatively high Reynolds numbers [46, 47, 48, 52, 93], and has been used to reveal the unsteady development of intrinsically unstable flow discontinuities [45, 46].

The classical two-dimensional vortex method divides the flow domain into an interior and a wall region. The wall region is a relatively thin *numerical shear layer* within which Prandtl's boundary layer approximation is applied to the governing equations. Inside the wall region, vortex sheets are used to discretize the vorticity; whereas desingularized vortex elements are used to discretize the vorticity in the interior of the flow domain [20]. In both regions, the viscous splitting technique [9] is used to decompose the vorticity transport equation into an advection and a diffusion component. While advection is expressed in terms of a set of coupled ordinary differential equations and is solved using a second-order predictor-corrector method, molecular diffusion is simulated stochastically by random-walking the vortex elements according to Gaussian statistics [19, 20, 40, 42, 43, 93]. During the course of a simulation, the flow field in each region is solved consecutively and the solution in the wall region is matched to the interior solution at each time step in order to obtain the complete solution. At each time step, vortex sheet elements are generated at the solid wall boundaries to satisfy the no-slip wall boundary condition and a fraction of these elements are being carried out into the flow domain by molecular diffusion (random walk). A major advantage of this approach is that the method bypasses some of the difficulties associated with the convective nonlinearity substantial derivatives of the Navier-Stokes equations. Another advantage of the scheme over other numerical methodologies is its self-adaptive capability. During a simulation, the vortex elements discretizing the vorticity field tend to migrate to regions of high velocity gradients, resulting in an efficient adaptive solution scheme which is capable of capturing serve and rapid distortions of the flow map, while concentrating the computational effort in zones of finite gradients. Using this scheme to investigate high-Reynolds-number flows, minimum computational effort is required for a given numerical accuracy [17, 19, 41, 42, 93].

A rigorous convergence proof has been presented by Beale and Majda [9] showing that viscous-splitting algorithms converge to solutions of the Navier-Stokes equations in all space, at a rate which improves as the fluid viscosity decreases. A complete convergence proof for the vortex method, in which the boundary conditions of a viscous flow are satisfied by vorticity generation on no-slip walls, is not yet available. Nonetheless, many analyses of related schemes and subalgorithms have been performed. Hald [58] was first to prove that in an infinite domain, the solution obtained by an inviscid vortex scheme converges to the solution of the Euler equation provided that all the numerical parameters are chosen appropriately. In his analysis, it was shown that the rate of convergence of the scheme depends on 1) the form of the interpolation or core function, and 2) the ratio between the core radii and the initial separation between vortex elements. Based on this analysis, Beale and Majda [10] were able to constructed a class of core functions that produces arbitrary high-order schemes. In all these studies, however, the flow was assumed to occupy an infinite domain, the total vorticity was assumed constant, and the time integration of the ordinary differential equations governing the convective motion of the vortex elements was assumed to be exact. Anderson and Greengard [2] extended this analysis to include the effect of a finite-order time integration scheme. Numerical experiments were conducted by Nakamura *et al.* [102] to verify these results for an inviscid flow in infinite domain. The accuracy of the two-dimensional vortex method has been checked against well-documented experimental data by Ghoniem, Gagnon, Najm, Givi, Ng, and Martins [42, 45, 46, 47, 50, 51, 93].

3.1 THE AXISYMMETRIC VORTEX-ELEMENT METHOD

For this research, the flow is assumed to be axisymmetric with the motion of the large-scale flow structures approximately the same in every longitudinal plane passing through the axis of symmetry. The numerical scheme used to integrate the hydrodynamic equations is the axisymmetric vortex-element method first used by Martins to study high-Reynolds-number, confined axisymmetric flows [93]. Similar to the two-dimensional vortex method, the viscous-splitting technique is applied to the vorticity transport equation in order to decompose the equation into a convection and a diffusion component. Within the interior of the flow domain, the vorticity field is discretized by a set of finite-area vortex ring elements whose configuration is updated every time step according to the flow governing equations. For the molecular diffusion, an additional deterministic displacement is added to the radial component of the random-walk displacements of the vortex rings [93]. Numerical diffusion is minimized by eliminating the need of having to have a set of grid points in the interior of the flow domain for the discretization of the velocity gradients. Notice that a minimum resolvable length scale is imposed when the continuous vorticity field is discretized by a finite number of discrete vortex ring elements, while the size of the time step used in the numerical integration of the governing equations imposes a minimum time scale.

As discussed earlier in Chapter 1, isothermal reactive flows with different inflow boundary conditions, both steady and time-dependent, first will be investigated. Thus, the dynamics of the quasi-axisymmetric large-scale flow structures and the large-scale entrainment and mixing can be studied in a simpler environment without having to worry about the effects of the thermal energy released from combustion on the flow field. In this case, the incompressible viscous fluid flow model used by Martins is applicable, and the energy equation can be excluded from the solution procedure. For exothermic reactive-flow calculation with low heat release, we will use a model in which the only knowledge about the burning comes from the expansion velocity field generated at the reaction regions in the flow, and from the changing Reynolds number due to the variation of the density field. As will be discussed in Chapter 5, owing to the fast-chemistry assumption and the unique mixing pattern of this bluff-body flow, a large fraction of the fuel reacts completely within the recirculation region a short distance downstream of the jet exit and quickly diluted by the excess air before leaving the recirculation region. In this case, compared to the volumetric expansion term, the effect of the baroclinic vorticity generation is mostly localized and has little impact on the overall vorticity dynamics. The flow field in the near-wake region is affected most significantly by the nonhomogeneous density distribution caused by the thermal expansion of the fluid. For the sake of simplicity, baroclinic vorticity generation will be neglected in the exothermic reactive-flow calculation. Under these assumptions, the hydrodynamic field is decoupled from the scalar field and the formulation of the axisymmetric vortex method can be proceeded without much regard for the effects of the combustion on the vorticity field.

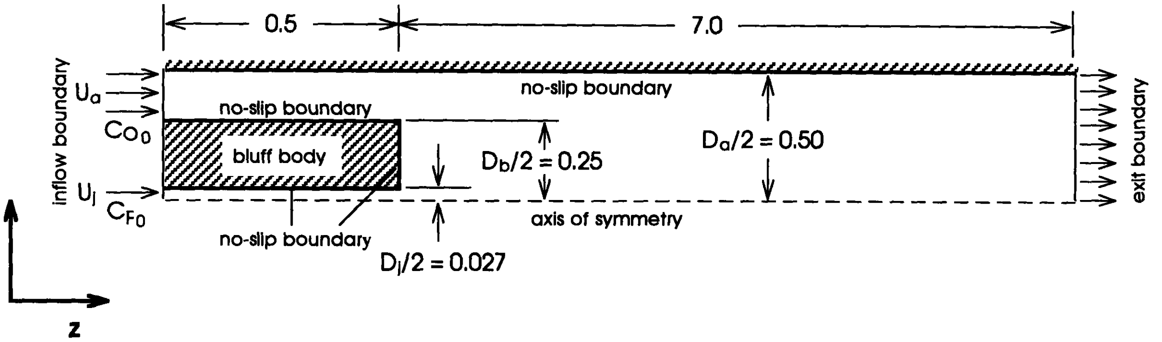

Figure 3.1 Axisymmetric computational domain (geometry not to scale). U_a = annular inflow velocity, U_j = jet inflow velocity, D_a = duct diameter, D_b = bluff-body diameter, and D_j = jet diameter.

3.1.1 Solution for the Vortical Velocity Field in an Axisymmetric, Unbounded, Simply-Connected Flow Domain With a Specified Vorticity Distribution

As shown by Sherman [129], for a flow with nearly constant density and transport properties, or an anelastic flow, the governing equations can be simplified considerably. Under this assumption, the equations governing the time-evolution of the vortical velocity field are [93]

$$\mathbf{u}_\omega = \nabla\psi = \left(\frac{-1}{r}\frac{\partial\psi}{\partial z}, \frac{1}{r}\frac{\partial\psi}{\partial r}\right) = (v_\omega, u_\omega) \tag{3.1}$$

$$\nabla^2\psi = \frac{1}{r}\frac{\partial}{\partial r}\left(r\frac{\partial\psi}{\partial r}\right) + \frac{\partial^2\psi}{\partial z^2} = -\omega(\mathbf{r},t) \tag{3.2}$$

$$\frac{D\omega}{Dt} = \frac{1}{Re_{D_a}}\nabla^2\omega. \tag{3.3}$$

Recall that $\mathbf{u}_\omega$ is the inviscid velocity field due to a specified distribution of vorticity in an unbounded, simply-connected fluid domain at rest at infinity. In this case, no boundary conditions will be imposed on the Poisson equation given in (3.2) for the solution of the stream function. The solution to the equation can be given in term of the Green's function of the Poisson equation [6], and the vortical velocity can be obtained, by integration, from the Biot-Savart integral [122, 129].

As shown by Lamb [81] and Martins [93], the solution to the Poisson equation (3.2) can be expressed as the sum of the complete elliptic integral of the first and second kind

$$\psi(r,z) = \frac{\Gamma}{2\pi}(S_1 + S_2)\,[\mathbf{K}(\lambda) - \mathbf{E}(\lambda)], \qquad 0 \le \lambda \le 1 \tag{3.4}$$

where

$$S_1 = \sqrt{(z-z')^2 + (r-r')^2}, \tag{3.5}$$

$$S_2 = \sqrt{(z-z')^2 + (r+r')^2}, \tag{3.6}$$

$$\lambda = \frac{S_2 - S_1}{S_2 + S_1}, \tag{3.7}$$

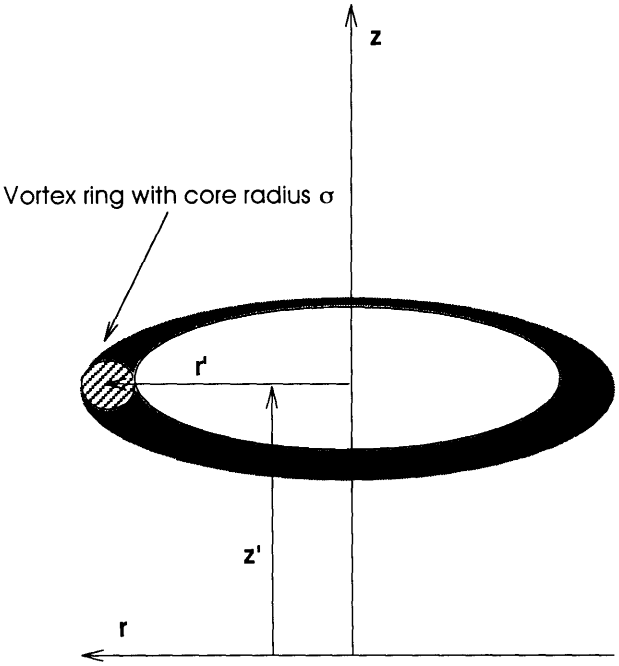

Figure 3.2 Schematic drawing of a vortex ring.

and the complete elliptic integral of the first and second kind are given by

$$\mathbf{K}(\lambda) = \int_0^1 \frac{1}{\sqrt{(1-\tau^2)(1-\lambda^2\tau^2)}}\,d\tau \tag{3.8}$$

and

$$\mathbf{E}(\lambda) = \int_0^1 \sqrt{\frac{1-\lambda^2\tau^2}{1-\tau^2}}\, d\tau, \tag{3.9}$$

respectively. Since

$$\mathbf{u}_\omega = (v_\omega, u_\omega) = \left(\frac{-1}{r}\frac{\partial\psi}{\partial z}, \frac{1}{r}\frac{\partial\psi}{\partial r}\right), \tag{3.10}$$

differentiating Equation (3.4) with respect to z and r we get

$$v_\omega(r,z) = \frac{-\Gamma}{2\pi r}\frac{(z-z')(S_1+S_2)}{S_1 S_2}\left[\mathbf{K}(\lambda) - \frac{\mathbf{E}(\lambda)}{2}\left(\frac{S_2^2+S_1^2}{S_1 S_2}\right)\right] \tag{3.11}$$

$$u_\omega(r,z) = \frac{\Gamma}{2\pi r}\left[\left(\frac{r-r'}{S_1}+\frac{r+r'}{S_2}\right)(\mathbf{K}(\lambda)-\mathbf{E}(\lambda)) + \left(\frac{S_2-S_1}{2}\right)\left(\frac{r+r'}{S_2^2}-\frac{r-r'}{S_1^2}\right)\mathbf{E}(\lambda)\right]. \tag{3.12}$$

Equations (3.11) and (3.12) are the radial and streamwise velocity, respectively, induced by a vortex ring filament at any point (r, z) in the flow domain. However, a constraint on the size of the vortex filament's cross sectional area is needed before these equations can be used in a simulation. It has been shown that for a vortex ring filament with infinitesimal core radius σ and cross sectional area δA, the axial velocity component diverges to infinity at a rate proportional to $\log[(r-\sigma)^2+z^2]$, as the vortex ring is approached from any direction by another vortex ring filament [7, 81]. To remove this singularity, we introduce a finite smoothing core for the vortex ring elements. Following Martins, the Rankine core function distribution is assumed [93]. By modelling a vortex ring filament with finite-area core, we have introduced a small but finite amount of viscosity into the vortex filament. The vorticity of the element, instead of concentrating in an infinitesimally small area, is allowed to diffuse away from the center of the ring. Note that since this effect is not cumulative and there is a finite cut-off core radius, the viscosity introduced here is artificial rather than physical. The core radius σ is the free parameter controlling the amount of artificial viscosity being introduced into the flow solution. For a finite-core filament with Rankine core function, we have a uniform distribution of vorticity $\omega = \omega_0$ inside the core but zero everywhere else. This artificially smoothing of the distribution of vorticity within the core guarantees a finite velocity at the center of the vortex ring filament [93]. For an assumed Rankine vortex core function, it is found that within the core of element i, the velocity (v_ω, u_ω) induced by element i on another vortex ring element j varies linearly with the radial position from the center of element i. The velocity varies from the finite self-induced velocity u_I (to be discussed later) at the center of element i, to the convection velocity calculated from Equations (3.11) and (3.12) at the edge of the core radius of element i.

During the course of a flow simulation, the continuous vorticity distribution in the flow field is approximated by a linear combination of discrete vortex ring filaments with small but finite core radii. The vortex ring elements are convected across the flow domain by the velocity field induced by the vorticity distribution according to the vorticity transport equation (3.3). This discretization procedure replaces the partial differential equation governing the motions of the Lagrangian fluid particles by a system of ordinary differential equations which can be integrated in time using conventional numerical integration scheme. Thus, instead of solving a set of coupled nonlinear partial differential equations, the trajectories of the N vortex elements are obtained by solving a system of N ordinary differential equations. Notice that the numerical scheme, as implemented in this work, has also made the assumption that the cross sectional areas of the vortex ring filaments are not distorted by the strain field and remain circular at all time.

Unlike the two-dimensional vortex elements, a curved vortex ring filament with a finite cross-sectional area has a small but finite self-induced velocity [81]. In the case of an axisymmetric vortex ring, the direction of this self-induced velocity is parallel to the streamwise coordinate (the z-axis of the vortex ring). For a vortex ring of small cross section $\pi\sigma^2$ with core radius σ and ring radius a, under the condition $(\sigma/a) \ll 1$ and with a Rankine core function, the self-induced velocity in a perfect fluid is given by Kelvin's formula [81, 93]

$$u_l(t) = \frac{\Gamma}{4\pi a}\left[\ln\left(\frac{8a}{\sigma}\right) - \frac{1}{4} + O\left(\frac{\sigma}{a}\right)\right]. \tag{3.13}$$

Note that the value of the error term in Equation (3.13), $O(\sigma/a)$, has been shown to be negligibly small [81] if the ring radius, a, is much greater than the core radius, σ. Nonetheless, Martins has shown in his numerical studies that even for the limiting case $a \sim \sigma$, Equation (3.13) can still be used as the first-order approximation to the self-induced velocity of the ring elements [93].

As mentioned earlier, the flow is simulated by approximating the continuous vorticity field by the superposition of a set of vortex ring filament each with circulation Γ_i. Thus, the continuous vortical velocity field $\mathbf{u}_\omega$ is approximated by

$$\mathbf{u}_\omega(\mathbf{r},t) \sim \mathbf{u}_v(\mathbf{r},t) + \mathbf{u}_l(t) \tag{3.14}$$

where $\mathbf{u}_v = (v_v, u_v)$ is the discrete convection velocity given by Equations (3.11) and (3.12), and $\mathbf{u}_l$ is the self-induced velocity. (The self-induced velocity has a zero radial component and a streamwise component given by Equation (3.13).) In a simulation, the streamwise vortical velocity of the *ith* vortex ring element $u_v^i(t)$ is the sum of the vortical velocity induced by all the other vortex elements in the flow domain at the centroid of the element, plus its self-induced velocity

$$u_v^i(t) = \sum_{\substack{j=1 \\ j \neq i}}^{N} u_v^j(t) + u_l^i(t) \tag{3.15}$$

where u_v^j is the streamwise vortical velocity induced by the *jth* element at the centroid of the *ith* element, u_l^i is the self-induced velocity of element i, and N is the total number of vortex ring elements in the flow domain. From Equation (3.12) and the definition of the Rankine core function [93], it is clear that the streamwise velocity induced by the *jth* element at the centroid of the *ith* element is given by

$$u_v^j(t) = \frac{\Gamma_j}{2\pi r_i}\left[\left(\frac{r_i - r_j}{S_{1,ij}} + \frac{r_i + r_j}{S_{2,ij}}\right)(\mathbf{K}(\lambda_{ij}) - \mathbf{E}(\lambda_{ij})) + \left(\frac{S_{2,ij} - S_{1,ij}}{2}\right)\left(\frac{r_i + r_j}{S_{2,ij}^2} - \frac{r_i - r_j}{S_{1,ij}^2}\right)\mathbf{E}(\lambda_{ij})\right] \tag{3.16}$$

if the distance between the centers of the two elements, $\|\mathbf{r}_{ij}\| = \sqrt{(r_i - r_j)^2 + (z_i - z_j)^2}$, is greater than the core radius, σ_j, of the *jth* element. In Equation (3.16), $S_{1,ij} = \sqrt{(r_i - r_j)^2 + (z_i - z_j)^2}$, $S_{2,ij} = \sqrt{(r_i + r_j)^2 + (z_i - z_j)^2}$, and $\lambda_{ij} = (S_{2,ij} - S_{1,ij})/(S_{2,ij} + S_{1,ij})$. When the distance between the centers of the two elements is less than the core radius of the *jth* element, the streamwise velocity is given by

$$u_v^j(t) = u_l^j + (u_v^J - u_l^j)\left[\left(\sqrt{(r_i - r_j)^2 + (z_i - z_j)^2}\right)/\sigma_j\right], \tag{3.17}$$

where

$$u_v^J = \frac{\Gamma_j}{2\pi r_i}\left[\left(\frac{r_J - r_j}{S_{1,Jj}} + \frac{r_J + r_j}{S_{2,Jj}}\right)(\mathbf{K}(\lambda_{Jj}) - \mathbf{E}(\lambda_{Jj})) + \left(\frac{S_{2,Jj} - S_{1,Jj}}{2}\right)\left(\frac{r_J + r_j}{S_{2,Jj}^2} - \frac{r_J - r_j}{S_{1,Jj}^2}\right)\mathbf{E}(\lambda_{Jj})\right], \tag{3.18}$$

$S_{1,Jj} = \sqrt{(r_J - r_j)^2 + (z_J - z_j)^2}$, $S_{2,Jj} = \sqrt{(r_J + r_j)^2 + (z_J - z_j)^2}$, $\lambda_{Jj} = (S_{2,Jj} - S_{1,Jj})/(S_{2,Jj} + S_{1,Jj})$, (r_J, z_J) is the point on the circumference of the core σ_j along the radius vector $\mathbf{r}_{ij}$ containing the centroid of the *ith* element (r_i, z_i), and $u_l^j = u_l^j(r_j, z_j)$ is the self-induced velocity of the *jth* element. Note that the self-induced velocities in Equations (3.15) and (3.17) are given by Equation (3.13).

Similarly, the radial vortical velocity of the *ith* vortex ring element is the sum of the vortical velocity induced by all the other vortex elements in the flow domain at the centroid of the *ith* element

$$v_v^i(t) = \sum_{\substack{j=1 \\ j \neq i}}^{N} v_v^j(t) \tag{3.19}$$

where, according to Equation (3.11),

$$v_v^j(t) = \frac{-\Gamma_j}{2\pi r_i} \frac{(z_i - z_j)(S_{1,ij} + S_{2,ij})}{S_{1,ij} S_{2,ij}} \left[\mathbf{K}(\lambda_{ij}) - \frac{\mathbf{E}(\lambda_{ij})}{2} \left(\frac{S_{2,ij}^2 + S_{1,ij}^2}{S_{1,ij}^2 S_{2,ij}^2} \right) \right] \tag{3.20}$$

if $(\|\mathbf{r}_{ij}\| = \sqrt{(r_i - r_j)^2 + (z_i - z_j)^2}) \geq \sigma_j$ and

$$v_v^j(t) = \frac{-\Gamma_j}{2\pi r_J} \frac{(z_J - z_j)(S_{1,Jj} + S_{2,Jj})}{S_{1,Jj} S_{2,Jj}} \left[\mathbf{K}(\lambda_{Jj}) - \frac{\mathbf{E}(\lambda_{Jj})}{2} \left(\frac{S_{2,Jj}^2 + S_{1,Jj}^2}{S_{1,Jj}^2 S_{2,Jj}^2} \right) \right] [(\sqrt{(r_J - r_j)^2 + (z_J - z_j)^2}) / \sigma_j] \tag{3.21}$$

if $\|\mathbf{r}_{ij}\| \leq \sigma_j$. Finally, the vortical velocity at any given field point $\mathbf{r} = (r,z)$ in the flow domain induced by a system of N vortex ring element is given by

$$\mathbf{u}_v(\mathbf{r},t) = (v_v(\mathbf{r},t), u_v(\mathbf{r},t)) \tag{3.22}$$

where

$$v_v(\mathbf{r},t) = \sum_{\substack{j=1 \\ r_j \neq r}}^{N} v_{v,\mathbf{r}}^j(t) \tag{3.23}$$

and

$$u_v(\mathbf{r},t) = \sum_{\substack{j=1 \\ \mathbf{r}_j \neq \mathbf{r}}}^{N} u_{v,\mathbf{r}}^{j}(t) + \sum_{j=1}^{N} u_{l,\mathbf{r}}^{j}\,\delta(\mathbf{r}-\mathbf{r}_j) \tag{3.24}$$

where δ is the delta function.

3.1.2 SOLUTION FOR THE IRROTATIONAL VELOCITY FIELD IN A BOUNDED FLOW DOMAIN

As discussed in the last chapter, the vortical velocity field, as given in Equation (3.22), is defined in an infinite domain and contains no information about the boundaries of the enclosure. An irrotational field $\mathbf{u}_\varphi$, prescribed by the domain boundaries, provides the necessary correction to have the total velocity field **u** conforming to a specified normal velocity at the boundaries. Furthermore, for exothermic reactive flows, the total velocity field **u** consists of an additional velocity component $\mathbf{u}_\varepsilon$, where $\mathbf{u}_\varepsilon$ is also defined in an infinite domain and contains no information about the domain boundaries. Since both $\mathbf{u}_\varphi$ and $\mathbf{u}_\varepsilon$ are irrotational, a vector field $\mathbf{v} = \mathbf{u}_\varphi + \mathbf{u}_\varepsilon$ can be defined and the solution of **v** can be obtained from a velocity potential φ such that $\mathbf{v} = \nabla\varphi$. The equation governing the velocity potential is given by the Poisson equation

$$\nabla^2\varphi = \frac{1}{T}\frac{DT}{Dt} = \varepsilon \tag{3.25}$$

with the boundary condition

$$\mathbf{u}_\varphi \cdot \mathbf{n} = (\mathbf{u} \cdot \mathbf{n}) - (\mathbf{u}_\varepsilon + \mathbf{u}_\omega) \cdot \mathbf{n} \tag{3.26}$$

where $\mathbf{u} \cdot \mathbf{n}$ are the prescribed velocities at the boundaries of the flow domain. Equation (3.26) is, again, the classical Poisson equation with Neumann boundary condition. The solution of the equation with the imposed boundary condition provides a velocity field $\mathbf{v} = \mathbf{u}_\varphi + \mathbf{u}_\varepsilon$ that satisfies the continuity equation, is irrotational, and on the boundaries of the flow domain exactly cancel the normal velocity component induced by the vortex ring elements (and also the expansion sources for exothermic reactive flows). Adding **v** to $\mathbf{u}_\omega$ produces the required velocity field in the domain interior. The Poisson problem with Neumann boundary condition is a well-known classical problem. Many different solution methods have been developed to solve this problem. Instead of solving the partial differential equation directly, a popular solution procedure is to apply the variation principle to the problem in order to obtain the extremal formulation of the Poisson equation, and use the finite-element form of the Rayleigh-Ritz method to reduce the equation to a system of n equations with n unknowns [26]. In the following section. we will demonstrate the procedure of applying the variation principle in order to obtain the weak formulation of the Poisson equation with Neumann boundary condition.

3.1.2.1 EXTREMAL FORMULATION OF THE POISSON EQUATION

From classical physical mathematics, it is known that a partial differential equation describing a physical phenomenon can often be formulated equivalently as a variation problem. A partial differential formulation of a problem is to find an unknown function which satisfies a relation between the function itself and its partial derivatives and which is, moreover, subject to given boundary conditions. A variation, or extremal formulation is a problem of the type: find a function that minimizes, maximizes or make stationary a *functional* subject to given boundary conditions. The two formulations are called equivalent if both problems admit the same unique solution. A functional is mapping from a set of admissible functions into the real numbers. The set of admissible functions consists of those functions for which the functional takes finite values and which satisfy imposed boundary conditions. Functional formulations are commonly known as the *weak* forms of stating the governing equations of the problem and the differential equations themselves comprise the strong forms. The weak form enforces conditions in an average or integral sense, whereas the strong form enforces them at every point.

It follows from the calculus of variations that a necessary and sufficient condition for a functional to be extremized or made stationary is that the *Euler-Lagrange equation* is satisfied for the sought solution together with boundary conditions [26]. This Euler-Lagrange equation is precisely the partial different equation of the problem. The variation formulation often has the advantages over the partial differential formulation, especially from the numerical point of view. This is due to the fact that the functional contains derivatives of lower order than the differential problem. Consequently, an approximate solution can be sought in a larger class of functions. Furthermore, the variation formulation treats in a simple way complicated boundary conditions, such as, for instance, Dirichlet, Neumann, or Robbins boundary conditions in non-rectangular domains.

Consider a bounded open region D belonging to an n-dimensional domain R^n, $D \subset R^n$, with smooth boundary ∂D where ∂D is subdivided into four disjoint parts ∂D_0, ∂D_1, ∂D_2, and ∂D_3. Given the following minimization problem:

– Find a function $\varphi = \varphi(\mathbf{r})$, $\mathbf{r} \in D \cup \partial D$ with $\varphi(\mathbf{r}) = g_0(\mathbf{r})$ for $\mathbf{r} \in \partial D_0$, that minimizes the functional

$$J(w) = \frac{1}{2}\int_D |\nabla w|^2 d\Omega - \int_D f w \, d\Omega - \int_{\partial D_1} g_1 w \, d\Gamma + \frac{1}{2}\alpha \int_{\partial D_3} |w|^2 d\Gamma \tag{3.27}$$

over the class of functions which are equal to g_0 on ∂D_0 for given functions $f = f(\mathbf{r})$, $\mathbf{r} \in D$, and $g_i = g_i(\mathbf{r})$, $\mathbf{r} \in \partial D_i$ $i = 0,1$, and $\alpha \geq 0$. To solve the problem, we assume that a solution $\varphi \in C^2(D) \cap C^1(D + \partial D)$ exists (C^1 and C^2 stand for the function is once and twice differentiable, respectively). The set of admissible functions is defined as the subset of $C^2(D) \cap C^1(D + \partial D)$ containing functions that are equal to g_0 on ∂D_0. Let $\upsilon \in C^2(D) \cap C^1(D + \partial D)$ with $\upsilon|_{\partial D} = 0$, and substitute the family of admissible functions

$$w = \varphi + \lambda\upsilon \tag{3.28}$$

with parameter λ into Equation (3.27), we get

$$J(w) = J(\varphi + \lambda\upsilon) \equiv K(\lambda) \tag{3.29}$$

where

$$K(\lambda) = \frac{1}{2}\int_D |\nabla(\varphi + \lambda\upsilon)| \, d\Omega - \int_D f(\varphi + \lambda\upsilon) \, d\Omega - \int_{\partial D_1} g_1(\varphi + \lambda\upsilon) \, d\Omega + \int_{\partial D_3} |\varphi + \lambda\upsilon|^2 d\Gamma \, . \tag{3.30}$$

From basic calculus, a necessary condition for minimization of $K(\lambda)$ is

$$\frac{d}{d\lambda} K(\lambda) = 0 \tag{3.31}$$

at $\lambda = 0$ for all $\upsilon \in C^2(D) \cap C^1(D + \partial D)$ with $\upsilon|_{\partial D} = 0$. Carrying out the procedure we get

$$\frac{d}{d\lambda} K(\lambda)|_{\lambda=0} = \frac{1}{2}\int_D 2[\nabla(\varphi + \lambda\upsilon)][\nabla\upsilon] \, d\Omega - \int_D (f)(\upsilon) \, d\Omega \; -$$

$$\int_{\partial D_1} (g_1)(\upsilon) \, d\Gamma + \frac{1}{2}\alpha\int_{\partial D_3} 2(\varphi + \lambda\upsilon)\upsilon \, d\Gamma = 0 \tag{3.32}$$

or

$$\frac{d}{d\lambda}K(\lambda)\,|_{\lambda=0} = \int_D [\nabla\varphi \cdot \nabla\upsilon]\, d\Omega - \int_D (f)\,(\upsilon)\, d\Omega - \int_{\partial D_1} (g_1)(\upsilon)\, d\Gamma + \int_{\partial D_3} \alpha\,(\varphi)\,(\upsilon)\, d\Gamma = 0. \tag{3.33}$$

Using Green's first identity

$$\int_D (-\nabla^2\varphi)\,\upsilon\, d\Omega = \int_D (\nabla\varphi) \cdot (\nabla\upsilon)\, d\Omega - \int_{\partial D} (\upsilon\nabla\varphi) \cdot \mathbf{n}\, d\Gamma, \tag{3.34}$$

we can transform the first integral of Equation (3.33) to

$$\int_D [\nabla\varphi \cdot \nabla\upsilon]\, d\Omega = \int_D (-\nabla^2\varphi)\upsilon\, d\Omega + \int_{\partial D} (\upsilon\nabla\varphi) \cdot \mathbf{n}\, d\Gamma. \tag{3.35}$$

Therefore, Equation (3.33) becomes

$$\int_D (-\nabla^2\varphi)\upsilon\, d\Omega + \int_{\partial D} (\upsilon\nabla\varphi) \cdot \mathbf{n}\, d\Gamma - \int_D (f)\,(\upsilon)\, d\Omega - \int_{\partial D_1} (g_1)(\upsilon)\, d\Gamma + \int_{\partial D_3} \alpha\,(\varphi)\,(\upsilon)\, d\Gamma = 0, \tag{3.36}$$

or

$$\int_D [-\nabla^2\varphi - f]\upsilon\, d\Omega + \int_{\partial D} \upsilon\frac{\partial\varphi}{\partial n} d\Gamma - \int_{\partial D_1} (g_1)(\upsilon)\, d\Gamma + \int_{\partial D_3} \alpha\,(\varphi)\,(\upsilon)\, d\Gamma = 0 \tag{3.37}$$

since $\nabla\varphi \cdot \mathbf{n} = \frac{\partial\varphi}{\partial n}$. Note that also $\partial D = \partial D_0 + \partial D_1 + \partial D_2 + \partial D_3$, we have

$$\int_{\partial D} \upsilon\frac{\partial\varphi}{\partial n} d\Gamma = \int_{\partial D_0} \upsilon\frac{\partial\varphi}{\partial n} d\Gamma + \int_{\partial D_1} \upsilon\frac{\partial\varphi}{\partial n} d\Gamma + \int_{\partial D_2} \upsilon\frac{\partial\varphi}{\partial n} d\Gamma + \int_{\partial D_3} \upsilon\frac{\partial\varphi}{\partial n} d\Gamma. \tag{3.38}$$

The first integral on the right-hand of Equation (3.38) is identically zero since by construction $\upsilon|_{\partial D} = 0$. Substituting the above equation into (3.37) we get

$$\int_D [-\nabla^2\varphi - f]\upsilon\, d\Omega + \int_{\partial D_1} \left(\frac{\partial\varphi}{\partial n} - g_1\right)(\upsilon)\, d\Gamma + \int_{\partial D_2} \upsilon\frac{\partial\varphi}{\partial n} d\Gamma + \int_{\partial D_3} \upsilon\left(\frac{\partial\varphi}{\partial n} + \alpha\varphi\right) d\Gamma = 0. \tag{3.39}$$

Since $\upsilon \in C^2(D) \cap C^1(D + \partial D)$ with $\upsilon|_{\partial D} = 0$, but otherwise is an arbitrary function, in order for the above equation to be true, we must have

$$-\nabla^2\varphi - f = 0 \qquad \text{in } D \tag{3.40}$$

and

$$\frac{\partial\varphi}{\partial n} - g_1 = 0 \qquad \text{on } \partial D_1 \tag{3.41}$$

$$\frac{\partial\varphi}{\partial n} = 0 \qquad \text{on } \partial D_2 \tag{3.42}$$

$$\frac{\partial\varphi}{\partial n} + \alpha\varphi = 0 \qquad \text{on } \partial D_3 \tag{3.43}$$

with

$$\varphi = g_0 \qquad \text{on } \partial D_0 . \tag{3.44}$$

Notice that the nonhomogeneous Dirichlet condition on ∂D_0 is essential since it was imposed on the solution of the extremal formulation. The nonhomogeneous Neumann boundary condition on ∂D_1, the homogeneous Neumann condition on ∂D_2, and the homogeneous Robbins condition on ∂D_3 are natural since they are automatically satisfied by the variational formulation. Note that the above derivation relates the Poisson equation (with all boundary condition except on ∂D_3) to the minimization problem. Since the natural conditions for a minimization problem are satisfied automatically by the solution, we only have to prescribe the essential boundary conditions. For the three types of boundary conditions: Dirichlet, Neumann and Robins, only Dirichlet conditions are essential, the other two are natural conditions.

As discussed earlier, the variation formulation often has the advantages over the partial differential formulation, especially from the numerical point of view. This is due to the fact that the functional contains derivatives of lower order than the differential problem. Consequently, an approximate solution can be sought in a larger class of functions. Furthermore, the variation formulation treats in a simple way complicated boundary conditions. We have also demonstrated that the equivalency of solving the integral given in Equation (3.39) and the partial differential equation for the Poisson equation (3.40-3.44). Given the advantages of the extremal formulation of the problem, we will solve the problem using the functional approach. The method we will use to solve the equation is known as the finite-element form of the Rayleigh-Ritz method. The first step of the method is to subdivide the domain into K finite elements. After the subdivision of the domain, a basis (shape) function N_i is defined for each nodal point in the flow domain. The basis functions N_i, i = 1, 2, 3,..., M where M = total number of nodes in $D \cup \partial D$. The basis functions have the following three properties:

1) $N_i(\mathbf{x}_j) = \delta_{ij}$.

2) N_i is continuous on $D \cup \partial D$.

3) N_i has a prescribed behavior on each subregion (for example, linear or quadratic).

The approximate solution of the minimization problem is now assumed to take the form

$$\tilde{\varphi}(\mathbf{x}) = \sum_{j=1}^{M} \tilde{\varphi}_j N_j(\mathbf{r}) \qquad (3.45)$$

where $\tilde{\varphi}_j$ is the unknown value of $\tilde{\varphi}$ at $\mathbf{r} = \mathbf{r}_j$. Note that the approximate function given in Equation (3.45) must satisfy the essential (Dirichlet) boundary conditions on ∂D_0. In this case, we have $\varphi(\mathbf{r}) = 0$ for $\mathbf{r} \in \partial D_0$, therefore, we take $\tilde{\varphi}_j = 0$ for those values of j for which $\mathbf{r}_j \in \partial D_0$. A renumbering of the nodal points now leads to the following general form of an approximate solution

$$\tilde{\varphi}(\mathbf{r}) = \sum_{j=1}^{L} \tilde{\varphi}_j N_j(\mathbf{r}) \qquad (3.46)$$

where L is the total number of nodal points which do not belong to ∂D_0. Now, substituting equation (3.46) into (3.27) we get

$$J(\tilde{\varphi}) = K(\tilde{\varphi}_1, \tilde{\varphi}_2, \dots, \tilde{\varphi}_L) = \frac{1}{2}\int_D \left[\nabla \sum_{j=1}^{L} \tilde{\varphi}_j N_j\right]^2 d\Omega - \int_D \left[f \sum_{j=1}^{L} \tilde{\varphi}_j N_j\right] d\Omega -$$

$$\int_{\partial D_1} \left[g_1 \sum_{j=1}^{L} \tilde{\varphi}_j N_j\right] d\Gamma + \frac{1}{2}\alpha \int_{\partial D_3} \left[\sum_{j=1}^{L} \tilde{\varphi}_j N_j\right]^2 d\Gamma . \qquad (3.47)$$

Now, applying the stationary principle, we take the derivative of $K(\tilde{\varphi}_n)$, $n = 1, L$ with respect to $\tilde{\varphi}_n$ and set it to zero,

$$\frac{\partial}{\partial \varphi_i} K(\tilde{\varphi}_n) = 0 \qquad n = 1, L \qquad i = 1, L, \tag{3.48}$$

or

$$\frac{1}{2}\int_D 2\left[\sum_{j=1}^{L} \tilde{\varphi}_j \nabla N_j\right]\left[\frac{\partial}{\partial \varphi_i}\sum_{j=1}^{L} \tilde{\varphi}_j \nabla N_j\right] d\Omega - \int_D f \frac{\partial}{\partial \varphi_i}\left(\sum_{j=1}^{L} \tilde{\varphi}_j N_j\right) d\Omega \;-$$

$$\int_{\partial D_1} g_1 \frac{\partial}{\partial \varphi_i}\left(\sum_{j=1}^{L} \tilde{\varphi}_j N_j\right) d\Gamma + \frac{1}{2}\alpha \int_{\partial D_3} \frac{\partial}{\partial \varphi_i}\left(\sum_{j=1}^{L} \tilde{\varphi}_j N_j\right)^2 d\Gamma = 0. \tag{3.49}$$

Since $\frac{\partial}{\partial \varphi_i}\sum_{j=1}^{L} \tilde{\varphi}_j \nabla N_j = \nabla N_i$ and $\frac{\partial}{\partial \varphi_i}\left(\sum_{j=1}^{L} \tilde{\varphi}_j N_j\right) = N_i$, therefore

$$\int_D \left[\sum_{j=1}^{L} \tilde{\varphi}_j \nabla N_j\right] \cdot \nabla N_i \, d\Omega - \int_D f N_i \, d\Omega - \int_{\partial D_1} g_1 N_i \, d\Gamma + \alpha \int_{\partial D_3}\left[\sum_{j=1}^{L} \tilde{\varphi}_j N_j\right] N_i \, d\Gamma = 0. \tag{3.50}$$

Note that we can interchange the order of integration and summation in the first and the last integral of the above equation:

$$\sum_{j=1}^{L} \tilde{\varphi}_j \int_D (\nabla N_j \cdot \nabla N_i) \, d\Omega + \alpha \sum_{j=1}^{L} \tilde{\varphi}_j \int_{\partial D_3} N_j N_i \, d\Gamma = \int_D f N_i \, d\Omega + \int_{\partial D_1} f N_i \, d\Gamma \tag{3.51}$$

for all $j \in L$, where L denotes the set of indices corresponding to those nodal points which do not belong to ∂D_0. The integral given in Equation (3.51) can be split up into a sum of integrals over the subregions. Doing so gives

$$\sum_{k=1}^{K}\sum_{j=1}^{L} \tilde{\varphi}_j \int_{D_k} (\nabla N_j \cdot \nabla N_i) \, d\Omega + \alpha \sum_{q=1}^{Q}\sum_{j=1}^{L} \tilde{\varphi}_j \int_{\partial D_{3q}} (N_j N_i) \, d\Gamma = \sum_{k=1}^{K}\int_{D_k} f N_i \, d\Omega + \sum_{p=1}^{P}\int_{\partial D_{1p}} g_1 N_i \, d\Gamma \tag{3.52}$$

where D_k = volume of finite element k (the domain is being discretized into K discrete parts), ∂D_{1p} is the discrete boundary element of ∂D_1 (∂D_1 is being discretized into P boundary elements), ∂D_{3q} is the discrete boundary element of ∂D_3 (∂D_3 is being discretized into Q boundary elements). In the potential problem we are solving, ∂D_{3q} = 0. Thus, Equation (3.52) becomes

$$\sum_{k=1}^{K}\sum_{j=1}^{L}\tilde{\varphi}_j\int_{D_k}(\nabla N_j \cdot \nabla N_i)\,d\Omega = \sum_{k=1}^{K}\int_{D_k} fN_i\,d\Omega + \sum_{p=1}^{P}\int_{\partial D_{1p}} g_1 N_i\,d\Gamma . \tag{3.53}$$

Note that Equation (3.53) is a set of linear algebraic equations and is exactly identical to the equation obtained from using the finite-element weighted-residual Galerkin method [93]. This is due to the fact that for a given problem, if differential equations and a variational principle are both available, then the finite-element Galerkin method and the finite-element Rayleigh-Ritz method yield identical solutions when both use the same approximate function $\tilde{\varphi}$. Thus, the integral equation given in (3.27) yields an approximate solution to the same potential problem given by the following Poisson equation

$$\nabla^2\varphi = -f \qquad \text{in } D \tag{3.54}$$

with boundary conditions

$$\varphi = 0 \qquad \text{on } \partial D_0 \tag{3.55}$$

$$\frac{\partial\varphi}{\partial n} = g_1 \qquad \text{on } \partial D_1 \tag{3.56}$$

where $\partial D = \partial D_0 + \partial D_1$. In the following section, we will demonstrate the procedure of using linear triangular elements to solve the integral equation (3.53).

3.1.2.2 FINITE-ELEMENT SOLUTION OF THE IRROTATIONAL VELOCITY FIELD

As demonstrated in Section 3.1.2, the following Poisson equation governing the irrotational velocity field of the problem

$$\nabla^2\varphi = -\varepsilon \qquad \text{in } D \tag{3.57}$$

$$\varphi = 0 \qquad \text{on } \partial D_0 \tag{3.58}$$

$$\frac{\partial \varphi}{\partial n} = g_1 \qquad \text{on } \partial D_1 \tag{3.59}$$

where $\partial D = \partial D_0 + \partial D_1$ and $\varepsilon = (1/\rho)(D\rho/Dt) = (-1/T)(DT/Dt)$ is the expansion source term, has an equivalent weak formulation:

$$\sum_{k=1}^{K} \sum_{j=1}^{L} \tilde{\varphi}_j \int_{D_k} (\nabla N_j \cdot \nabla N_i)\, d\Omega = \sum_{k=1}^{K} \int_{D_k} f N_i \, d\Omega + \sum_{p=1}^{P} \int_{\partial D_{1p}} g_1 N_i \, d\Gamma . \tag{3.60}$$

As discussed before, the variation formulation often has the advantages over the partial differential formulation, especially for problems with nonrectangular domains with Neumann boundary conditions. In this section, we will demonstrate the solution of Equation (3.60) using the classical finite element method.

The finite-element method is a systematic procedure for generating a basis function on arbitrary region D which will give rise to a sparse matrix $\underset{\sim}{\mathbf{A}}$. It is clear that the matrix $\underset{\sim}{\mathbf{A}}$ will be sparse if the basis functions have *small support*. The support of a function defined on D is the closure of the subregion of D on which the function differ from zero. It is evident that the matrix element A_{ij} equals zero whenever the support of φ_i and φ_j have empty intersection. Note that Equation (3.60) can be written in matrix notation as

$$\underset{\sim}{\mathbf{A}} \tilde{\varphi} = \mathbf{F} \tag{3.61}$$

where $\underset{\sim}{\mathbf{A}}$ is an $L \times L$ matrix, $\tilde{\varphi}$ is an $L \times 1$ (unknown) vector, and $\mathbf{F}$ is an $L \times 1$ vector of forcing terms, and

$$A^e_{ij} = \int_{e_k} (\nabla N_j \cdot \nabla N_i)\, d\Omega \tag{3.62}$$

is the element stiffness matrix (L is the total number of nodal points not belonging to ∂D_0). On a linear triangular element, only the basis function $N_1, N_2,$ and $N_3 \neq 0$. This implies that for each $k = 1, 2, 3, \ldots, K$ the integral in Equation (3.62) gives rise to a 3×3 element matrix

$$\lfloor \mathbf{N} \rfloor = \lfloor N_1 \quad N_2 \quad N_3 \rfloor \qquad \text{(linear element)} \tag{3.63}$$

where

$$N_1 = \xi_1 ,\ N_2 = \xi_2 ,\ N_3 = \xi_3 \tag{3.64}$$

and

$$\xi_1 = \left(\frac{1}{2A_e}\right)[(z_2 r_3 - z_3 r_2) + (r_2 - r_3) z + (z_3 - z_2) r] \tag{3.65}$$

$$\xi_2 = \left(\frac{1}{2A_e}\right)[(z_3 r_1 - z_1 r_3) + (r_3 - r_1) z + (z_1 - z_3) r] \tag{3.66}$$

$$\xi_2 = \left(\frac{1}{2A_e}\right)[(z_3 r_1 - z_1 r_3) + (r_3 - r_1) z + (z_1 - z_3) r] \tag{3.67}$$

$$\frac{\partial N_1}{\partial z} = \frac{\partial \xi_1}{\partial z} = \frac{r_2 - r_3}{2A_e} \tag{3.68}$$

$$\frac{\partial N_1}{\partial r} = \frac{\partial \xi_1}{\partial r} = \frac{z_3 - z_2}{2A_e} \tag{3.69}$$

$$\frac{\partial N_2}{\partial z} = \frac{\partial \xi_2}{\partial z} = \frac{r_3 - r_1}{2A_e} \tag{3.70}$$

$$\frac{\partial N_2}{\partial r} = \frac{\partial \xi_2}{\partial r} = \frac{z_1 - z_3}{2A_e} \tag{3.71}$$

$$\frac{\partial N_3}{\partial z} = \frac{\partial \xi_3}{\partial z} = \frac{r_1 - r_2}{2A_e} \tag{3.72}$$

$$\frac{\partial N_3}{\partial r} = \frac{\partial \xi_3}{\partial r} = \frac{z_2 - z_1}{2A_e} . \tag{3.73}$$

For each finite element, we have a 3×3 elemental stiffness matrix with each component in the matrix given by

$$A_{ij}^{e_k} = \int_{e_k} \left[\frac{\partial N_j}{\partial z}\frac{\partial N_i}{\partial z} + \frac{\partial N_j}{\partial r}\frac{\partial N_i}{\partial r} \right] d\Omega$$

$$= \int_{e_k} \left(\frac{1}{4A_e^2} \right) \int_0^{2\pi} \left[\frac{\partial N_j}{\partial z}\frac{\partial N_i}{\partial z} + \frac{\partial N_j}{\partial r}\frac{\partial N_i}{\partial r} \right] r\,dr\,d\theta\,dz \qquad i, j = 1, 2, 3 \qquad (3.74)$$

Therefore, for each finite element the elemental stiffness matrix is

$$A_k^e = \frac{2\pi(r_1+r_2+r_3)}{3} \begin{bmatrix} (r_2-r_3)^2+(z_3-z_2)^2 & (r_3-r_1)(r_2-r_3)+(z_1-z_3)(z_3-z_2) & (r_1-r_2)(r_2-r_3)+(z_2-z_1)(z_3-z_2) \\ (r_2-r_3)(r_3-r_1)+(z_3-z_2)(z_1-z_3) & (r_3-r_1)^2+(z_1-z_3)^2 & (r_1-r_2)(r_3-r_1)+(z_2-z_1)(z_1-z_3) \\ (r_2-r_3)(r_1-r_2)+(z_3-z_2)(z_2-z_1) & (r_3-r_1)(r_1-r_2)+(z_1-z_3)(z_2-z_1) & (r_1-r_2)^2+(z_2-z_1)^2 \end{bmatrix}$$

$k = 1, 2, \ldots, K.$ (3.75)

Now, we can calculate the load vector on the right-hand side of the equation. Notice that the integral over e_k of the first term on the right-hand side of Equation (3.60) is differ from zero when the shape function N_i corresponds to one of the three nodal points of e_k. For e_k with nodal points $\mathbf{x}_1$, $\mathbf{x}_2$, and $\mathbf{x}_3$, this leads to a three-component element vector $\mathbf{F}_{e_k}$ where

$$\mathbf{F}_{e_k} = \begin{bmatrix} \int_{e_k} f N_1 d\Omega \\ \int_{e_k} f N_2 d\Omega \\ \int_{e_k} f N_3 d\Omega \end{bmatrix} \qquad k = 1, 2, 3, \ldots, K. \qquad (3.76)$$

If we assume f = constant = f^* in element e_k, then

$$\mathbf{F}_{e_k} = f^* \begin{bmatrix} \int\limits_{e_k} \xi_1 d\Omega \\ \int\limits_{e_k} \xi_2 d\Omega \\ \int\limits_{e_k} \xi_3 d\Omega \end{bmatrix} = f^* \begin{bmatrix} \int\limits_{e_k}\int_0^{2\pi} \xi_1 r\, d\theta dr dz \\ \int\limits_{e_k}\int_0^{2\pi} \xi_2 r\, d\theta dr dz \\ \int\limits_{e_k}\int_0^{2\pi} \xi_3 r\, d\theta dr dz \end{bmatrix} = 2\pi f^* \begin{bmatrix} \int\limits_{e_k} \xi_1 r dA \\ \int\limits_{e_k} \xi_2 r dA \\ \int\limits_{e_k} \xi_3 r dA \end{bmatrix} = \frac{A_e \pi f^*}{6} \begin{bmatrix} 2r_1 + r_2 + r_3 \\ r_1 + 2r_2 + r_3 \\ r_1 + r_2 + 2r_3 \end{bmatrix} . \quad (3.77)$$

The last term on the right-hand side of Equation (3.60) gives rise to the line element vector

$$\mathbf{F}_{\Gamma_{1p}} = \begin{bmatrix} \int\limits_{\Gamma_{1p}} g_1 N_1 d\Gamma \\ \int\limits_{\Gamma_{1p}} g_1 N_2 d\Gamma \end{bmatrix} = \begin{bmatrix} \int\limits_{\Gamma_{1p}} g_1 \xi_1 d\Gamma \\ \int\limits_{\Gamma_{1p}} g_1 \xi_2 d\Gamma \end{bmatrix} = \begin{bmatrix} \int_0^l \int_0^{2\pi} g_1 \xi_1 r\, dl\, d\theta \\ \int_0^l \int_0^{2\pi} g_1 \xi_2 r\, dl\, d\theta \end{bmatrix} = 2\pi \begin{bmatrix} \int_0^l g_1 \xi_1 r\, dl \\ \int_0^l g_1 \xi_2 r\, dl \end{bmatrix} . \quad (3.78)$$

If g_1 is assumed to be constant along l, then the integrals in the above equation can be solved analytically to give

$$\mathbf{F}_{\Gamma_{1p}} = \frac{\pi g_1 l}{3} \begin{bmatrix} 2r_1 + r_2 \\ r_1 + 2r_2 \end{bmatrix} . \quad (3.79)$$

Once the velocity potential $\tilde{\varphi}$ has been obtained by solving Equation (3.61), the potential velocity field $\mathbf{v} = \mathbf{u}_\varphi + \mathbf{u}_\varepsilon$ can be evaluated using the equation $\nabla\tilde{\varphi} = (v_p, u_p)$. For a generic field point $\mathbf{r}_i$ within a finite element e, the potential velocity is given by

$$\mathbf{v}(\mathbf{r}_i) = (v_p, u_p) = \left(\frac{\partial\tilde{\varphi}^e}{\partial r}, \frac{\partial\tilde{\varphi}^e}{\partial z}\right) = \sum_{i=1}^{3} \left(\frac{\partial N_i^e}{\partial r}, \frac{\partial N_i^e}{\partial z}\right) \tilde{\varphi}_i^e \quad (3.80)$$

where N^e is the shape function of the element as given by Equations (3.63-3.67).

3.1.3 UPDATING THE VORTICITY FIELD IN THE INTERIOR OF THE FLOW DOMAIN BY ADVECTION AND SIMULATION OF MOLECULAR DIFFUSION

Each vortex ring filament in the interior of the flow domain is advected by the velocity field induced by all the other vortex ring filaments in the flow domain, plus its self-induced velocity and the potential velocity

$$\left.\frac{\partial \mathbf{r}_i}{\partial t}\right|_{adv} = \mathbf{u}_v + \mathbf{u}_i + \mathbf{v} \tag{3.81}$$

with the two components of $\mathbf{u}_v$ given by Equations (3.15) and (3.19), $\mathbf{u}_i$ is given by Equation (3.13), and the potential velocity **v** is given by Equation (3.80). Notice that Equation (3.81) simply states that the vortex ring filaments are advected along the trajectories of material particles. Numerically integration of Equation (3.81) is done using the second-order modified Euler method [93]. With Δt equal to the discrete time step size, for the *ith* vortex element in the flow domain, the discrete analogue of Equation (3.81) is

$$\mathbf{r}_{i,adv}^{n+1} = \mathbf{r}_i^n + \Delta t(\mathbf{u}_i^n + \mathbf{u}_i^*)/2 \tag{3.82}$$

where

$$\mathbf{u}_i^n = \mathbf{u}_{v,i} + \mathbf{u}_{i,i} + \mathbf{v}_i(\mathbf{r}_i^n) \tag{3.83}$$

$$u_i^* = \mathbf{u}_{v,i}(r_i^*) + \mathbf{u}_{i,i} + \mathbf{v}_i(\mathbf{r}_i^*) \tag{3.84}$$

and

$$\mathbf{r}_i^n = (r_i(n\Delta t), z_i(n\Delta t)) \tag{3.85}$$

Equations (3.81-3.85) give the transport of the vortex filaments by the advection velocity only. For viscous flows, an additional transport of the vorticity is due to diffusion. In the random-vortex method, the second fractional step, diffusion, is simulated by the dispersion of the vortex elements' coordinates using a set of (two) independent Gaussian random number (η_r, η_z) according to the two-dimensional Gaussian statistics. These two Gaussian random numbers each has a zero mean and a standard deviation $\sigma = \sqrt{(2\Delta t)/Re_{D_a}}$. Thus, the diffusion of the vorticity

$$\frac{\partial \omega}{\partial t} = \nabla^2 \omega \tag{3.86}$$

is simulated by

$$r_j^{n+1} = r_j^n + \eta_{j,r} \tag{3.87}$$

and

$$z_j^{n+1} = z_j^n + \eta_{j,z}. \tag{3.88}$$

As mentioned earlier, in addition to the conventional diffusion component, an additional diffusion component in the radial coordinate is applied to the displacements of the vortex elements. From the differential equation

$$\frac{\partial(\omega/r)}{\partial t} = \left(\frac{1}{Re_{D_a}}\right)\left(\frac{1}{r}\frac{\partial(\omega/r)}{\partial r}\right) \tag{3.89}$$

and using the transformation of variable given by

$$\zeta = \frac{\omega}{r}, \tag{3.90}$$

Equation (3.89) becomes

$$\frac{\partial\zeta}{\partial r} - Re_{D_a} r\frac{\partial\zeta}{\partial t} = 0. \tag{3.91}$$

The left-hand side of Equation (3.91) is exactly the expression we would use to calculate $\frac{d}{dr}[\zeta(r,t(r))] = \frac{\partial\zeta}{\partial r} + \frac{\partial\zeta}{\partial t}\frac{dt}{dr}$, where $t(r)$ satisfies the equation $dt/dr = -r\,Re_{D_a}$. That is,

$$t = \frac{-1}{2}Re_{D_a}r^2 + C_1 \tag{3.92}$$

along any of the family of curves and the total derivative of ζ with respected to the spatial coordinate r vanishes:

$$\frac{d}{dr}[\zeta(r,t(r))] = 0, \tag{3.93}$$

where C_1 is a constant. The family of curves defined by Equation (3.93) are the characteristic curves of the differential equation (3.91). Hence, along any characteristic curve we have

$$\zeta = \frac{\omega}{r} = \text{constant}, \tag{3.94}$$

which means that ζ is conserved along the characteristic curves. In that case, it is required that

$$\zeta(r(t+dt), t+dt) = \zeta(r(t), t) \tag{3.95}$$

and this would be true if and only if

$$r^2(t+dt) + 2\frac{t+dt}{Re_{D_a}} = r^2(t) + 2\frac{t}{Re_{D_a}}. \tag{3.96}$$

Hence,

$$r(t+dt) = \sqrt{r^2(t) - 2(dt/Re_{D_a})}. \tag{3.97}$$

Therefore, Equation (3.89) is approximated by

$$r_j^{n+1} = \sqrt{(r_j^n)^2 - (2\Delta t)/Re_{D_a}}, \tag{3.98}$$

and the incremental radial displacement, $(\Delta r_j)_{diff}$, due to this diffusion component is equal to

$$r_j^{n+1} = r_j^n + \sqrt{(r_j^n)^2 - (2\Delta t)/Re_{D_a}} \tag{3.99}$$

In summary, given the position of N vortex ring filaments at time $t = n\Delta t$, their position at time $t = (n+1)\Delta t$ is given by the combination of Equations (3-82), (3-87), (3-88), and (3-98). Thus, the algorithm

$$r_j^{n+1} = r_{j,adv}^{n+1} + \eta_{j,r} + (\Delta r_j)_{diff} \tag{3.100}$$

$$z_j^{n+1} = z_{j,adv}^{n+1} + \eta_{j,z} \tag{3.101}$$

approximates a subset (incompressible) of the axisymmetric Navier-Stokes equations as given in Table 2.5 for the interior of the flow domain.

3.1.4 VORTICITY DYNAMICS IN THE WALL REGION

As discussed at the beginning of this chapter, the wall region is a thin *numerical shear layer* with thickness Δ_s, within which Prandtl's boundary layer approximation is applied to the transport equations. Vorticity is generated on the solid walls in order to satisfy the no-slip boundary condition. This vorticity generation algorithm first was used by Chorin [19] in the random-vortex method to study a two-dimensional slightly viscous flow. In the original two-dimensional algorithm, the vorticity generated along a solid wall is discretize into vortex sheet elements separated by a distance h. In order improve the boundary layer resolution, the required circulation generated at each wall point to satisfy the no-slip boundary condition is distributed among several sheets such that each sheet has a certain maximum circulation Γ_m. After being generated, these sheets leave the numerical boundary layer by diffusion to become part of the interior vorticity. As soon as a vortex sheet enters the interior of the flow domain, it is converted to a vortex element of appropriate core radius in order to satisfy compatibility between the interior and the wall region.

In the wall region of the axisymmetric domain, the numerical boundary layer thickness is assumed to be small compared to the longitudinal as well as the lateral radius of curvatures. Furthermore, since the walls of the flow domain used in this research are either zero or 90 degrees with respect to the axis of the combustor, Martins [93] has shown that the two-dimensional sheet generation algorithm developed by Chorin can be used for the vertical walls with no modification. For the horizontal walls, Martins also showed that if the shear layer thickness is much smaller than either the longitudinal or lateral radius of curvature, the same two-dimensional sheet generation algorithm can also be used in this axisymmetric flow domain. Following Martins, we will also use the two-dimensional vorticity generation algorithm on the solid wall as a first-order approximation. Detailed descriptions of the two-dimensional sheet generation algorithm can be found in [93, 101].

In order to match the interior and the wall solution, it is necessary that we calculate the tangential velocity at the no-slip check points on the solid walls induced by the vortex ring elements and the associated potential velocity field. Using this tangential velocity as an approximation for the freestream velocity as seen at infinity by the flow within the wall region. This procedure allows the interior flow to affect the production of vorticity within the wall region. Vorticity is transferred from the wall region into the interior region by converting those vortex sheets located at a local vertical distance greater than Δ_s from the wall to become vortex rings. Conservation of circulation allows the determination of the initial core radius of a vortex ring element given the length of the vortex sheet h [93].

3.2 SIMULATION OF NONPREMIXED COMBUSTION WITH LOW HEAT RELEASE

For the exothermic reactive-flow simulation with low heat release, Lagrangian scalar elements are being used to transport the species concentration fields in order to maintain the grid-free, self-adaptive nature of the algorithm. Furthermore, different sets of particles can be used to transport the concentration fields of different species with different diffusivities. Thus, a wide disparity in diffusive length scales can be accommodated naturally without posing any particular difficulty. The method solves the appropriate scalar transport equations which describe the reactive field directly without making restrictive assumptions about the structure of the reaction zone. The application to two-dimensional reactive shear layer simulation using the vortex-scalar element method with low heat release has been reported by Ghoniem and Givi [47, 50]. The scalar-element method used in this research has been modified and is capable of resolving the reactive field in more detail than the original scheme used by Ghoniem and Givi. The method, as implemented in this study, is relatively simple and robust. It is capable of handling a variety of initial and complex boundary conditions and is not limited to simple flow domains. It also allows simulations of flows with high Reynolds number and Peclet number.

The infinite-rate kinetics chemical model is used for the reactive-flow simulations in all the studies. Under this assumption, the reactants are assumed to mix and react instantly as soon as they are in contact with one another. Since the primary objective of this research is to study the effects of the large-scale structures on the mixing and the burning rate, all simulations to be performed in this research are limited to low-Mach-number flows only. For reactive-flow simulations, only low-heat-release cases will be studied.

3.2.1 THE SCALER-ELEMENT METHOD

The scalar-element method used in this study incorporated a combined mixing and reaction model, which is an improved version of the original model used by Ghoniem and Givi [47, r37]. The method uses a set of finite-area scalar elements to discretize the inflow fuel and oxidizer concentration field. These elements are conceptual computational elements originated at the inflow boundary where the inflow temperature and species concentration fields are being discretized. Each element, with circular cross section and an initial temperature, is assumed to carry a concentrated point mass at the geometric center and has a volume associated with it whose value depends only on the initial spatial discretization at the injection boundary. Within the volume of an element, species concentration is assumed to be a step function whose strength depends on the initial discretization of the species concentration field. That is, the species concentration carries by an element is assumed to be finite and uniform within the volume, and is zero elsewhere. Thus, the discrete scalar field is given by

$$s(r, t) = \sum \sigma_{s_i} \delta(r - r_i) \tag{3.102}$$

where s is the scalar field; σ_{s_i} is the strength of scalar element i, defined as the amount of the scalar carries by the element; δ is the Dirac delta function; and $\mathbf{r}_i$ is the geometric center of scalar element i. The elemental strength is given by

$$\sigma_{s_i} = \frac{1}{\vartheta}\int s(\mathbf{r}, t)\ dV \tag{3.103}$$

where

$$\vartheta = (2\pi r)(\Delta r)(\Delta z) \tag{3.104}$$

is the volume of the fluid element; and Δr, Δz are the radial distance between the centers of two consecutive elements and the length of the elements in the streamwise direction, respectively. After the discretization, the transport equation for the scalar element σ_{s_i} is then solved in the same Lagrangian manner as that used in the random-vortex method for the transport of the vorticity elements. Note that Equation (3.103) gives only the discrete local species concentration at a given point in the flow field. For displaying purpose, a set of grid is used to discretize the flow domain and the moving-average method commonly known as the *Kriging algorithm* [33] is used to interpolate the data onto the grid in order to obtain the continuous scalar field.

It should be noted that the elementary volume, ϑ, as defined in Equation (3.104), is the discrete material volume of the incoming fluid element carrying the species concentration σ_{s_i} with meridian cross sectional area $(\Delta r)(\Delta z)$. The cross section of the corresponding scalar element is assumed to be circular, and the maximum initial core radius of the element, δ_s, is obtained from the equation

$$\delta_s = \Upsilon \cdot \sqrt{\frac{(\Delta r)(\Delta z)}{\pi}} \tag{3.105}$$

where Υ is a user-input resolution parameter equal to or slightly greater than one in order to ensure that the material volume is being enclosed by the scalar element at all time, and the initial overlapping of the scalar elements used to discretize the concentration field. At each time step, the local velocities at the centers of the injection points are computed. The discrete volume of fluid with cross sectional area $(2\pi r)(\Delta r)$ and axial length $(\mathbf{u}\cdot\mathbf{n})\Delta t$, where Δt is the flow time step size, is then discretized by a number of scalar elements as shown in Figure 3.3a. Notice that in this setup, the specified radial discretization also limits the maximum streamwise length of the material volume of each scalar element.

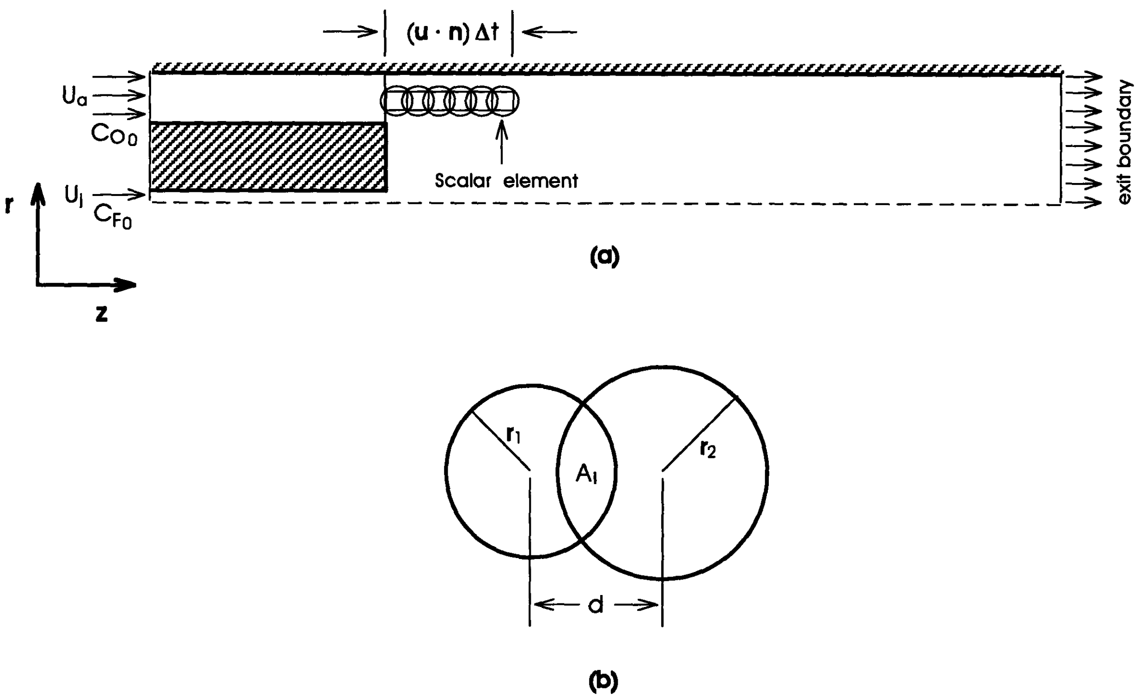

Figure 3.3 (a) Injection of the scalar elements into the flow domain. (b) Schematic drawing showing the the intersection of a fuel and an oxidizer element.

Once in the flow domain, the transport of the reactive scalar elements is governed by

$$\frac{\partial s}{\partial t} + \mathbf{u} \cdot \nabla s = \frac{1}{\lambda_s}\nabla^2 s + D_s \dot{W} \tag{3.106}$$

where

$D_s = -Da$ if $s = C_F$ and C_O

$D_s = Da$ if $s = C_P$

$D_s = (Pe)(H)$ if $s = T$

and

$\lambda_s = (Pe)(Le)$ if $s = C_F$, C_O, or C_P

$\lambda_s = Pe$ if $s = T$

and Da is the Damköhler number. In the solution procedure, Equation (3.106) is split into three fractional steps: advection, diffusion, and reaction [42]. For the advection step, the positions of the scalar elements are updated by integrating the equation

$$\frac{\partial s}{\partial t} + \mathbf{u} \cdot \nabla s = 0. \tag{3.107}$$

The second component of motion, diffusion, is implement by solving

$$\frac{\partial s}{\partial t} = \frac{1}{\lambda_s}\nabla^2 s. \tag{3.108}$$

Convection and diffusion transport of the scalar elements are implemented in a similar fashion as in the vortex method. That is, for the advection step the scalar elements are transported across the flow domain along particle trajectories. The diffusion step is performed by using a set of Gaussian random variables with zero mean and a standard deviation equal to $\sqrt{(2\Delta t)/(N\lambda_s)}$. The flow solver was constructed such that N diffusion and reaction steps are performed for the scalar elements per flow time step in order to obtain higher temporal and spatial resolution of the scalar field; therefore, $\Delta t/N$, which is the combustion time step size used in the simulations, is used in the calculation of the standard deviation for the scalar elements instead of the flow time step size, Δt.

In this study, two diffusion and reaction steps were performed after each convection step in all the simulations. That is, we compute the random-walk displacement $\eta_i = (\eta_r, \eta_z)_i$ using a time step size equal to $\Delta t/N$, where N = 2 in the simulations. Chemical reaction changes the amount of scalar carry by the elements. Since infinite-rate kinetics model is used in this study, instead of modifying the amount of scalar carries by an element using the equation

$$\frac{\partial s}{\partial t} = D_s\dot{W}, \tag{3.109}$$

the chemical equation (2.114) is used directly in the calculation. The procedure for modifying the amount of scalar carrying by an element is as follow. Reaction between a fuel and an oxidizer element is allowed to occur only when these two elements intersect. Given any two intersecting elements carrying non-zero amount of reactants with radii $\delta_{s,1}$ and $\delta_{s,2}$ (Figure 3.3b), with $\delta_{s,1} \le \delta_{s,2}$ (1 can be a fuel element and 2 can be an oxidizer element or vise versa), whose centers are a distance d apart, the area of intersection A_i is given by

$$A_i = \begin{cases} \pi\delta_{s,1}^2 & \text{for} \quad d \le \delta_{s,2} - \delta_{s,1} \\ 0 & \text{for} \quad d \ge \delta_{s,2} - \delta_{s,1} \end{cases} \tag{3.110}$$

$$A_i = \begin{cases} \pi\,\delta_{s,1}^2 - a(S, \delta_{s,1}) + a(S+d, \delta_{s,2}) & \text{for } d^2 < \delta_{s,2}^2 - \delta_{s,1}^2 \\ a(x_1, \delta_{s,1}) + a(x_2, \delta_{s,2}) & \text{for } d^2 \geq \delta_{s,2}^2 - \delta_{s,1}^2 \end{cases} \tag{3.111}$$

where

$$x_1 \equiv \frac{d^2 + \delta_{s,1}^2 - \delta_{s,2}^2}{2d} \tag{3.112}$$

$$x_2 \equiv \frac{d^2 + \delta_{s,2}^2 - \delta_{s,1}^2}{2d} \tag{3.113}$$

$$S \equiv \frac{\delta_{s,2}^2 - \delta_{s,1}^2 - d^2}{2d} \tag{3.114}$$

and

$$a(x, \delta_s) \equiv \frac{1}{2}\pi\,\delta_s^2 - x\sqrt{\delta_s^2 - x^2} - \delta_s^2 \operatorname{asin}\left(\frac{x}{\delta_s}\right). \tag{3.115}$$

At every reaction step, the distance between the centers of each pair of fuel and oxidizer elements $d_{ij} = \|\mathbf{r}_i - \mathbf{r}_j\|$ is computed. The area A_i for each pair of intersected elements is calculated according to Equations (3.110-3.115). Since chemical reaction is assumed to occur infinitely fast, whenever a fuel and an oxidizer element intersect, the intersected volume is assumed to behave like a well-stirred reactor. The reactants contained within the intersected volume are assumed to mix and to react instantly according to Equation (2.114). Products generated from the reaction are then distributed between the two elements based on conservation of mass. One should note that since the effect of the heat of reaction on the hydrodynamic field is neglected and the fluid density is assumed constant in this study, the scalar elements will never intersect without the random-walk step if the simulations were performed on a machine with infinite precision. Thus, the intersection of two initially non-overlapping scalar elements in this case should be considered as caused by the diffusion velocity of the fluid elements.

4. ISOTHERMAL REACTIVE-FLOW SIMULATIONS

In this chapter, the vortex-scalar element method developed in Chapter 3 will be used to investigate the dynamics of the near-wake region downstream of the bluff body as well as the isothermal large-scale entrainment and mixing in a two-stream, coaxial-jet, axisymmetric bluff-body combustor. The investigation of the underlying flow dynamics under the assumption of isothermal reaction, excluding the effects of the thermal energy on the mixing field, is a good prelude to the more complex exothermic reactive-flow study to be presented in Chapter 5. For this isothermal reactive-flow study, the dynamics of the recirculation zone and the large-scale entrainment and mixing will be investigated under both steady and time-dependent inflow boundary conditions.

For consistency in extrapolation as well as for meaningful comparison of the results present in this chapter to the results of exothermic reactive flow with low heat release to be presented in Chapter 5, only high-Reynolds-number flows will be simulated in all studies. That is, flows with $Re_{D_a} = (U_a^* D_a^*)/\nu^* > 2000$, where U_a^* is the magnitude of the annular flow, D_a^* is the diameter of the combustor, and ν^* is the kinematic viscosity of the fluid. The main reason for imposing this restriction is to limit the study to the high-Reynolds-number range so that the complication of the Reynolds-number dependency of the flow can be avoided[1]. It has been observed that the shear layers as well as the recirculation region generated by the bluff body are highly unstable at high Reynolds numbers. This instability of the near-wake region causes quasi-periodic shedding of large-scale vortical structures from the recirculation region at distinct characteristic frequencies which are relatively independent of the Reynolds number, especially for velocity ratios U_j/U_a which are less than unity [52, 93]. At low Reynolds number (say $Re_{D_a} \sim O(100)$), however, the unsteady flow dynamics are highly Reynolds-number dependent. Moreover, the flow tends to be stable due to the high viscous dissipation, which damps the shear layer instability and diffuses the vortical structures before they have the chance to grow to any significant sizes to affect the stability of the recirculation region. From numerical experiments, it was found that the unsteady large-scale dynamics vary insignificantly with Reynolds number for $Re_{D_a} > 2500$, as is expected for high-Reynolds-number flows. In addition, it was observed in numerous experimental studies that when the flow Reynolds number based on the combustor diameter is in the range of $O(1000)$, the recirculation region and unsteady motions of the large-scale structures are quasi-axisymmetric [85, 120]. Thus, it was decided that all simulations for the isothermal reactive-flow study will be performed with $Re_{D_a} = 3000$. This Reynolds number is high enough such that the large-scale flow dynamics is relatively independent of the flow Reynolds number, and yet is still

---

[1] Although the Reynolds-number dependency of the flow is also of high interest, however, we would like to limit the study to the high-Reynolds-number range in this research.

low enough for the axisymmetric approximation to remain valid.

The geometry of the computational domain employed in the numerical simulations to be presented in this chapter is given in Figure 1.1, repeated here in Figure 4.1 for convenience. One important aspect of this bluff-body configuration that has been shown to be relevant in terms of determining the unsteady dynamics of the near-wake region is the bluff-body-to-jet diameter ratio, D_b/D_j. As showed by Martins and Ghoniem [97], combustors with small values of D_b/D_j exhibit unsteady dynamics which are quite different from those with large values of D_b/D_j. For geometries with large values of D_b/D_j, there are two significant instability mechanisms dictating the unsteady behaviors in the near-wake region of the bluff body. These are the shear layer instability (between the jet and the recirculation bubble and between the recirculation bubble and the outer annular flow) and the recirculation region instability. For large values of D_b/D_j coupling with inflow velocity ratios[1] U_j/U_a which are less than unity, the dynamics of the near-wake region are dominated by the recirculation region instability manifested by the shedding of large coherent structures from the region at distinctive frequencies [91]. As the ratio of D_b/D_j is decreased, the size of the recirculation region diminishes and the shear layer instability dominates the unsteady dynamics of the near-wake region. In that case, the flow behaves very much like a simple axisymmetric shear layer.

The governing equations and the numerical schemes used in the simulations have been presented in Chapters 2 and 3, respectively. In this study, owing to the assumption of isothermal reaction, the expansion velocity field $\mathbf{u}_\varepsilon$ is identically zero and the flow Reynolds number based on the combustor diameter is constant throughout the whole flow field ($Re_{D_a} = 3000$). As mentioned earlier, one of the main characteristics of turbulence is the three-dimensional vortex stretching. The axisymmetric-flow model and the low-Mach-number assumption obviously restrict the physics of the flow that can be captured by the simulations. Notably, the suppression of certain flow instability modes as well as the vortex stretching in the third dimension. Nonetheless, results from the simulations are still useful for the investigation of the unsteady flow dynamics and the large-scale entrainment and mixing in the near-wake region. This presumption is supported by a number of previous experimental and numerical studies of two-dimensional and axisymmetric shear layers and recirculating flows [85, 86, 93, 134, 119], which have shown that the approximate model used in this research is able to reproduce most of the important large-scale flow features accurately under a restricted range of flow Reynold number.

We will begin the discussion of the present investigation by a survey of previous studies on

---

[1] Actually, the relevant parameter is the momentum flux ratio, $(\rho_j U_j^2)/(\rho_a U_a^2)$, rather than the velocity ratio. However, if the fluid densities are approximately the same and remain constant with time, the velocity ratio is directly proportional to the square root of the momentum flux ratio.

this bluff body flow, both experimental and numerical. Results from this study will then be reported and conclusions will be drawn.

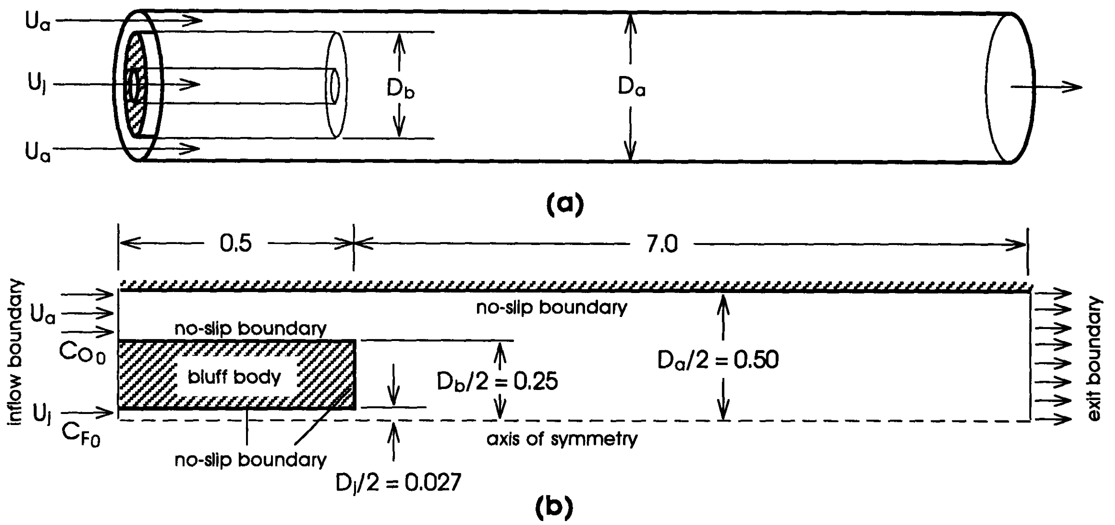

Figure 4.1 Geometry of the two-stream, coaxial-jet, axisymmetric bluff-body combustor used in this research. **(a)** Schematic drawing of the combustor. **(b)** Axisymmetric computational domain. All the dimensions in **(b)** are normalized by the annular diameter (= 0.1 m).

4.1 BACKGROUND

Many of the unsteady flow dynamics of nonpremixed turbulent combustion processes in practical energy conversion devices can be modelled by double concentric jets separated by an annular interface, similar to the axisymmetric flow configuration we are studying in this research. It is well-known that in nonpremixed combustion processes, under most conditions, the chemical time scales are much smaller than the flow time scales. Thus, the aerodynamics of mixing usually plays a very important role in ignition, flame stabilization, and the overall combustion processes in these systems [80, 84, 85]. The aerodynamics of confined bluff-body flow, both isothermal and exothermic reacting, have been extensively studied by Roquemore and coworkers of the Wright Aeronautical Propulsion Laboratory [117, 119, 120]. From their experimental studies, it was shown that downstream of the bluff-body recirculation region the flame consists of large, discrete *fireballs*, or *flame turbules*, separated by axial regions where no flame is visible [119]. These so-called flame turbules are shed from the recirculation region quasi periodically and are found to retain their identity for very large distance downstream of the recirculation region. The structures of these flame turbules were found to be quasi axisymmetric under certain Reynolds number range, as can be seen in the high-speed Schlieren photographs presented in Figure 4.2a and the simultaneous time recordings of the flame intensity by the photo detectors presented in Figure 4.2c. The axial velocity of the flame turbules was observed to govern by the annular air jet velocity, for almost all the air and fuel flow conditions they have studied. The characteristic frequency of the flame turbules at a given axial location near where they are being formed was also found to increase with an increase in fuel flow rate.

The shedding frequencies of confined bluff-body flows have also been investigated extensively in experimental studies. works by Kiya and Sasaki [73], Parker and Welsh [109], Kenworthy [71], and Cherry *et al.* [18] all have reported that the Strouhal number based on the diameter of the bluff body, S, in the range from 0.1 to 0.2. The Strouhal numbers for unconfined cylinders with different diameters at various flow Reynolds numbers have also been extensively measured by Roshko [121], as shown in Figure 4.3. It was observed from the experimental data that the Strouhal number is a function of the Reynolds number for $Re_D < O(10^3)$, and remains approximately constant at $S = 0.21$ for higher Reynolds numbers. This value of S was found to prevail up to a Reynolds number $Re_D = 2 \times 10^5$. These experimental studies suggest that the shedding frequency of the bluff body is an important parameter governing the unsteady dynamics of the near-wake region of the confined bluff-body flow we are studying.

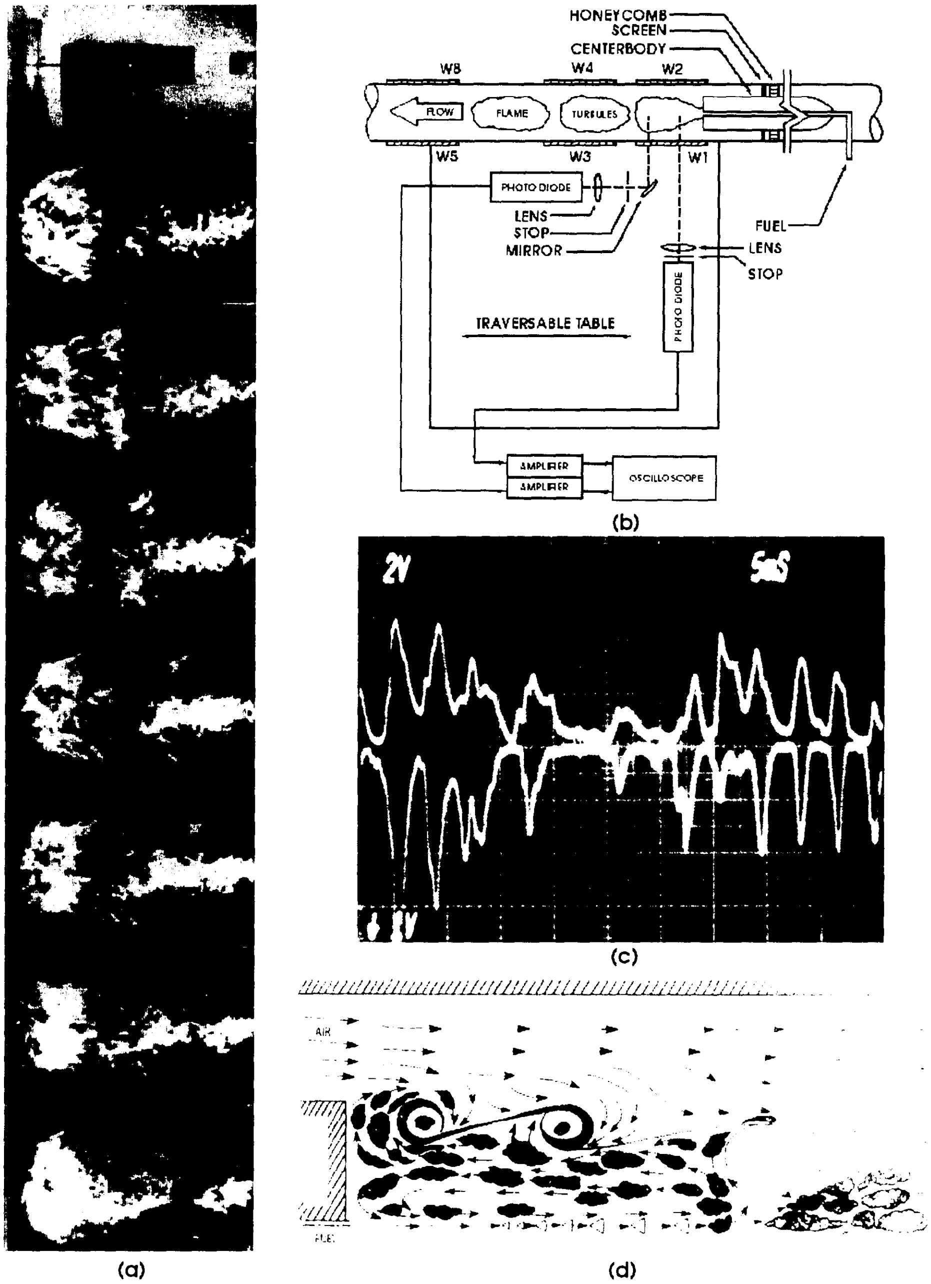

Figure 4.2 Experimental study performed by Roquemore and coworkers (119). **(a)** High-speed (3000 frames/s) Schlieren photographs of the flame observed through a window of the experimental combustor with a camera using a wide-angle lens showing the symmetrical shedding of a large-scale reactive flow structure from the recirculation region. **(b)** Schematic drawing showing the setup of the experimental study. **(c)** Simultaneous time recordings of the flame intensity as observed by the photo detectors located at the top and the bottom edges of the bluff body. **(d)** Illustration of a proposed mechanism by Roquemore whereby shed vortices give rise to the formation of flame turbules.

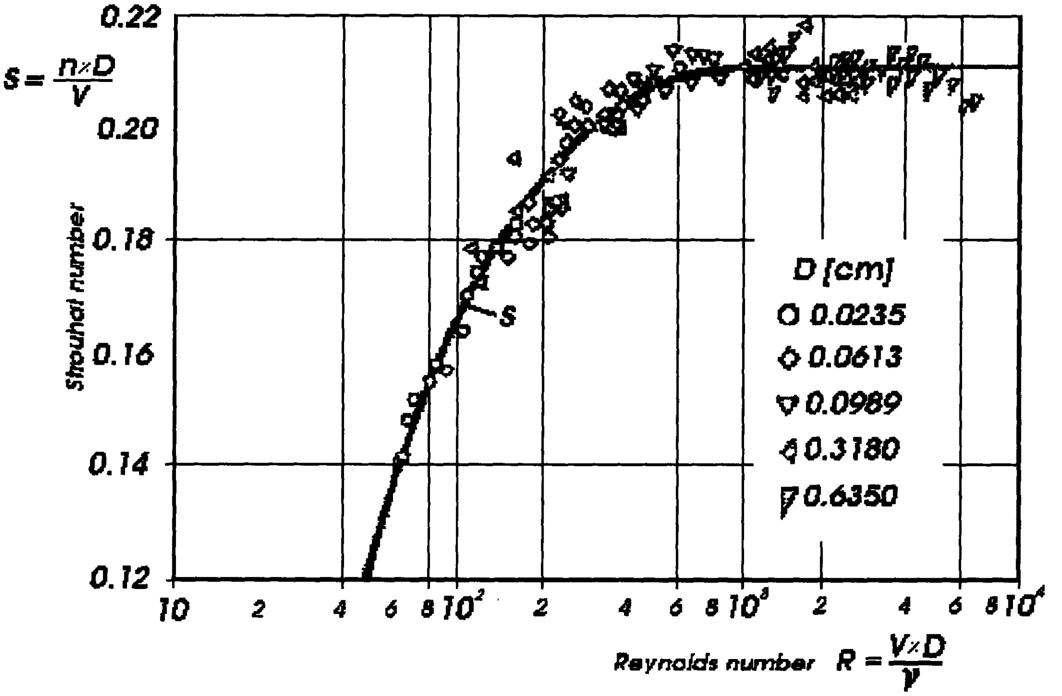

Figure 4.3 The Strouhal number in terms of the Reynolds number for the flow past a circular cylinder as measured by A. Roshko (125).

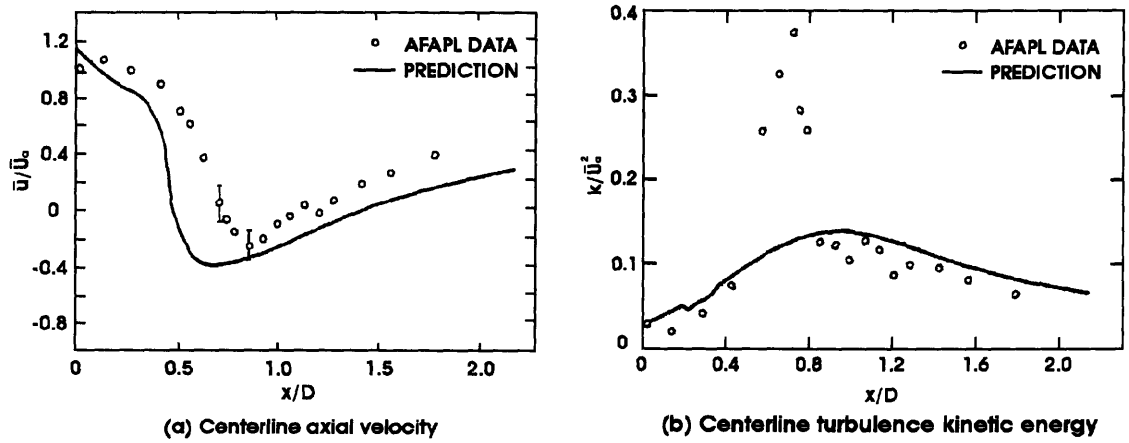

(a) Centerline axial velocity

(b) Centerline turbulence kinetic energy

Figure 4.4 Centerline axial velocity and turbulence kinetic energy predicted by Correa (22).

Extensive visual experimental studies of isothermal and exothermic reactive flows over axisymmetric, unducted, vertically-mounted bluff-body combustors at low Reynolds numbers have been carried out by Li and Tankin [85]. The flow visualizations in their studies were accomplished by adding $TiCl_4$ vapor into the central gaseous propane jet for both nonreactive and reactive flows, or by injecting $TiCl_4$–N_2 mixture into the flow field. Laser light sheets were used to illuminate the flow for visualization. From their studies, they have found that the size of the recirculation zone was significantly enlarged when a central jet was introduced into the flow. For exothermic reactive flows, they found that the annular vortices in the recirculation region appeared to be more organized, stationary and intense for attached flames as compared to the isothermal reactive flows, and the size of the recirculation region as well as the height of the central jet are reduced by at least half. For detached flames, they found that the height of the central jet is greatly reduced; whereas the length of the recirculation region is increased, when compared to the corresponding isothermal reactive flows.

Nonreactive bluff-body flow calculations using the two-equation κ–ε turbulence model have been reported by Sturgess and Syed [137] and Sturgess, Syed, and McManus [139]. Axisymmetric finite-difference discretization of the incompressible, time-averaged Navier-Stokes equations, with two-equation turbulence closure was used in the simulations. Results from the simulations yield acceptable agreement with experimental data in many respects, however, they are deficient in predicting the recovery rate of the central near-wake region. It was hypothesized that the probable cause is the inability of the turbulence model to account for the effects on Reynolds stresses due to the curvature of the streamlines in that region. Sturgess and Syed [140] have extended their method to handle reactive flow using the fast-chemistry model similar to the one being used in this research for the treatment of combustion. The same authors have, subsequently, extended their method for multi-species, variable-density flow [138].

Correa [22] applied a model based on the density-weighted averaged Navier-Stokes equations with an eddy-viscosity turbulence closure based on a two-equation κ–ε turbulence model. Comparisons with limited available experimental data have shown similar discrepancies. While mean flow features were accurately predicted by the numerical simulation, turbulent kinetic energy was significantly underestimated, as can be seen in Figure 4.4. Discrepancies between predicted and experimental results were found to increase for higher jet velocities, where the flow field was observed to be dominated by large-scale vortical structures. More recently, Correa and Gulati [23] applied a model based on the Favre-averaged Navier-Stokes equations to a bluff-body stabilized flame of 27.5% CO, 32.2% H_2, and 40.2% N_2 fuel mixture injected into air. The model assumes partial equilibrium for the radical pool, assumed-shape probability density functions (PDFs) for the two thermochemical variables required, and a two-equation κ–ε turbulence closure. While the predicted mean and variance of mixture fraction, temperature, and species concentration fields showed good agreement with the experimental results, shortcomings in the turbulence model were again noted and suggestions for improved modelling of the turbulence were proposed that included a PDF transport method.

Krishnamurthy and Park [77] examined the streamline curvature effects in an isothermal bluff-body flow using CO_2 as the jet fluid. Numerical simulations were carried out based on the Reynolds-averaged Navier-Stokes equations with $\kappa-\varepsilon$ turbulence closure. A comparison with measured mean and fluctuating axial velocity and CO_2 mole fraction has shown that the model predicted the general flow features satisfactorily. Similar findings were obtained by Krishnamurthy *et al.* [78, 79] and by Memering and Krishnamurthy [96]. In their studies, they found that calculations using modelling approach correctly predicted the observed flow similarity and the vortex center characteristics with respect to various inlet flow variables.

Calculations described by Roquemore *et al.* [118], using similar time-averaged method, showed agreement with experimentally measured mean axial velocity and CO_2 concentration within 15 percent. However, error in the predicted turbulence intensities was again found to be considerably greater. In particular, the turbulence intensities were significantly underpredicted in the stagnation regions of the jet flow.

The dynamics of the nonreactive flow inside several axisymmetric bluff-body combustors similar in geometry to the one used in this study have been investigated numerically using the axisymmetric *Random-Vortex method* and were reported in the works of Martins and Ghoniem [52, 53, 93, 94]. Results from their studies have shown that the dynamics of this confined bluff-body flow strongly depended upon the bluff-body-to-jet diameter ratio, D_b/D_j, the inflow velocity or momentum ratio, U_j/U_a, and the blockage ratio, D_b/D_a. For a given inflow velocity ratio, it was shown that the level of unsteady fluctuations in the recirculation region and the frequency of shedding increase with the diameter ratio. Stability of the recirculation region was found to decrease as the velocity ratio approaches unity, but increase again as the velocity ratio becomes >> 1. The fluctuation intensities were also found to increase significantly with blockage ratio. In all their investigations, Martins and Ghoniem analyzed the flow field by studying the instantaneous streamline contours, vortex-element trajectories, mean velocity profiles, and Strouhal numbers. The temporal and spatial distribution of the fluctuation kinetic energy, which is an important flow quantity for the understanding of the unsteady large-scale mixing field, was not explored. In addition, the combustor confinement used in their studies was assumed to have an inviscid wall. Thus, interactions between the large-scale vortical structures shed from the recirculation region and the wall boundary layer could not be captured in the simulations. It is known from experimental studies that the presence of the wall boundary layer has a significant effect on the aerodynamics of the recirculation region and the flame stability in exothermic reactive flows, especially for combustor geometries with high blockage ratio. Therefore, it is important that these issues be addressed and the effects of the wall boundary layer on the recirculation region be investigated.

In this study, we supplement the results obtained by Martins and Ghoniem on the bluff-body flow by investigating the unsteady fluctuation kinetic energy and the large-scale entrainment and mixing as a function of the inflow velocity ratio. The destability mechanisms of the recirculation region and the interactions between the wall boundary layer and the recirculation region are analyzed in terms of the local unsteady fluctuating kinetic energy. The results are then used to quantify the dominant physical processes controlling the large-scale entrainment and mixing in this flow. For this study, all the simulations were performed for a combustor with diameter ratio $D_b/D_a = 1/2$, and bluff-body-to-jet diameter ratio $D_b/D_j = 9.26$ (Figure 4.1) at three inflow velocity ratios: $U_j/U_a = 0.62$, 1.04, and 2.08.

The numerical parameters used in all the simulations in this study are as follows. The flow time step size $\Delta t = 0.01$; the Reynolds number based on the annular diameter and the magnitude of the annular inflow velocity $Re_{D_a} = 3000$; the length of the vortex sleeves used to satisfy the no-slip boundary condition on the solid walls, $h = 0.009$; the absolute value of the maximum circulation assigned to each vortex element, $\Gamma_m = 0.00225$; and the numerical sublayer thickness at each wall is one-and-a-half times the standard deviation of the random-walk displacement. The stoichiometric coefficients (per mole of fuel) of the chemical equation α, β, and σ are equal to 2, 0, and 3, respectively. Finally, the ratio of the oxidizer molar flow rate to the fuel molar flow rate divided by their stoichiometric ratio is 1.5.

4.2 LARGE-SCALE DYNAMICS AND THE MIXING FIELD UNDER THE ASSUMPTION OF ISOTHERMAL REACTION WITH STEADY INFLOW BOUNDARY CONDITIONS

In this section, results from the isothermal reactive-flow simulations with three different (steady) inflow velocity ratios (0.62, 1.04, and 2.08) are presented and discussed. Before we begin the presentation, we would like to point out that the region of interest in the flow under investigation is, mostly, the recirculation zone located between the face of the bluff body and the beginning of the fully-developed region, which is approximately a couple of bluff-body diameters downstream of the bluff-body face. The unsteady dynamics in this region and the large-scale entrainment and mixing as a function of the inflow velocity ratio will be studied in detail. The flow dynamics will be investigated under both steady and time-dependent inflow boundary conditions. For all the simulations, fuel and oxidizer, both assumed to be diluted in an inert gas and with the same molecular weight, are introduced into the reaction zone through the jet and the annular flow, respectively. Chemical reaction is assumed to be described by a binary, single-step, irreversible equation with infinite-rate kinetics and with negligible heat of reaction (Equation 2.80). Under these assumptions, the flow is treated as isothermal and the fluid density can be approximated as constant. Thus, the transport equations of the hydrodynamic field and the scalar field are decoupled. Since chemical time scales are much less than the flow time scales under the flow conditions we are studying, the infinite-rate kinetics model is an acceptable first-order approximation. It helps to eliminate the complication associated with higher-order model. Together with the negligible heat-of-reaction assumption, it allows us to isolate the effect of the mixing enhancement brought about by the quasi axisymmetric large-scale structures on the rate of product formation, which is the primary objective of this part of the research. With the above assumptions, the simulation yields an upper bound on the amount of products can be generated and the most compact mixing zone possible for a given inflow velocity ratio.

4.2.1 The TIME-AVERAGED STATISTIC FLOW PROPERTIES

The time-averaged statistic properties of the flow first are presented and discussed in this section. In analogy to performing experiments in the laboratory, since the unsteady evolution of a spatially inhomogeneous flow is simulated, spatial as well as temporal averaging are necessary in order to obtain the flow statistic properties. For the purpose of obtaining the flow statistics and for visual presentation, a mesh with variable-size cells covering the region of interest was used for the calculations. To obtain the continuous product mole fraction field, the concentration within a given cell was computed by averaging the strength of the Lagrangian scalar elements located within the cell over a large number of time steps after stationary state of the flow has been established. The sizes of these cells were chosen to be larger than the average distance between two neighboring elements in order to ensure that a good fraction of the scalar elements are located in each cell at each time step, but is smaller than the relevant length scale of the smallest resolvable eddies in order to guarantee adequate spatial resolution.

All simulations performed for this study were started impulsively at $t = 0.0$ with different (constant) inflow velocity ratios. Vortex elements are introduced on the solid walls in the flow domain at the predetermined check points every time step to satisfy the no-slip wall boundary condition, and they are deleted at the exit boundary of the flow domain. Figure 4.5 presents the total number of vortex elements in the flow domain as a function of time for all three cases. As can be seen from the figure, the total number of vortex elements increases rapidly from t = 0.0 to approximately t =12.0. Within this time period, the flow inside the channel has gone through a transient period from a start-up fully potential flow to a stationary shear flow in which the flow features repeated themselves quasi periodically. After stationary state of the flow has been established, the total number of vortex elements in the flow domain is seen to fluctuate weakly with time due to the formation and the departure of the large-scale vortical flow structures in the computational domain. The time beyond which the flow field has reached a stationary state is clearly evident in this figure. Since all the time-averaged flow quantities are meaningful only when the flow is statistically stationary, it is obvious from this figure that the flow data in the range t < 12.0 for all three cases must be discarded for the purpose of calculating statistical quantities. Thus, all the statistical properties of the flow presented in this study were obtained by averaging the quantities of interest after t = 12.0 for a total of 7300 time steps, corresponding to a total of 73 units of dimensionless time.

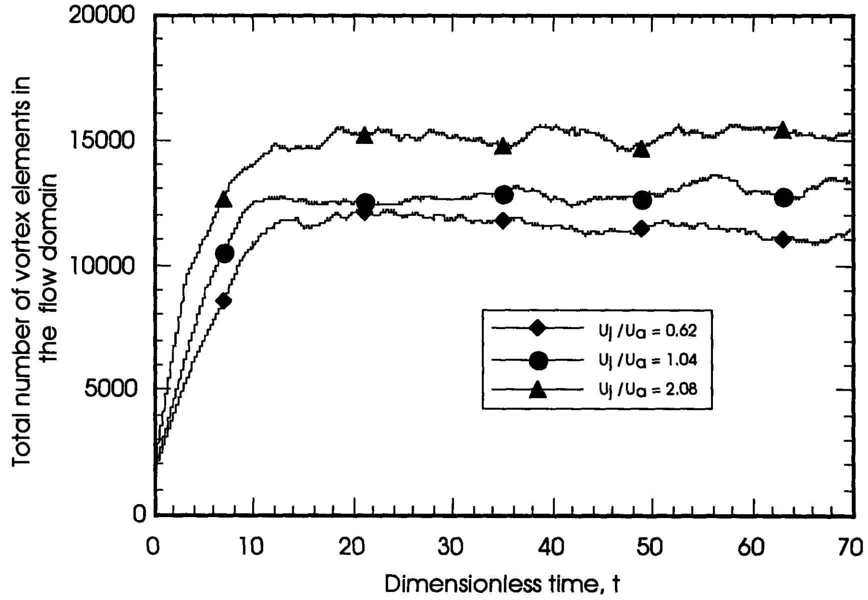

Figure 4.5 Total number of vortex elements in the computational domain as a function of time.

For a stationary random process, time averaging can be expressed mathematically as [63]

$$\overline{\Phi}(\mathbf{r}) = \lim_{t \to \infty} \frac{1}{2T} \int_{-T}^{T} \Phi(\mathbf{r},t)\, dt \tag{4.1}$$

where Φ is any flow quantity and $\overline{\Phi}$ is the corresponding time-averaged value. Obviously, for practical reasons, we cannot carry out the averaging procedures for an infinite value of T. If we take T to be a finite time interval, then this interval must be sufficiently large compared with the time scale of the flow dynamics we wish to regard as belonging to the turbulent motion of the flow before the statistical quantities are meaningful. On the other hand, the interval must be small compared with any slow variations in the flow field that we do not wish to consider as significant to the problem. Clearly, there is a certain arbitrariness in the choice of the fluctuations that we think is relevant to the problem at hand. However, by taking samples at different values of T, it is possible to determine the appropriate value of T to use such that all statistical quantities obtained from the averaging procedures are meaningful. Furthermore, the average value should be independent of the origin t of the averaging procedure. Thus, $\partial\overline{\Phi}/\partial t$ should be either zero or, in the case of a slightly varying main flow, negligibly small.

Figures 4.6-4.8 show the time-averaged radial distributions of the axial velocity, the fluctuation kinetic energy, $\overline{u'u'} + \overline{v'v'}$, and the product mole fraction at axial station z = 0.7551 (this is approximately the axial station containing the time-averaged centroid of the recirculation region) as a function of the data sampling size for all three cases. The information provides by these plots can be used to establish the value of T we should use in the time-averaging procedure in order to obtain meaningful statistics for this study. From the figures, it is seen that both the velocity and the product mole fraction mean profiles have high convergence rates, and the variations of the profiles from one sampling size to the next also remain small. However, the product of the velocity fluctuations, $\overline{u'u'}$ and $\overline{v'v'}$, which are the second moments of the flow velocity, converge much more slowly, especially in the shear layer regions. Nonetheless, it is clear from these plots that a total of 7300 time steps are sufficient to establish stationary state for all the time-averaged statistic flow properties.

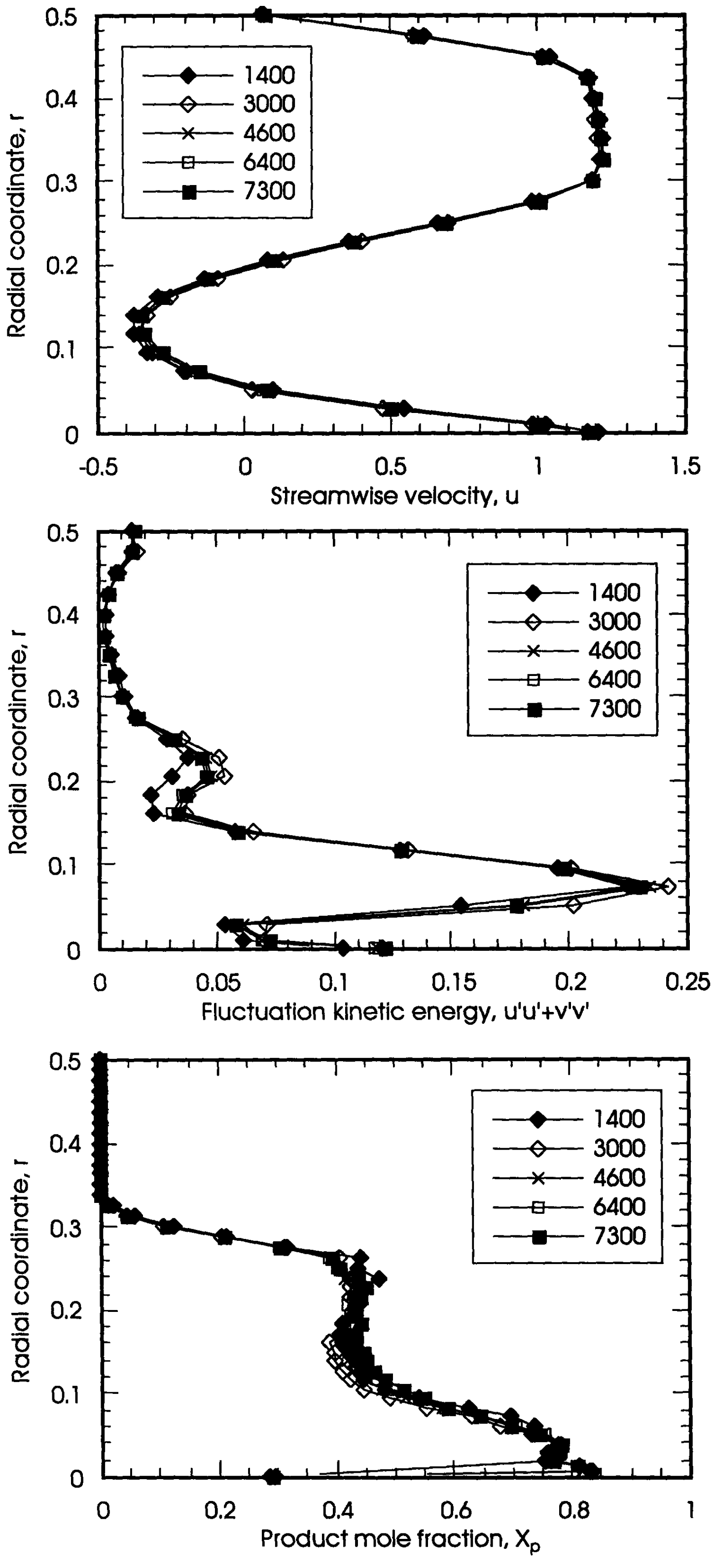

Figure 4.6 Time-averaged flow properties as a function of sampling size of the data. U_j/U_a = 0.62, z = 0.7551.

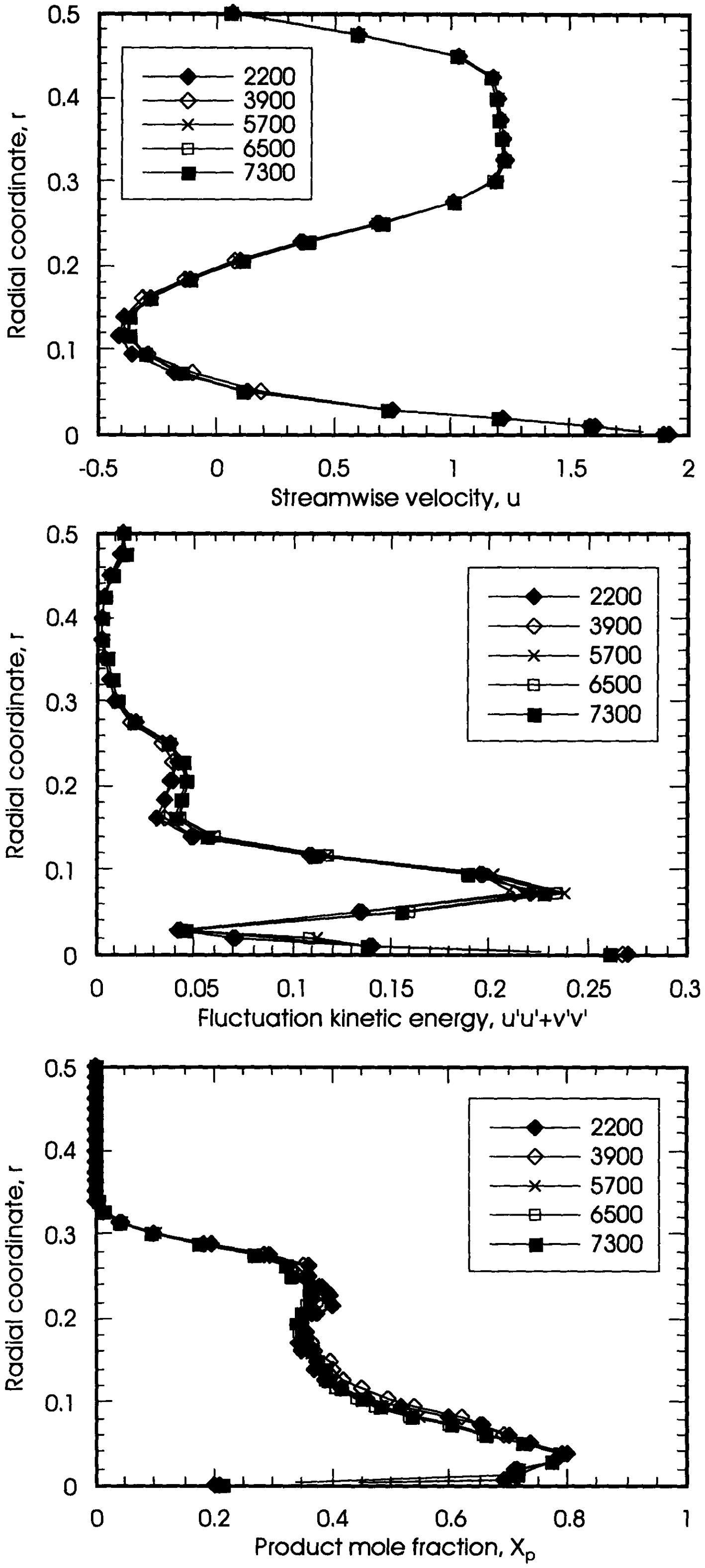

Figure 4.7 Time-averaged flow properties as a function of sampling size of the data. U_j/U_a = 1.04, z = 0.7551.

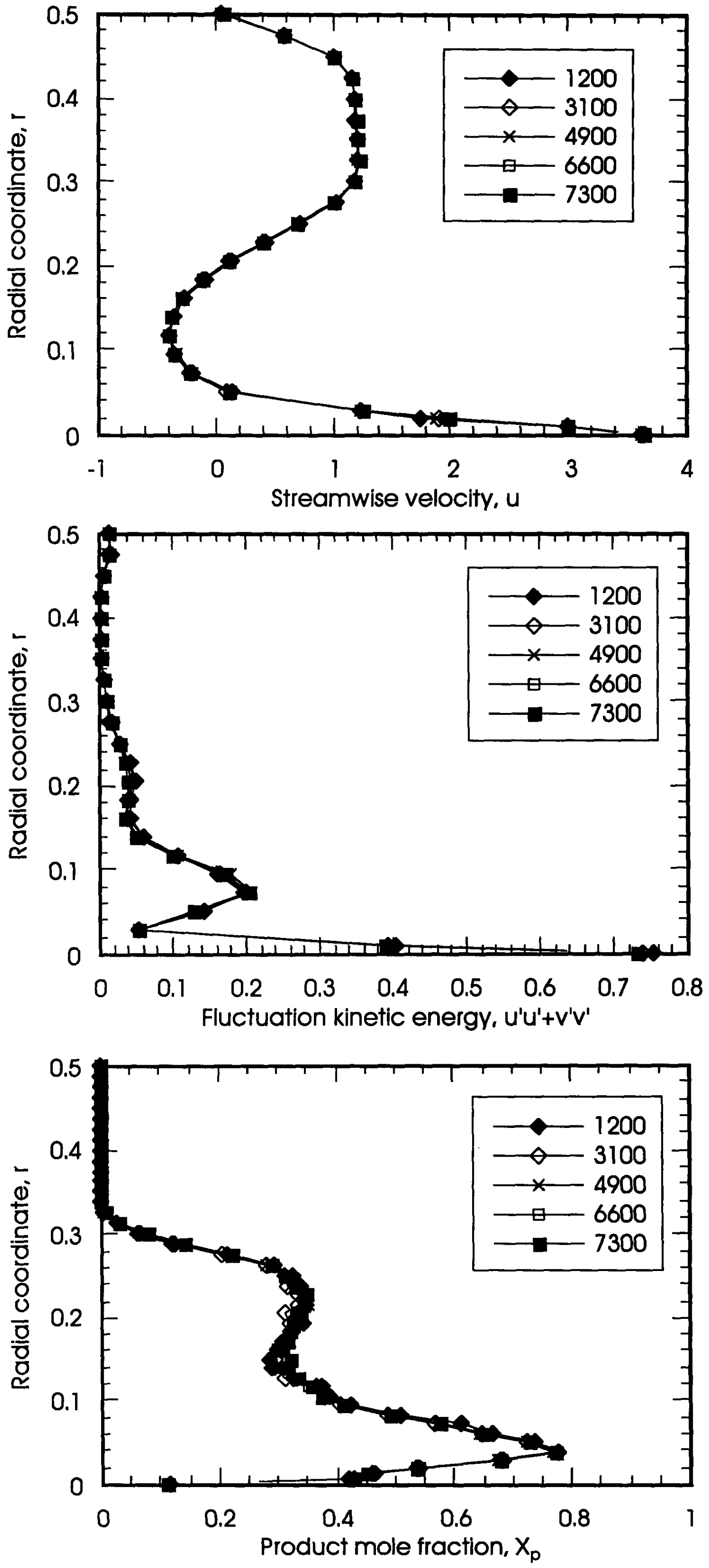

Figure 4.8 Time-averaged flow properties as a function of sampling size of the data. U_j/U_a = 2.08, z = 0.7551.

4.2.2 THE TIME-AVERAGED VELOCITY FIELD, THE PRODUCT MOLE FRACTION, AND THE FLUCTUATION KINETIC ENERGY

The magnitude of the time-averaged velocity field and the product mole fraction field are presented in Figure 4.9. Before we begin the discussion of this figure, it is necessary to point out that the contour levels of the time-averaged velocity field (Figure 4.9a) were cut off at 1.25 in this figure. Thus, detailed internal structures of the jet flow are not resolved for the two cases with velocity ratio U_j/U_a = 1.04 and 2.08. This is necessary in order to prevent the important flow features in the main part of the flow domain from being washed out, and for meaningful comparisons among the three cases. From this figure, it is seen that the main feature of the flow field, regardless of the inflow velocity ratio, is a narrow potential core at the center of the channel where the annular velocity is being accelerated from a mean value slightly greater than 1.0 before the bluff body face, to approximately 1.25 over the recirculation zone. The flow is seen to decay gradually back to 1.0 at a distance about three bluff-body diameters downstream of the bluff-body face. The time-averaged wall boundary layer increases its thickness considerably near the end of the recirculation region, and reaches to almost a constant thickness downstream of the recirculation region regardless of velocity ratio. As will be shown later in the unsteady velocity field, this sudden increase in boundary layer thickness is associated with the formation of large vortices in the boundary layer, synchronizing with the shedding frequency of the large-scale vortical structures originated from the recirculation region. This strong interaction between the large vortices and the wall boundary layer, which is highly prominent in the unsteady fluctuation kinetic energy field, affects the dynamics of the near-wake region significantly and was not captured by the simulations of Martins due to his assumption of inviscid-wall confinement [93]. Notice that a well-defined shear layer between the jet and the outer flow and between the annular flow and the recirculation region are clearly visible in these time-averaged velocity fields.

The effect of varying the inflow velocity ratio on the flow field development is also quite noticeable in this figure. In qualitative agreement with the inferred flow field development reported by Roquemore [117] and Namazian [103], when the jet momentum is weak relative to the recirculating flow, the central jet penetrates only a short distance into the recirculation region. This flow pattern gives rise to two stagnation points: the *forward stagnation point* which is that of the central jet and an *aft stagnation point*, which defines the end of the recirculation zone established by the annular-flow separation (Figure 4.9a-1 and Figure 4.10a). As the magnitude of the jet velocity is increased, it penetrates the recirculation region completely and no stagnation points exist along the centerline. This seems to be the flow pattern for both U_j/U_a = 1.04 and 2.08 (Figures 4.9a-2, a-3, 4.10b and c). Notice that the time-averaged velocity fields presented in Figure 4.9a indicate that a well-defined recirculation region exists behind the bluff body regardless of the velocity ratio. However, as will be seen in the Section 4.2.4 where we present and discuss the unsteady results, the recirculation region of these three cases has very different unsteady dynamical behaviors, and it is this strong dissimilar unsteady dynamics that gives rise to the very different time-averaged mixing fields as shown in Figure 4.9b.

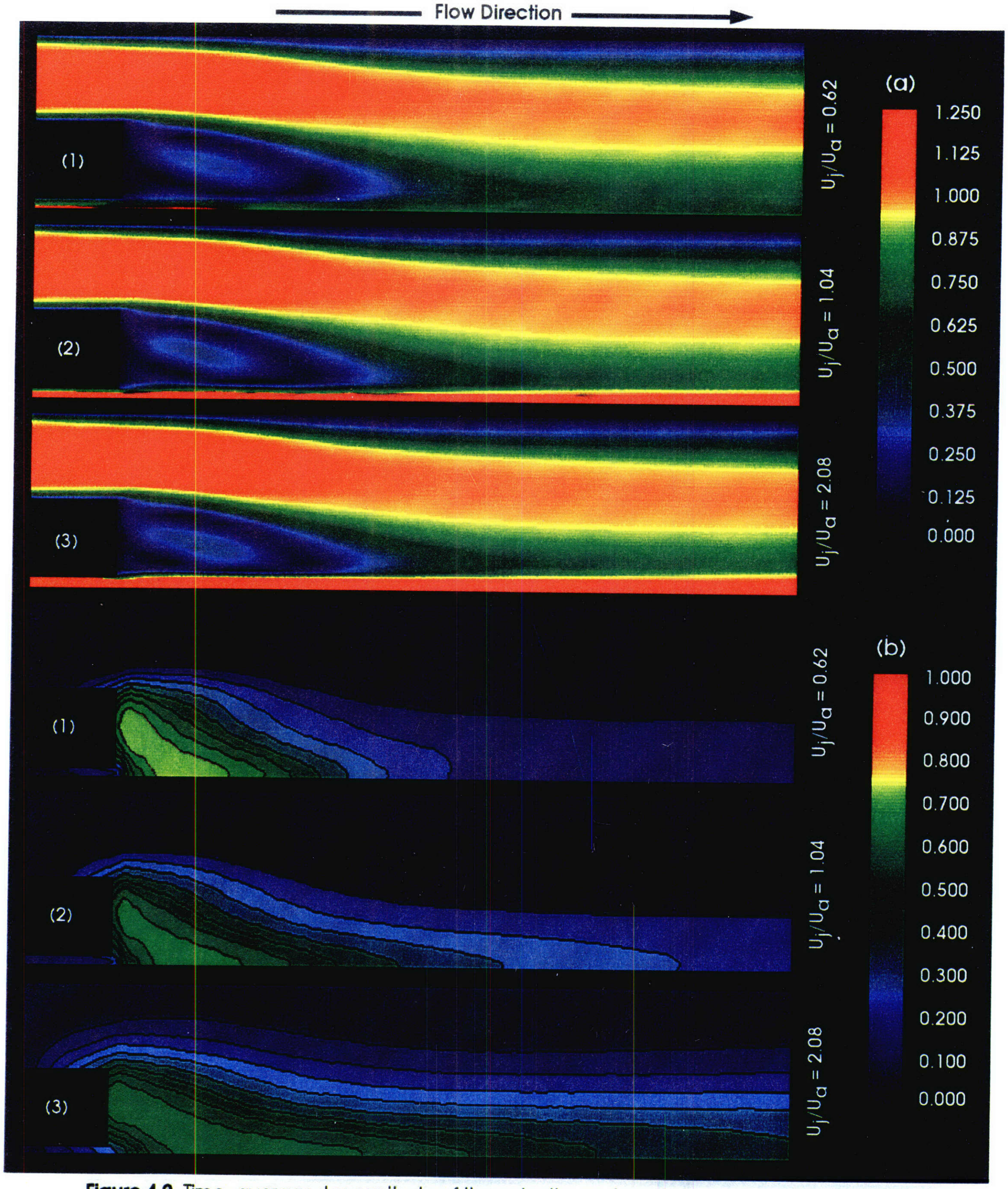

Figure 4.9 Time–averaged magnitude of the velocity and product mole fraction contours. **(a)** Magnitude of the velocity. **(b)** Product mole fraction.

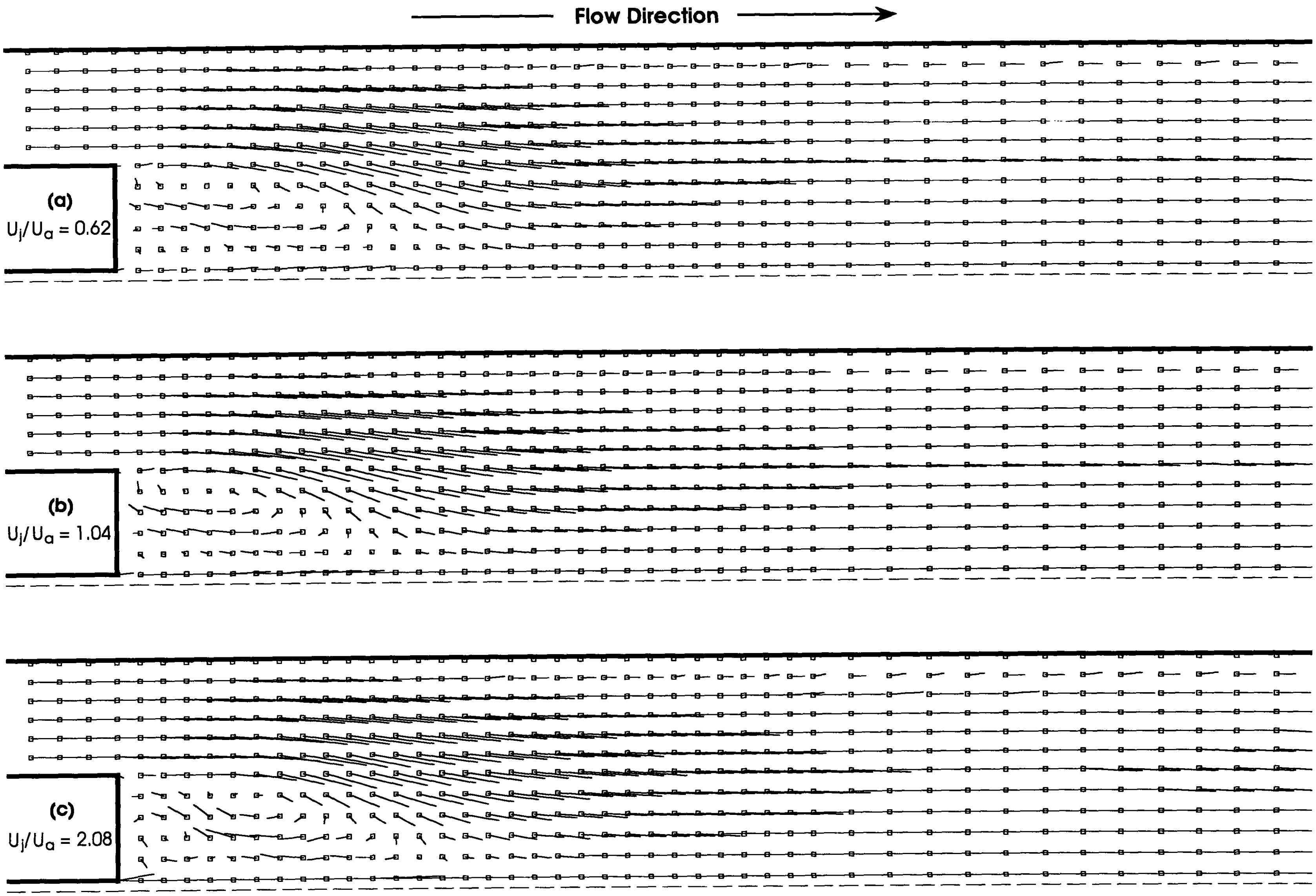

Figure 4.10 Time-averaged total velocity field.

The bottom three pictures in Figure 4.9 show the time-averaged product mole fraction contours corresponding to the three velocity ratios as shown in Figure 4.9a. In qualitative agreement with the experimental results of Namazian [103], the distribution of the mean product mole fraction varies substantially as a function of the velocity ratio. For the case $U_j/U_a = 0.62$, the jet fluid is being stagnated a short distance from the exit plane. Thus, mixing of the fuel with the oxidizer and chemical reaction are mostly completed within the recirculation region. In this case, highest product concentration is found within the recirculation region a short distance downstream of the exit plane. Hence the mixing zone is compact, having approximately the same length as the recirculation region established by the bluff body. As the velocity ratio is increased to 1.04, we see that the length of the mixing zone extended past the time-averaged length of the recirculation region (Figures 4.9a-2, b-2). At this velocity ratio, a large fraction of the fuel has sufficient momentum to penetrate into the flow field much further before reacting with the oxidizer. Thus, a significant amount of reaction is seen to occur a short distance downstream of the recirculation region in this case. Notice that in this case the maximum of the product contour level within the recirculation region is about 15 percent lower compared with the case $U_j/U_a = 0.62$. Finally, for $U_j/U_a = 2.08$, the momentum of the fuel jet is so much higher than the annular flow that the latter has essentially no effect on the jet flow, and the fuel behaves almost like a free jet. Most of the fuel elements are seen to remain close to the centerline of the combustor where mixing and chemical reaction are most intense. In this case, much lower product concentration within the recirculation region is observed, and the mixing zone extends many bluff body diameters downstream of the recirculation region. The variation of the time-averaged product mole fraction contours as a function of inflow velocity ratio presented in Figure 4.9 is consistent with the experimental results obtained by Namanzian [103]. In his experimental studies, he found that for low fuel-to-air velocity ratios, the flame is broad, short and blue, exhibiting more well-mixed fuel and air within the recirculation region similar to Figure 4.9b-1. For very high velocity ratios, he found that the flame is long and narrow, confining primarily near the centerline of the combustor and has much lower product concentration within the recirculation region. This trend can also clearly be seen in Figure 4.11 where we show the product flux, defined as[1]

$$\int_0^R (\rho u Y_p \, 2\pi r) \, dr, \tag{4.2}$$

integrated across the combustor cross section as a function of the axial coordinate. From this figure, we see that the product flux at a given axial station within the recirculation region decreases as the velocity ratio increases, indicating that mixing and reaction within the recirculation region decrease with an increase in velocity ratio.

---

[1] Y_p is the product mass fraction.

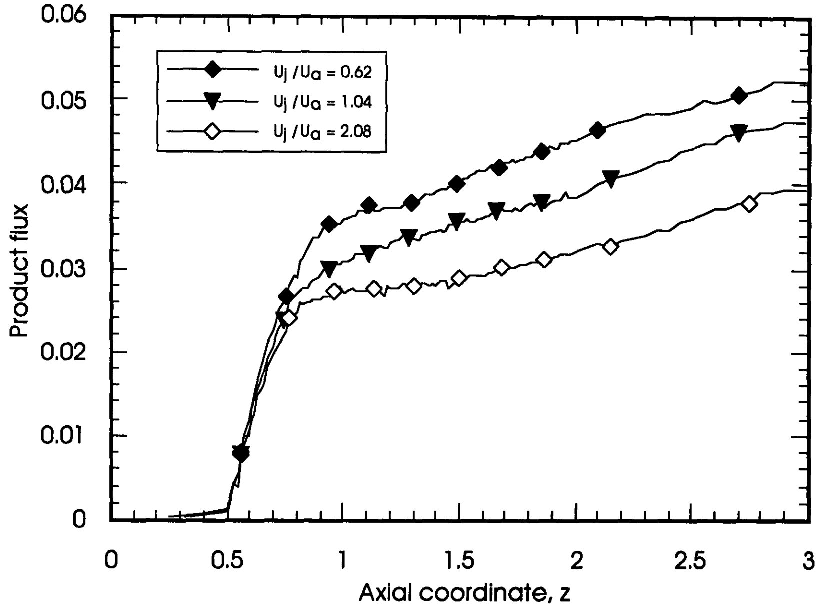

Figure 4.11 Product flux integrated across the combustor cross section as a function of the axial coordinate.

Figures 4.12-4.14 show the time-averaged radial distributions of the flow properties at axial station z = 0.7551 for all three cases. Results at this axial station are presented since they are characteristic representations of the distributions obtained within the recirculation region of the flow. Notice that the corresponding radial profiles presented in these three figures are quite similar in shape. All three velocity profiles show an inviscid core flow with steep velocity gradient at the top wall. The radial distributions of $\overline{u'v'}$ and $\overline{u'u'} + \overline{v'v'}$ exhibit significant Reynolds stress and fluctuation kinetic energy within the shear layer between the outer annular flow and the recirculation region, as well as within the shear layer between the recirculation region and the jet. The $\overline{u'v'}$ correlations are seen to attain their maxima inside the two shear layers, corresponding to the regions with highest mean velocity gradients and the most intense mixing. The direction of momentum transfer hence, large-scale transport and mixing, within the shear layers is clearly evident in the $\overline{u'v'}$ profiles. On the top shear layer, the axial velocity and the fluctuation are, on the average, positive. A negative value of $\overline{u'v'}$ at this location indicates that momentum is being transferred from the annular flow into the recirculation bubble. On the other hand, the axial velocity and the fluctuations in the jet shear layer are, in general, in the negative streamwise direction. A negative value of $\overline{u'v'}$ at this location indicates that the jet fluid is being transported upward radially across the jet shear layer. Thus, the amplitude of the Reynolds shear stress gives a good measure of the relative intensity of the large-scale mixing in these regions. One point of significance which should be mentioned here is the value of $\overline{u'v'}$ at r = 0. A value of zero was predicted by the simulations. This is contrary to many experimental results, which often show significantly large nonzero values of Reynolds stresses near the centerline. However, this is to be expected since the numerical results were obtained from axisymmetric simulations. By construction the radial velocity hence, the fluctuations, at the centerline is identically zero under the axisymmetric assumption. However, the motions of the eddies near the centerline are usually three-dimensional in real flows. Consequently, it is not possible to precisely predict and quantitatively reproduce all the details as seen in laboratory experiments using the axisymmetric model.

The experimental measurements of the (two-component) fluctuation kinetic energy $\overline{u'u'} + \overline{v'v'}$ and the Reynolds stress $\overline{u'v'}$ for the cases $U_j/U_a = 0.62$ and 1.04, respectively, reported by Namazian [103], are used to check the accuracy of the numerical solutions. The comparisons of the radial profiles at axial station $z = 0.3$ are presented in Figures 4.15. When studying these comparisons, one should keep in mind that the flow Reynolds number used in the experiments is much higher than the one used in this numerical study. In addition, the combustor used in the experimental studies was unducted. Thus, some discrepancies between the experimental and the numerical results should be expected. Nevertheless, Figures 4.15 shows good agreement between the computed profiles and the experimental results, except near the centerline and at $r \sim 0.5$. As mentioned earlier, the eddies moving near the centerline in most real flows are usually three-dimensional and contain irregular small-scale turbulence. Thus, the dynamics near the centerline cannot be captured by our axisymmetric model. As for $r = 0.5$, our model has a viscous confinement whereas the experimental studies were performed with an unducted combustor. This dissimilarity in combustor configuration accounts for the discrepancies between the predicted and the experimental results at $r \sim 0.5$.

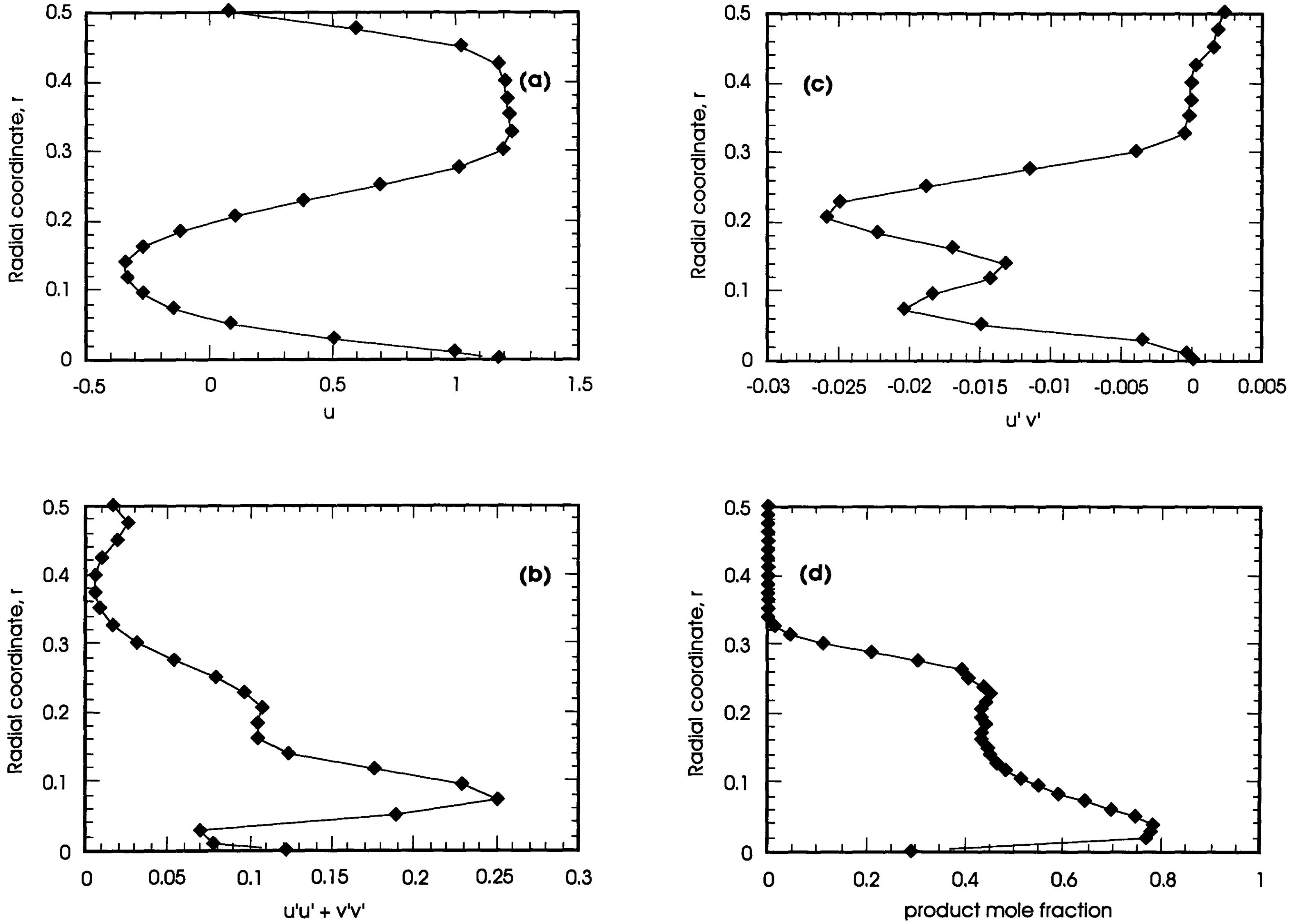

Figure 4.12 Time-averaged flow properties at $z = 0.7551$, $U_j/U_a = 0.62$.

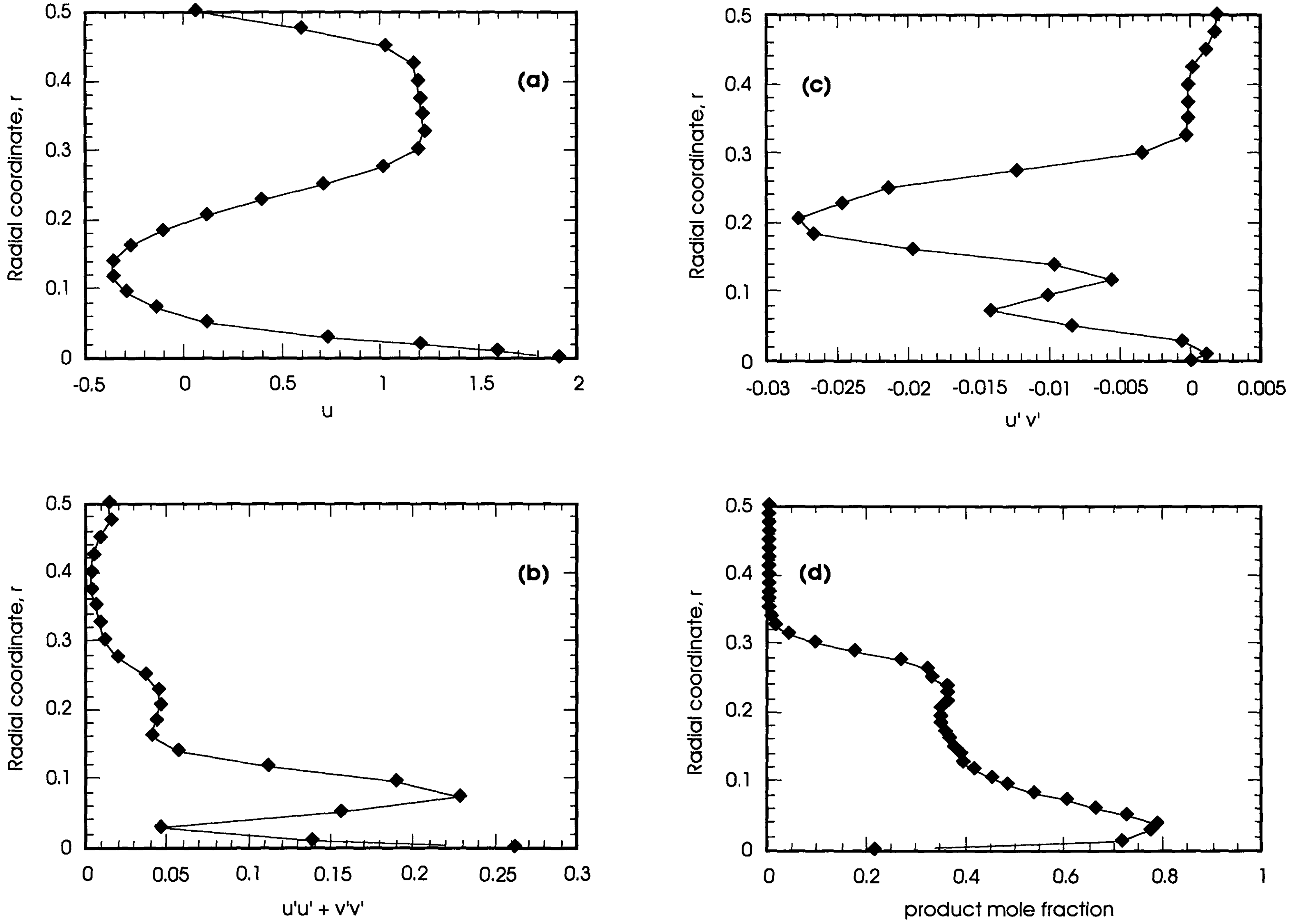

Figure 4.13 Time-averaged flow properties at $z = 0.7551$, $U_j/U_a = 1.04$.

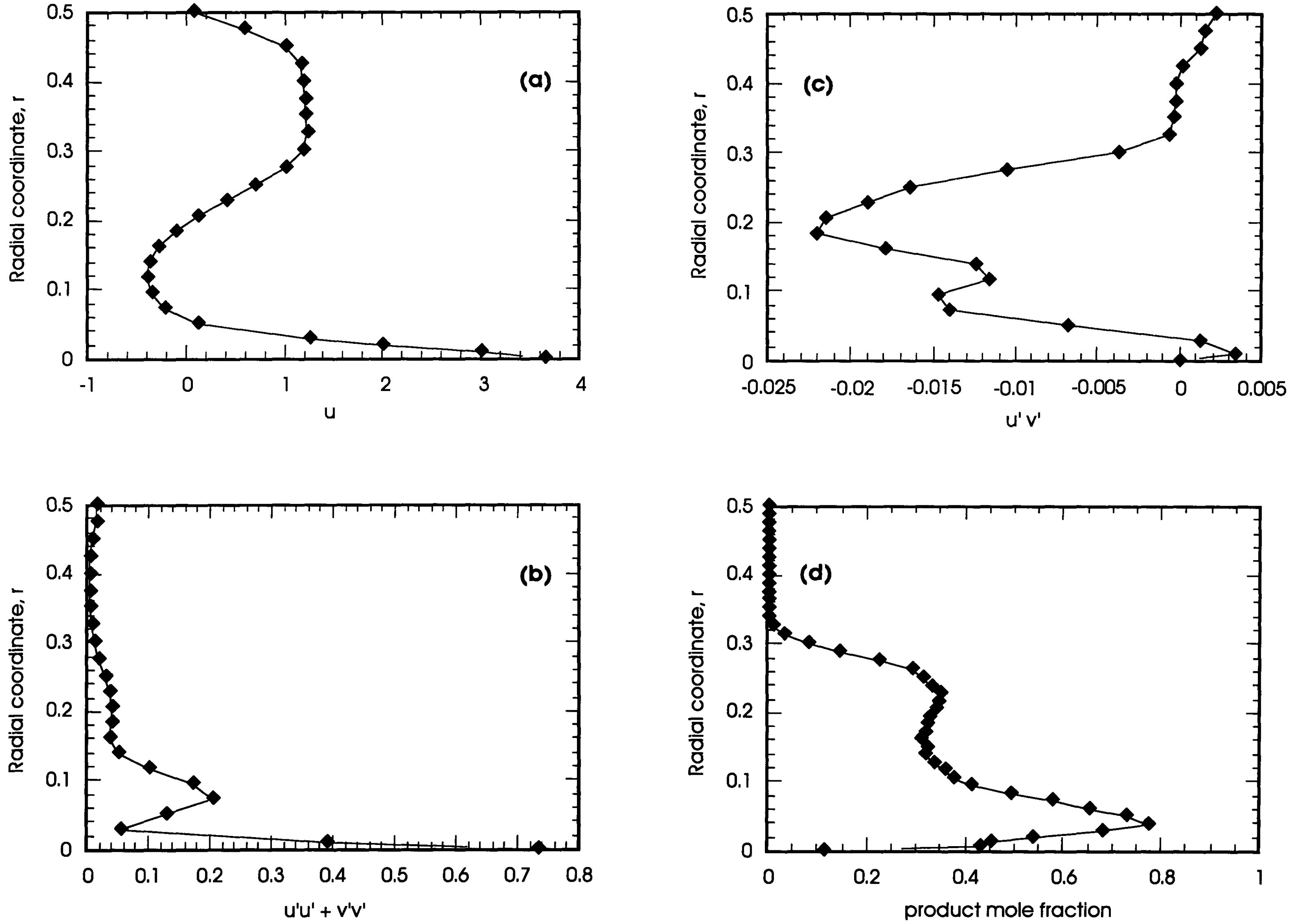

Figure 4.14 Time-averaged flow properties at z = 0.7551, $U_j/U_a = 2.08$.

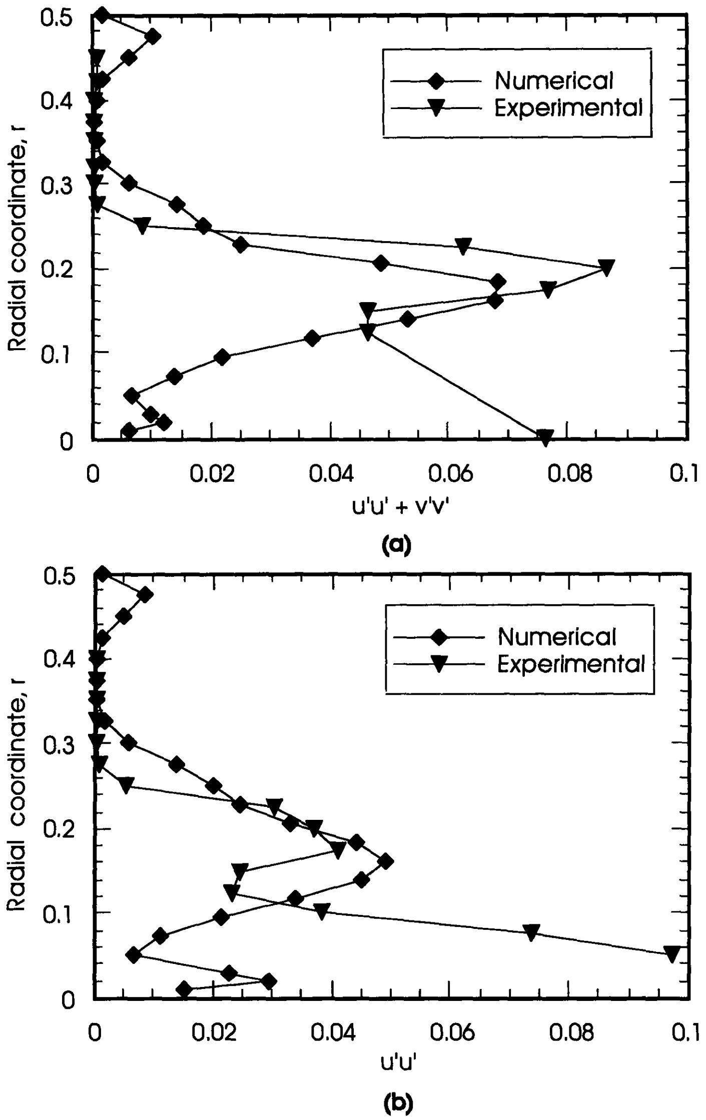

Figure 4.15 comparisons of radial distributions between the measurements of Namanzian [103] and the computed fluctuation kinetic energy and Reynolds stress for the two cases $U_j/U_a = 0.62$ and 1.04, respectively. **(a)** $U_j/U_a = 0.62$. **(b)** $U_j/U_a = 1.04$.

4.2.3 PROBABILITY DENSITY FUNCTIONS OF THE VELOCITY DISTRIBUTIONS

In most classical turbulent flow studies, the investigations are usually centered around the spectrum tensor because it is the statistical quantity which lends itself readily to the formation of hypotheses about the mechanism of decay of turbulence [8]. However, there are many other statistical quantities whose meanings are readily understood and are relevant to the basic mechanical process of the motion. Almost all of these quantities can be determined by the probability distributions of the velocity or its derivatives at one point, or the joint-probability distribution of the velocity at two points. Thus, the probability distributions of the velocity are important quantities in studying high-Reynolds-number flows. In this section, we will present and discuss the representative probability distributions of u' and v' in the near-wake region, and to assess the effects, if any, of the inflow velocity ratio on the characteristics of the flow structure in terms of the probability density functions (PDFs).

The *central-limit theorem* states that the probability distribution of a continuous variable, which is the sum of a large number of independent variables, is approximately normal or Gaussian [12]. Nearly all the random processes occur in nature have Gaussian probability distribution, including stationary homogeneous turbulence. The existence of an approximately Gaussian distribution of the velocity in homogeneous turbulence has been known for many years [8], and was one of the first experimental results concerning homogeneous turbulent motions to be established. However, it is important to realize that this result is only valid for homogeneous turbulence. For flows in which the dynamics are dominated by large-scale structures, similar to the flow which is being investigated in this research, the velocity probability distribution functions are generally skewed, and in some instances, bimodal. This fact has been observed in numerous experiments [103].

Figures 4.16-4.21 show the normalized probability density functions (PDFs) of u' and v' for all three cases at six spatial locations in the flow domain: (r, z) = (0.027, 0.6051), (0.25, 0.6051), (0.027, 0.9051), (0.25, 0.9051), (0.027, 1.2051), and (0.25, 1.2051). These PDFs were obtained from samples each containing 8400 data points, using 70 phase bins which are spaced equally over the three sigma limits of the data. The axial coordinates of these points were chosen such that they are located at a short distance downstream of the bluff-body face, approximately in the middle, and at the end of the recirculation region. The radial coordinates of these points were chosen to be located inside the shear layers of the recirculation bubble. This conditional spatial sampling approach allows us to conveniently map out the characteristic behaviors of the flow in the recirculation region.

The probability density for a single variable say u', at a single point, $P(u')$, is defined by saying that $P(u')du'$ is the fraction of the total duration of a long sample for which the variable lies between $u' - (1/2)du'$ and $u' + (1/2)du'$. In all the plots presented in Figures 4.16-4.21, the y-axis is dimensionless and the integral of Pdu' is unity. The distributions presented in these figures resembled of those measured in two-dimensional shear layers separating two flows of different velocities. Notice that the shapes of the PDFs vary greatly from one point to another for all three cases, indicating that the flow is highly inhomogeneous. Since the flow is not homogeneous, obviously it cannot be isotropic [15]. This fact can easily be seen by comparing the PDFs of u' with those of v' for the same velocity ratio. Overall, the PDFs of u' are far from a Gaussian distribution and most of them are highly skewed. For points near the stagnation region, the probability density functions can exhibit bimodal distributions, as shown in Figure 4.16b.

In order to put the above discussion on a more quantitative basis, the skewness, α_3, and the flatness factors, α_4, of the PDFs have been calculated and presented in Figure 4.22. The skewness, which is the third moment of the PDF, measures the symmetry of the distribution. It is given by

$$\alpha_3 = \frac{\frac{1}{n}\sum_{i=1}^{n}(x_i - \bar{x})^3}{\left(\frac{1}{n}\sum_{i=1}^{n}(x_i - \bar{x})^2\right)^{3/2}} \tag{4.3}$$

where x is either the axial or the radial velocity. When a distribution is asymmetric about the maximum and has one of its tails longer than the other, the measure of this asymmetry is described by the skewness. If the longer tail occurs to the right, the distribution is said to be skewed to the right, and if the longer tail occurs to the left, it is said to be skewed to the left. The measure of α_3 will be positive or negative depending on if the distribution is skewed to the right or to the left, respectively. Moreover, the PDF distribution may have its values concentrated near the mean so that the distribution has a large peak, or the distribution may be relatively flat. The flatness factor, also known as the kurtosis, is the forth moment of the PDF. It describes the degree of peakness of the distribution and is given by

$$\alpha_4 = \frac{\frac{1}{n}\sum_{i=1}^{n}(x_i - \bar{x})^4}{\left(\frac{1}{n}\sum_{i=1}^{n}(x_i - \bar{x})^2\right)^{2}} - 3. \tag{4.4}$$

A Gaussian distribution has zero skewness and a flatness factor of three. With this in mind, we can analyze the PDFs in terms of the skewness and the flatness factors in order to assess the degree of departure of the PDFs from a Gaussian distribution. From Figure 4.22, it is interesting to see that although the underlying unsteady dynamics of the three cases differ greatly, the variations of skewness and kurtosis of both u' and v' with axial location follow approximately the same trend. However, this alikeness should probably be expected since all three simulations have identical Reynolds number. From Figure 4.22, we see that the skewness of $P(u')$ for all three cases is almost zero near the bluff-body face, indicating a symmetric PDF distribution, and varies greatly with axial locations. For r = 0.027, the skewness of $P(u')$ becomes more positive (skewing toward positive velocity) with axial location, while the skewness of $P(u')$ becomes more negative (skewing toward negative velocity) for r = 0.25. The kurtosis, however, has the same trend for both radial locations, becoming more positive with z. Notice that the variations of both the skewness and the kurtosis are greatest in the shear layer between the recirculation region and the annular flow. This strong non-Gaussian behavior can be explained by considering the origin and the shedding of the large-scale vortical structures from the recirculation region. In all three simulations, vortices are being formed continuously at the edge of the bluff body. While at the early stage of their formation, the sizes of these eddies are quite small and hence, disturbance to the local mean velocity caused by these small eddies is less substantial and more Gaussian-like. These eddies entrain fluid and continue to grow in size while being convected down stream along the shear layer. Near the end of the recirculation region, the eddies have grown sufficiently in size. Some eddies might even have merged with the eddies originated from the central jet for cases with lower velocity ratio. Since the velocity of the fluid convected by the large-scale structures departs more radically from the mean velocity than the velocity variation due to small-scale eddies, these large-scale eddies affect the local velocity distribution much more significantly and abruptly, causing greater deviation of the PDFs from a Gaussian distribution.

One should also note that the magnitude of the skewness and kurtosis variation for all three cases are all very similar up to the second station. However, near the end of the recirculation region, the magnitude of the skewness and the kurtosis increased considerably for the case U_j/U_a = 2.08. Since the kurtosis of a Gaussian distribution has a value of three, greater values indicate that the distribution decreases faster than a Gaussian distribution. The sharp increase of kurtosis at the third station for the case U_j/U_a = 2.08 means that the PDF at this station is highly concentrated in a small range of velocity and has a very steep drop-off rate. Checking Figure 20f, we see that it is indeed the case. Notice that in this case the PDF is concentrated around zero and highly skewed toward left. This distribution of the PDF suggests that the local velocity field is relatively uniform in this region, and disturbances cause by the passage of the eddies are quite significant (up to one-and-a-half times the local mean speed) but very infrequent.

Another interesting feature of the skewness of u' one should note is that the instantaneous velocity of the flow in the shear layer between the jet and the recirculation region is, on the average, negative. However, the fluctuations at this location are positive. The same kind of opposite trend is observed in the shear layer between the recirculation region and the annular flow. (In the outer shear layer, the mean velocity is positive but the fluctuations are negatively skewed.)

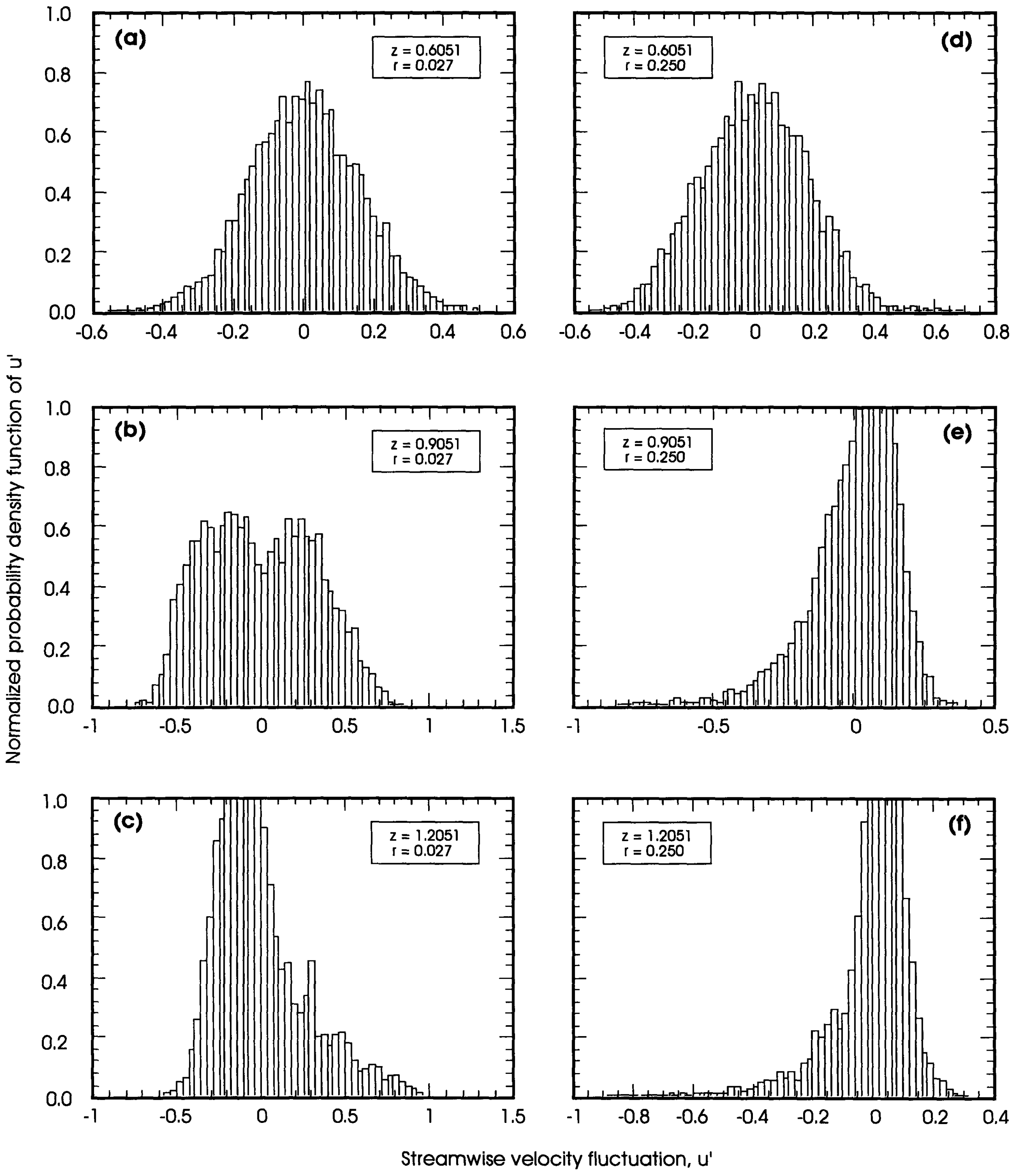

Figure 4.16 Normalized probability density function of u', U_j/U_a = 0.62 .

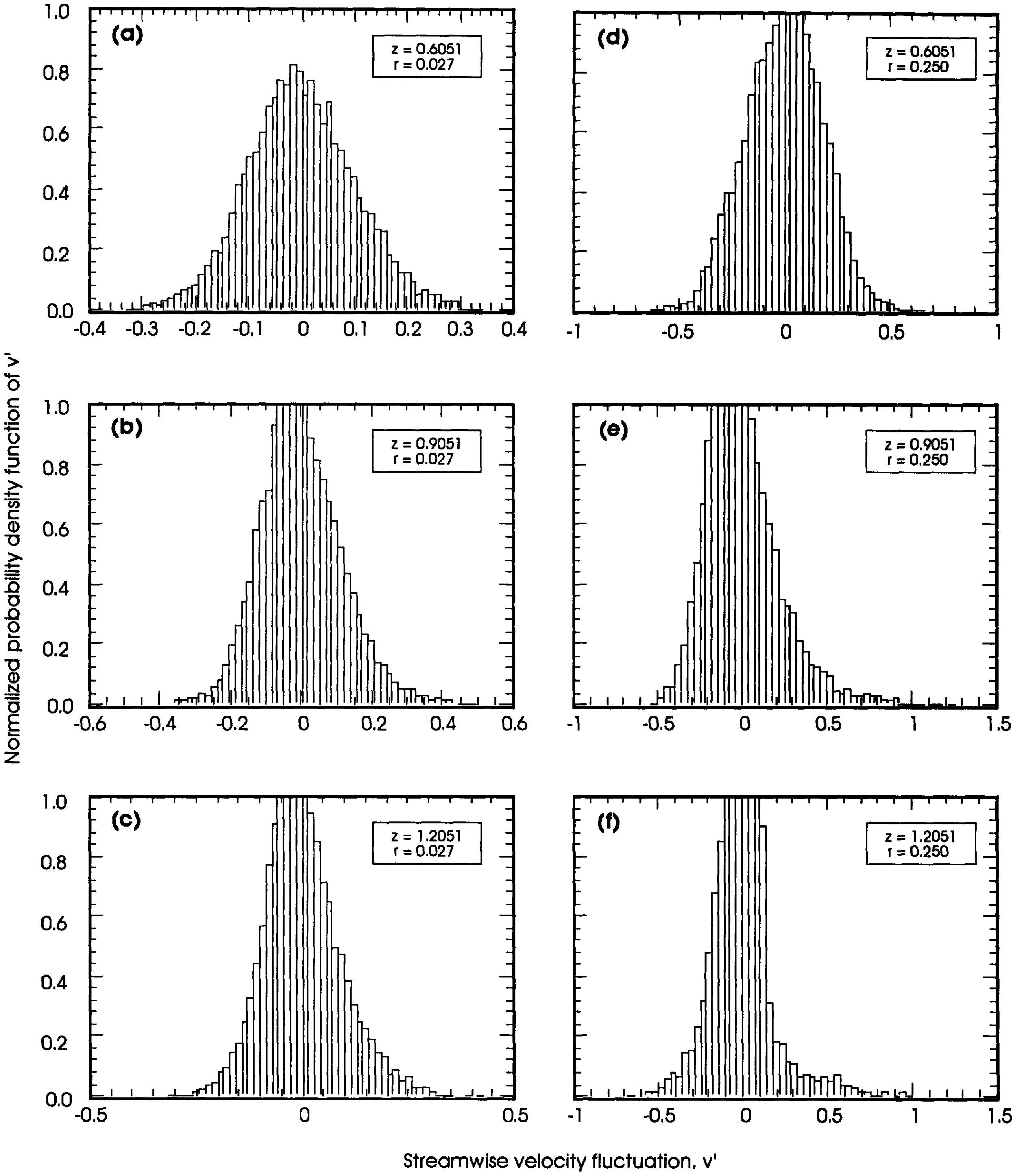

Figure 4.17 Normalized probability density function of v', $U_j/U_a = 0.62$.

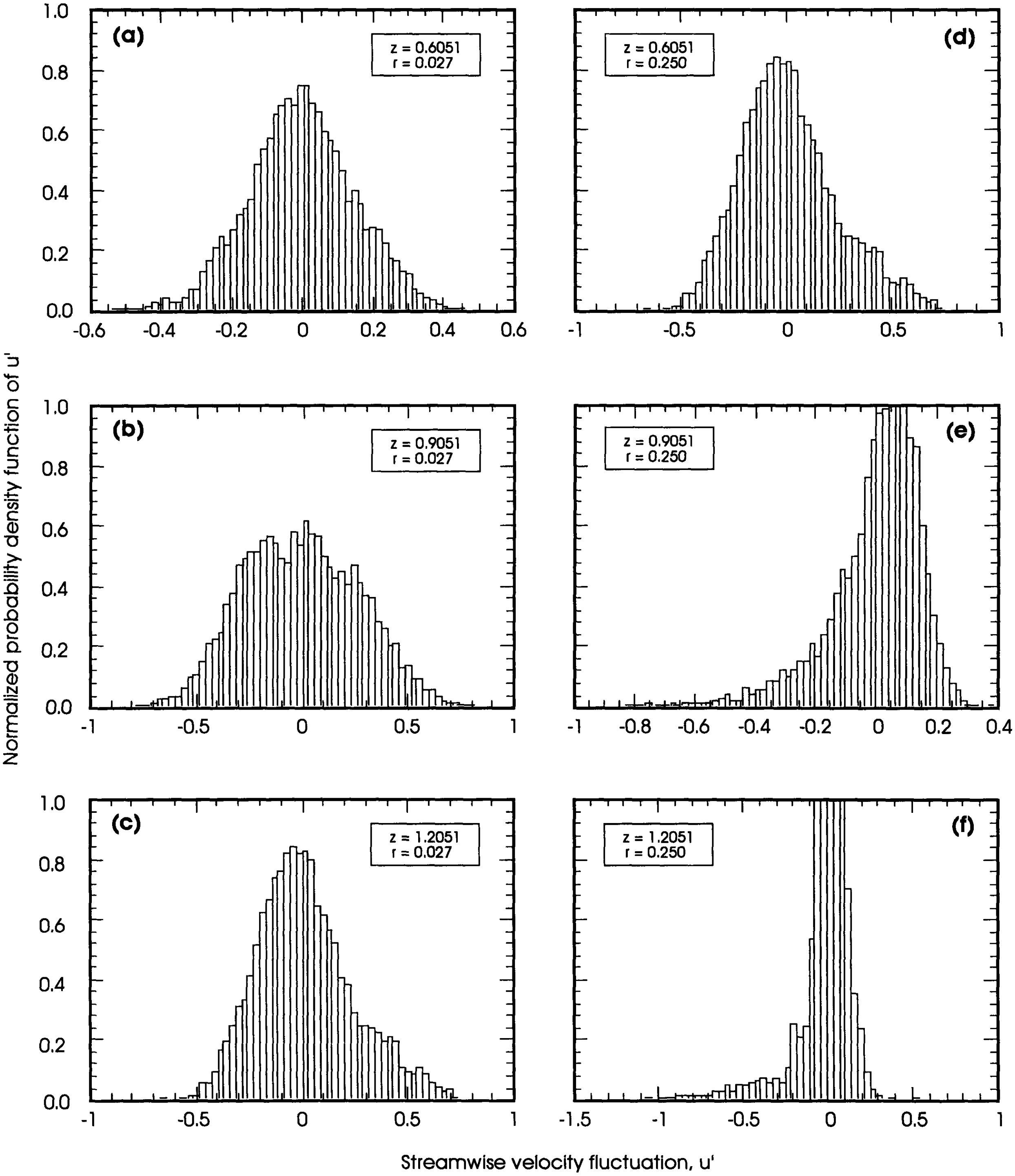

Figure 4.18 Normalized probability density function of u', U_j/U_a = 1.04.

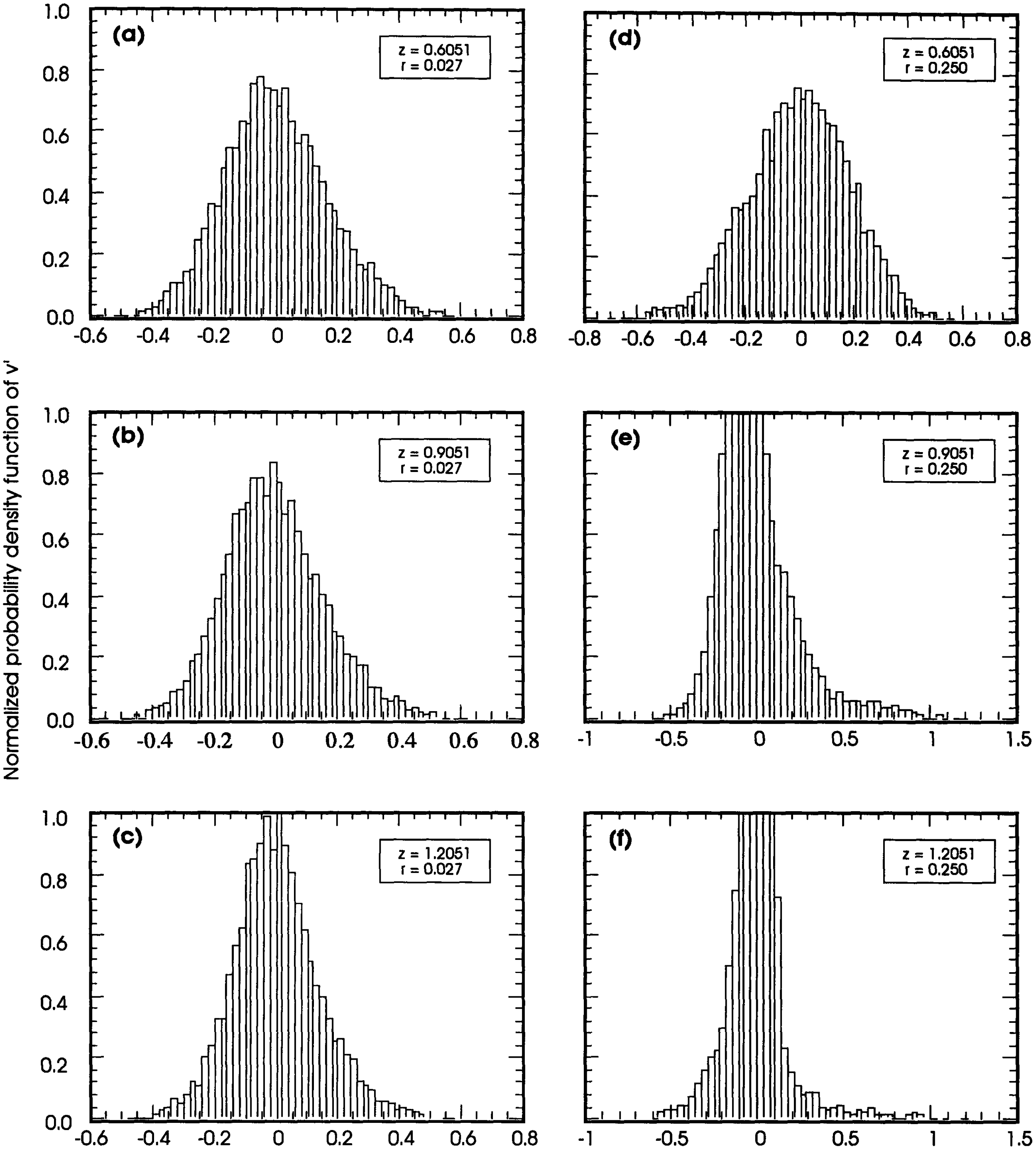

Figure 4.19 Normalized probability density function of v', U_j/U_a = 1.04.

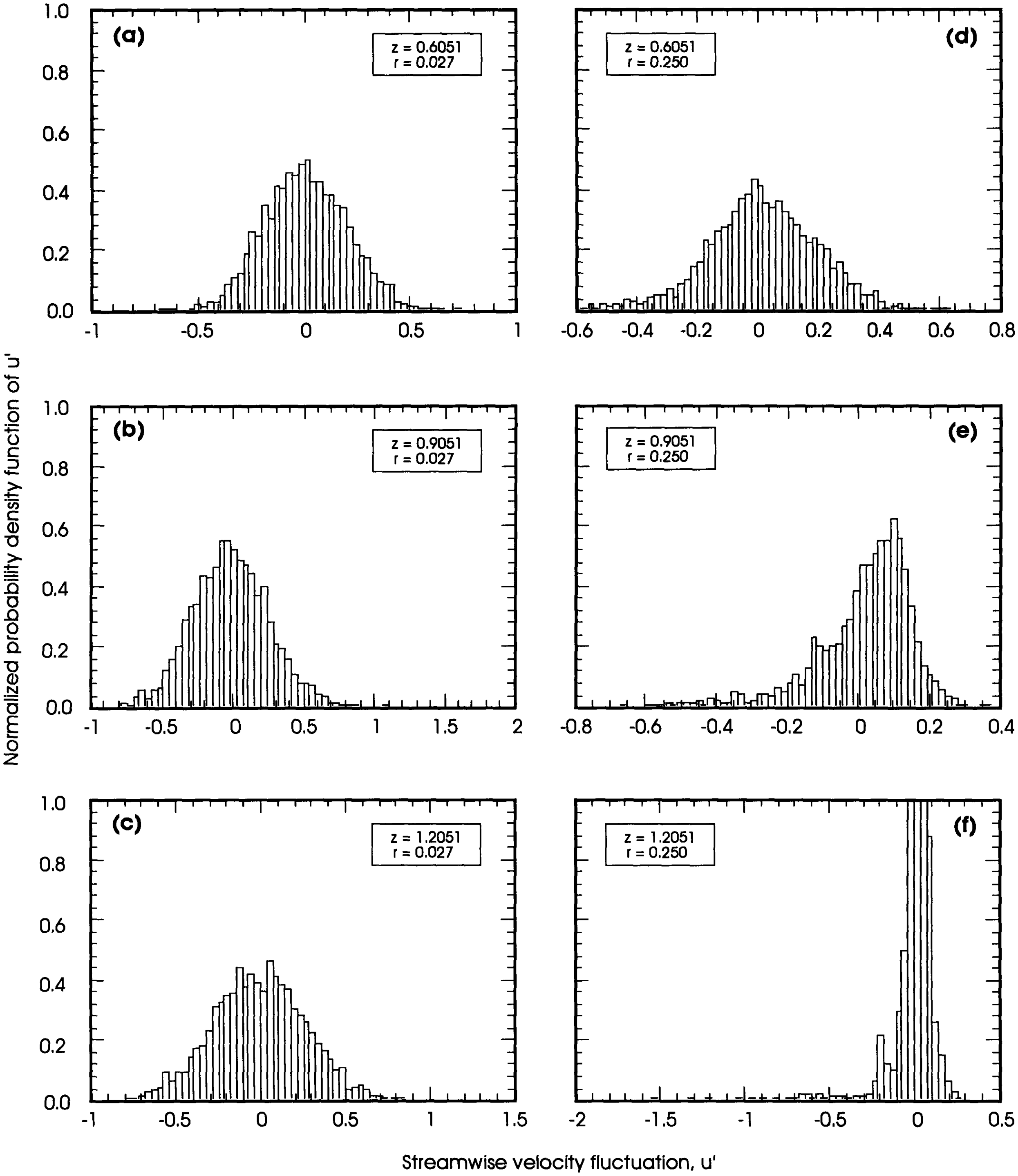

Figure 4.20 Normalized probability density function of u', U_j/U_a = 2.08.

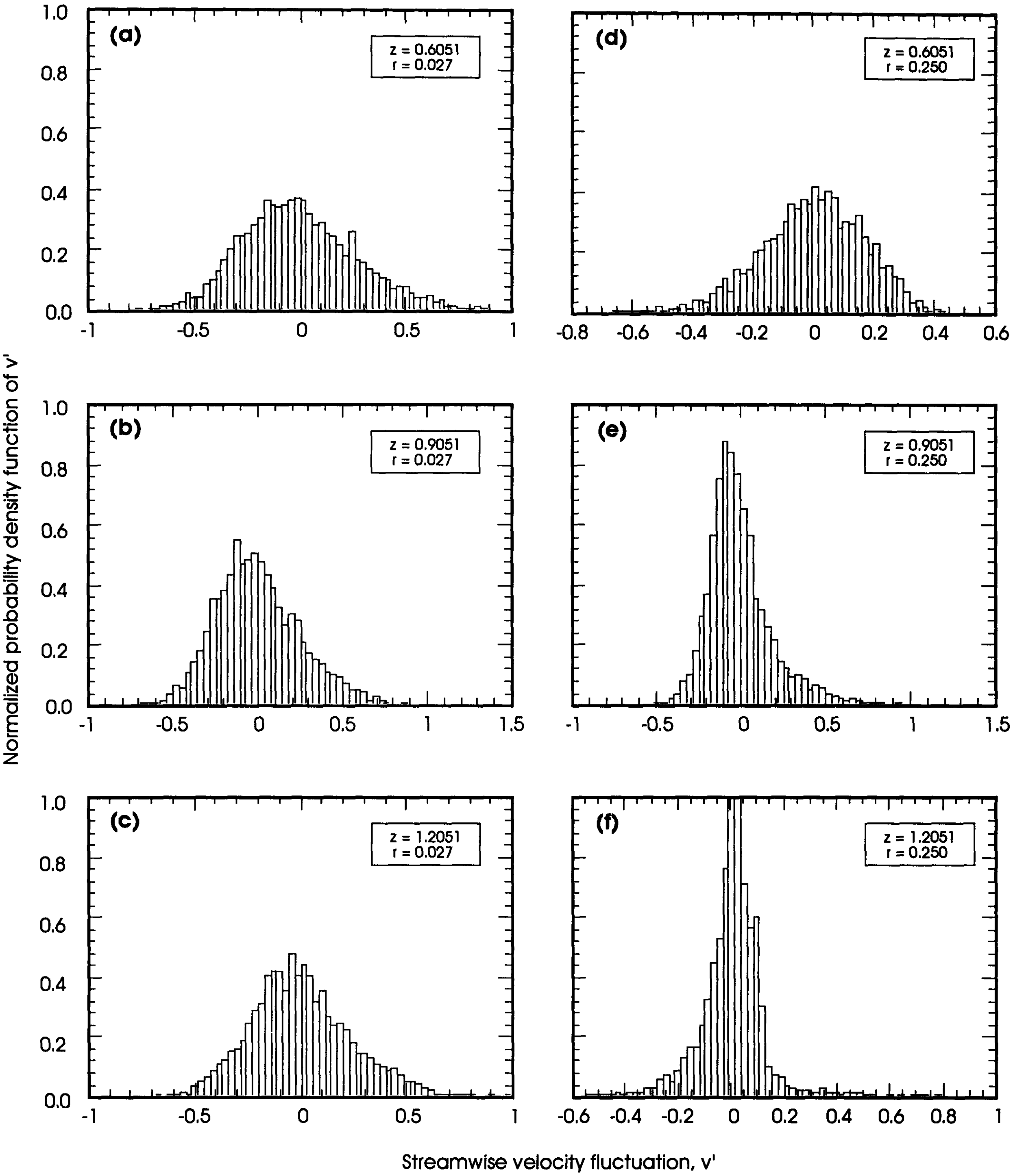

Figure 4.21 Normalized probability density function of v', U_j/U_a = 2.08.

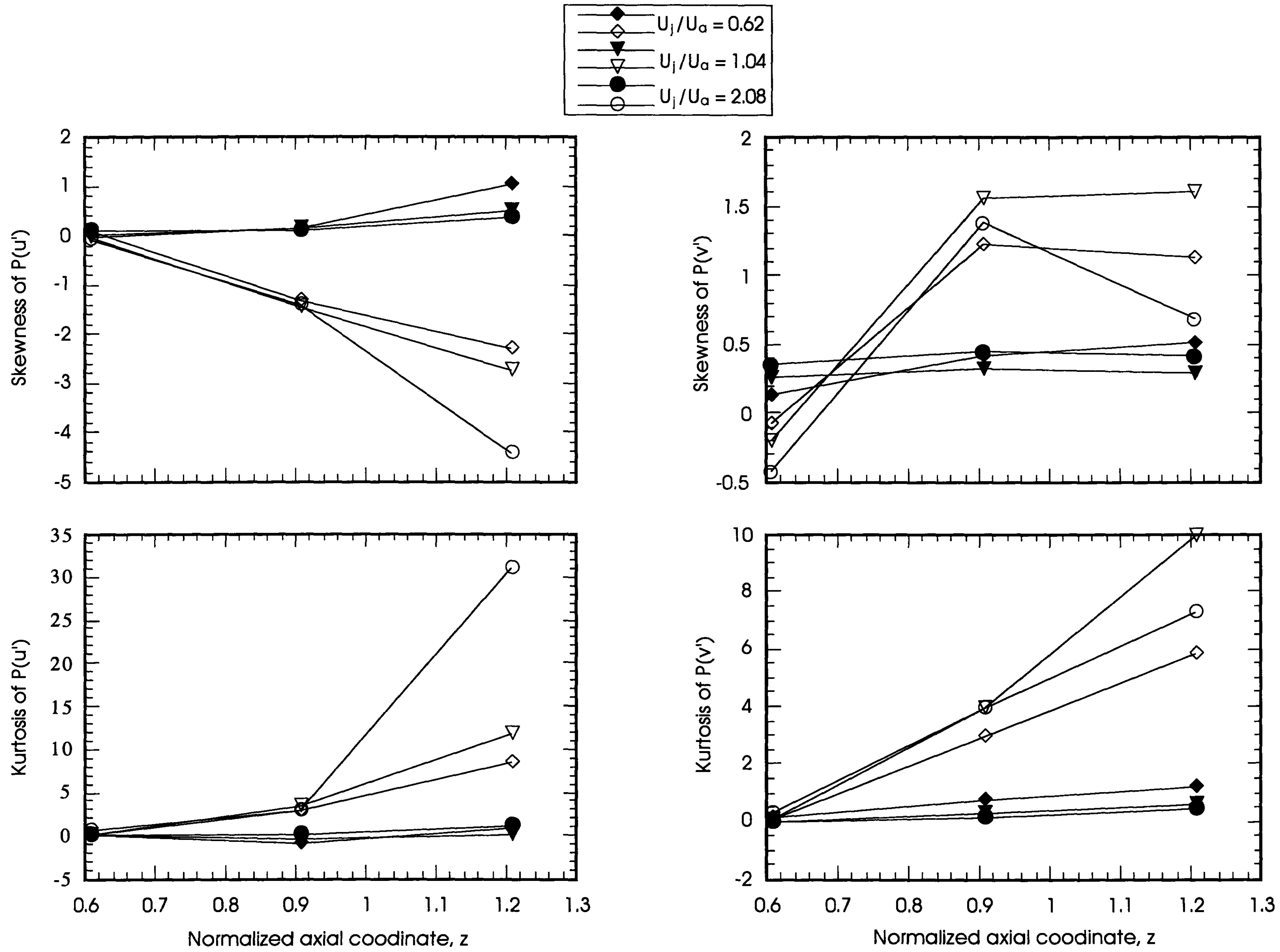

Figure 4.22 Skewness and kurtosis for P(u') and P(v') for all three cases. Filled symbols: r = 0.027, open symbols: r = 0.25.

4.2.4 VORTICITY DYNAMICS AND THE UNSTEADY PRODUCT CONCENTRATION FIELD

In a turbulent diffusion flame, chemical reaction occurs primarily on the surfaces where the ratio of the reactant fluxes is in stoichiometric proportion [80]. Therefore, combustion processes are highly time-dependent and are expected to be very sensitive to the instantaneous local species concentration and local fluctuations. The time-averaged flow properties presented earlier, while providing a global description of the steady flow dynamics and the mixing field, do not yield sufficient information required for detailed assessment of the large-scale entrainment and mixing and flow-combustion interaction. In this section, we will present the time-dependent solutions and to study the unsteady large-scale dynamics and their effects on the instantaneous mixing field and the rate of product formation.

We begin the analysis of the unsteady dynamics of the near-wake region and the mixing field by looking at the time evolution of the large-scale structures in terms of the vortex-element distribution in the interior of the flow domain and the corresponding product concentration field. Figure 4.23 shows the formation, merging, and the shedding of a composite vortical structure from the recirculation region for the case $U_j/U_a = 0.62$. In this figure, the instantaneous locations of the vortex elements are depicted by small squares, and the line segments initiating from the centers of the squares represent the velocity vectors of the elements. Notice that the most prominent unsteady flow feature in this series of time frames is the presence of the two-eddy system in the recirculation region: a clockwise-rotating eddy created by the separation of the annular air at the outer edge of the bluff body, and a counterclockwise-rotating eddy created by the separation of the jet fluid from the bluff body's inner edge. This time series clearly showed that in this case the dominant physical process modulating the mixing and the reaction in the near-wake region is the formation, merging, and the shedding of the large-scale composite eddies from the recirculation zone.

Figure 4.23 shows a typical shedding cycle of the recirculation region. The roll up of the inner jet boundary layer forms a counterclockwise-rotating eddy situating above the exit of the jet nozzle which entrains most of the jet fluid entering the flow domain. The rest of the jet fluid not entrained by this fuel eddy penetrates into the recirculation region a short distance before being stagnated and turned to flow backward upstream along the shear layer between the jet and the recirculating air eddy. Mixing of the jet fluid with the annular air and reaction in this case is largely confined to this thin shear layer, and along the interface between the recirculating air eddy and the counterclockwise-rotating fuel eddy. This can be seen clearly by comparing the first frame of Figure 4.23 with the corresponding instantaneous product concentration field given in Figure 4.24. In this case, the flame will be confined primarily to the shear layer between the jet and the recirculating air eddy for exothermic reaction.

As more fuel is being engulfed by the counterclockwise-rotating eddy, it begins to grow in size and to compete with the air eddy for the available space within the recirculation region. This process causes the air eddy to drift away from the face of the bluff body. Meanwhile, a new air eddy begins to form at the outer edge of the bluff body (second frame of Figure 4.23). The formation of the new air eddy destabilizes the fuel eddy, and causes it to move away from the face of the bluff body also. Merging between the fuel and the air eddy is clearly evident in the third frame of Figure 4.23. While the eddies are being merged, mixing and reaction between the jet fluid and the annular air continue to take place. (second and third frame of Figure 4.24). Beyond t = 28.53, the composite eddy breaks away from the recirculation region. However, mixing and reaction are seen to continue on the surface of the composite eddy as it is being convected downstream (the last two frames of Figure 4.24). Meanwhile, the recirculation region is occupied by the newly generated air eddy and the shedding cycle is ready to repeat again. This unsteady ejection of discrete reactive flow structures from the recirculation region resembles the intermittent and discrete combustion process of exothermic reactive flows as observed in many experimental studies [103, 120]. Notice that in this case the unsteady mixing zone is never much longer than the recirculation region.

Since all the numerical simulations are performed with steady inflow boundary conditions, the unsteady shedding of large-scale structures from the recirculation region observed here is the intrinsic dynamics of this confined bluff-body flow, and the corresponding shedding frequency is the property of the flow system. Vortex shedding inside combustors has been known to interact with the acoustic waves in exothermic reactive flows and to generate intense pressure fluctuations which can cause structural damage to the combustion system [27, 113]. These instabilities are usually triggered when the shedding frequency of burning vortices is in resonance with one or more of the natural instability modes of the combustion system, causing large-scale temporal and spatial variations in heat release rate within the combustor. Thus, the natural shedding frequency of a system is usually of great interest to combustion system designers. To further characterize the unsteady shedding of these coherent structures from the recirculation region, we have calculated the frequency spectra at the exact same locations where the PDFs were obtained by taking the Fourier transform of the fluctuation kinetic energy $u'u' + v'v'$ at these locations. Note that the power spectra at a given point in the flow domain provide a quantitative measure of the relative size and the energy content of the large-scale eddies passing by the vicinity of that point. From the power spectra presented in Figure 4.25, we see that the dominant Strouhal number is centered approximately around 0.15, which is close to the well-known bluff-body shedding frequency at this Reynolds number [125]. As mentioned earlier, the unsteady dynamics of bluff-body flows are generally characterized by the recirculation bubble instability for low inflow velocity ratios. Experimental studies have found the shedding frequencies of many bluff bodies are in the range of $O(0.1)$. Works by Kiya and Sasaki [73], Parker and Welsh [109], and Cherry *et al.* [18] all have found the Strouhal number based on the bluff-body diameter and the freestream velocity in the range from 0.1 to 0.2. Thus, the information provided by the power spectra confirmed the early speculation that the dynamics and the large-scale mixing field in the near-wake region are governed by the natural unsteady shedding dynamics of the bluff body. As we move further downstream, a lower value of Strouhal number, centered around 0.06, also becomes noticeable. This Strouhal number is most likely associated with the dynamics of the merged structures being convected away from the recirculation region [93]. The shedding of these large-scale structures from the recirculation region can also clearly be seen from the time traces of the axial velocity fluctuations presented in Figure 4.26. These time traces show remarkably well that the quasi-periodic disturbances on the local velocity field due to the passage of the large eddies. Noticeably, the magnitude of the disturbances can reach as high as 90 percent of the mean local velocity (the last plot on the left-hand column of Figure 4.26).

Figures 4.27 and 4.28 show the time-dependent velocity field in terms of the vortex elements in the flow domain and the corresponding product concentration field for the case $U_j/U_a = 1.04$. The most prominent feature of the flow dynamics at this velocity ratio is also the quasi-periodic shedding of well-organized reactive flow structures from the recirculation region. A typical shedding cycle is depicted in the time series given in Figure 4.27. Notice that the destabilization of the air eddy due to the growth of the fuel eddy, the merging of the two eddies and, finally, the shedding of the composite structure from the recirculation region are almost identical to the case $U_j/U_a = 0.62$. However, since the momentum of the jet flow is comparable to the annular flow in this case, a large percent of the fuel penetrates and escapes the recirculation region remains unreacted. Thus, mixing and reaction are not confined within the recirculation region at this velocity ratio. In additional to the shedding of large-scale structures from the recirculation region similar to that of the previous case, mixing and reaction also occur along the centerline extending several bluff-body diameters downstream of the recirculation region in this case (Figure 4.28). Notice that reaction along the centerline occurs only discretely. From Figure 4.28, it is seen that regions of high product concentration are separated by distinct regions of low product concentration along the centerline of the combustor. This is because of the jet fluid escaping the near-wake region in short bursts at this velocity ratio due to the unsteady nature of the recirculation region, and results in the supplying of fresh fuel to the oxidizer elements in a pulsating fashion. This phenomenon has also been observed by Namazian in his experimental studies [103].

The power spectra for this case are presented in Figure 4.29. Again, the spectra were calculated at the exact same locations where the PDFs were obtained. Notice that the distribution of the spectra is very similar to the previous case, revealing the similarity of the large-scale flow structures and the shedding behaviors of these two cases despite differences in velocity ratio and the flow dynamics near the axis of the combustor.

The large-scale entrainment and mixing can further be investigated by injecting passive particles in the central jet stream at every time step. By following their trajectories as these particles are being dispersed in the flow domain, the simulation mimics the dispersion of a passive dye injected with the jet stream into the annular flow. Thus, the resulting dispersion pattern can be used to study the effects of the large-scale structures on the entrainment and the mixing in the near-wake region. Two series of time frames showing the unsteady dispersion of the passive particles into the annular flow are presented in Figure 4.30 for the two cases $U_j/U_a = 0.62$ and 1.04. Again, the instantaneous locations of the particles are depicted by small squares, and the line segments initiating from the centers of the squares represent the velocity vectors of the particles.

For the case $U_j/U_a = 0.62$, we see two time-dependent stagnation points exist along the centerline of the combustor. At these locations, the axial velocity of the particles becomes zero as they are being entrained into the reverse flow stream of the clockwise-rotating recirculation region established by the bluff body. These particles are being transported upstream along the jet shear layer . As the particles move closer to the face of the bluff body, they bifurcate between two directions. Most of the particles are seen to get engulfed by the counterclockwise-rotating eddy. A small fraction of the particles, however, escapes by moving radially upward along the face of the bluff body and then along the outer fringe of the recirculating air eddy. As the size of the counterclockwise-rotating eddy increases, it destabilizes the recirculation region. Mixing of the passive particles with the annular air can clearly be seen in the fifth and the sixth frame in the left-hand column of Figure 4.30. This unsteady interaction between the counterclockwise-rotating eddy and the recirculation region eventually leads to the complete breakdown of the recirculation region, and the escape of the particles which are trapped in the clockwise-rotating eddy from the recirculation zone.

Similar entrainment and mixing pattern in the jet shear layer within the recirculation region is also observed for the case $U_j/U_a = 1.04$. However, since the momentum of the jet fluid is comparable to the momentum of the recirculating annular flow in this case, a large percent of the passive particles penetrates and escapes the recirculation region. In this case, in addition to the unsteady large-scale dynamics within the recirculation region, mixing and entrainment of the particles into the annular flow also take place along the centerline of the combustor downstream of the recirculation zone.

Figure 4.32 shows comparisons between the predicted jet-fluid concentration and the experimental data provided by Namazian [103] as a function of the axial coordinate. The numerical data were obtained by overlaying a mesh of identical square cells onto the domain of interest and calculating the concentration of the jet fluid in each cell as a function of time[1] (Figure 4.31). Since the dimensions of all the cells in the mixing domain as well as the source cells at the exit of the jet nozzle are identical, the concentration of the jet fluid in each cell at any given instant of time can easily be found by dividing the instantaneous number of particles in the cell by the total number of particles in a source cell (10 in this case). From the figure, it is seen that the numerical predictions show reasonable agreement with the experimental data. Maximum disagreement in both cases occurs at approximately one-and-a-half times the bluff body diameter, near the end of the recirculation region and in the vicinity of the stagnation region. This disagreement can be attributed to the modelling errors introduced by interpolation in regions of high velocity gradient.

---

[1] Reducing the cost of the computation is the primary reason behind limiting the overall size of the mesh. From the simulations, it was found that all the particles, once they have moved past axial station $z = 4.0$, did not recirculate back upstream. Therefore, it was decided to delete these passive particles once they have moved past axial station $z = 4.0$ in order to reduce the computational cost.

Finally, the velocity field in terms of the vortex elements and the corresponding unsteady product mole fraction field for the case U_j/U_a = 2.08 are presented in Figures 4.33 and 4.34, respectively. At this velocity ratio, the jet momentum is so much stronger than the recirculating flow, the recirculation region has essentially no effect on the dynamics of the jet flow. In essence, all the fuel elements escape the recirculation region remain unmixed and unreacted. In this case, the product distribution is seen to concentrate mainly along the axis of the combustor, with small excursions away from the centerline. These excursions correspond to the products entrained by the large-scale eddies which form occasionally on both sides of the bluff body. Notice that the maximum level of the product concentration in the recirculation region in this case is much lower than the previous two cases. Mixing, hence reaction, seems to take place starting near the end of the recirculation region only. At this velocity ratio, the recirculation region becomes relatively stable and the flow experiences much less entrainment and fluctuation in the near-wake region. Most of the fuel elements are seen to confine to a narrow region very close to the centerline where mixing and reaction are most intense.

The power spectral density plots for this case are shown in Figure 4.35 (the sampling locations are exactly the same as the other two cases already presented). Notice that since the recirculation region is much more stable, large-scale shedding from the recirculation region is less frequent. Thus, the bluff-body shedding frequency is less pronounced in most locations except near the point (r, z) = (0.25, 0.6051) (Figure 4.27d). In all other locations at r = 0.25, we see that the spectra have many narrow high-frequency peaks, indicating that a wide range of different sizes small eddies are being shed from the upper shear layer instead. Another interesting point worth noting here is that the spectral peaks in the jet shear layer are all concentrated in the lower frequency range. The natural frequencies observed in these plots form the basis for the selection of forcing frequencies when we study the same flow with different monochromatic forcing jet inflow boundary conditions in Section 4.3.

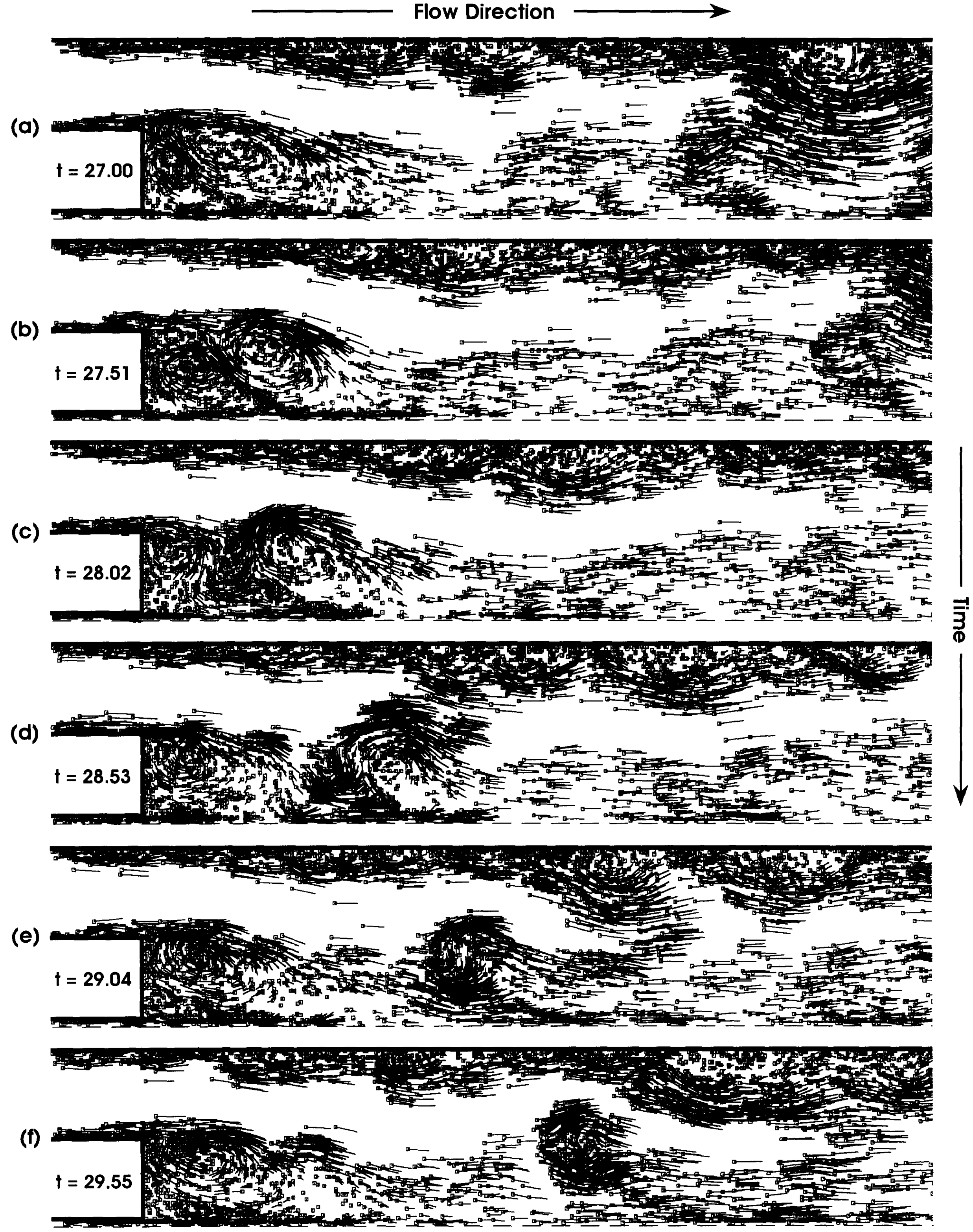

Figure 4.23 A series of time frames showing the evolution of the large-scale vortical structures in the near-wake region in terms of the distribution of the vortex elements in the interior of the flow domain. $U_j/U_a = 0.62$.

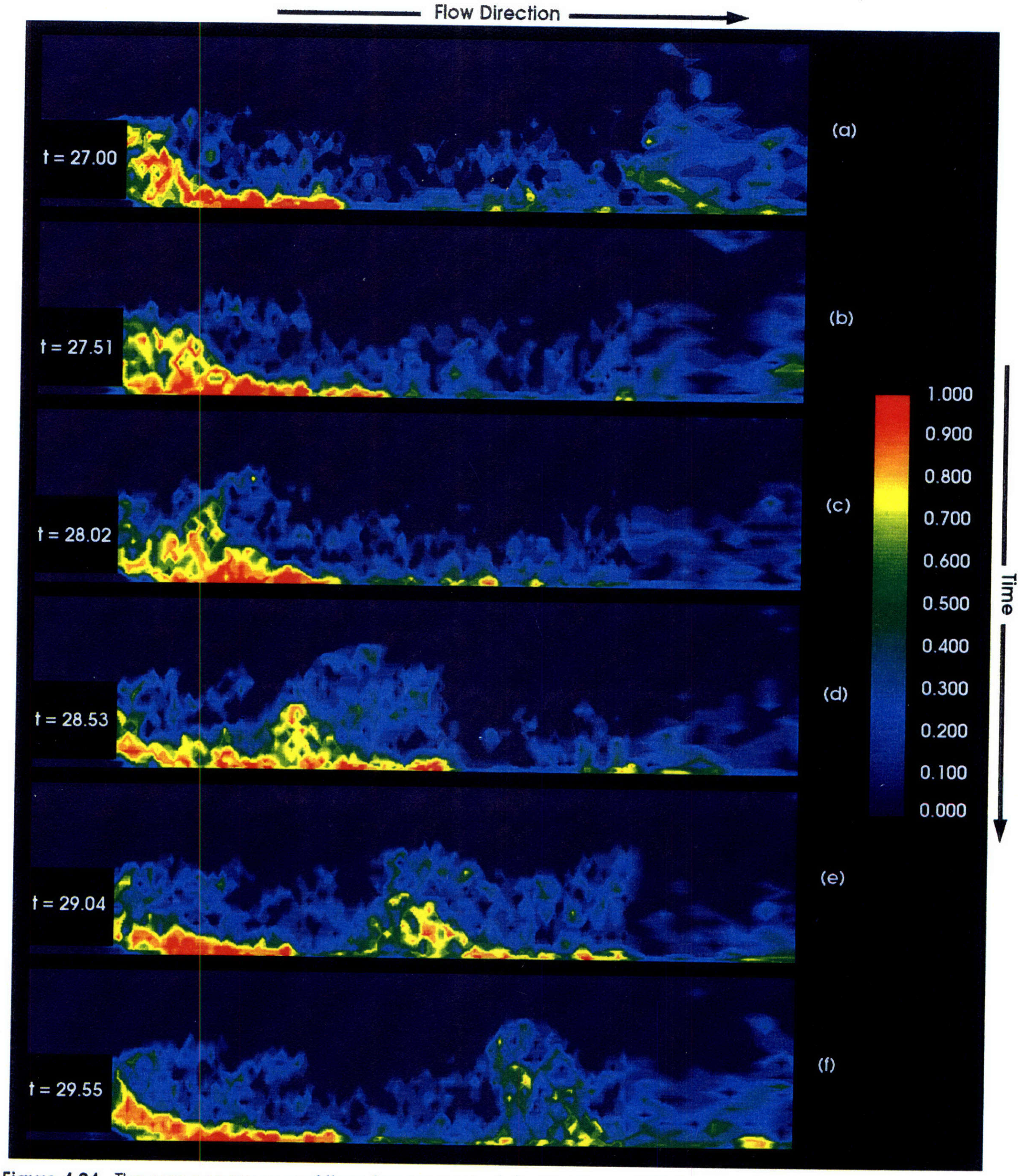

Figure 4.24 The same sequence of time frames as depicted in Figure 4.23 showing the instantaneous product concentration field. $U_j/U_a = 0.62$.

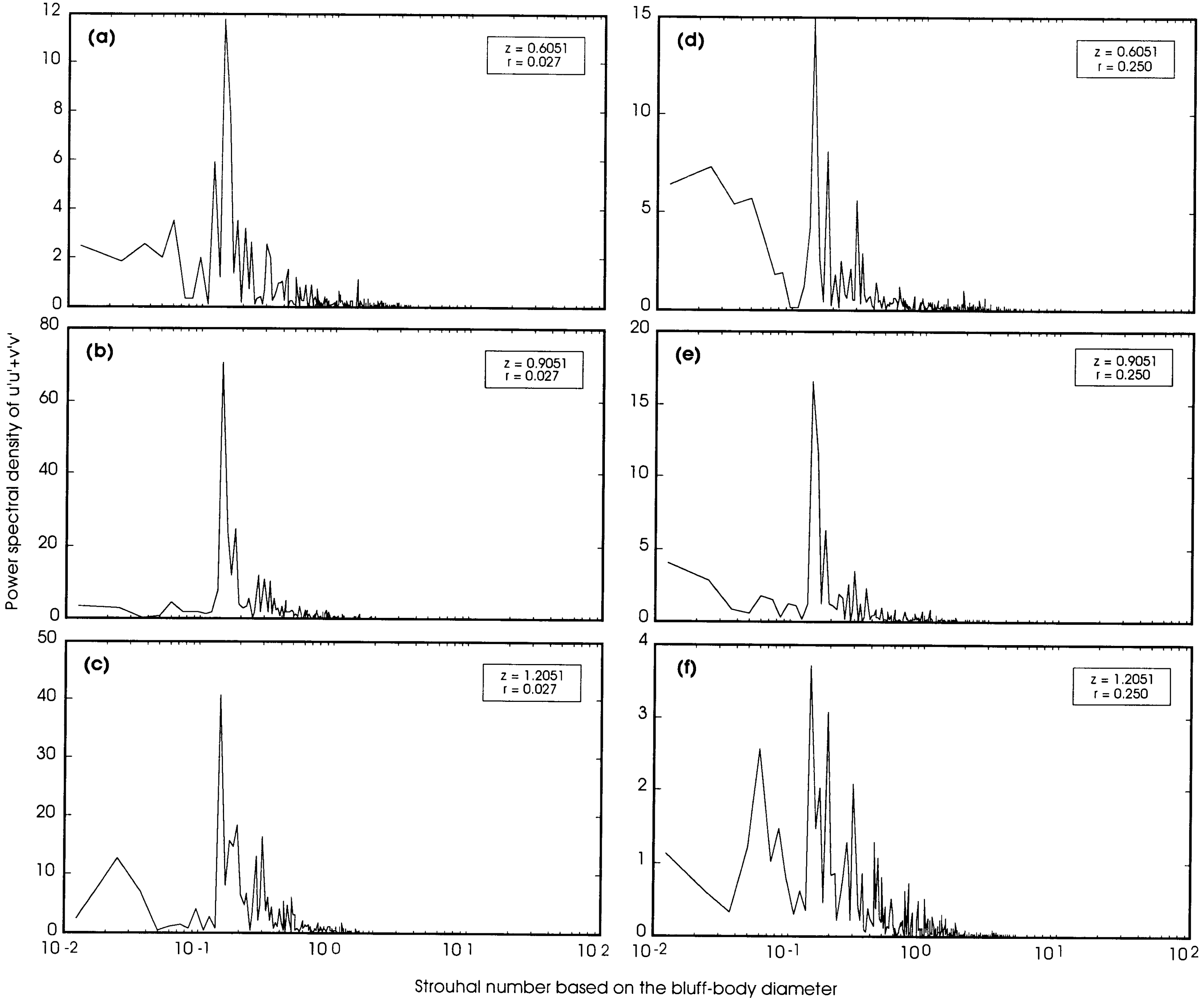

Figure 4.25 Power spectral density of u'u'+v'v'. $U_j / U_a = 0.62$.

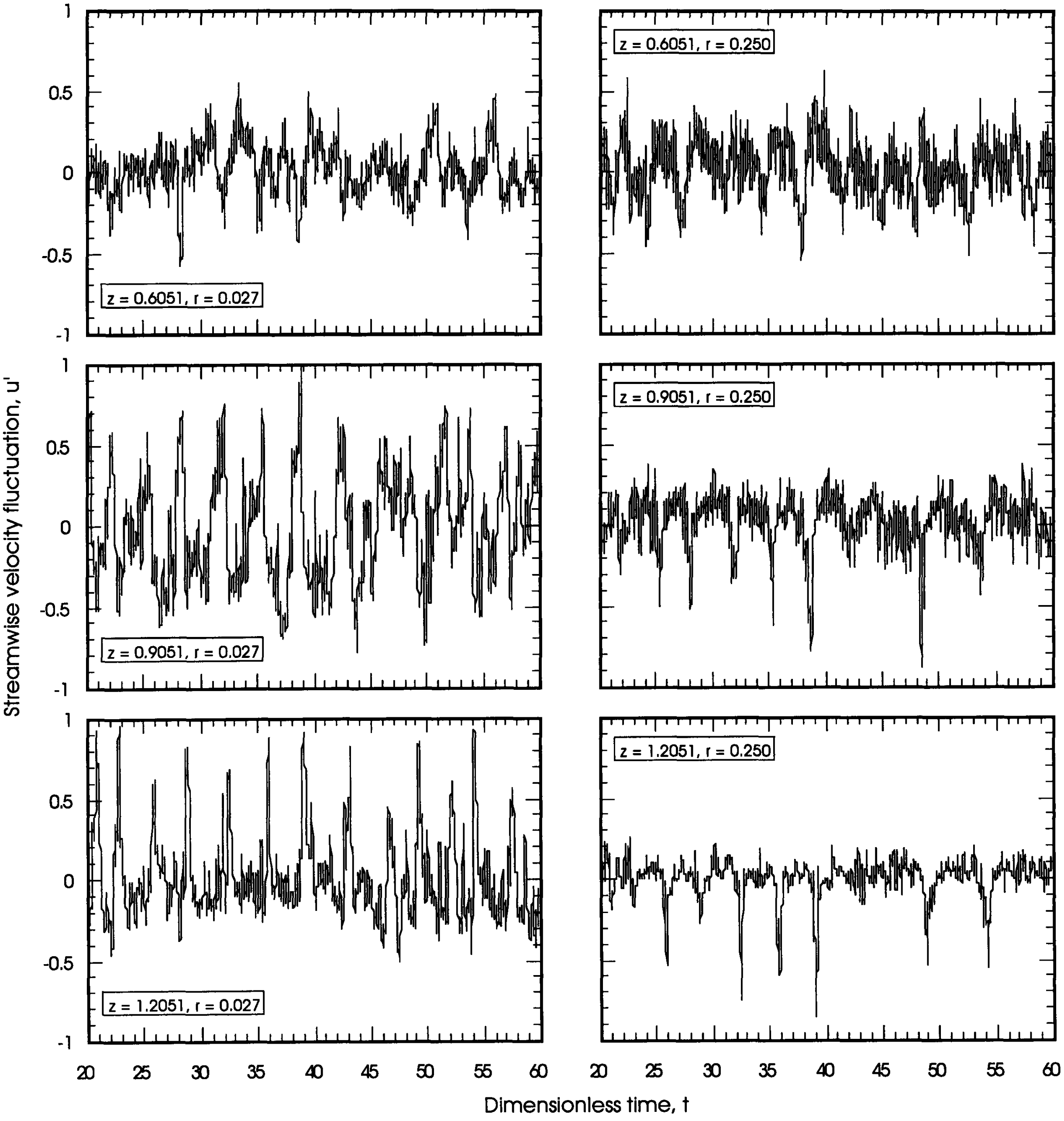

Figure 4.26 The instantaneous axial velocity fluctuation. $U_j/U_a = 0.62$.

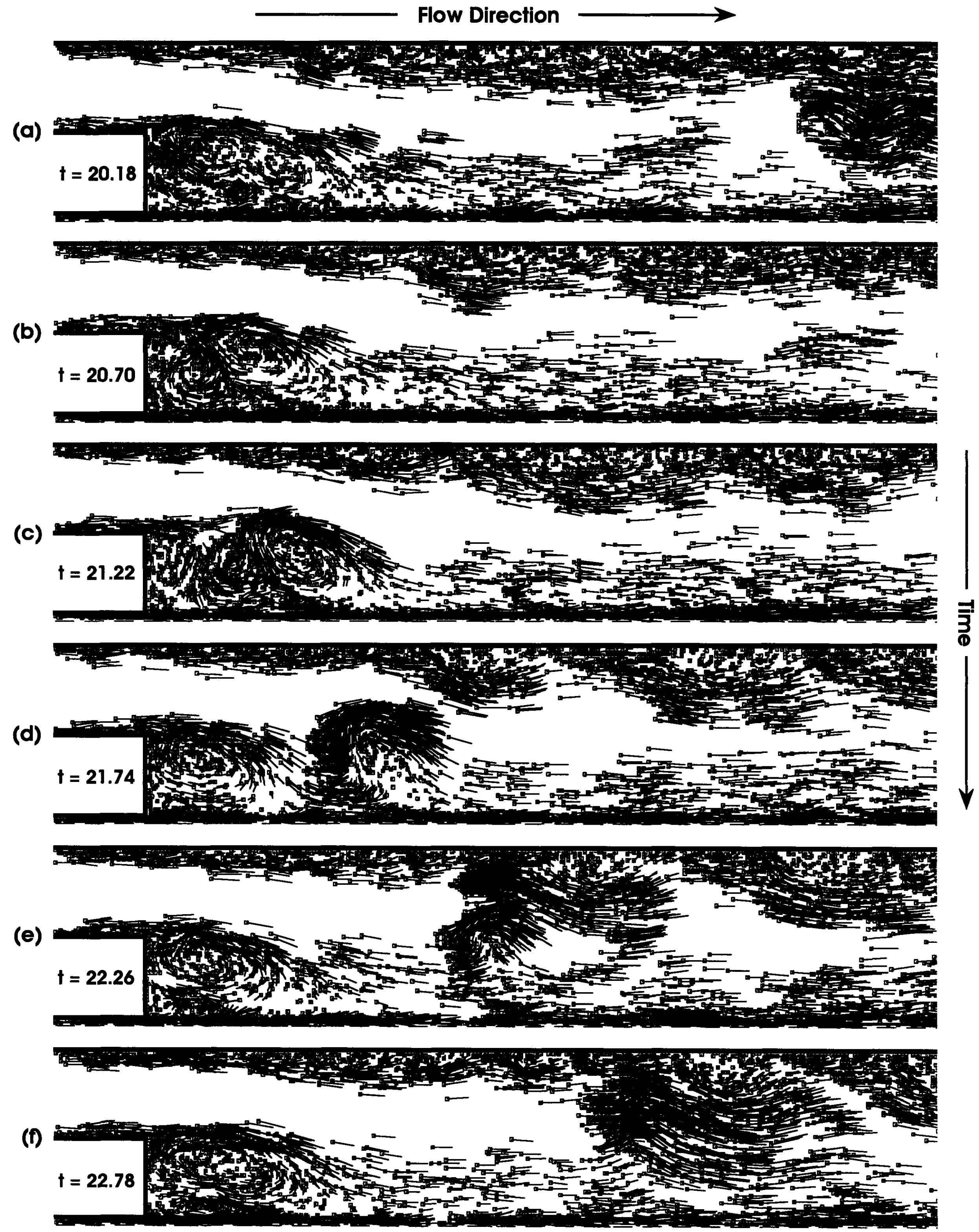

Figure 4.27 A series of time frames showing the evolution of the large-scale vortical structures in the near-wake region in terms of the distribution of the vortex elements in the interior of the flow domain. $U_j/U_a = 1.04$.

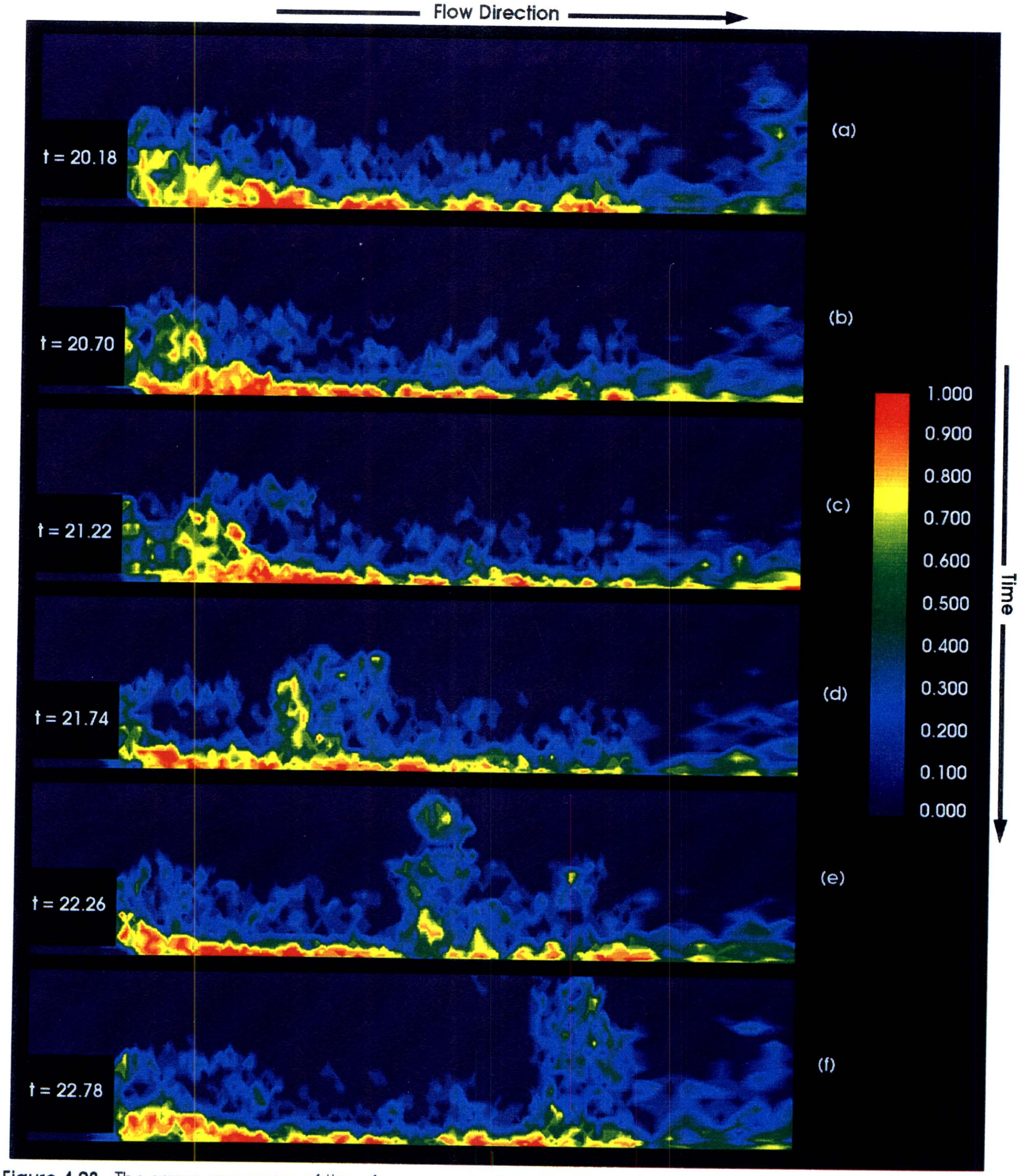

Figure 4.28 The same sequence of time frames as depicted in Figure 4.27 showing the instantaneous product concentration field. $U_j/U_a = 1.04$.

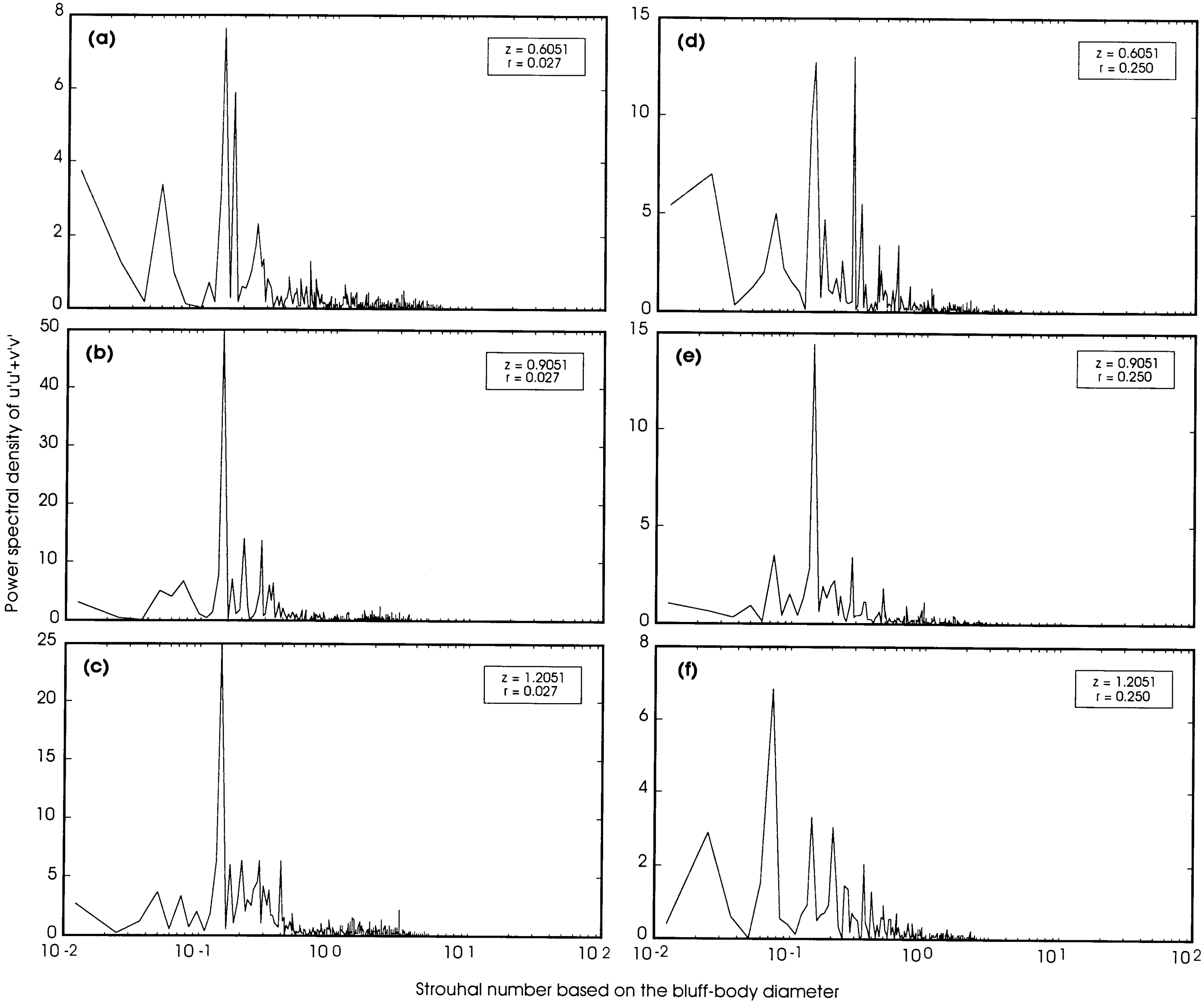

Figure 4.29 Power spectral density of u'u'+v'v'. $U_j / U_a = 1.04$.

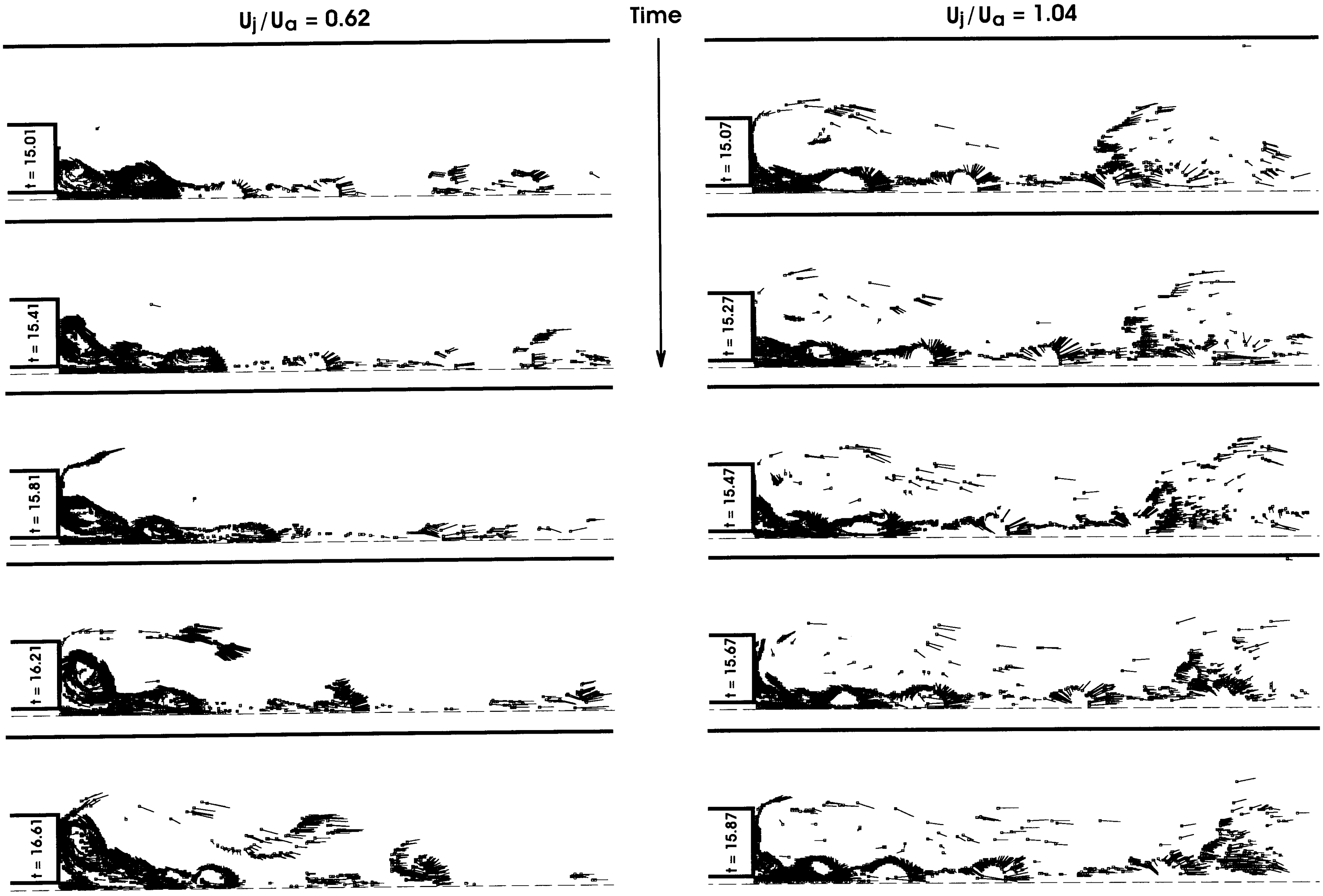

Figure 4.30 Continued on next page.

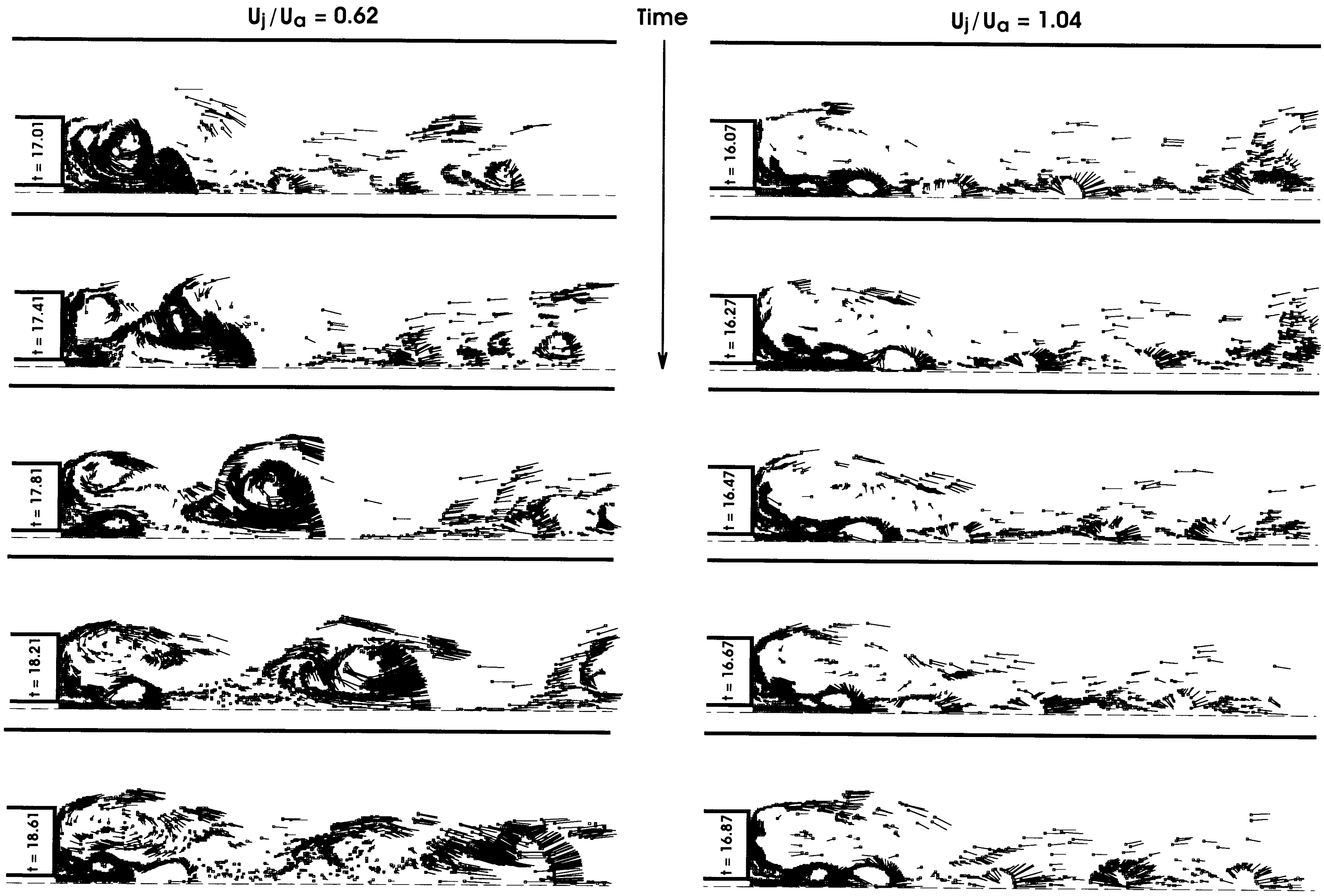

Figure 4.30 A series of time frames showing the entrainment of the jet fluid into the large-scale vortical structure.

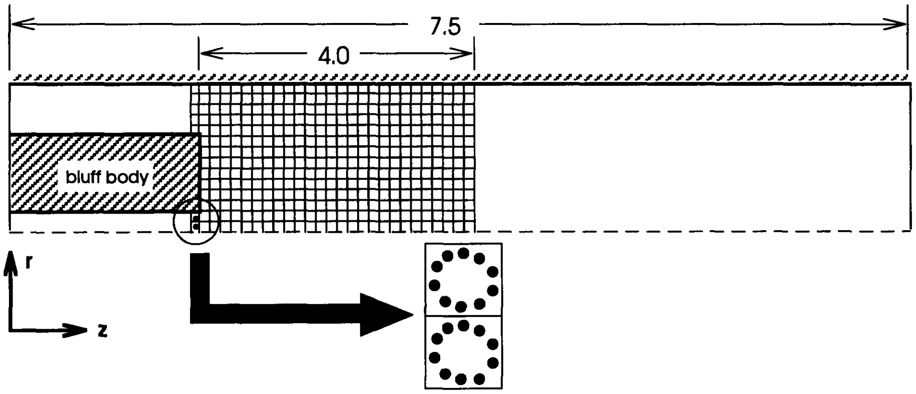

Figure 4.31 The mesh used in the calculation of the jet-fluid concentration.

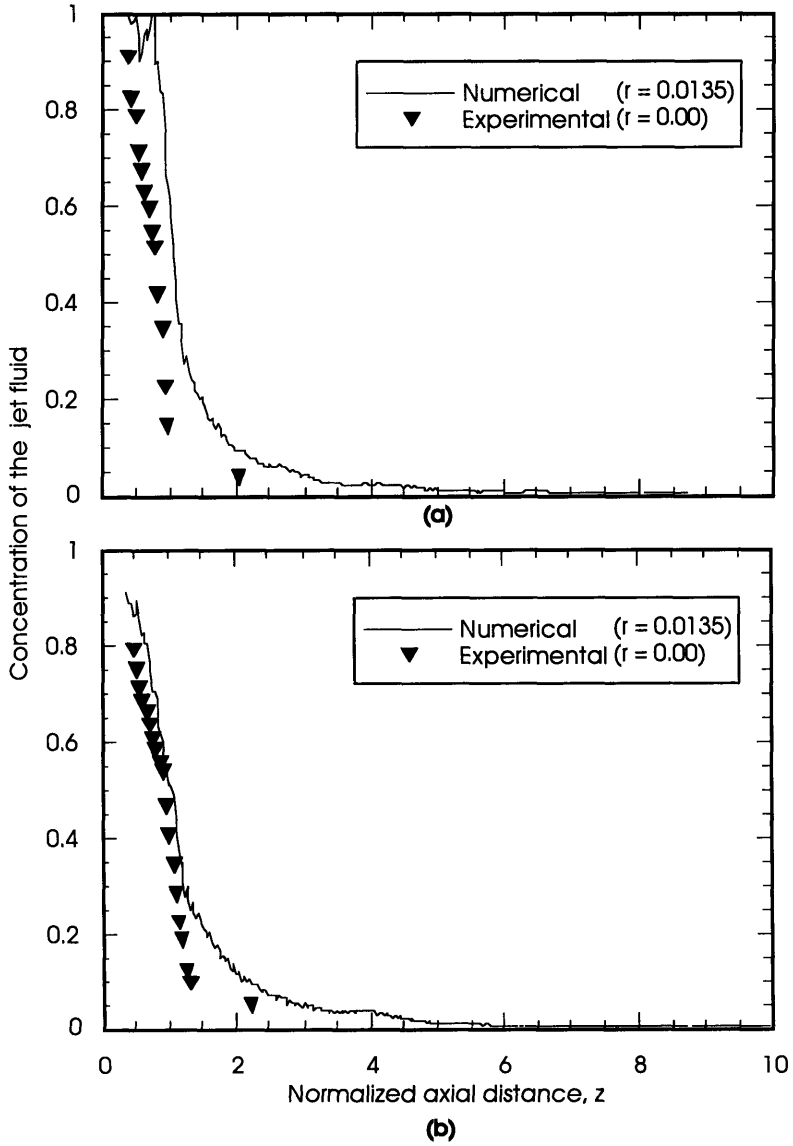

Figure 4.32 Concentration of the jet fluid as a function of the axial coordinate. Experimental data provided by Namazian [103]. **(a)** $U_j/U_a = 0.62$. **(b)** $U_j/U_a = 1.04$.

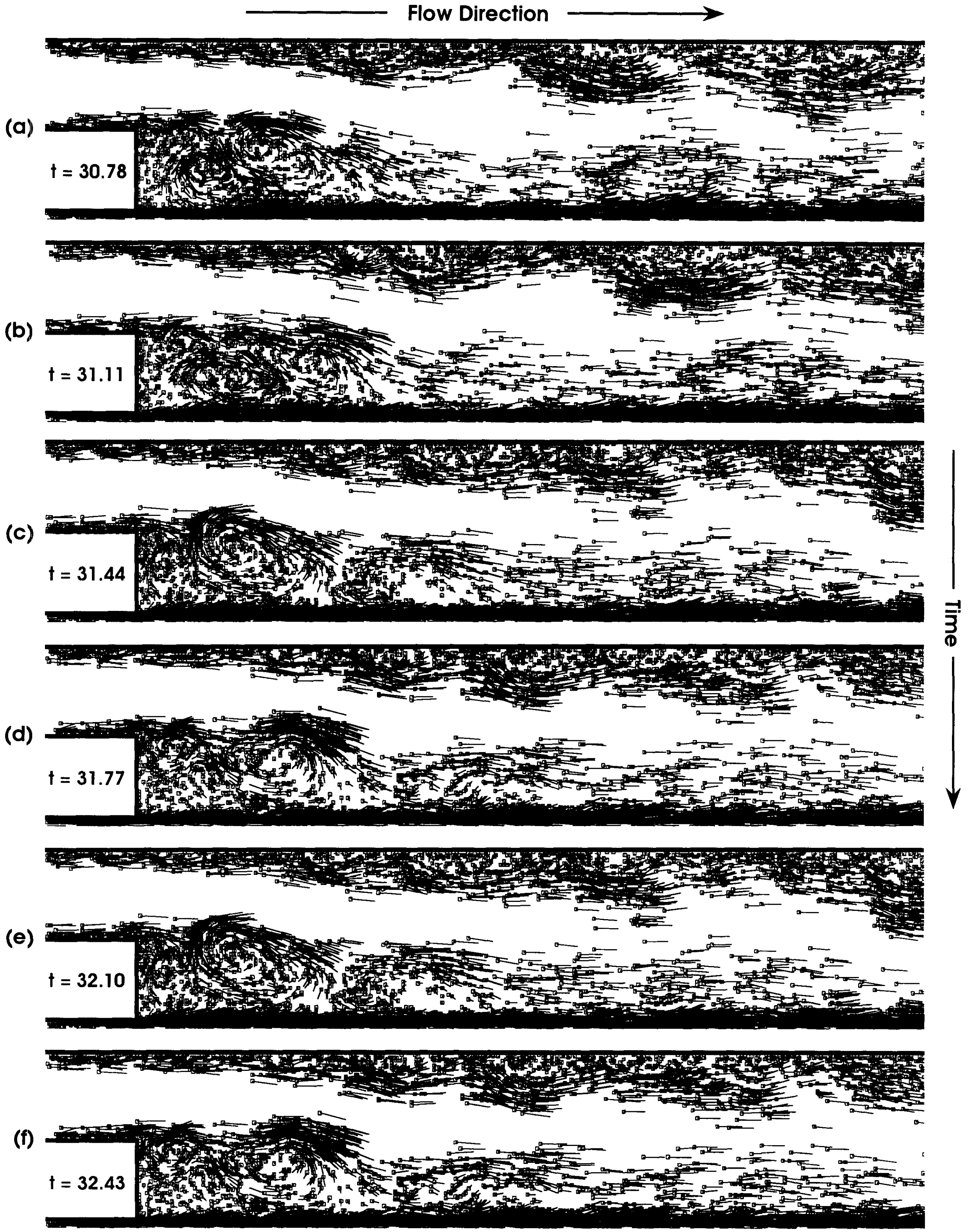

Figure 4.33 A series of time frames showing the evolution of the large-scale vortical structures in the near-wake region in terms of the distribution of the vortex elements in the interior of the flow domain. $U_j/U_a = 2.08$.

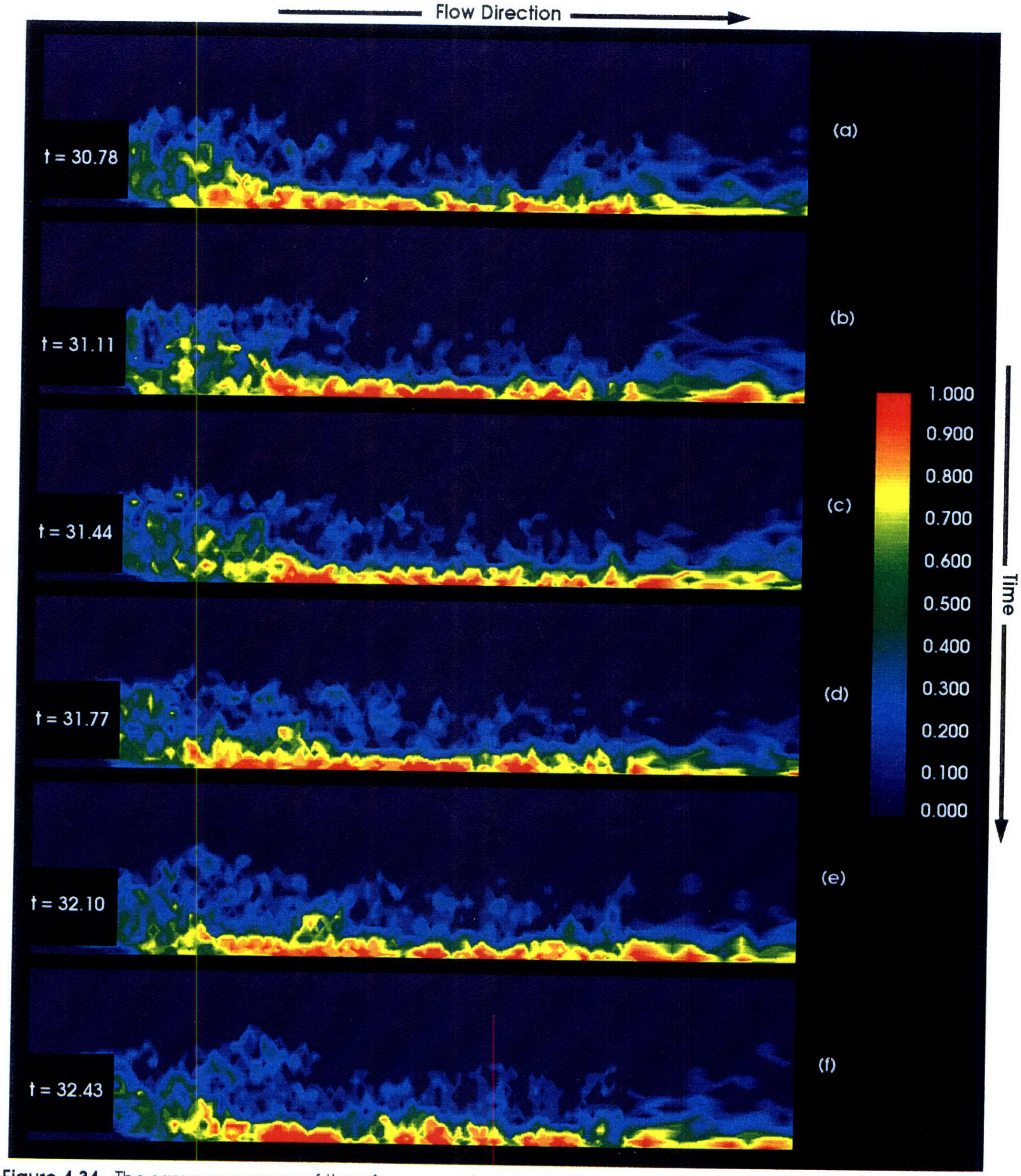

Figure 4.34 The same sequence of time frames as depicted in Figure 4.33 showing the instantaneous product concentration field. $U_j / U_a = 2.08$.

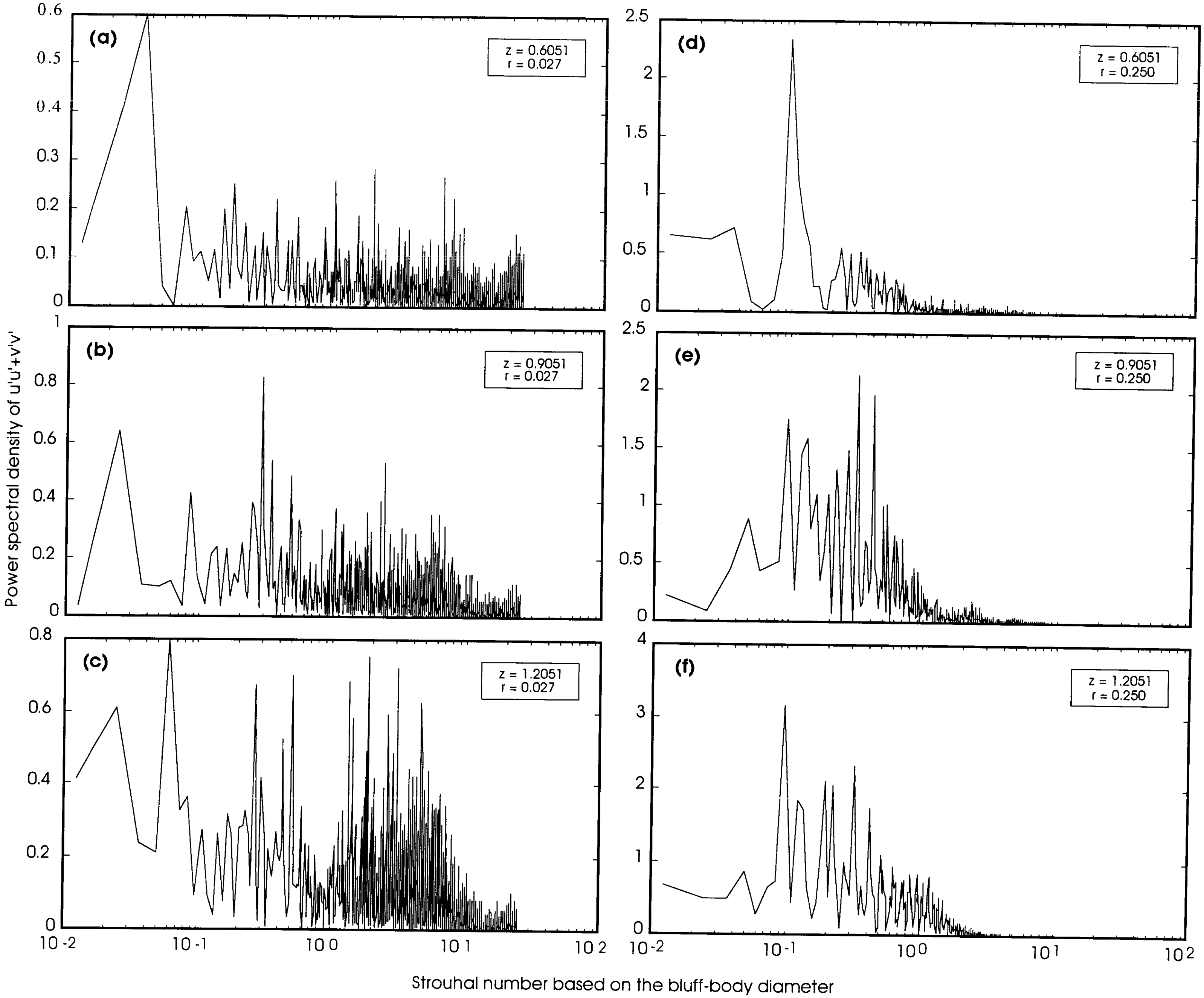

Figure 4.35 Power spectral density of u'u'+v'v'. $U_j / U_a = 2.08$.

4.2.5 THE UNSTEADY FLUCTUATION KINETIC ENERGY

Inspection of the unsteady vorticity dynamics and the product concentration field in the previous section unveiled much details of the large-scale interactions within the recirculation region. To further investigate the dynamics of the near-wake region, we have obtained correlation between the concentration of the unsteady fluctuation kinetic energy and the dynamics of the large-scale eddies within the recirculation. The production, redistribution, and dissipation of the unsteady fluctuation kinetic energy are important aspects of the flow dynamics and must be treated explicitly in many turbulence models currently being used in the moment-equation methods for simulating turbulent reactive flows (see the discussion in the Introduction). The instantaneous fluctuation kinetic energy $u'u' + v'v'$ in the flow domain for all three cases are presented in Figures 4.36-4.38. These figures show that the distribution of the unsteady fluctuation kinetic energy in the flow field is discrete and highly non-uniform, with most of the energy being concentrated in the well-defined, large-scale vortical structures. Shedding events and the trajectories of the large-scale structures are seen to be quite pronounced from inspecting the fluctuation kinetic energy distribution in the flow field. From these figures, it is seen that instability of the near-wake region starts as the eddies within the recirculation region begin to accumulate fluctuation kinetic energy. The eddies begin to pair as the perturbation continues to get amplified. Except for the case $U_j/U_a = 2.08$, this strong unsteady fluctuation inside the recirculation region is seen to reach a maximum value prior to the shedding of the composite eddy. Notice that the magnitude of the fluctuation kinetic energy in the recirculation region decays quickly after the eddy is being ejected. Thus, the perturbation kinetic energy level within the recirculation zone gives a quantitative measure of the stability of the region. Since the shedding dynamics are quasi-periodic, the same events as depicted in these figures will repeat themselves for the next shedding cycle. Notice that the large eddies being ejected from the recirculation region retain their identities as well as the energy levels even at a large distance downstream of the recirculation zone.

Unlike the other two cases, for $U_j/U_a = 2.08$, a buildup of the unsteady fluctuation kinetic energy within the recirculation region does not cause the complete break down of the structure within recirculation region and the shedding of large composite eddies. Instead, the fluctuation kinetic energy is carried away from the recirculation region by the continuous shedding of smaller eddies from the upper shear layer.

As mentioned before, the shedding of a large-scale eddy from the recirculation region is usually accompanied by the appearance of a smaller eddy inside the top wall boundary layer being convected downstream, which is clearly evident in Figure 4.36. The modulation of the wall boundary layer by the recirculation region causes a significant increase in the boundary thickness every time a large eddy is ejected from the recirculation zone. The eddy within the wall boundary layer usually interacts with the large vortical structure shed from the recirculation region. This interaction causes complicated flow pattern several bluff-body diameters downstream of the recirculation region, as seen in the last two frames of Figure 4.27. The results presented in this section also revealed that the three cases under investigation have quite different flow dynamics; however, the values of the fluctuation kinetic energy varied between zero to approximately 12 percent of the mean flow for all cases.

Figure 4.39 shows the time-averaged fluctuation kinetic energy field and the corresponding product concentration field for all three cases. From this figure, we see that all three cases have high fluctuation intensity in the jet shear layer, corresponding to the location where large-scale entrainment and mixing are the most intense. For the two cases with higher velocity ratio, intense fluctuation can also be seen along the axis of the combustor near the centerline.

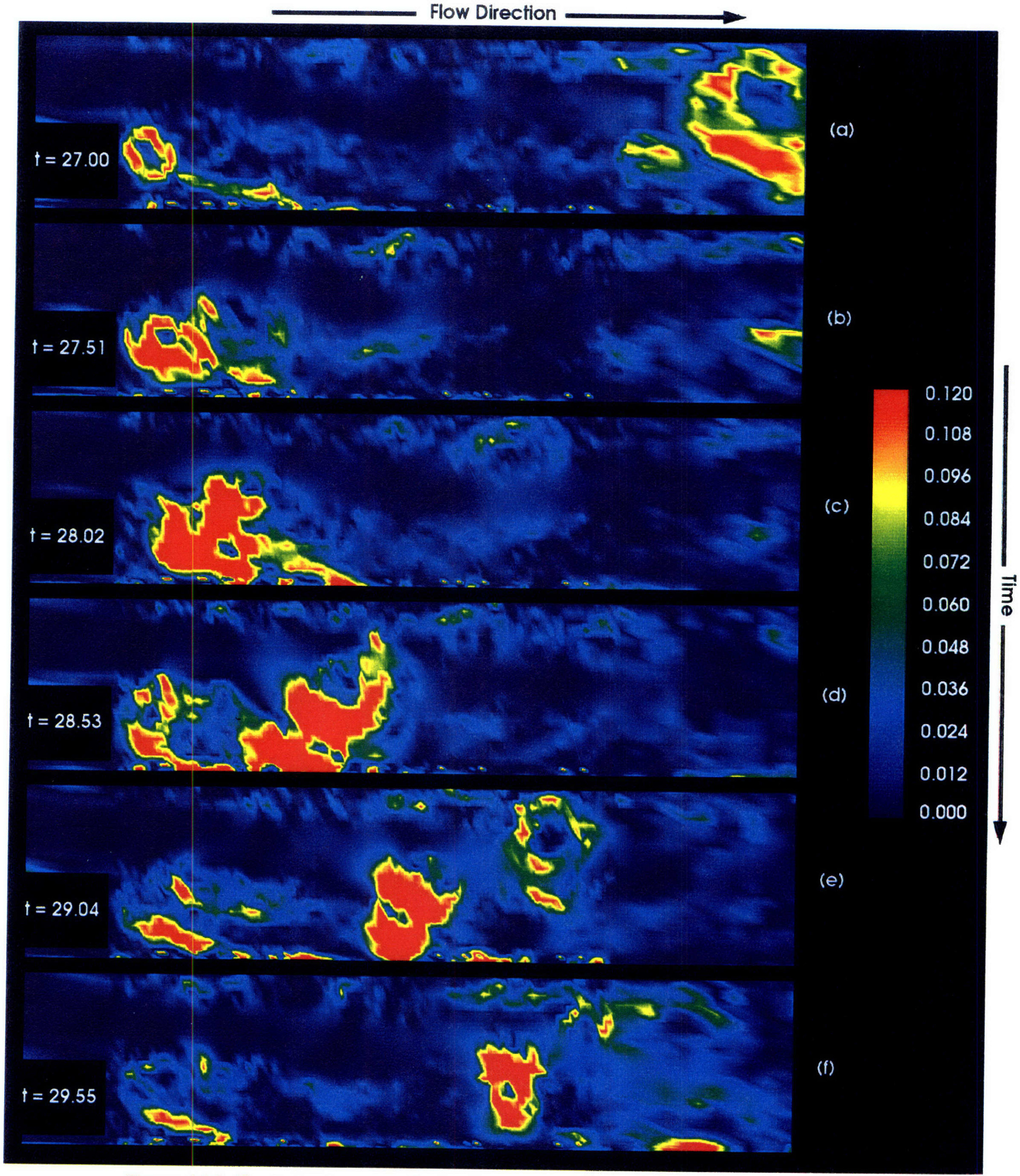

Figure 4.36 The instantaneous fluctuation kinetic energy u'u' + v'v'. $U_j/U_a = 0.62$.

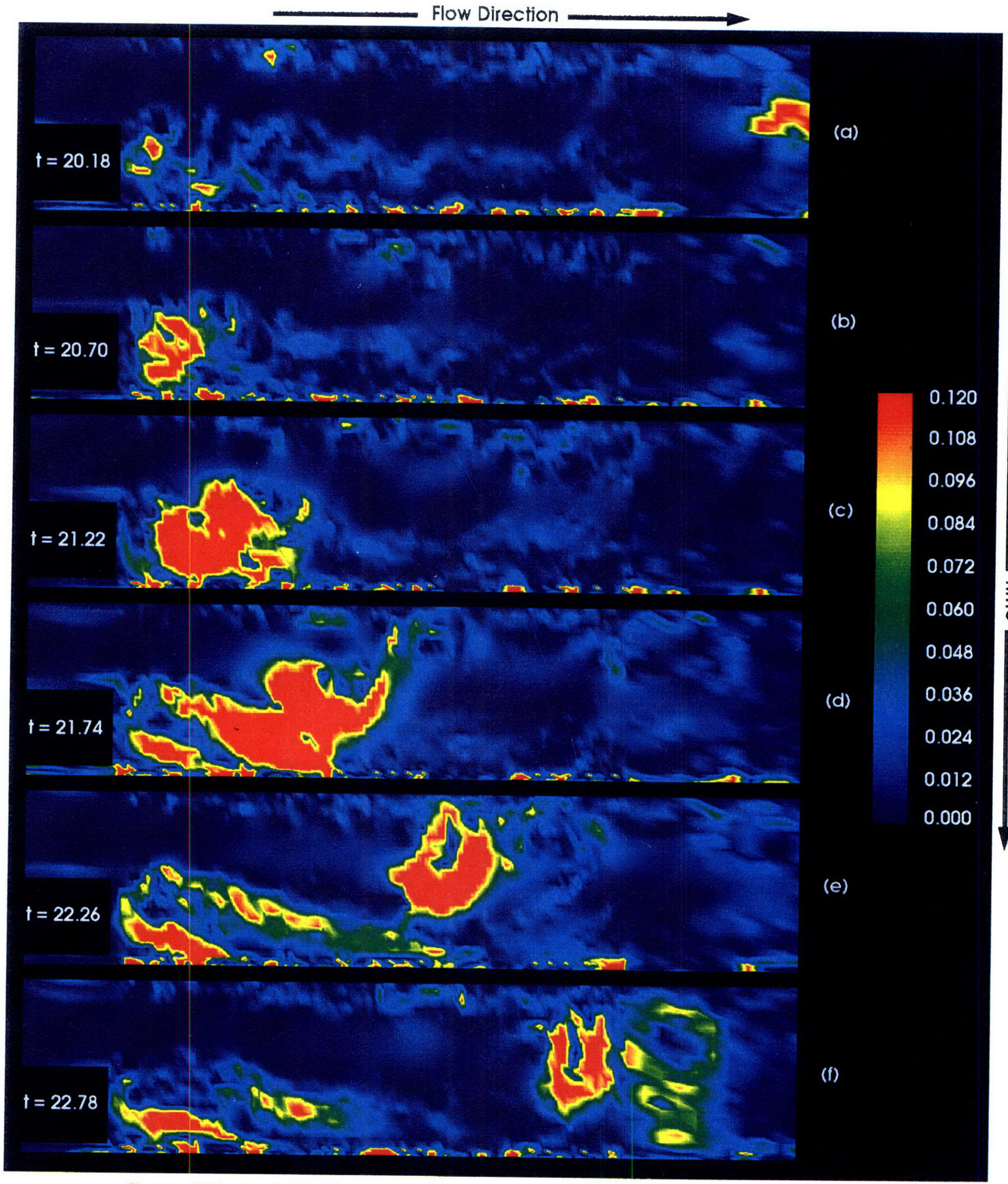

Figure 4.37 The instantaneous fluctuation kinetic energy u'u' + v'v'. $U_j/U_a = 1.04$.

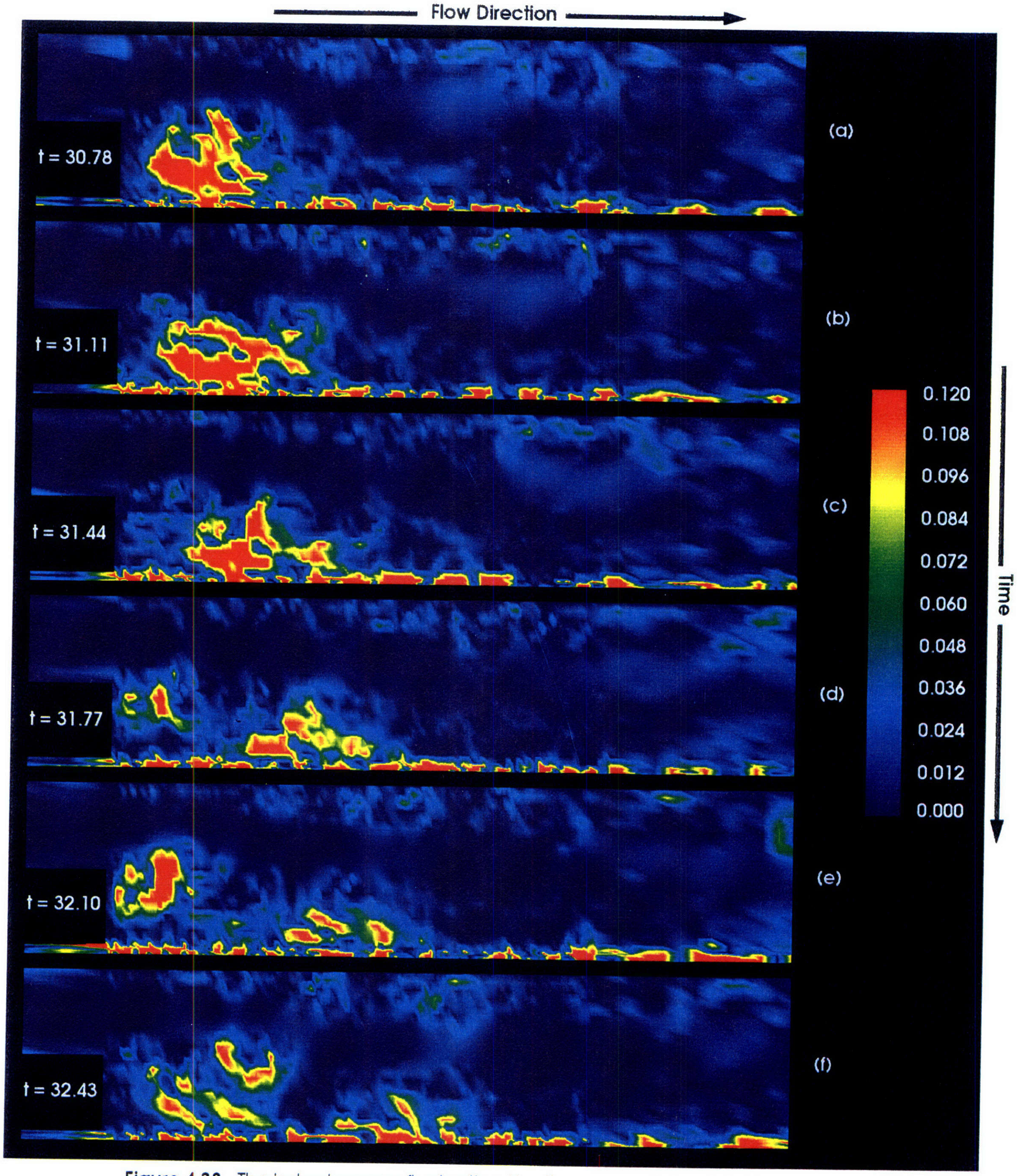

Figure 4.38 The instantaneous fluctuation kinetic energy u′u′ + v′v′. $U_j/U_a = 2.08$.

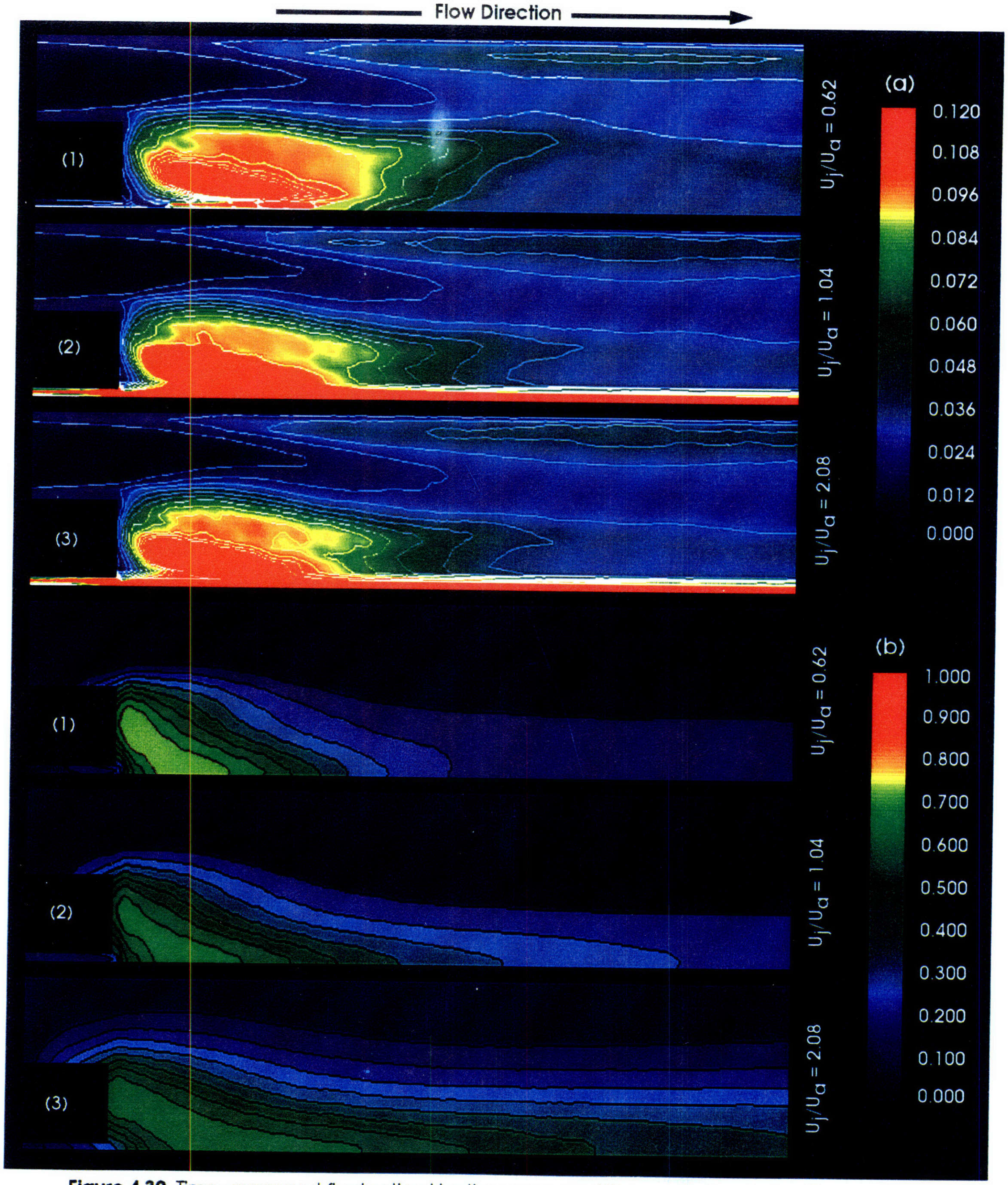

Figure 4.39 Time–averaged fluctuation kinetic energy and the product mole fraction contours. **(a)** Fluctuation kinetic energy. **(b)** Product mole fraction.

4.3 LARGE-SCALE DYNAMICS AND THE MIXING FIELD UNDER THE ASSUMPTION OF ISOTHERMAL REACTION WITH PERIODIC FORCING INFLOW BOUNDARY CONDITION

In Section 4.2, the unsteady flow dynamics and the large-scale entrainment and mixing in the near-wake region of the bluff body as a function of the (steady) inflow velocity ratio were studied in detail. In this section, we will consider the unsteady flow dynamics and the large-scale entrainment under various sinusoidal forcing inflow boundary conditions for the case U_j/U_a = 2.08. The study presented in Section 4.2 has shown that intense mixing in the near-wake region downstream of the bluff body for the two cases U_j/U_a = 0.62 and 1.04 is achieved mainly due to the strong interaction and pairing of the large-scale vortices, generated at the inner and the outer edge of the bluff body, within the recirculation region. The unsteady kinetic energy in the flow field was found to concentrate predominantly in the coherent structures, and the energy level of the large eddies persisted at quite large distance downstream of the recirculation region after they are being shed. Shedding events and the stability of the recirculation were quite predictable from examining the unsteady fluctuation kinetic energy field. For the case with U_j/U_a = 2.08, it was found that the large-scale dynamics within the recirculation region were less consequential, and the entire region was not very susceptible to small perturbations compared with the other two cases U_j/U_a = 0.62 and 1.04. At this high velocity ratio, mixing and reaction activities were limited mostly to regions close to the axis of the combustor, and extended many bluff-body diameters downstream of the recirculation region along the centerline.

The study presents in this section is intended to demonstrate that for the case with velocity ratio U_j/U_a = 2.08, the flow structure near the jet exit and the characteristics of the recirculation region can be altered significantly by introducing axisymmetric longitudinal perturbations to the jet flow. We will show in this study that, by applying external perturbations to the jet flow at frequencies closest to the most unstable frequency of the system and with a forcing amplitude exceeding a minimum threshold, it is possible to induce instability of the flow near the jet exit and the subsequent roll up of the jet shear layer into large eddies in phase with the excitation frequency. Under this condition, a notable increase in entrainment of the jet fluid near the jet exit from the unforced case is observed. The size and the energy level of the shear layer eddies generated from forcing the jet flow are seen to get amplified continuously with time due to the locking of the unsteady forcing energy into these large-scale structures. Similar to the two cases with lower inflow velocity ratio, these eddies interact and pair with the recirculating air eddy and, eventually, cause instability of the flow within the recirculation region and the shedding of large-scale composite structures. This enhanced entrainment within the recirculation region increases local mixing rate considerably which, in turn, increases the rate of fuel consumption in the near-wake region of the bluff body and effectively shortened the entire mixing length.

Although few studies have been conducted in the past of a forced jet in a confined, bluff-body flow configuration, a considerable amount of research has been done on forced, nonreactive as well as reactive free jet flows [25, 67, 68, 149, 150]. The works of Hussain *et al.* [66, 68, 149, 150] have shown that excitation of a free jet can occur for a range of Strouhal numbers based on the jet diameter and the magnitude of the jet velocity in the range from 0.1 to 0.9, and that the preferred excitation frequency depends, in fact, on the shear layer and can be predicted by linear stability theory in many cases [99, 112]. He has also found that the effects of forcing on the jet-flow structure generally disappear at a distance $x/D \cong 20$, where D is the jet diameter.

Numerous experiments have been conducted in the past mainly to determine the increase in entrainment associated with excited jets. Favre-Marinet and Binder [36] used a spinning valve to modulate a turbulent air jet with a forcing frequency S = 0.23 and a forcing amplitude equal to 42 percent of the jet velocity. The local entrainment was found to increase by up to 35 percent within $x/D \cong 15$, but the effects vanished by $x/D \cong 20$. Parikh and Moffat [108] used a spinning plate to modulate an air jet at the resonant frequency of the jet nozzle $(S \cong 0.85)$ with forcing amplitude of 37 percent. Their results indicated that very close to the jet exit the local entrainment was increased by as much as 300 percent. Sarohia and Bernal [124] excited a high-Reynolds-number air jet (Re = 90000) using a pneumatic transducer and found that the jet structure could be altered significantly near the exit for a range of frequencies S = 0.1-0.56 with a forcing amplitude of only 10 percent. The jet entrainment was found to increase roughly by 25 percent, but the effects vanished by x/D = 5. These studies all show that significant increases in jet entrainment can be achieved by moderate forcing at the appropriate forcing frequencies. However, the effects of forcing usually disappear a short distance downstream of the jet nozzle.

Extensive studies have also been conducted with jet excited by very high forcing amplitude at a wide range of forcing frequencies. Curtet and Girard [28] used a piston to excite a turbulent air jet with S = 0.11 and forcing amplitude of up to 80 percent. They observed that large coherent vortex rings grew quickly within one diameter of the jet exit. Bremhorst and Harch [16] employed segmented rollers on the air jet supply to produce a complete on-off pulse with a duty cycle of 1/3 and with two forcing frequencies S = 0.0071 and 0.018. The jet entrainment from this experiment was found to increase by up to 300 percent within a distance $x/D \cong 17$. Direct measurements of entrainment were made by Vermeulen *et al.* [145] on an air jet with very strong forcing amplitude (270 percent) and S = 0.25. Unlike other experimental investigations, however, in this study the effects of the forcing were observed at distance as far as $x/D \cong 70$ downstream of the jet nozzle. The local entrainment was found to increase by 200 percent near the jet exit. These experimental studies all have shown that the structure of the jet flow can also be significantly altered by high-amplitude forcing.

The above brief survey reveals that the structure of the flow near the jet exit can be altered under high-amplitude forcing at the appropriate frequencies. All the experimental studies have shown that the application of external excitations at the characteristic frequencies of the system destabilizes the jet flow near the exit, causes roll up of the shear layer and produces strong vortices. In most experimental studies, instability of the jet shear layer generally occurs at frequencies such that the Strouhal numbers based on the jet diameter and the jet velocity in the range of 0.1 to 0.9 for low-amplitude forcing, and can go down as low as $O(0.001)$ if the forcing amplitude is high. On the average, the effects of forcing are seen to vanish by $x/D \cong 20$. Accordingly, it is anticipated that by applying external perturbations to the jet flow in our confined bluff-body flow at certain selected frequencies which are closest to the characteristic frequency of the system, it will have the same destabilizing effect on the flow structure near the exit; thus, influencing the stability and the mixing characteristics of the recirculation region. However, one should keep in mind that the flow configuration we are studying here is far more complicated than a free jet, and many of the results found in the free-jet experiments may not be applicable in this case. Therefore, a direct comparison between the free-jet experimental results and the system we are studying here is not appropriate and should not be attempted. The free-jet experimental studies should only be treated as a guide for this forcing study.

The free-jet experimental studies described above have shown that the two significant governing parameters in any externally controlled excitation of a flow system are the forcing frequency and the forcing amplitude. Thus, selecting the correct forcing frequency and coupling it with the appropriate forcing amplitude is essential if we wish to modulate the jet flow in the hope that it would alter the flow structure of the recirculation region. Given all this, the immediate issue we are facing before the numerical experiments can be performed is the identification of the significant frequencies of the system, and to determine the minimum threshold level of the forcing amplitude. One way of identifying the significant frequencies is to perform many simulations with the forcing frequency applied at a fixed increment, starting at a small but finite value. In doing so, the impact of varying the excitation frequency on the flow structure in the near-wake region can be examined and the effectiveness of a given forcing frequency on the stability of the flow field can be assessed visually. However, a more systematic approach of identifying the significant frequencies of the flow system at this velocity ratio is to examine the natural shedding frequencies of the unforced study presented in Section 4.2. Specifically, we want to examine the power spectral density plots presented in Figure 4.35. Since the power spectra presented in Figure 4.35 were obtained from a simulation with steady inflow condition, the significant shedding frequencies observed in these plots are the intrinsic properties of the flow system at this velocity ratio. Thus, by applying external perturbations to the inflow jet velocity close to these natural frequencies of the system at an appropriate amplitude, it is anticipated that we will be able to excite the jet shear layer instability near the exit, inducing local changes of the flow structure and to affect the large-scale entrainment in the near-wake region.

From Figure 4.35, we see that the power spectra have high-energy isolated peaks centered around 0.03, 0.06, 0.1, and 0.2. Again, since these are the natural shedding frequencies of the system, it is anticipated that studying the effects of forcing on the flow dynamics using these frequencies will be sufficient because they represent the essential physics of the flow. A total of eight simulations with the jet flow varying sinusoidally at dimensionless frequencies $S = 0.03$, 0.06, 0.1, and 0.2 at two forcing amplitudes: 30 and 60 percent of the mean value of the jet velocity were performed for this study. The matrix of the forcing parameters for the simulations are presented in Table 4.1. The forcing function used in the simulations is given by

$$U_j = U_o[1 + A_f \sin(\varpi t)] \tag{4.5}$$

where $U_o = 2.08$ is the mean jet inflow velocity, ϖ is the angular frequency calculated using the chosen Strouhal numbers, and $A_f = 0.3$ or 0.6 is the forcing amplitude. These two forcing amplitudes were chosen based on the results of the experimental studies on pulsed free-jet as discussed earlier. Typical time traces of the jet flow at two different forcing amplitudes are shown in Figure 4.40. Notice that longitudinal excitations are used in this study. However, it has been shown that longitudinal and transversal excitations on the flow dynamics are effectively equivalent [46, 134]. Thus, the mode of excitation applied is irrelevant in regard to the flow development. It should also be pointed out that although data are available for the complete matrix of forced conditions, not every simulation made in the course of this study is presented and discussed in detail here in order to avoid drudgery. The data present in the next few sections represent results which are deemed most significant from the investigation and from which meaningful conclusions can be drawn. In the following, we will study in detail of the characteristics of the unsteady near-wake region dynamics and the large-scale entrainment with forced jet inflow boundary condition, and to discuss the significant differences between the forced and the unforced flow dynamics.

Before we proceed to discuss the results of the numerical experiments, it should be pointed out that external perturbations applied at frequencies close to the natural frequencies of the system may cause sustained large-amplitude pressure oscillations and destructive combustion instabilities in real combustion devices [62]. Thus, the benefits gained in enhanced mixing and reduction of NO_x emissions from externally applied excitation must be weighted against the possibility of inducing destructive combustion instability and may, in the extreme cases, lead to the total loss of the system [5, 24, 59, 147].

Case	Dimensionless Forcing Frequency	Forcing amplitude
1	0.03	30%
2	0.06	30%
3	0.10	30%
4	0.20	30%
5	0.03	60%
6	0.06	60%
7	0.10	60%
8	0.20	60%

Table 4.1 Inflow parameters for the forcing study.

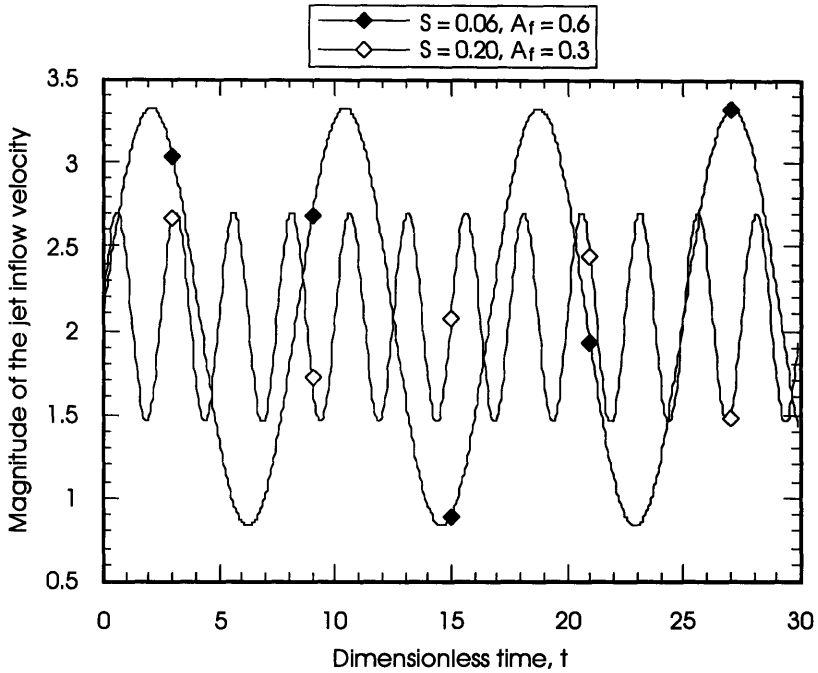

Figure 4.40 Typical time traces of the jet inflow velocity for the forcing study.

4.3.1 The TIME-AVERAGED PRODUCT CONCENTRATION FIELD

A primary finding from this investigation is that the unsteady dynamics and the entrainment in the near-wake region respond to all the forcing frequencies chosen for this study to some degree. However, the most significant reduction in the time-averaged mixing zone length is observed when the perturbation is applied at a dimensionless frequency based on the magnitude of the annular inflow velocity and the bluff-body diameter $S = O(0.06)$, with a forcing amplitude $A_f = 0.6$. When forcing the jet flow at this frequency and amplitude, significant amount of fuel elements are seen to disperse radially within the recirculation region, resulting in a reduction of the time-averaged mixing zone by approximately 11 percent compared with the unforced case. This reduction in the mixing zone length would translate into noticeable shortening of the flame length for exothermic reactive flows. Extrapolating from the results of this study, it is expected that when the perturbation is applied with a forcing amplitude $A_f > 0.6$ at this frequency, the reduction in the mixing zone length would be more pronounced.

In order to examine the effects of the forcing frequency and the amplitude independently, it is necessary that the amplitude of the pulsation be maintained constant as the perturbation frequency is being varied. Figures 4.42 and 4.43 show the time-averaged product concentration field as a function of the perturbation frequency for the two forcing amplitudes studied. The time-averaged product concentration field provides a valuable visualization as well as a quantitative measure of the global changes in mixing in the near-wake region as functions of the perturbation frequency and amplitude. Figure 4.42 shows comparisons of the time-averaged mixing field between the unforced (4.42a) and the forced (4.42b-e) cases with a forcing amplitude equal to 30 percent of the mean value (see Equation 4.5). Although perturbation applied at this amplitude produced small changes in the unsteady large-scale entrainment in the near-wake region for all the frequencies considered (Figure 4.49), the change on the time-averaged mixing zone length appeared to be negligibly small when the perturbation is applied at this pulse amplitude.

As the experiment is repeated by retaining the same perturbation frequencies but with the amplitude of the perturbation increased to 60 percent of the mean value, remarkable changes in the stability and the flow structure of the jet shear layer near the exit are observed for the case with forcing frequency S = 0.06. From the simulation, it was found that external perturbation applied at this frequency and amplitude increased the local entrainment and mixing of the jet flow near the exit in two ways. Forcing the jet flow magnified the shear layer instability and enhanced the growth of the vortical structures within the shear layer, as can be seen in Figure 4.44. In addition, the unsteady energy delivered to the flow from forcing increased the local unsteady fluctuation kinetic energy considerably, which can clearly be seen in Figure 4.45 where we compare the instantaneous fluctuations between the forced and the unforced case at three points along the jet shear layer within the recirculation region. This changes to the local flow dynamics and the large-scale entrainment are reflected in the time-averaged mixing field, as can be seen in Figure 4.43. It is seen that the most significant enhancement to mixing in the near-wake region when forcing the jet flow at this frequency comes from the amplification of the inherent unstable recirculation zone dynamics of this coaxial-jet configuration, and that this amplification occurs as the forcing frequency approaches the natural pairing and shedding frequency of the eddies within the recirculation region. Forcing the jet flow causes the roll up of the jet shear layer near the exit and produces a counterclockwise-rotating eddy (similar to the two cases with lower velocity ratio) in phase with the forcing frequency. This eddy entrains most of the jet fluid entering the flow domain, and it interacts vigorously with the recirculating air eddy. Similar to the two cases with lower velocity ratio, the interaction generates strong local fluctuations between the interface of the two eddies and decreases the stability of the recirculation region substantially. The interaction eventually leads to the merging and the shedding of the large-scale vortical structure from the recirculation region (Figure 4.44). This increase in entrainment and mixing in the recirculation region causes the fuel in the jet flow to react sooner in space, decreasing the overall time-averaged mixing length as shown in Figure 4.43c. The reduction of the mixing zone length, as obtained from measuring the difference in the concentration contours presented in Figure 4.43a and 4.43c, was found to be approximately 11 percent.[1] This increase in entrainment and mixing in the recirculation region from forcing can also clearly be seen in Figure 4.41, where we compare the product flux as a function of the axial coordinate between the unforced

---

[1] The measurement was taken from the face of the bluff body to the maximum streamwise location of the contour with the highest product concentration.

and the forced case.

Since the reference velocity of this study is 0.45 m/s and the reference length is 0.1 m, by rescaling the most effective Strouhal number, we see that the flow responds to a dimensionless forcing frequency based on the jet diameter and the magnitude of the inflow-velocity difference of 0.003. One might (correctly) suspect that this Strouhal number seems to be unrealistically low. Since the amplification of the inherent unsteady dynamics of the recirculation region leading to the interaction and pairing of the fuel and air eddies is mainly responsible for the entrainment and the enhanced mixing in the near-wake region, the Strouhal number based on the bluff-body diameter and the magnitude of the annular inflow velocity, S = 0.06, is more appropriate in this case. Forcing the jet flow has the effect of causing the jet shear layer to roll up at the forcing frequency, and the increase in entrainment by the jet shear layer due to forcing cannot account for the remarkable increase in mixing in the near-wake region. Thus, the Strouhal number based on the jet diameter and the magnitude of the jet velocity is inappropriate in this case. To further illustrate the effects of the forcing on the flow structures, we will present and discuss the changes in the probability density functions of the velocity distributions and the unsteady large-scale entrainment in the near-wake region as functions of the perturbation frequency and amplitude in the next two sections.

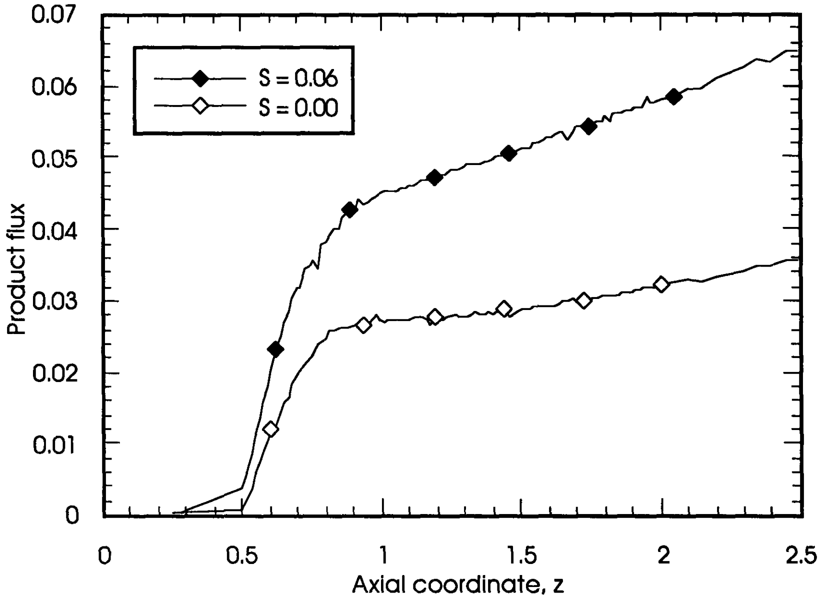

Figure 4.41 Comparison of the product flux as a function of the axial coordinate between the unforced and the forced case. For the forced case, S = 0.06, A_f = 0.6.

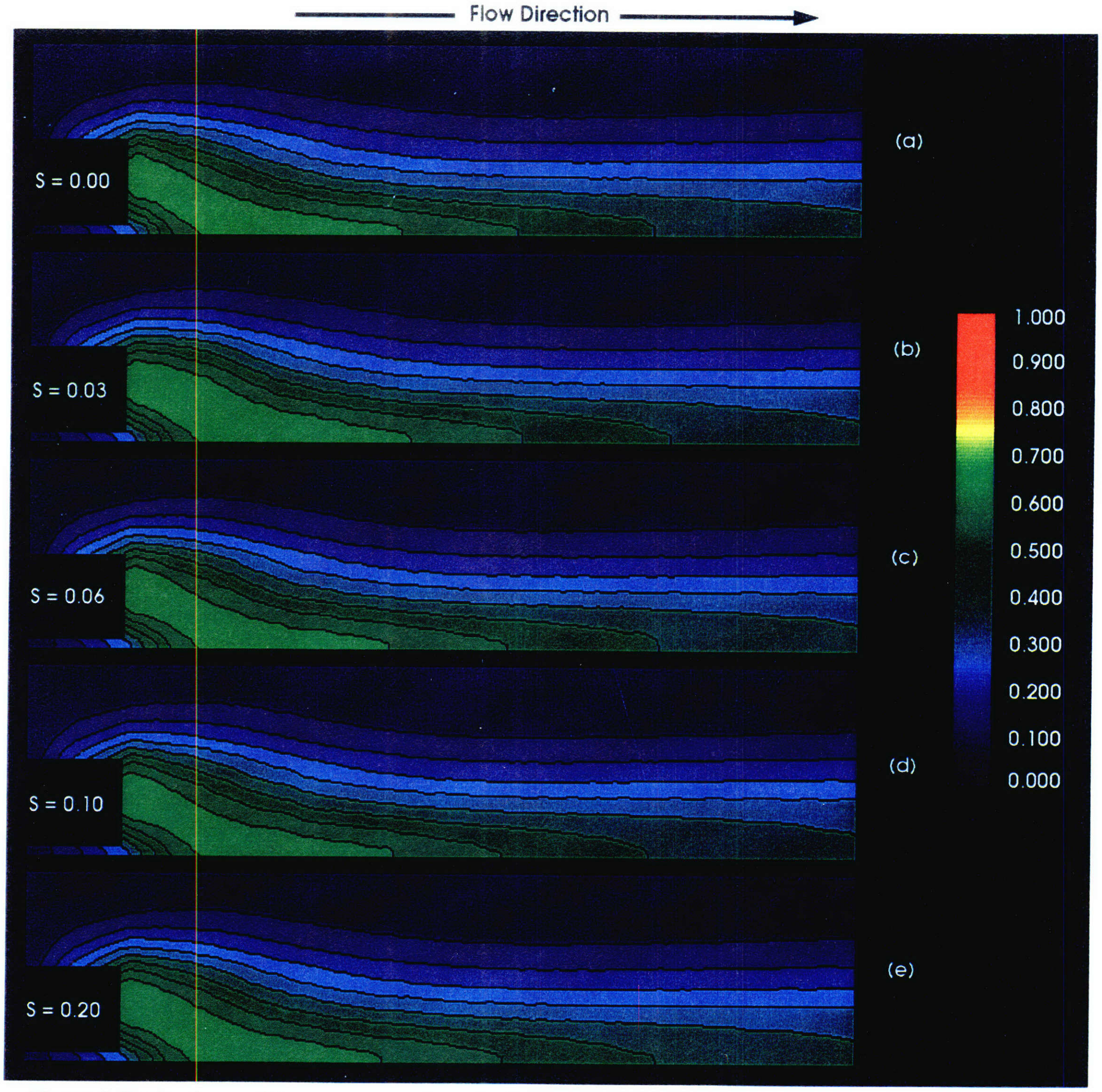

Figure 4.42 Contours of time–averaged product concentration as a function of the inflow perturbation frequency. Forcing amplitude $A_f = 0.3$, mean value of $U_j / U_a = 2.08$.

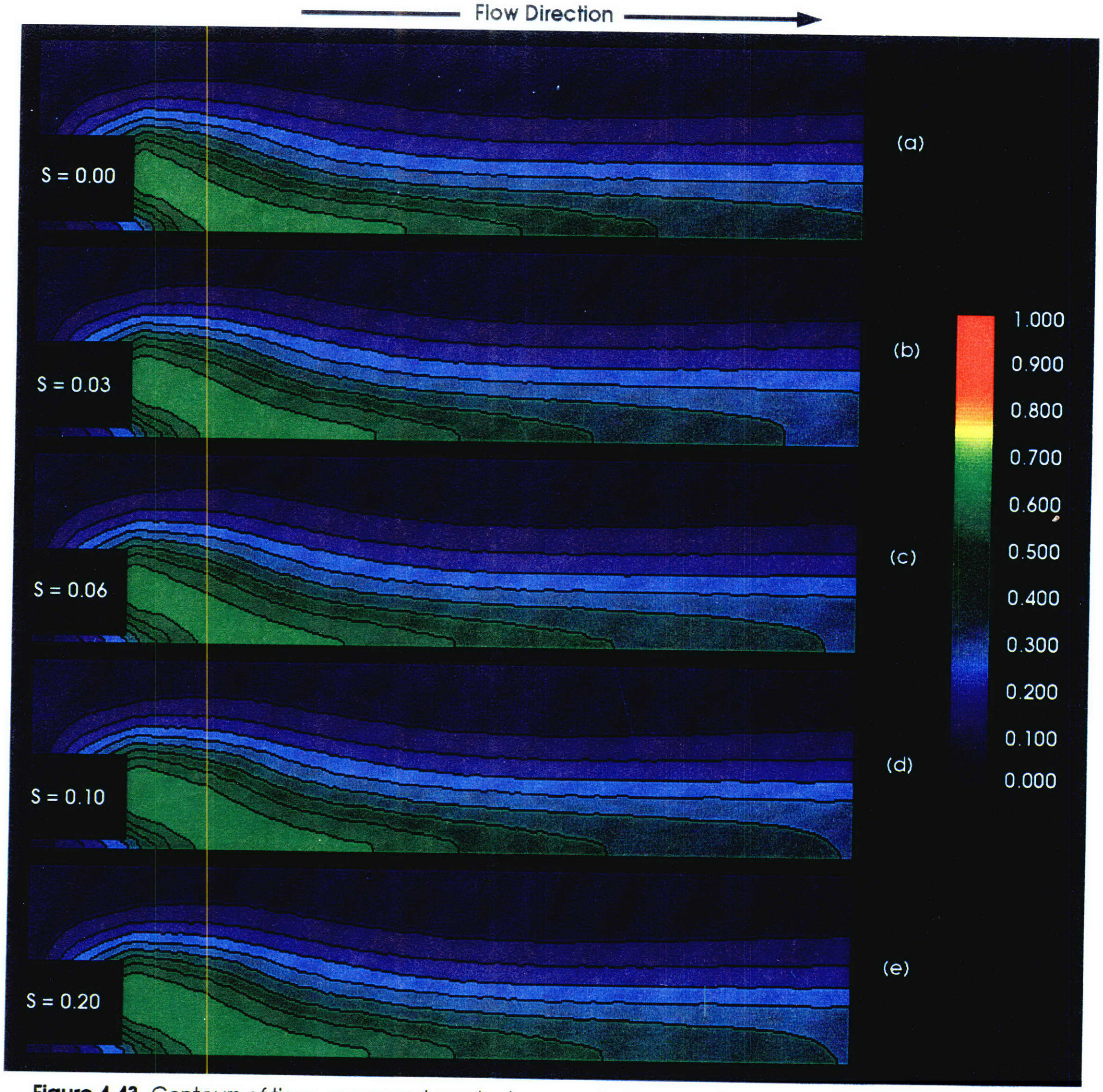

Figure 4.43 Contours of time–averaged product concentration as a function of the inflow perturbation frequency. Forcing amplitude $A_f = 0.6$, mean value of $U_j / U_a = 2.08$.

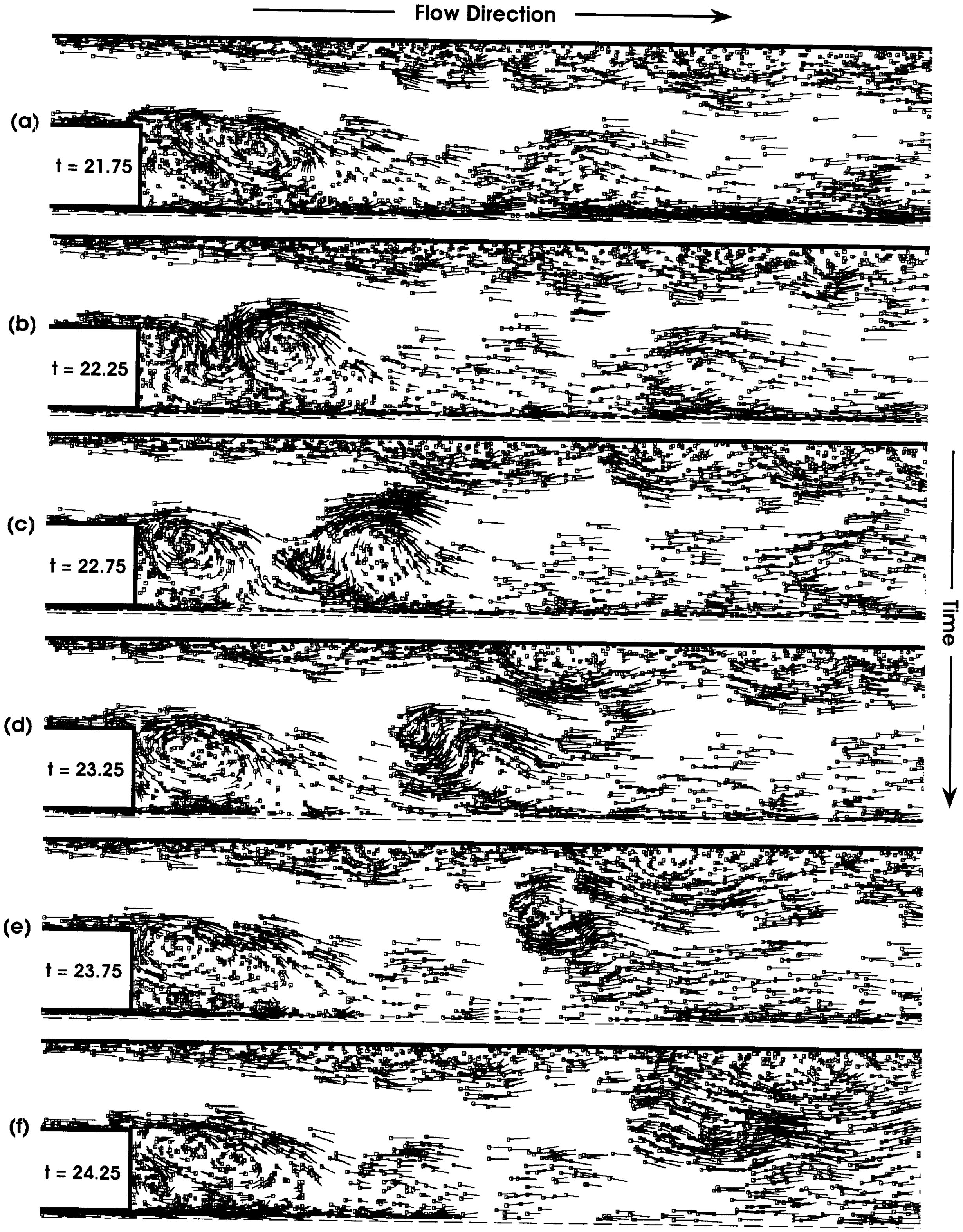

Figure 4.44 The unsteady flow dynamics in the near-wake region in terms of the vortex elements. Mean value of $U_j/U_a = 2.08$. Forcing amplitude $A_f = 0.6$. Forcing frequency $S = 0.06$.

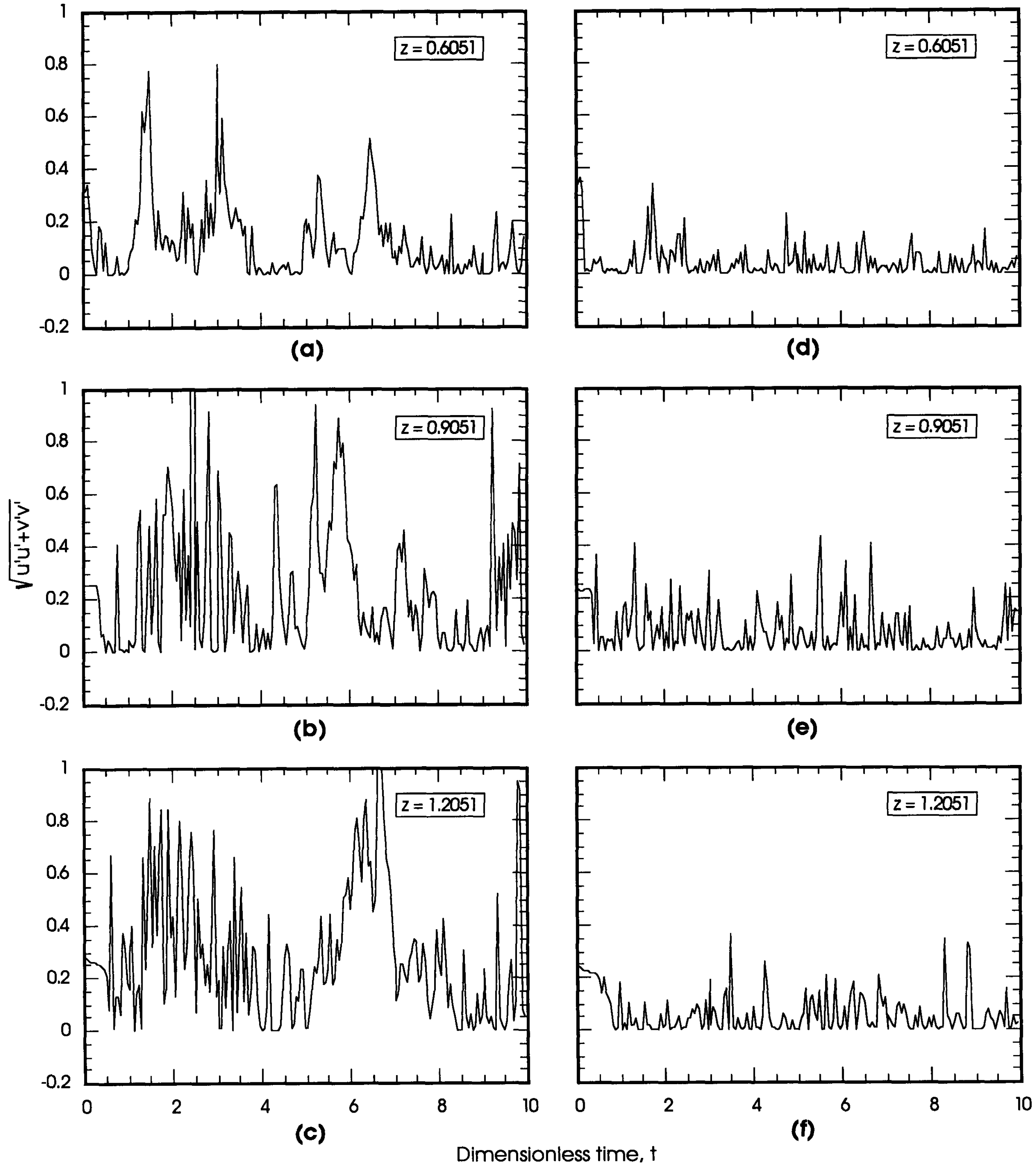

Figure 4.45 Comparison of the square root of the instantaneous fluctuation kinetic energy, $\sqrt{u'u' + v'v'}$, between the forced (a-c) and the unforced case (d-f) along the jet shear layer. For the forced case, mean value of U_j/U_a = 2.08, S = 0.06, and A_f = 0.6.

4.3.2 PROBABILITY DENSITY FUNCTIONS OF THE VELOCITY DISTRIBUTIONS

From the discussion in Section 4.2.3, we see that the probability density functions (PDFs) of the velocity distributions are effective in terms of separating the large-scale mixing from the more classical small-scale mixing flow features of high-Reynolds-number flows. Much of the flow dynamics within the recirculation region and the characteristics of the shear layers were brought out by the PDFs of the velocity distributions. The PDFs of u' and v' for the case U_j/U_a = 2.08 with steady inflow boundary condition are presented in Figures 4.20 and 4.21. For comparison, the PDFs of the velocity fluctuations for the case with forcing frequency S = 0.06 and forcing amplitude A_f = 0.6 at exactly the same locations as those presented in Figures 4.20 and 4.21 are shown in Figures 4.46 and 4.47. By analyzing the differences of the corresponding plots in these figures, the effects of externally applied perturbation on the structures of the shear layers in the recirculation region can readily be deduced. Notice that we have chosen the case with forcing frequency S = 0.06 and amplitude A_f = 0.6 for further detailed discussion since most significant changes in the flow dynamics are observed when these perturbation parameters are used in the simulation.

The probability density functions of u' and v' for the unforced case reveal that the distributions in the jet shear layer along the centerline of the combustor are typically unimodal and nearly Gaussian at all three sampling locations (Figures 4.20a, b, c and 4.21a, b, c). Since the velocity at any point in the shear layer is generally subjected to disturbances from the passage of a large number of random eddies, the probability density functions provide a good indicator to the general characteristics of these disturbance eddies. PDFs having approximately normal distributions usually indicate that the disturbance eddies are mostly small scale in nature, and the sizes of these eddies are quite uniform.

External perturbation applied to the jet flow at a dimensionless frequency S = 0.06 with an amplitude A_f = 0.6 changes the characteristics of the jet shear layer significantly. The excitation intensifies the vortex-roll up activities near the jet exit, accelerates the growth rates of the eddies in the jet shear layer by enhancing the fluid entrainment rate and the coalescence of the eddies. Since disturbance to the local mean velocity induced by the passage of a large-scale eddy are generally more dramatic, the formation of the large-scale eddies in the shear layer causes significant departure of the probability density functions from a Gaussian distribution. From Figures 4-46a, b, and c, we see that the major effects of the perturbation on the PDFs of u' in the jet shear layer are the broadening of the distributions and changing the shape of the distributions to bimodal, with two slight peaks centered around -0.5 and 0.5. The bimodal peaks are especially noticeable at the axial station z = 1.5051 (Figure 4-46c). However, external perturbation doesn't seem to affect the flow structure of the shear layer in between the annular flow and the recirculation bubble. Comparing Figures 4.20d, e, and f with the corresponding plots in Figure 4.46, we see that forcing the jet flow causes only a small spreading out of the fluctuation velocity distributions in the negative direction in the upper shear layer. This behavior qualitatively agreed with the general experimental results of forced free jet that the effect of external applied perturbation to the jet flow is usually localized, produces noticeable difference in the flow structures only near the jet exit, and disappears very quickly with axial distance. Thus, the marked increase in entrainment and mixing from forcing the jet flow alone comes directly as a result of the formation of the large counterclockwise-rotating eddy near the jet exit, which entrains most of the fuel elements entering the flow domain. The existence of this large-scale eddy causes substantial local changes in the flow structure of the recirculation region, and greatly increase the entrainment and mixing of the jet fluid within the recirculation region as it interacts and merges with the recirculating air eddy.

Comparing the PDFs of v' between the forced and the unforced case shown in Figures 4.21 and 4.47, we see that the effect of external perturbation on the distribution of v' is to cause the spreading out of the PDFs in the positive direction at the jet shear layer, indicating that forcing induces a small increase in the fluctuation intensity of v in the positive radial direction. However, this would translate into enhancement of momentum transfer across the jet shear layer into the recirculation bubble. Again, similar to the distributions of u', Figures 4.47d, e, and f show external perturbation applied to the jet flow has minimal effect on the PDFs of v' on the upper shear layer.

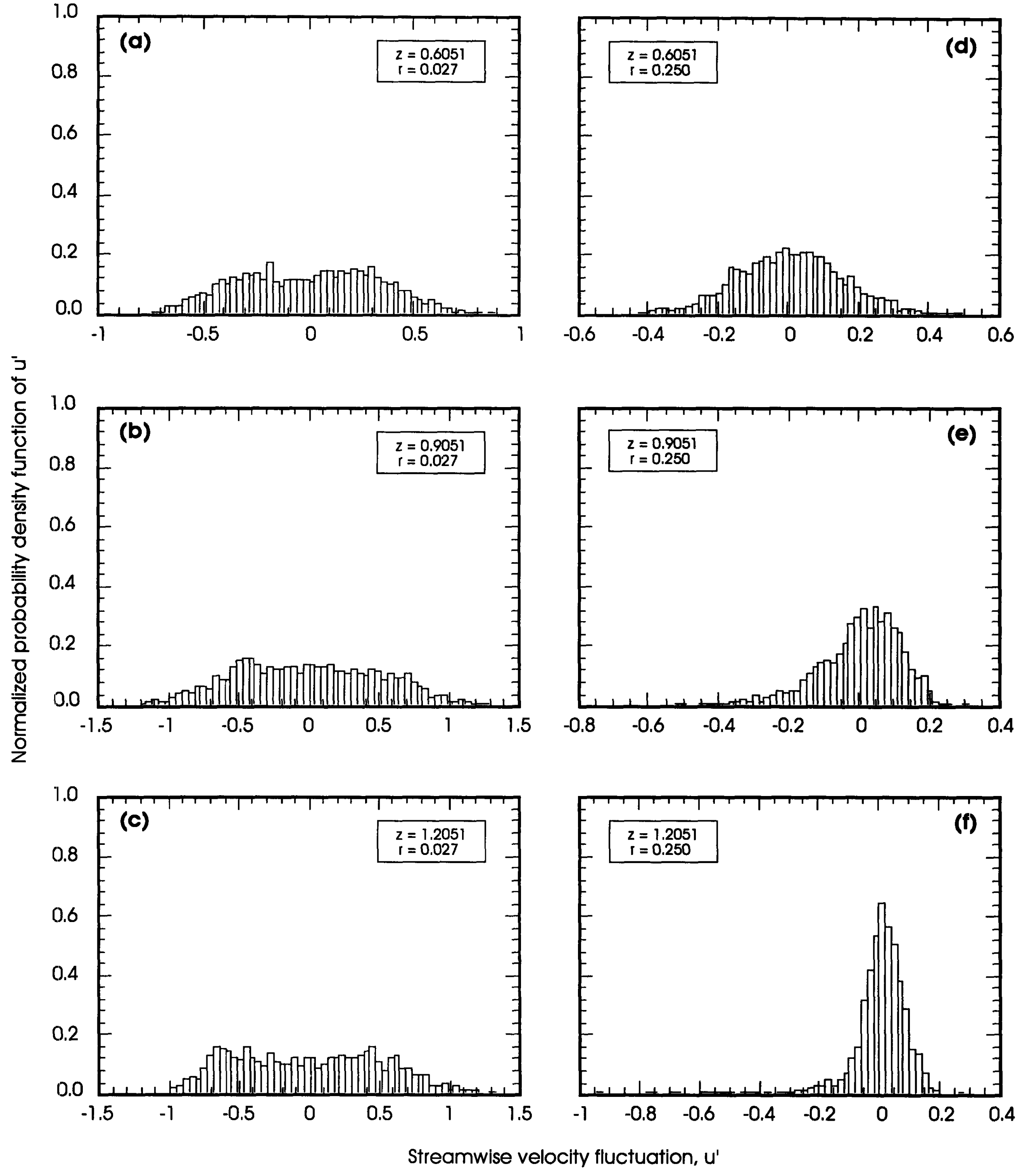

Figure 4.46 Normalized probability density function of u'. Mean value of $U_j/U_a = 2.08$, $S = 0.06$, and $A_f = 0.6$.

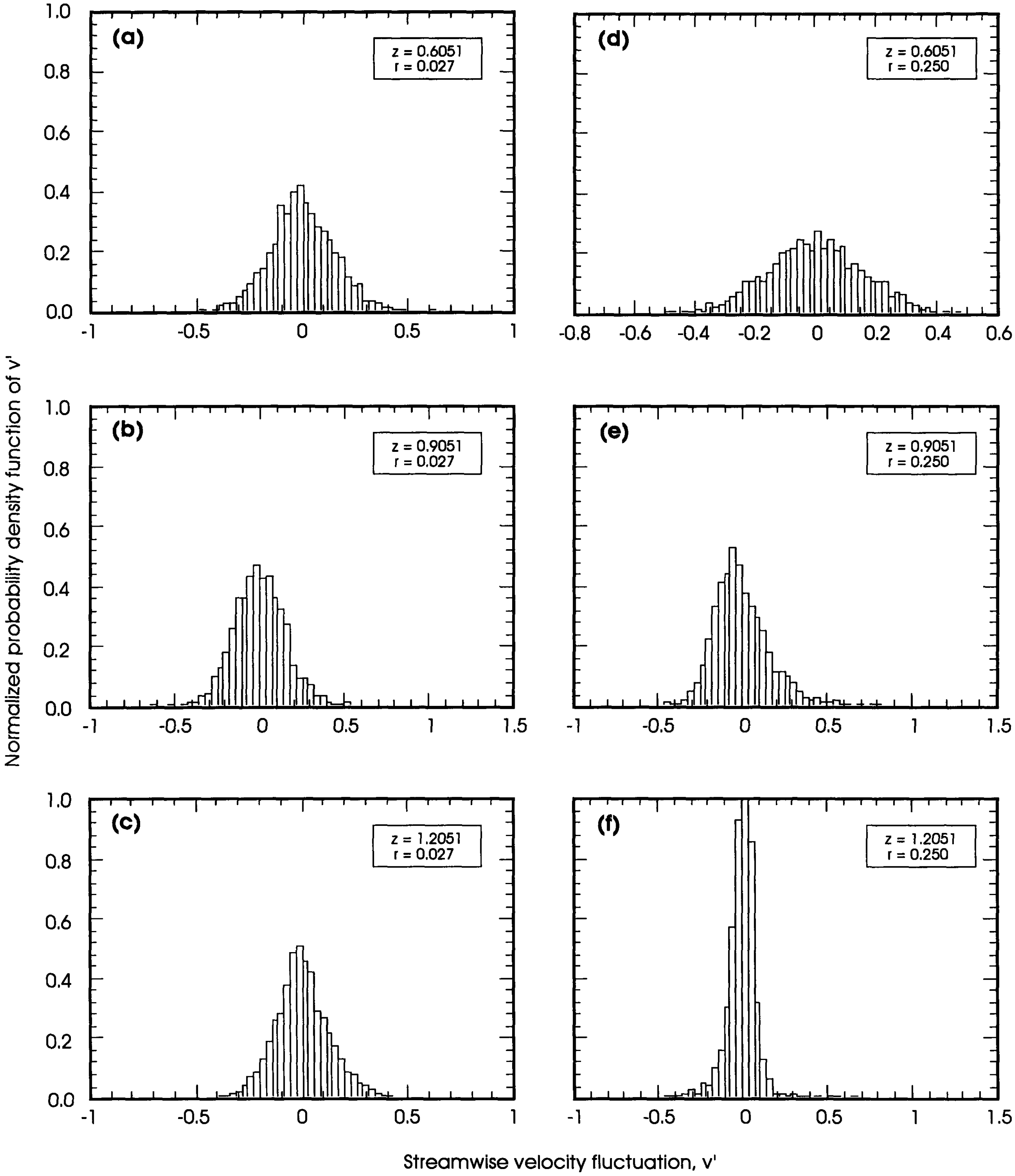

Figure 4.47 Normalized probability density function of v′. Mean value of $U_j/U_a = 2.08$, $S = 0.06$, and $A_f = 0.6$.

4.3.3 VORTEX DYNAMICS AND THE UNSTEADY FLOW PROPERTIES

The discussions in the last two sections have focused on the effects of the externally applied perturbations on the global flow features. Results from the simulations have demonstrated that external perturbation applied at the appropriate frequency and amplitude can lead to the roll up of the jet shear layer near the exit to form large-scale structures and, subsequently, affecting the global mixing field. In this section, we will examine in detail the unsteady flow dynamics and the large-scale entrainment and mixing in the near-wake region as functions of the applied perturbation frequency and amplitude. The main objectives of this section are to highlight the role plays by the jet shear layer in determining the unsteady flow dynamics, and to examine more closely the unsteady response of the recirculation region to external perturbations. In the results to be presented below, we will again discuss the Fourier analyses of the velocity fluctuations in the shear layers as well as the instantaneous flow visualization at selected time steps. For flow visualization, we will rely on the product concentration field, the velocity field in terms of the vortex elements, and the unsteady fluctuation kinetic energy field in order to illustrate the changes in the recirculation-region dynamics due to the forcing of the jet flow. This combination of flow data presentation allows us to correlate and to keep track of the evolution of the coherent vortical structures and the merging patterns of the eddies induced by the external perturbations in the near-wake region.

Let us begin the discussion by examining Figure 4.48, showing the instantaneous mixing field at $t = 22.5$ for all four forcing frequencies studied with a forcing amplitude $A_f = 0.6$. In this figure, frame a shows the mixing field for the unforced case and frames b-e show the mixing fields for the cases with forcing frequencies $S = 0.03$, 0.06, 0.1, and 0.2, respectively. The most notable feature of this figure is the shedding of a large-scale vortical structure from the recirculation region for the case $S = 0.06$ (Figure 4.48c). At this forcing frequency, the instantaneous product concentration along the centerline is seen to decrease quickly with axial distance downstream of the recirculation region, indicating that much of the jet fluid leaving the recirculation region is being engulfed by the large-scale vortical structure; hence, less fuel elements are available to react with the oxidizer elements downstream of the recirculation region. In this case, reaction is seen to occur mostly on the surface of the large-scale vortex. On the contrary, when the inflow boundary condition is steady, the recirculation region is stable and most of the jet fluid escapes the region remains unreacted (Figure 4.48a). In this case mixing and reaction occur mostly downstream of the recirculation region along the axis of the combustor. Hence, high product concentration along the centerline is observed.

When external perturbation is applied to the jet flow, the structure of the recirculation region changes more or less depending on the applied perturbation frequency. Forcing at frequencies $S = 0.03$, 0.1, and 0.2 induces a small increase in the small-scale eddy shedding activities from the outer shear layer. These eddies entrain the jet fluid which has moved radially upward along the face of the bluff body as they are being convected downstream, resulting in mixing and reaction to occur along the outer shear layer as can be seen in Figures 4.48b, d, and e. However, the overall effect of forcing on the stability of the recirculation region is seen to be minimal when the perturbation is applied at these frequencies. Instability in the jet shear layer near the exit did not get amplified significantly when forcing at S = 0.03. As for the higher forcing frequencies (S = 0.1 and 0.2), the disturbances were observed to decay quickly with axial distance and the effect of forcing on the stability of the shear layer is again minimal. However, when the disturbance was applied at the frequency S = 0.06, the instability of the shear layer near the exit was observed to get amplified noticeably. The strong local response to the disturbances in the jet shear layer causes it to roll up near the exit, and generates a distinctive counterclockwise-rotating eddy between the bluff-body face and the air recirculation bubble. Once this eddy is formed, it grows rapidly by the additional entrainment of the jet fluid entering the flow domain. Similar to the two cases with lower velocity ratio, this eddy interacts strongly with the recirculating air eddy and, eventually, causes the merging and the shedding of the large-scale composite structure. Details of the flow dynamics and interaction just described can clearly be seen in Figures 4.44 and 4.50.

The effectiveness of forcing the jet flow alone, in terms of increasing local entrainment and mixing within the recirculation region, also strongly depended upon the amplitude of the perturbation. From the study, it was found that external perturbations applied at an amplitude A_f which is less than approximately 60 percent of the mean value did not significantly affect the near-wake region flow dynamics, regardless of the applied frequency. To illustrate this, Figure 4.49 shows the same time step for the different cases as given in Figure 4.48 but with a forcing amplitude $A_f = 0.3$. Notice that at this amplitude, forcing has very little effects on the stability and the instantaneous flow structures for all forcing frequencies, and the large-scale entrainment in the near-wake region did not seem to get enhanced to any significant degree. The flow exhibits very similar behaviors for all applied frequencies at this forcing amplitude. The ineffectiveness of external perturbations applied at this particular amplitude can also clearly be seen in the time-averaged product concentration contours presented in Figure 4.42.

To further illustrate the effects of external perturbation on the near-wake region dynamics and the large-scale entrainment, Figures 4.50-4.52 highlight the differences of the instantaneous velocity field in terms of the vortex elements, the product concentration field, and the fluctuation kinetic energy field, respectively, between the forced (S = 0.06, $A_f = 0.6$) and the unforced case at several time steps. Interestingly, it is seen that a weak counterclockwise-rotating fuel eddy occurs naturally within the recirculation region for the unforced case (Figure 4.50a). However, the perturbations induced by the existence of this fuel eddy seem to be negligible and are not strong enough to cause instability of the recirculation region. Instead of merging with the air eddy, most of the fluid within the fuel eddy is being forced to move radially upward along the boundary between itself and the outer air eddy, and escapes along the upper shear layer (Figure 4.50b). This process gives rise to mixing and reaction activities along the upper shear layer as well as near the axis of the combustor along the centerline, as shown in the instantaneous product concentration field in Figure 4.51. Notice that in all the time frames presented in Figure 4.50 for the unforced case, the region with the most significant shedding activities is along the upper shear layer. Furthermore, a stable, well-defined recirculation region can be identified at any given instant of time in this case, and shedding of small-scale eddies from the upper shear layer dominates the flow dynamics in the near-wake region.

When external perturbation is applied to the jet flow at dimensionless frequency S = 0.06 and amplitude A_f = 0.06, we see that the relative size and the coherency of the fuel eddy increase significantly. Its existence is also more strongly felt by the recirculation region. The large eddies within the recirculation region in this case are also more distinctive and orderly, and have higher concentration of vorticity. This observation is supported by the vortex element plots, showing the more roll up of the eddies as well as having higher concentration of vortex elements in and around the outer edges of these large-scale structures. Figure 4.51g captures the merging of the fuel eddy with the air eddy within the recirculation region, as commonly seen in the two cases with lower velocity ratio. Forcing the jet flow at this frequency and amplitude enhances the growth of the jet shear layer, causes the layer to roll up and to form periodic coherent structures near the jet exit (this can clearly be seen in Figures 4.51h, i, and j). These large-scale vortical structures entrain much of the jet fluid entering the flow domain and continue to grow in size. As the fuel eddy has grown to a sufficiently large size, the recirculation region becomes unstable and the eddies begin to merge. After the eddies are merged, the composite structure breaks away from the recirculation region, entraining more fluid as it is being convected downstream (Figures 4.51h, i, and j). Notice that the eddy also remains coherent for a significant downstream distance after it is being shed. Meanwhile, a newly generated air eddy is seen to occupy the recirculation region.

From the simulations, it was noted that the shedding of large vortical structures from the recirculation region with forced inflow boundary condition is quasi-periodic in phase with the forcing frequency, which can also be seen clearly from the power spectral density plots presented in Figure 4.53. The coordinates of the sampling locations in these plots are exactly the same as those for the unforced case. Therefore, it is possible to see the effects of forcing on the characteristics of the eddies within the shear layers (see Figure 4.35 in Section 4.2.4). Examining the power spectra along the jet shear layer for the unforced case, we see that there are large number of high-frequency peaks in the power spectra (Figure 4.35a, b, and c), indicating that the existence of a wide range of small-scale eddies moving along the jet shear layer within the recirculation region. Forcing the jet flow causes organization and the coalescence of these small-scale eddies within the shear layer to form large-scale structures in phase with the forcing frequency. Notice that forcing also causes the energy of the power spectra to shift toward 0.06 in the upper shear layer, as can be seen in Figures 4.53d, e, and f.

The effects on the dynamics of the large-scale entrainment in the near-wake region can also be seen in the unsteady product concentration field. For the unforced case, Figures 4.51a-e show sharp irregular boundaries in terms of the product concentration along the axis of the combustor separating the central jet from the surrounding air. Looking down the time series, we see that the radial spread of the mixing zone is relatively constant with time and no significant large-scale entrainment activity is observed. However, these time series clearly show evidence of the presence of small eddies rolling along the shear layer of the jet. In this case, air flow penetration into the fuel jet is minimal. Examining the time series on the right-hand side of Figure 4.51 for the forced case, we see that a very different flow dynamics and large-scale entrainment in the near-wake region from the unforced case. Owing to the growth of the fuel eddy and the subsequent merging and ejection of the composite structure from the recirculation region, we see that a significant amount of fuel are entrained by the large-scale eddy as it is moving away from the recirculation region. Notice that the region along the axis of the combustor downstream of the recirculation region is almost void of products after the passage of the large composite structure (Figure 4.51j), providing more evidence that most products are carrying away by the large-scale vortical structure in this case.

Finally, Figure 4.52 shows the effects of forcing on the unsteady fluctuation kinetic energy. As discussed before, at this inflow velocity ratio the unsteady fluctuations within the recirculation region are much less intense than the two cases with lower velocity ratio, which can clearly be seen in Figure 4.38 as well as in Figures 4.52a-e. In this case, regions with high fluctuation kinetic energy within the recirculation region are found mostly along the shear layer between the jet flow and the clockwise-rotating air eddy a large fraction of the time. Moreover, the unsteady kinetic energy within the recirculation region in this case seems to build up rather slowly, and it affects the stability of the recirculation region insignificantly. The energy dissipates quickly after it is built-up due to the continuous shedding of small-scale eddies from the upper shear layer, rather than causing instability of the recirculation region as in the two cases with lower inflow velocity ratio. Forcing the jet flow causes the increase in the unsteady fluctuations near the centerline. Moreover, the large-scale vortical structures inside the recirculation region induced by this external forcing also accumulate a considerable amount of kinetic energy. This energy is being carried away from the recirculation region as the composite eddy is being shed. Similar to the two cases with lower velocity ratio, the kinetic energy within the recirculation region is observed to decrease to a minimum value after the composite eddy is being shed, and builds up to a maximum value prior to the shedding of the composite structure.

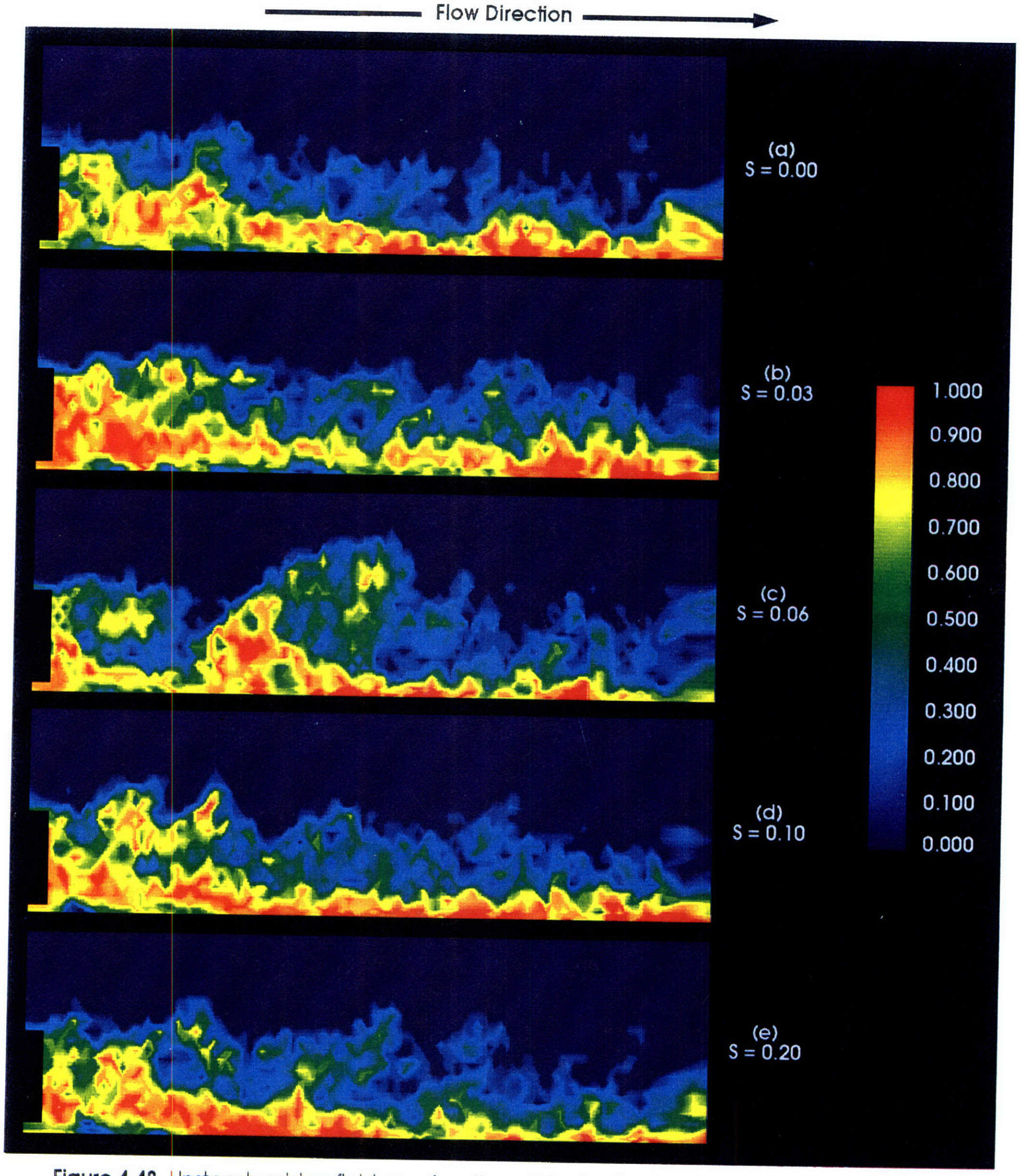

Figure 4.48 Unsteady mixing field as a function of the forcing frequency. Forcing amplitude $A_f = 0.6$, mean value of $U_j/U_a = 2.08$, $t = 22.75$.

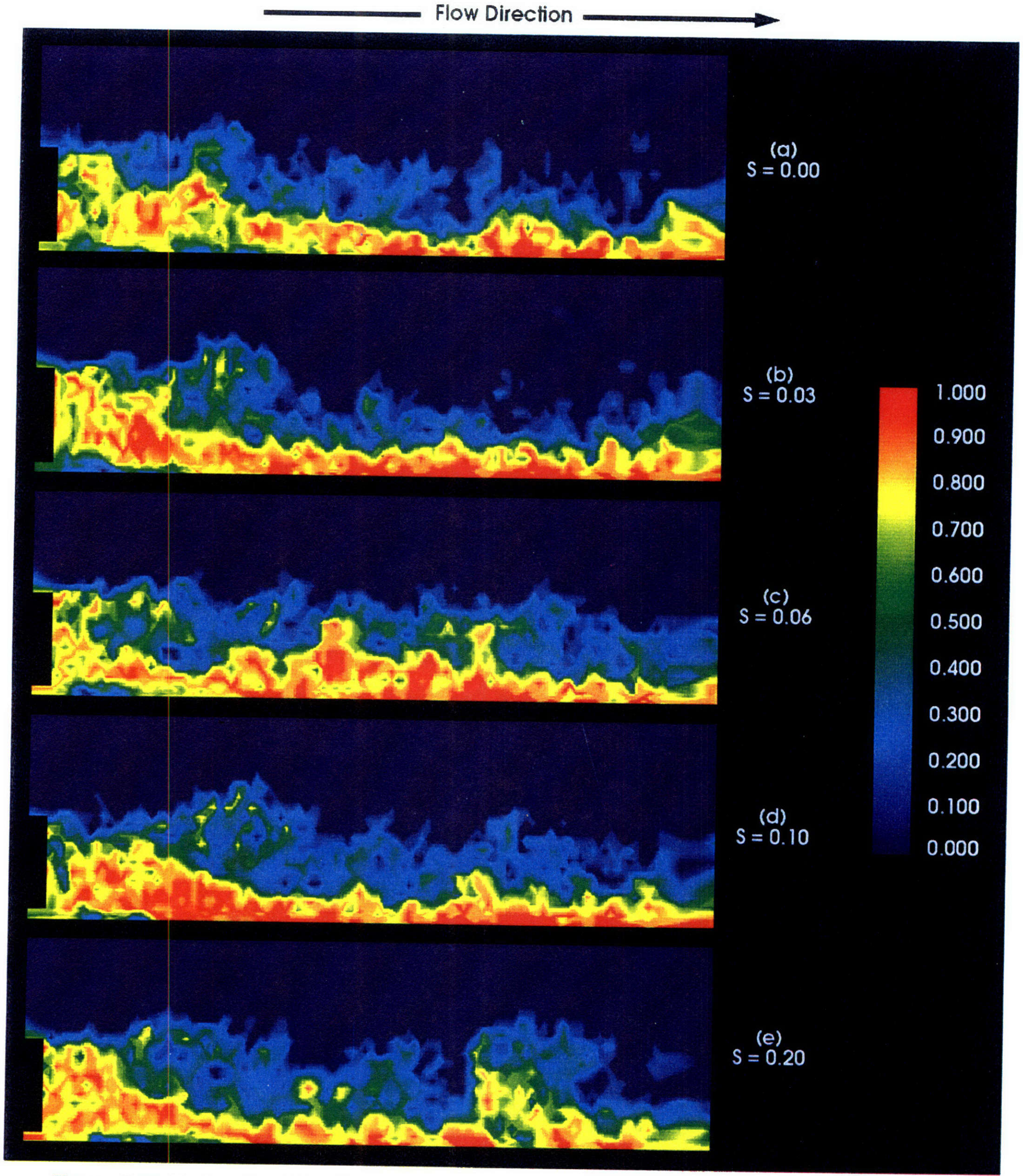

Figure 4.49 Unsteady mixing field as a function of the forcing frequency. Forcing amplitude $A_f = 0.3$, mean value of $U_j/U_a = 2.08$, $t = 22.75$.

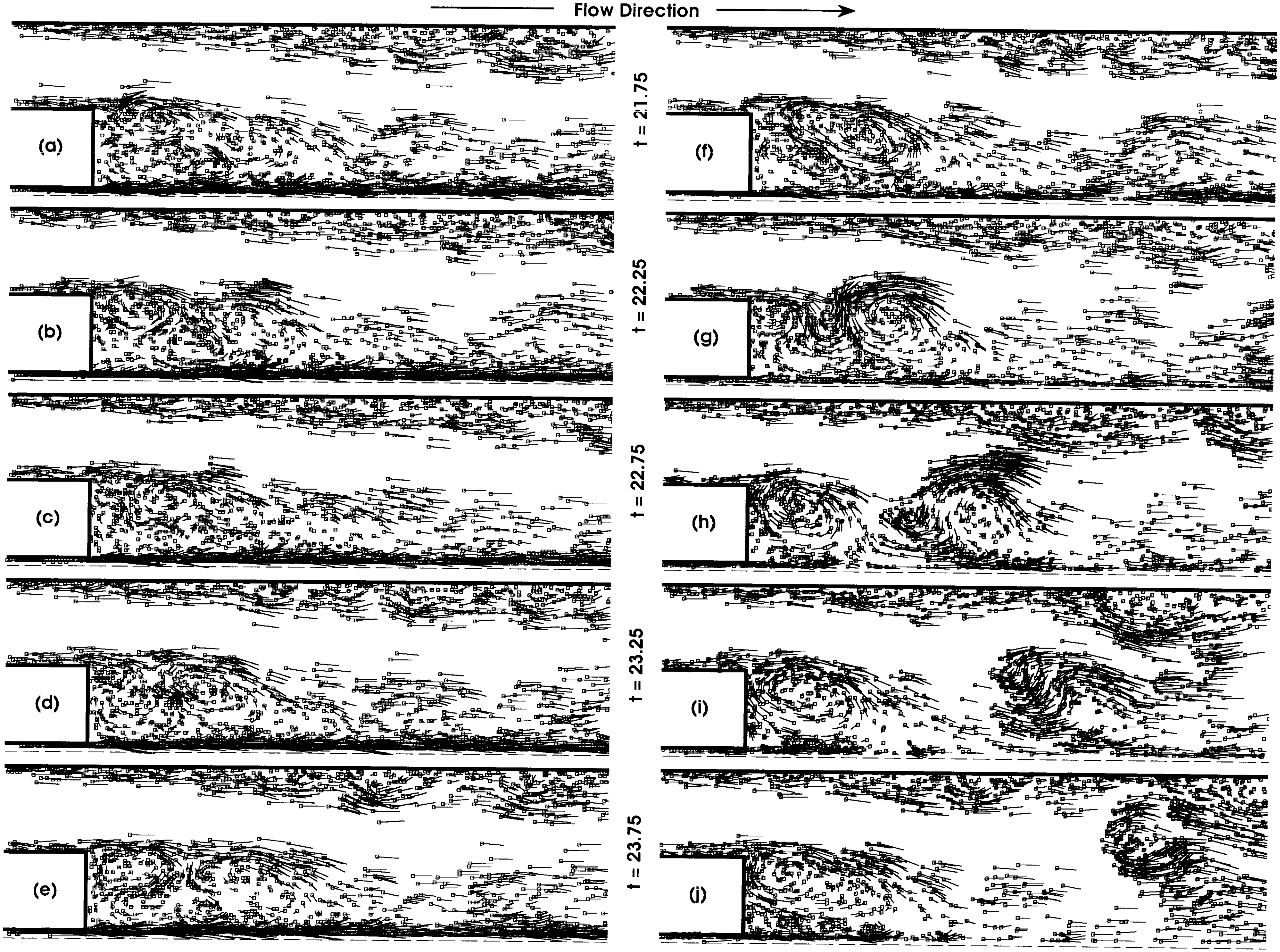

Figure 4.50 A comparison between the unforced and the forced flow dynamics in terms of the vortex elements. On the left, $S = 0.0$, on the right, $S = 0.06$. Mean value of $U_j/U_a = 2.08$. Forcing amplitude $A_f = 0.6$.

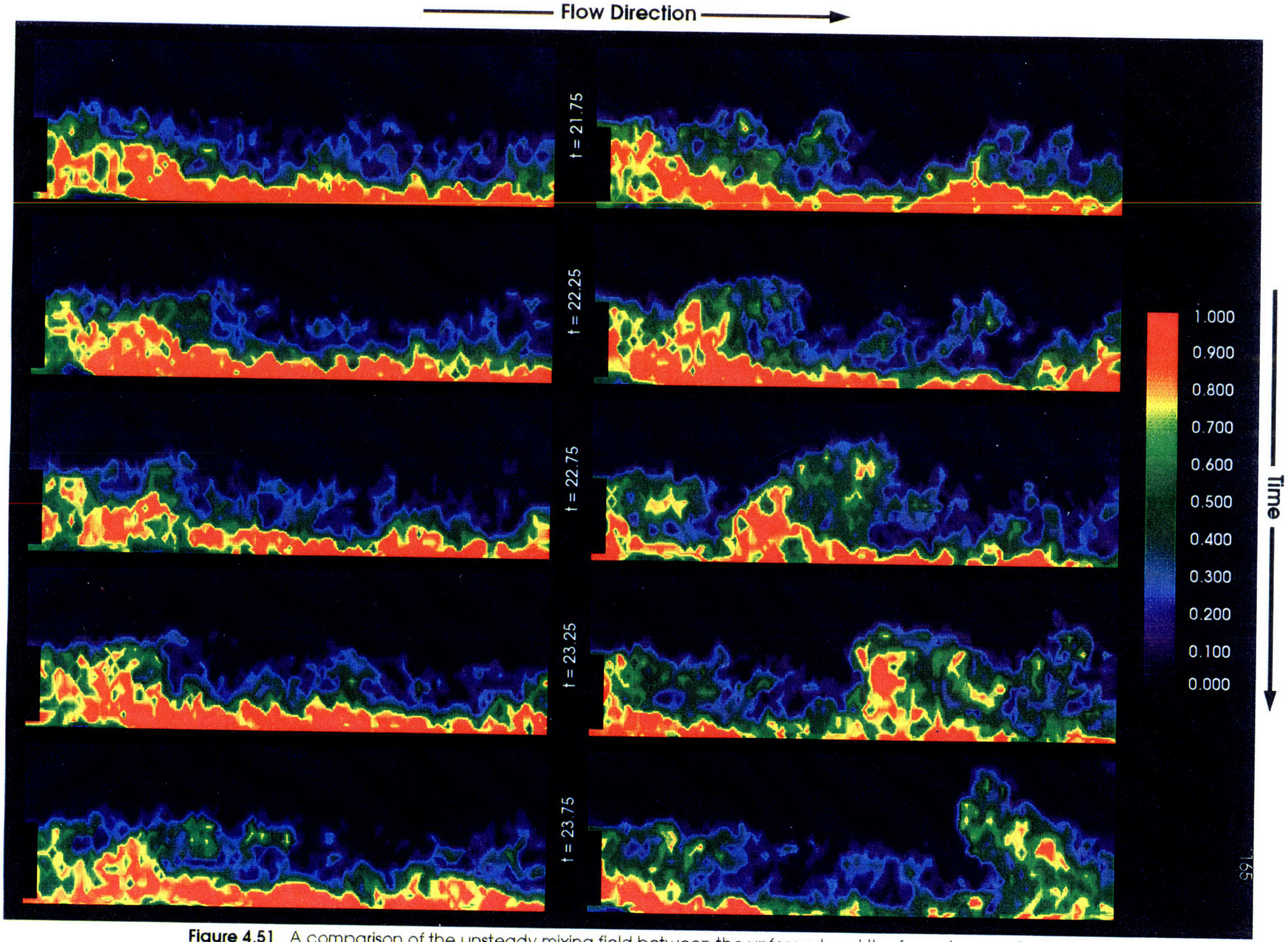

Figure 4.51 A comparison of the unsteady mixing field between the unforced and the forced case. On the left, $S = 0.0$, on the right, $S = 0.06$. Mean value of $U_j/U_a = 2.08$. Forcing amplitude $A_f = 0.6$

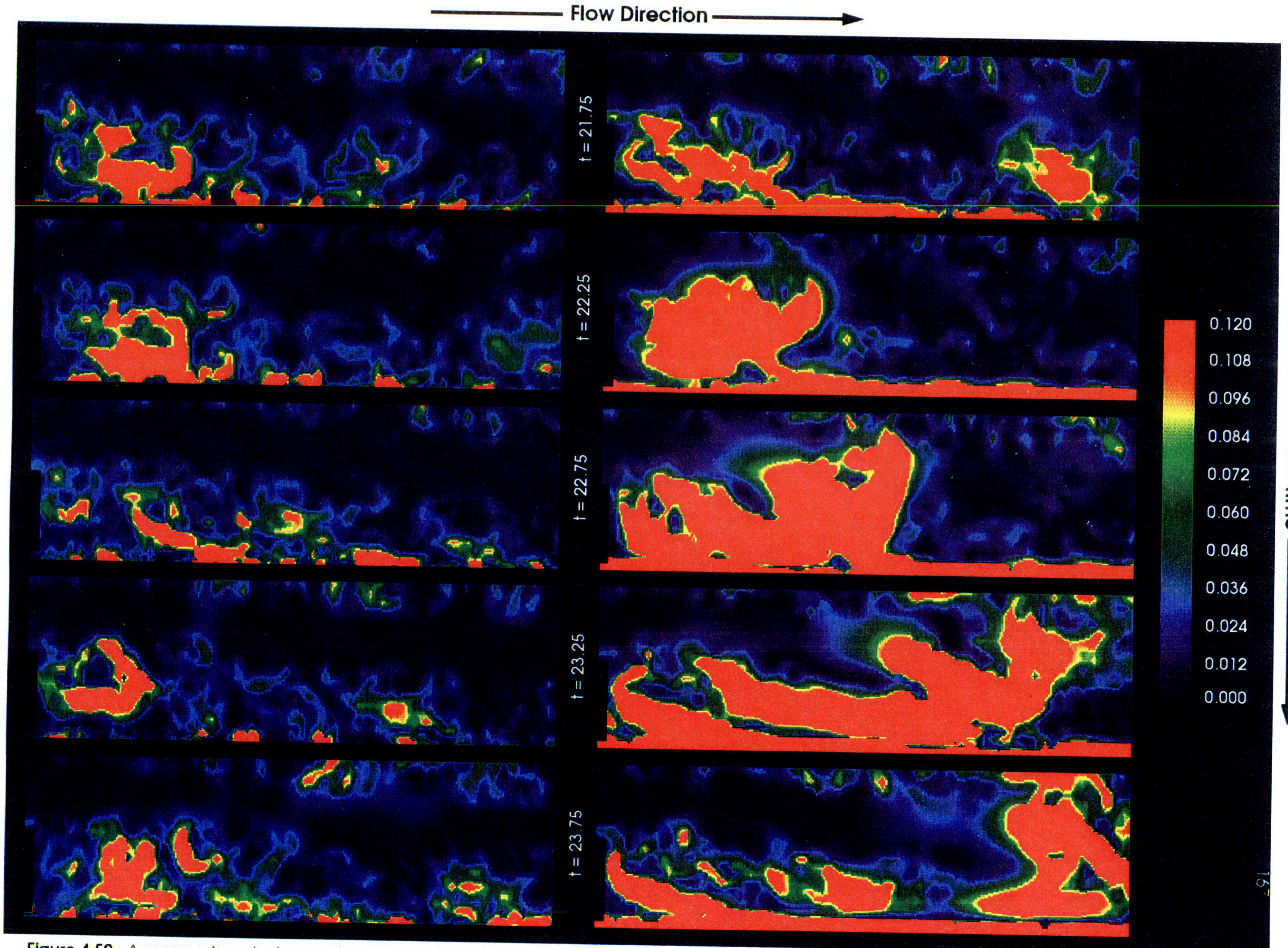

Figure 4.52 A comparison between the unforced and the forced unsteady fluctuation kinetic energy field. On the left, $S = 0.0$, on the right, $S = 0.06$. Mean value of $U_j/U_a = 2.08$. Forcing amplitude $A_f = 0.6$.

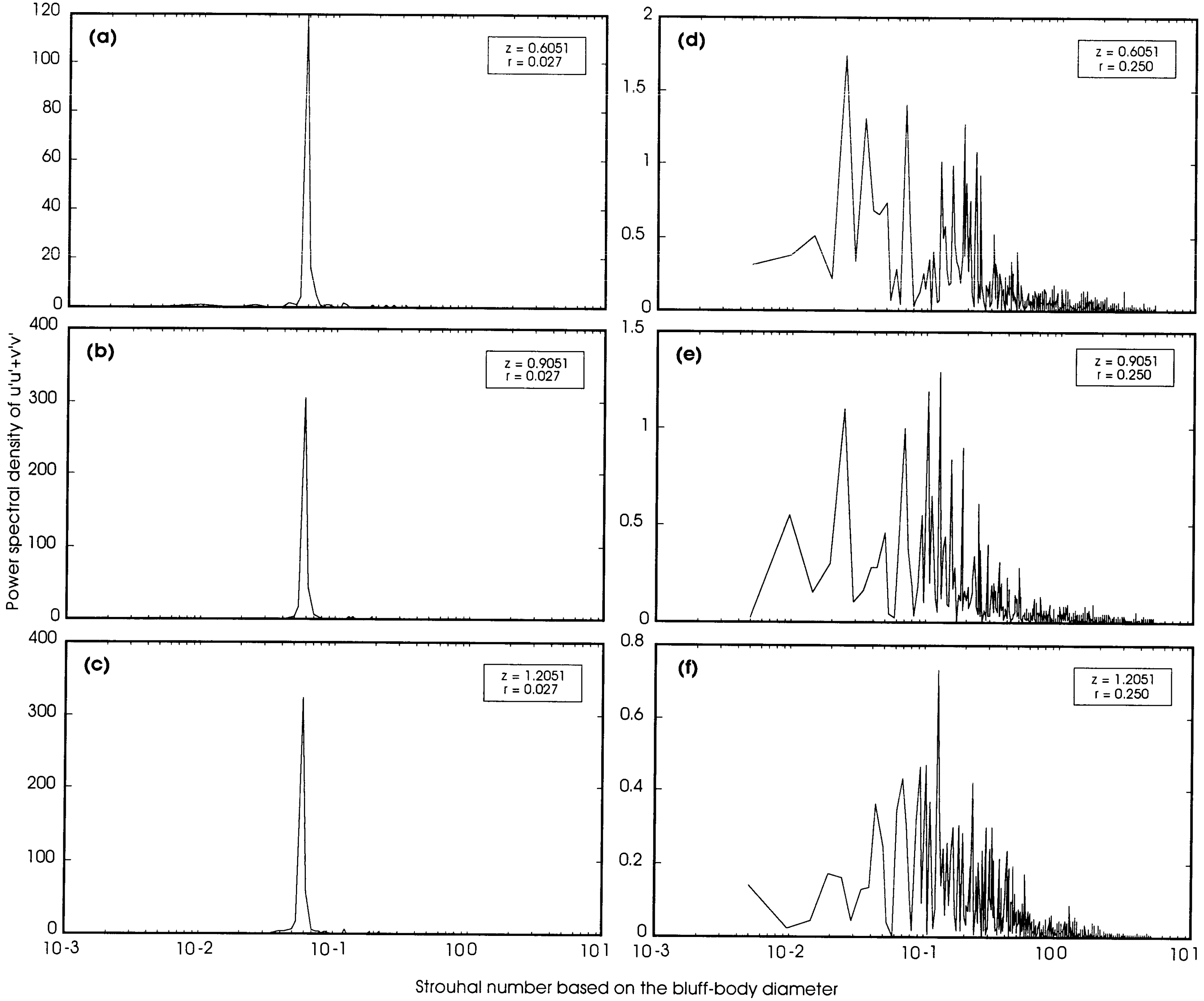

Figure 4.53 Power spectral density of u'u'+v'v'. Mean value of U_j/U_a = 2.08. Forcing amplitude A_f = 0.6, forcing frequency S = 0.06.

4.4 CONCLUSIONS

Axisymmetric vortex-scalar element method has been used to study the unsteady isothermal reactive flow in a two-stream, coaxial-jet, axisymmetric bluff-body combustor as a function of inflow velocity (momentum) ratio. The vortex method solves the vorticity transport equation at moderate-to-high Reynolds number without resorting to turbulence closure models. Scalar elements are used to transport the scalar concentration fields. The assumption of infinite-rate kinetics is used to model chemical reaction and to calculate the rate of product formation. Since the unsteady dynamics of the mixing field are known to be controlled by the large-scale structures to a great extent, and the actual flame length in an exothermic reactive flow is ultimately tied to the amount of mixing can be accomplished within the recirculation region, the investigation concentrated on the large-scale entrainment and mixing in the near-wake region downstream of the bluff body. The effects of the energy released from chemical reaction on the flow dynamics were neglected from the simulations so that the unsteady dynamics of the large-scale entrainment and the global mixing field can be studied in a simpler environment, and a better understanding of the basic mixing mechanisms can be developed. Three cases with three different inflow velocity ratios, U_j/U_a = 0.62, 1.04, and 2.08, were performed for a combustor with diameter ratio D_a/D_b = 2.0. The dynamics of the flow field as well as the large-scale entrainment and mixing were studied under both steady and externally imposed sinusoidal inflow boundary conditions. The followings are observed from the numerical simulations:

1) The complex flow structure in the near-wake region downstream of the bluff body is a dynamically unstable system involving two coexisting and interacting flow instabilities: the shear-layer instability and the recirculation-region instability. The flow in the near-wake region is highly nonhomogeneous and the velocity fluctuations exhibit strong non-Gaussian behaviors in the shear layer between the outer annular flow and the recirculation bubble, and between the recirculation bubble and the central jet. The PDFs of u' are mostly single-peaked and positively skewed in the jet/recirculation shear layer, and are negatively skewed in the recirculation/annular-flow shear layer. In the jet shear layer close to the stagnation region, the distributions are bimodal. This highly non-Gaussian behaviors of the velocity PDFs within the shear layers can be attributed to the existence of large-scale coherent structures within the shear layers, and they become more pronounced as one moves further downstream within the recirculation region. In general, the velocity fluctuations are in the opposite direction of the mean velocity.

2) The distribution of the unsteady fluctuation kinetic energy, $u'u' + v'v'$, in the flow field is highly nonuniform and discrete, with most of the energy being concentrated in the well-defined, large-scale vortical structures and the shear layers within the recirculation region. Instability of the recirculation region begins as the eddies within acquire fluctuation kinetic energy. The maximum amplitude of the fluctuations reaches its peak value prior to the shedding of the composite flow structures, and decays quickly after the eddies are being shed from the recirculation region. The large composite eddies being ejected from the recirculation region

retain their identities as well as their energy levels even at a large distance downstream of the recirculation zone.

3) The overall characteristics of the mixing field are controlled by the large-scale eddies, especially in the recirculation region. Reaction occurs mostly on the surfaces of these eddies as they entrain and mix the reactants. The quasi-periodic shedding of the large-scale coherent structures from the recirculation region strongly resembles the intermittent and discrete combustion processes in the exothermic reactive-flow experiments conducted by Roquemore *et al.* [119]. While the thermal energy released from combustion may affect the shedding frequency, the growth rate, or the size of the large-scale eddies generated inside the recirculation region, results from the simulations suggest that the mechanisms affecting the mixing field in the near-wake region are strongly tied to the instability of the recirculation region and to the inflow velocity ratio.

4) When the momentum of the central jet is weak relative to the recirculating flow, a short, compact mixing zone confined mainly to the near-wake region with quasi-periodic shedding of large-scale, reactive-flow structures from the recirculation zone is observed. As the velocity ratio is increased, an intermittent pulsating and reacting jet, extending several bluff body diameters downstream of the recirculation region, is noted in addition to the quasi-periodic shedding of reactive flow structures from the recirculation region. For the case with the highest velocity ratio, the recirculation region becomes relatively stable and the flow experiences less fluctuation and entrainment. In this case, shedding from the recirculation region is less frequent, and most of the jet fluid is confined to a narrow region close to the centerline where mixing and reaction are most intense.

5) Results from the periodic forcing study have shown that a preferred-mode coupling exists between the forced jet and the large-scale structures of the recirculation region. Time-averaged product concentration field indicates that the length of the mixing zone depends on the forcing frequency, as long as the pulse amplitude exceeds a minimum threshold to affect the stability of the shear layer near the jet exit. For the case with $U_j/U_a = 2.08$, it was found that controlled excitation amplifies the inherent recirculation zone dynamics, and as this amplification approaches the natural shedding frequency of the recirculation zone eddies, it causes instability in the otherwise stable recirculation region. This process produces interactions within the recirculation region similar to those occurring naturally in the two lower velocity cases. The most notable changes to the mixing field in the near-wake region was observed when the central jet was being forced at a dimensionless frequency based on the magnitude of the annular inflow velocity and the bluff-body diameter of $O(0.06)$, with forcing amplitude $A_f \geq 0.6$. Forcing the jet flow at this frequency and amplitude destabilizes the jet shear layer and increases the local entrainment and mixing of the jet flow near the exit in two ways. First, the process enhances the growth of the jet shear layer by amplifying the vortex structures in the shear layer, causing it to roll up and to form a counterclockwise-

rotating eddy. This eddy entrains most of the jet fluid entering the flow domain and interacts strongly with the recirculating air eddy. In addition, the unsteady energy added to the flow from forcing increases the fluctuation kinetic energy in the recirculation region. This process causes interaction among the large-scale flow structures within the recirculation region and, eventually, leads to the shedding of composite eddies from the recirculation region similar to the flow dynamics observed in the two cases with lower inflow velocity ratio.

5. EXOTHERMIC REACTIVE-FLOW SIMULATION

The main focus of the isothermal reactive-flow study presented in Chapter 4 is on the unsteady flow dynamics of the near-wake region downstream of the bluff body as a function of the inflow velocity (momentum) ratio. The dynamics of the recirculation region as well as the large-scale entrainment and mixing were studied under both steady and externally imposed sinusoidal inflow boundary conditions. The unsteady mixing process was investigated by assuming a fast second-order chemical reaction of the form $F + O \rightarrow P$ with negligible heat of reaction so that the dynamics of the unsteady large-scale entrainment and the global mixing field can be studied in a simpler environment, and a better understanding of the basic mixing mechanisms can be developed. In all the flow simulations, dilute fuel F and oxidizer O were added to the jet stream and the annular flow, respectively. Once inside the flow domain, the reactants, F and O, were assumed to react instantaneously and irreversibly upon contact with one another to form products, P. This simplified model leads to a diffusion-limited reaction, and the amount of products formed is directly proportional to the rate of consumption of the lean reactant F. Thus, the product concentration found within a small sample volume at any given time provides an approximation to the local instantaneous mixing rate. Despite the simplicity of the model, it is sufficiently accurate to be used for describing the mixing process. The study has given important physical insight into the process by which the large-scale vortical structures entrain fluid in the near-wake region and, subsequently, enhance the overall mixing. However, since the thermal energy released from combustion was neglected in the simulations, the chemical reaction was a passive process and did not influence the unsteady dynamics of the fluid motion. Thus, the role played by the thermal energy released from combustion on the development of the large-scale structures and the mixing field was not addressed by the simulations. From two-dimensional exothermic reactive shear layer studies, it is well-known that, in general, thermal energy released from combustion decreases the size of the shear layer mixing region via delaying the onset of the flow instability, and the suppression of eddy pairing. The changes in the unsteady flow dynamics, together with the decrease in fluid density within the mixing region, lead to significant reduction in product formation within the shear layer [95, 134]. Thus, it is expected that if the thermal energy released from chemical reaction is taken into consideration in our flow simulations, it would have similar effects on the flow dynamics and the mixing zone. In this chapter, we will again examine the flow dynamics and the large-scale entrainment and mixing while considering the effects of the thermal energy on the flow dynamics in terms of the expansion velocity alone. It is anticipated that the large-scale dynamics, which have already been shown to be quite important in the isothermal reactive flow study, will continue to be important in the exothermic reactive flow.

In an exothermic reactive flow, the unsteady dynamics of the fluid motion are highly coupled to the chemical reaction. The combustion process is generally influenced by the hydrodynamic field through such effects as strain rate, flame stretching, and curvature. The hydrodynamic field is, in turn, affected by the combustion process through volumetric expansion and baroclinic vorticity generation, among others [147]. It is this complicated close coupling and feedback between the flow and the chemistry that makes the analytical or numerical solution of the governing equations for a turbulent reactive flow a daunting task. Despite extensive research effort, no realistic solution of the turbulent flame equations has yet been achieved even after major simplification, nor is it likely to be, in the near future. Over the years, researchers have instead devoted great effort to developing simplified models to analyze flows in which only certain flow-combustion coupling mechanisms are considered significant. This effort had led to a substantial body of useful knowledge about the individual and collective effects of the flow-altering mechanisms induced by the thermal energy on the flow dynamics [11, 32, 42, 43, 49, 51, 134].

Owing to the fast-chemistry assumption and the unique flow configuration used in this research, in general, most fuel being injected into the flow domain reacts inside the recirculation region within a short distance downstream of the jet exit (except for the case $U_j/U_a = 2.08$). Under this flow condition, the release of thermal energy and the combustion-related density gradient are mainly confined to the near-wake region. Volumetric expansion of the fluid within the recirculation region induces a radial velocity component on the fluid elements, and causes the direction of the density gradient to point more or less radially outward from the center of the recirculation zone. The baroclinic torque, $(\nabla\rho \times \nabla p)/\rho^2$, describing the differential fluid accelerations resulted from the nonaligned pressure and density gradients in the flow field, can alter the vorticity field significantly under certain flow conditions. However, in this case most of the fuel reacts within the near-wake region and is quickly diluted by the excess air before leaving the recirculation region. Compared to the volumetric expansion, the effect of the baroclinic vorticity generation is mostly localized and has little impact on the overall vorticity dynamics. The flow field in the near-wake region is affected most significantly by the nonhomogeneous density distribution caused by the thermal expansion of the fluid. In order to simplify the solution procedure, we will neglect the baroclinic vorticity generation term in the governing equations and include only the expansion velocity term in this study. Furthermore, in this research we are mainly interested in the aerodynamic aspects of the flow rather than the chemical kinetics or the reaction mechanisms. For the sake of simplicity, we will also neglect the effects of the hydrodynamics on the combustion processes; namely, the effects of strain rate, flame stretching and curvature will not be considered in the simulation. Thus, the issues of ignition and flame extinction also will not be addressed in this exothermic reactive-flow study. Although many interesting features of real exothermic reactive flows can no longer be captured by this simplified model, many significant effects of the exothermic reaction on the flow dynamics can still be studied. In the following section, we will present the results obtained from the exothermic reactive-flow simulation, and discuss the effects of the expansion velocity on the unsteady flow dynamics and the large-scale entrainment and mixing. Qualitative comparisons with the isothermal reactive flow simulations presented in Chapter 4 and with experimental data will be made where applicable.

5.1 LARGE-SCALE DYNAMICS UNDER THE ASSUMPTION OF EXOTHERMIC REACTION WITH STEADY INFLOW BOUNDARY CONDITION

For this exothermic reactive-flow study, we consider the case with inflow velocity ratio U_j/U_a = 1.04. This particular case is selected for this study because the characteristic flow dynamics at this velocity ratio were observed to encompass the distinctive flow features of the other two cases in the isothermal reactive-flow study; namely, intense interaction between the fuel eddy and the air eddy within the recirculation region leading to periodic shedding of composite structures, and the penetration of the recirculation zone by the fuel jet (see Figure 4.27). Since the primary goal of this exothermic reactive-flow study is to determine the implication of the expansion velocity on the overall flow dynamics and the subsequent effects on the unsteady entrainment and mixing in the near-wake region, the investigation will be conducted by examining the flow with steady inflow boundary condition only. This way, the effects of the volumetric expansion on the unsteady dynamics of the recirculation region can readily be isolated and studied in a simpler environment. Furthermore, results from the simulation may be used to compare with the dynamics of the isothermal reactive-flow study discussed in Chapter 4.

As seen in the last chapter, the unsteady dynamics and the characteristic flow features of the recirculation region are most apparent in terms of the large-scale vorticity dynamics. Thus, we begin the discussion of the effects of the expansion velocity on the unsteady flow dynamics by first examining the velocity field in terms of the vortex elements. Examining the vorticity dynamics first allows us to obtain a global description and visualization of the impact of heat release on the flow directly in terms of the large-scale unsteady flow dynamics. It also provides us with a quick qualitative answer to the question of how the stability characteristics of the recirculation region are affected by the release of thermal energy within the region before we study the details of the unsteady mixing field.

A brief review of the characteristic flow features when the reaction is isothermal seems to be the most appropriate starting point for the discussion of the dynamical implication of the heat release on the recirculation region and the large-scale entrainment. After this brief review, the extent to which volumetric expansion alters the unsteady flow dynamics and the large-scale entrainment and mixing should readily be identified and isolated during the discussion of the exothermic reactive flow field.

In terms of the vortex elements within the interior of the flow domain, the sequence of time frames presented in Figure 5.1 illustrates the interaction between the jet and the annular air eddy within the recirculation region of the isothermal reactive flow. This strong interaction leads to the formation and, subsequently, the shedding of the composite structure from the recirculation region. It should be noted that in these vortex-element plots, the same notation used in the previous chapter also applied; namely, the instantaneous position of a vortex element is depicted with a small square, and its velocity vector is delineated by a straight line segment originating from the center of the square. Upon a careful inspection of this series of time frames, we see that the significant event within the recirculation region begins with the instability and the roll up of the jet shear layer to form a counterclockwise-rotating fuel eddy a short distance downstream of the jet exit. This eddy grows steadily in size as it continues to entrain more and more of the jet fluid entering the flow domain (Figure 5.1a). The remaining jet fluid not entrained by the fuel eddy penetrates and escapes the recirculation region along the centerline of the combustor in discrete bursts due to the unsteady motion of the recirculating air eddy. As the size of the fuel eddy continues to grow from the entrainment of more fluid delivered by the jet shear layer, it begins to occopy most of the space within the recirculation region and pushes the air eddy radially outward and away from the face of the bluff body (Figures 5.1a and b). This action marks the onset of the instability within the recirculation region. Eventually, the strong interaction between the two eddies leads to the merging of the eddies (Figure 5.1c) and, subsequently, the shedding of the composite structure from the recirculation region (Figures 5.1d and e). Meanwhile, the roll up of the outer annular flow shear layer creates a new recirculating air eddy. The entrainment of the jet fluid into the counterclockwise-rotating eddy downstream of the jet exit sets the stage for a new shedding cycle (Figures 5.1 e and f). This complicated unsteady shedding dynamics of the recirculation region is found to be quasi-periodic, and all the events associated with a single period are observed to repeat more or less in every shedding cycle.

Certain characteristic flow features of this isothermal reactive flow are noteworthy and should be pointed out here so that we can compare them with the exothermic reactive flow presents in Figure 5.3. First and foremost, a common characteristic shared by all the eddies in this isothermal reactive flow is that the eddies are coherent, and they all possess substantial amount of vorticity, as can be seen from the tightly roll-up of the eddies and the high concentration of vortex elements distributed within and on the surfaces of these large-scale structures. The air eddy and the fuel eddy inside the recirculation region before the pairing are distinctive, and the sizes of these two eddies are comparable. The structure of the recirculation region is seen to be well-organized and is mainly composed of these large-scale, oppositely rotating structures. After being shed from the recirculation region, the composite eddy remains coherent, and retains its identity for significantly large distance downstream of the bluff-body face. Within the shear layer in between the annular flow and the recirculation bubble, shedding activities are less prominent in this case, as most of the small-scale eddies in the shear layer are engulfed by the recirculating air eddy. Inside the recirculation region, the air eddy is usually the dominant flow structure before the fuel eddy has grown to a comparable size to affect the stability of the region. The growth of the fuel eddy in between the bluff-body face and the recirculating air eddy is clearly the primary destabilizing mechanism of the recirculation region. The unsteady reattachment point of the outer shear layer can usually be found at a distance slightly greater than a bluff-body diameter downstream of the bluff-body face, and the unsteady dynamics of the near-wake region are dominated by the interaction and shedding of the composite structure from the recirculation region. Mixing between the fuel and the oxidizer is largely accomplished by the merging of these two oppositely rotating large-scale structures. Since the inflow boundary condition is steady and the white noise associated with the random-walk diffusion has no preferred frequency, the unsteady dynamical events observed here are natural to this unique flow configuration with this inflow velocity ratio. These natural large-scale shedding dynamics are also captured by the power spectra present in Figure 5.2. From this figure, we see that the significant Strouhal numbers for this flow at the given velocity ratio included the well-known bluff-body shedding frequency, $S \sim 0.15$, as well as the frequency associated with the shedding of the composite structures, $S \sim 0.06$, as one moves downstream toward the end of the recirculation region (Figure 5.2f). These two Strouhal numbers, which are the fundamental frequency and its first subharmonic, respectively, have been observed in numerous experimental and numerical studies involving a wide range of bluff-body-to-jet diameter ratios and inflow velocity ratios [52, 53, 85, 93, 103, 118, 119, 120]. Notice that all the dominant peaks of the spectra in these plots are narrow and sharp, indicating the high energy contents of the large-scale eddies associated with these frequencies.

When the reaction is exothermic, volumetric expansion induces an expansion velocity field which is superimposed on the rotational vortical flow structures. As a consequence of this expansion velocity, the large-scale eddies in the exothermic reactive flow appear more diffuse, and their rotational rates decrease significantly. The entire structure of the recirculation region is slightly elongated, with the major axis of the structure becomes more aligned with the streamwise coordinate. A sequence of time frames showing the unsteady dynamics of the near-wake region in terms of the vortex elements for the exothermic reactive flow is presented in Figure 5.3. Comparing the two series of time frames presented in Figures 5.1 and 5.3, we see that many of the global characteristic flow features observed in the isothermal reactive flow also appear in the exothermic reactive flow. The large-scale vortical structures, although appear more diffuse and less orderly, are still very much discernible within the recirculation region of the exothermic reactive flow. Similar to the isothermal reactive flow dynamics, from Figure 5.3, we see that eddies are continuously being shed from the outer edge of the bluff body and the large-scale vortices interact vigorously with one another within the recirculation region. These large-scale vortices grow by entrainment and pairing, then detach from the recirculation region and are being convected downstream as distinct units of vortical structures. The exothermic reactive flow does differ, however, from the isothermal reactive flow in many subtle aspects, as can be seen by a careful comparison of the time-dependent flow structures of the near-wake region between Figures 5.1 and 5.3. One of the most apparent differences between the two flows is the maximum amplitude of the large-scale eddies' vorticity, found mainly in the vortex cores, has decreased substantially in the exothermic reactive flow. All the large-scale structures within the recirculation region as well as the shed eddy are more diffuse, and have much less concentration of vorticity than their counterparts in the constant-density case. Furthermore, the eddies within the exothermic reactive flow appear to be slightly flatten by the expansion velocity, and the major axes of these elliptical flow structures become more aligned with the streamwise coordinate (compare the composite eddy between Figure 5.1d and Figure 5.3e). As discussed at the beginning of this chapter, the most significant flow mechanisms altering the vorticity field in an exothermic reactive flow are the baroclinic vorticity generation and volumetric expansion. However, since the baroclinic vorticity generation term has been neglected in the present simulation, the changes of the vorticity field seen here are effectively caused by the volumetric expansion alone. The observed changes of the unsteady vorticity dynamics can qualitatively be explained as follow. The fluid density in an incompressible isothermal reactive flow remains constant with time and the flow has zero divergence. However, for an exothermic reactive flow, the divergence of the velocity field, $\nabla \cdot \mathbf{u}$, is positive. It is the volumetric expansion of the fluid that causes the decrease in the magnitude of the vorticity. This phenomenon can easily be understood by the angular-momentum consideration. As a rotating fluid element expands from the absorption of thermal energy released from combustion, its angular momentum is redistributed over a larger area. Thus, the magnitude of its local rotational rate, hence its vorticity, must decrease in order to conserve angular momentum, everything else being equal.

Thermal energy released from combustion also affects the maximum size of the air eddy within the recirculation region. Compared with its isothermal counterpart, the maximum size of the air eddy in the exothermic reactive flow is slightly reduced due to the presence of a significantly thicker jet shear layer, which takes up much of the space within the recirculation region. The roll up of the jet shear layer to form a counterclockwise-rotating fuel eddy can be seen in Figure 5.3a upon a careful inspection of that time frame. However, as soon as the fuel elements within the eddy come into contact with the oxidizer elements in the air eddy, chemical reaction occurs and the resulting expansion velocity diminishes the vorticity of the fuel eddy to the point that it becomes almost undetectable (Figures 5.3b and c). In addition to the expansion velocity, the existence of an expanded jet shear layer within the recirculation region pushes the air eddy radially outward and away from the face of the bluff body. Thus, the unsteady reattachment point of the outer shear layer is being moved further downstream, resulting in a slightly longer unsteady recirculation region for the exothermic reactive flow (compare the recirculation region of Figures 5.1b and c with Figures 5.3b and c). Unlike plane shear layers, however, the release of thermal energy in this flow configuration did not significantly dampen the instability of the recirculation region as initially expected (at least for the case of low heat release studied here[1]). This is due to the fact that the unsteady flow structure of the recirculation region is dominated by a highly unstable two-eddy dynamical system in this case. In the isothermal reactive flow, instability of the recirculation region was initiated by the growth of the fuel eddy between the jet shear layer and the recirculating air eddy. These two eddies have opposite-sign vorticity and they interact strongly with one another within the recirculation region. The interaction of these two eddies leads to the shedding of the composite structure from the recirculation region, which has a Strouhal number of $O(0.06)$ associated with the shedding process. The same destabilizing mechanism is also observed in the recirculation region of the exothermic reactive flow. However, owing to the additional expansion velocity and the existence of a relatively thick jet shear layer within the recirculation region displacing the air eddy further downstream, the instability of the composite structure is observed to occur sooner in the exothermic reactive flow, resulting in a slightly higher characteristic frequency associated with the shedding process. This observation can clearly be seen in the power spectra of the flow presented in Figure 5.4. Comparing the plots in Figures 5.2 and 5.4, we see that the corresponding power spectra of these two cases are very similar except that for the exothermic reactive flow, heat release seems to dampen certain high-frequency

---

[1] One-half of the lower heating value (LHV) of methane was used as the heat of reaction in the calculation ($2.5\times10^{7}\mathrm{J/kg}$). The maximum temperature rise was about 1160 K (less than 2 percent of the time in the whole simulation) and the average temperature rise was 38 K.

fluctuations, hence some small-scale eddies, in the jet shear layer. The dominant bluff-body shedding frequency does not change very significantly when the reaction is exothermic. However, the Strouhal number associated with the shedding of the composite eddy is seen to shift slightly toward 0.1 (compare the last plot of Figures 5.2 and 5.4).

Another significant difference between the isothermal and exothermic reactive flow is the time evolution and the structure of the composite eddy shed from the recirculation region. From Figure 5.1, we see that the composite eddy in the isothermal flow remains coherent, and the magnitude of it vorticity persists for a large distance downstream of the recirculation region. The structure of this eddy is compact, with high concentration of vortex elements on the surface of the structure. For the exothermic reactive flow, however, the large eddy loses it identity quickly because of the continuously spreading out of the vorticity over a larger area. The geometry of the eddy is slightly flattened, with the major axis of the eddy becomes more aligned with the streamwise coordinate (compare Figure 5.1d to Figure 5.3 e). Moreover, as will be shown later, the eddy in the isothermal reactive flow contains significantly high level of unsteady fluctuation kinetic energy, and this energy is retained by the eddy for very large distance downstream of the recirculation region. For the exothermic reactive field, however, the eddy has much less unsteady fluctuation kinetic energy to start with, and the amplitude of the unsteady fluctuation kinetic energy dissipates quickly to a point where it is indistinguishable from the background level within a bluff-body diameter downstream of the recirculation region. Furthermore, the upper wall boundary layer is thinner for the exothermic reactive flow, and less large-scale eddies are being generated in the boundary layer (compare the wall boundary layer between Figures 5.1 and 5.3). In this case, less interaction between the shed composite eddies and the wall boundary layer is observed in the exothermic reactive flow. Finally, the wake region downstream of the recirculation zone of the exothermic reactive flow is significantly thicker than that of the corresponding isothermal reactive wake, and has relatively lower concentration of vortex elements.

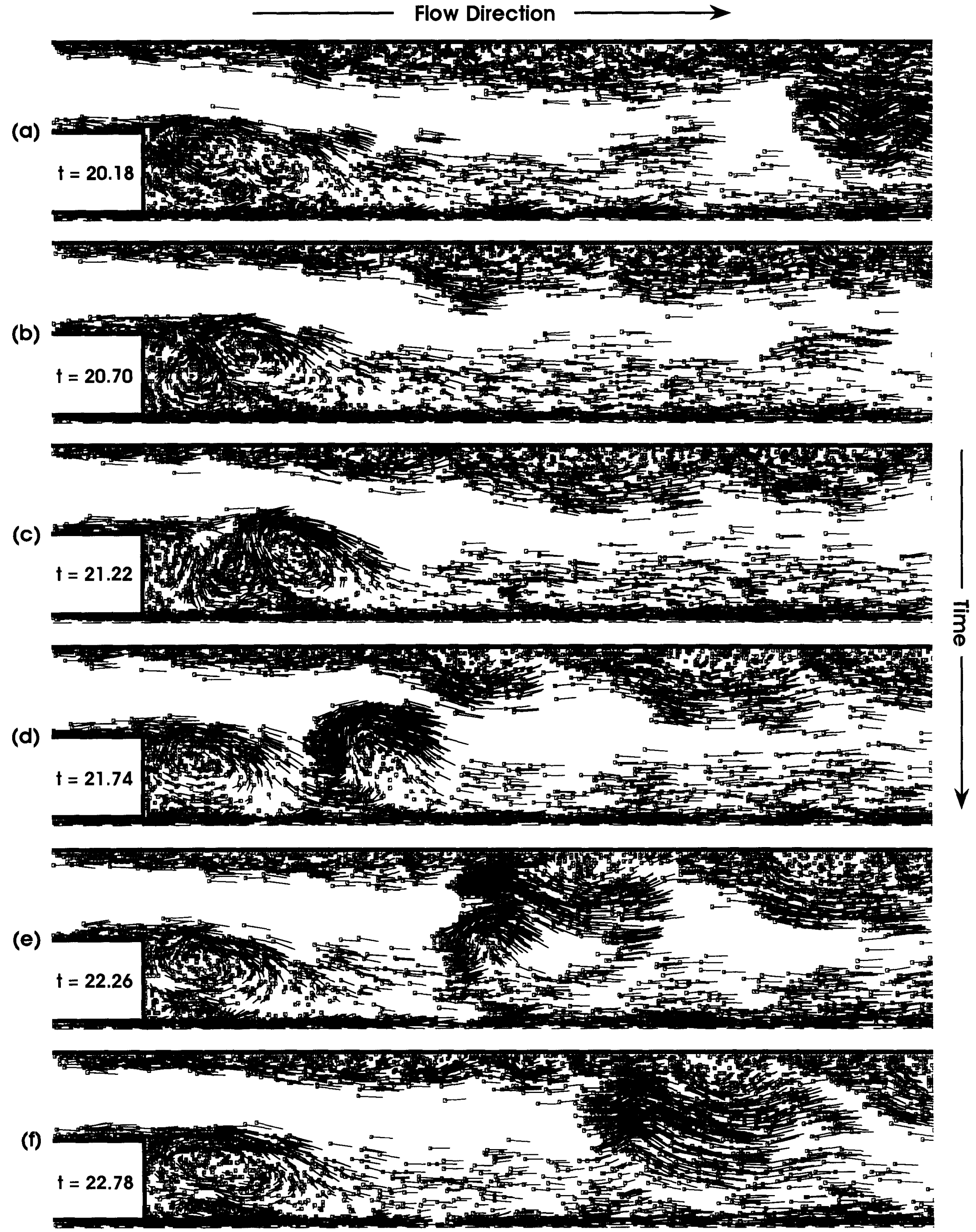

Figure 5.1 A series of time frames showing the time evolution of the large-scale vortical structures in the near-wake region of an isothermal reactive flow in terms of the vortex-element distribution in the interior of the flow domain. $U_j/U_a = 1.04$.

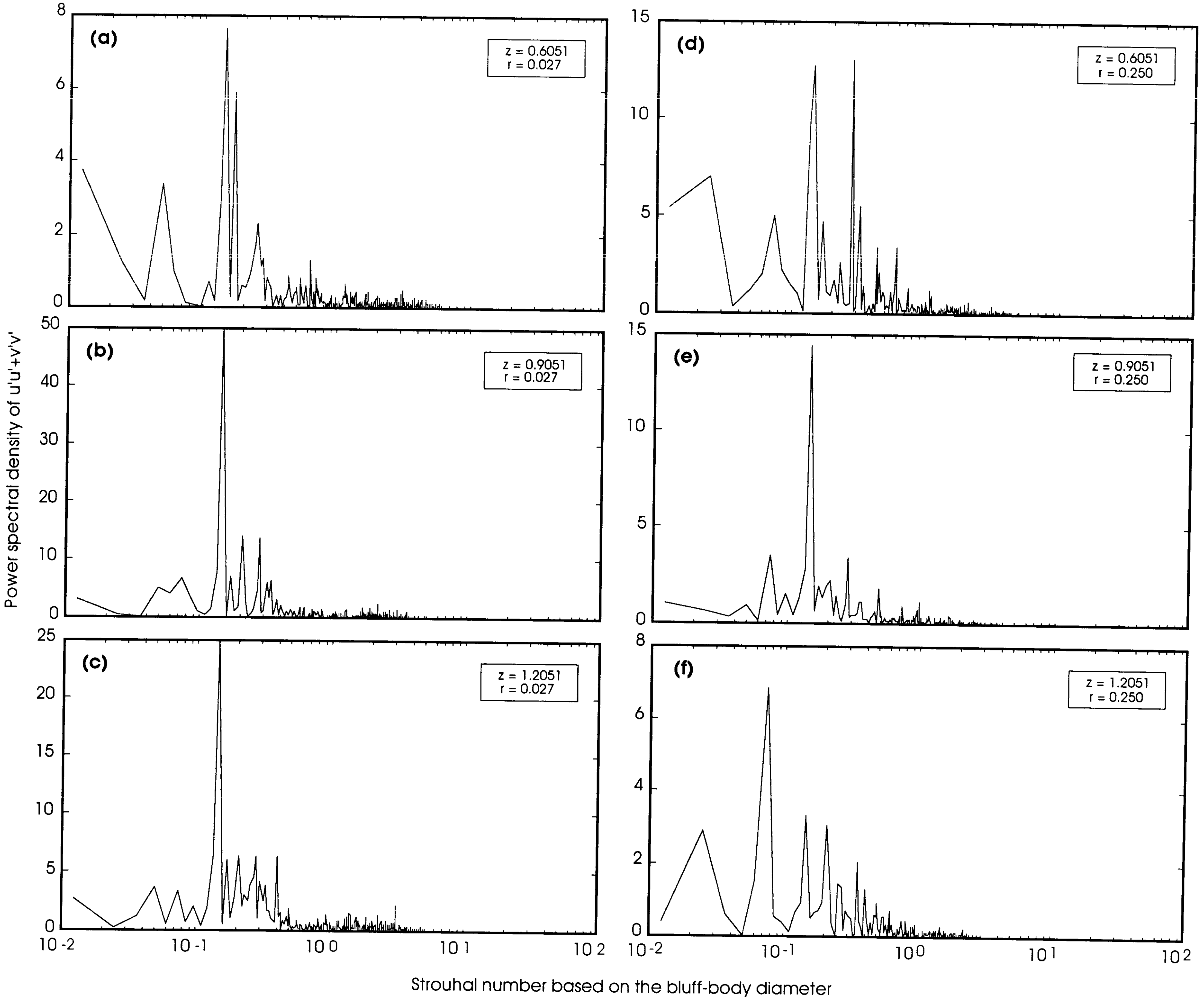

Figure 5.2 Power spectral density of u'u'+v'v' as a function of the Strouhal number. $U_j / U_a = 1.04$ (isothermal reactive flow).

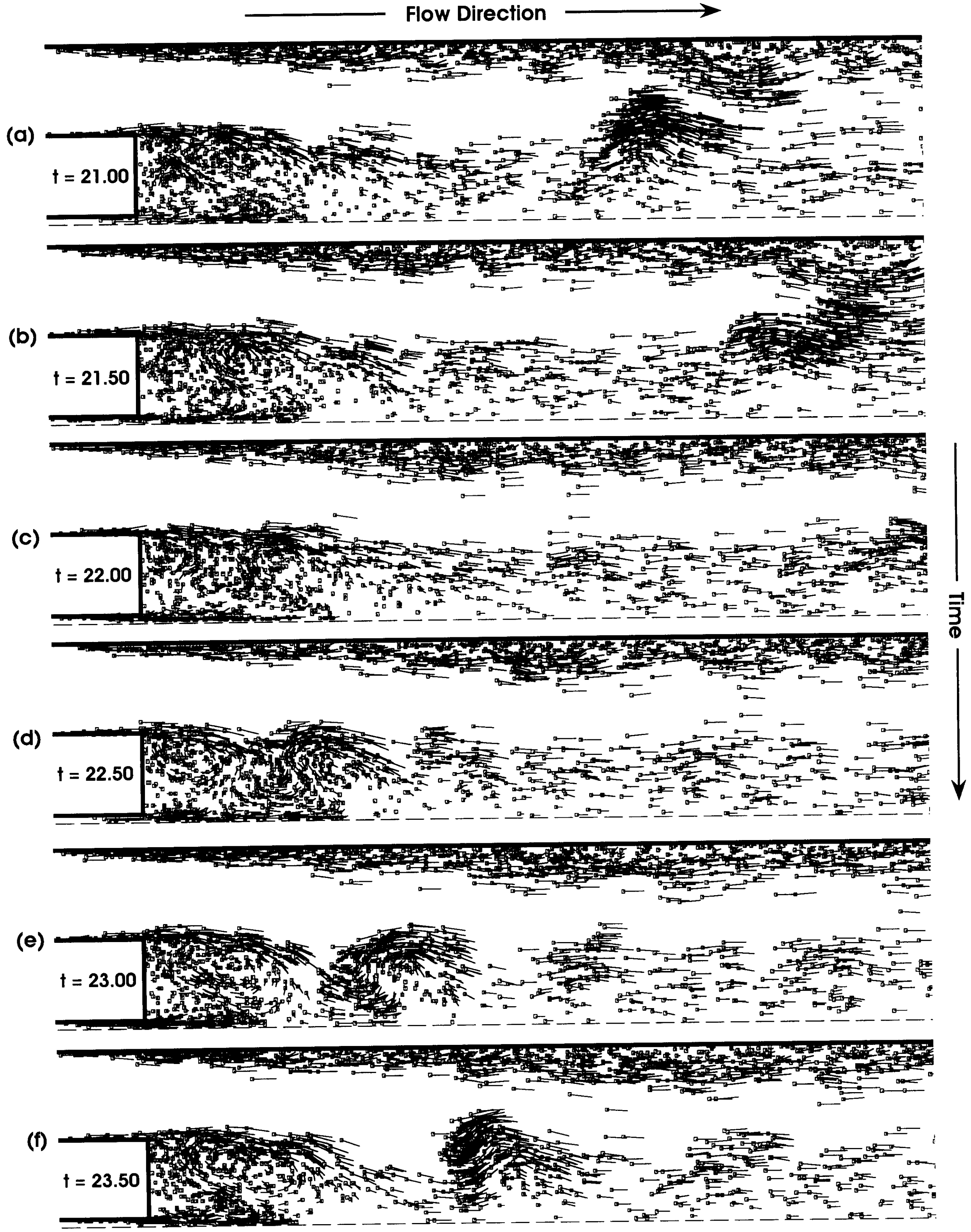

Figure 5.3 A series of time frames showing the time evolution of the large-scale vortical structures in the near-wake region of an exothermic reactive flow in terms of the vortex-element distribution in the interior of the flow domain. $U_j/U_a = 1.04$.

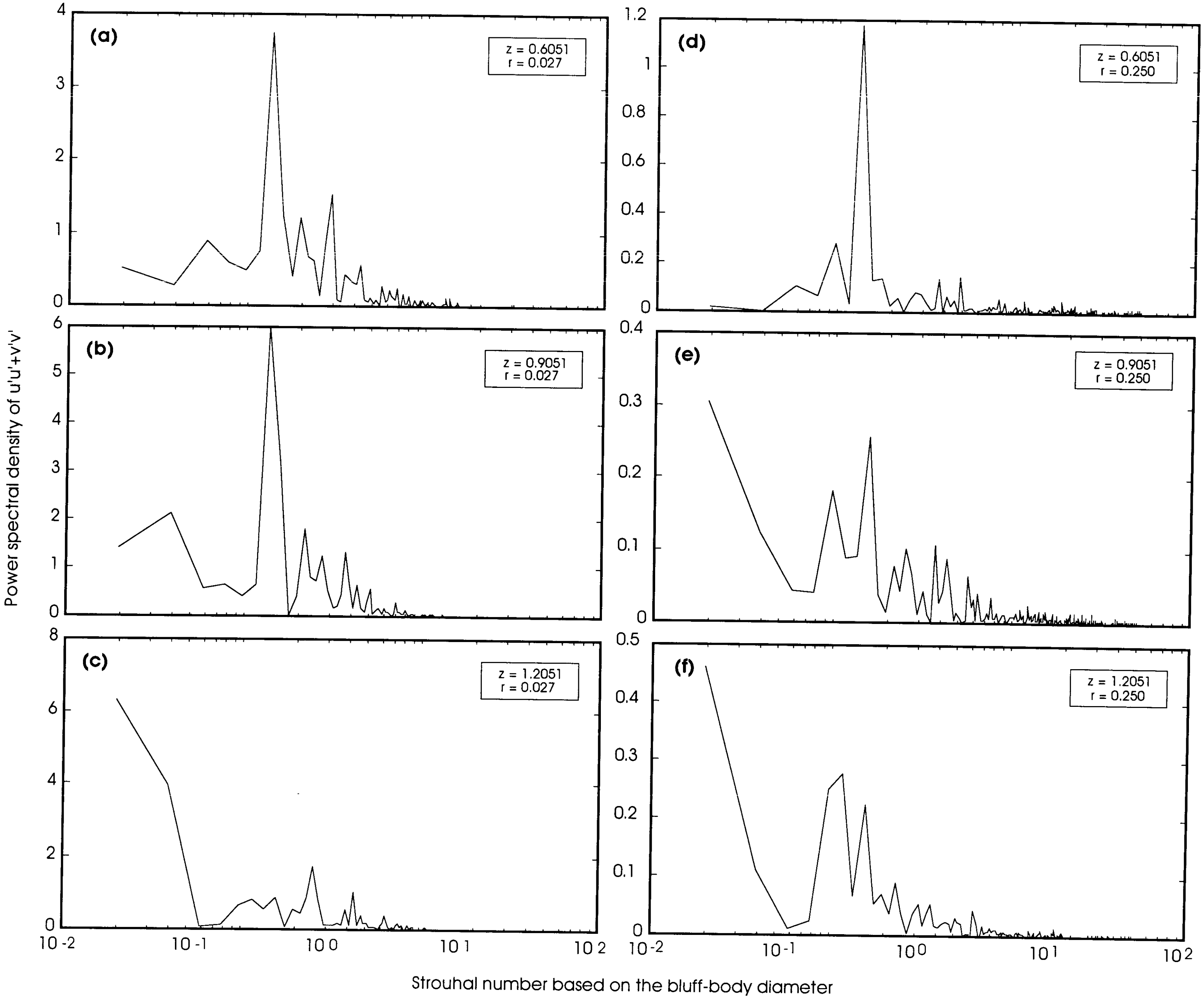

Figure 5.4 Power spectral density of u'u'+v'v' as a function of the Strouhal number. $U_j / U_a = 1.04$ (exothermic reactive flow).

A sequence of time frames showing the instantaneous isothermal product concentration field at the same time steps corresponding to Figure 5.1 is presented in Figure 5.5. From this figure, we see that the locations with highest product concentration are inside the recirculation region near the jet exit, and along the axis of the combustor extending from the end of the recirculation region to several bluff-body diameters down stream of the bluff-body face. This particular pattern of the product distribution indicates that mixing and chemical reaction generally occur inside the recirculation region close to the jet exit and along the centerline of the combustor downstream of the recirculation region. This series of time frames also shows that entrainment and mixing in the near-wake region are strongly modulated by the large-scale vortices, and the entrainment of the jet fluid into the counterclockwise-rotating eddy provides a continuous supply of fresh fuel to sustain the reaction within the recirculation region (Figures 5.5a and b). As the recirculation region becomes unstable, the shedding of the composite structure carries away most of the products accumulated in the region (Figures 5.5c and d). Notice that as the large composite structure is being convected downstream, it entrains additional jet fluid from the centerline of the combustor and mixes the fuel elements in the jet fluid with the oxidizer elements (Figure 5.5e). This unsteady entrainment process causes intense mixing and reaction to occur along the outer surface of the vortical structure continuously, as can clearly be seen in Figures 5.5d and e.

The instantaneous product concentration field of the exothermic reactive flow is different from its counterpart in the isothermal reactive flow in many subtle aspects. Figure 5.6 shows a similar sequence of time frames illustrating the unsteady product concentration field when the reaction is exothermic. Comparing the two time sequences shown in Figures 5.5 and 5.6, several differences between the two cases are immediately noticeable. First and foremost, the product concentration inside the recirculation region near the jet exit of the exothermic reactive flow is much lower than that in the isothermal case. High product concentration in this case begins to appear at approximately a bluff-body radius downstream of the jet exit. The changes in the mixing and reaction pattern observed here is clearly reflected in the value of ρY_p integrated across the combustor cross section as a function of the axial coordinate (Figure 5.11a) and can be attributed to the changes in the large-scale flow structure within the recirculation region. This changes can be seen by examining the corresponding vortex-element plots presented in Figure 5.3. Owing to the expansion velocity field, the air vortex in the exothermic reactive flow within the recirculation is slightly flattened, and the major axis of the structure becomes more aligned with the streamwise coordinate. As a result, the unsteady reattachment point of the upper shear layer is moved further downstream. Moreover, the expanded jet shear layer has shifted the entire structure of the recirculation region radially outward and away from the face of the bluff body, reducing the chances of the fuel elements to interact with the oxidizer elements near the jet exit. As a consequent, mixing and reaction are seen to occur mostly downstream of the recirculation region and along a more angled jet shear layer. The reaction pattern just described can clearly be seen by examining the flow structure near the end of the recirculation region in Figure 5.3a and the corresponding unsteady product concentration field in Figure 5.6a, as well as the instantaneous reaction zones in the flow field present in Figure 5.7 (to be discussed shortly). Another significant difference between the two cases is the boundary separating the jet and the outer annular flow along the axis of the combustor. For the isothermal case, we see that most products are confined very close to the centerline with sharp irregular boundary between the jet and the outer flow, indicating the existence of a large number of small-scale eddies inside the shear layer separating the two fluids. For the exothermic case, we see that the entire wake region downstream of the bluff body becomes much thicker, and the boundary separating the two fluids becomes more diffuse. Small-scale eddy activities along the shear layer are seen to be less intense than those in the isothermal reactive flow. This observation can also clearly be seen in Figures 5.1 and 5.3 as well as the comparisons of the unsteady and time-averaged product concentration field between the isothermal and the exothermic reactive-flow calculation presented in Figures 5.9 and 5.10.

The instantaneous locations in the flow field where chemical reactions are most intense, hence the flame surfaces for the exothermic reactive flow, are presented in Figure 5.7. For comparison, the same quantity for the isothermal reactive flow is presented in Figure 5.8. In these two figures, the first three frames show the instantaneous reaction zones in the flow field, and the last three frames show the corresponding instantaneous product concentration field. As observed in the experimental studies performed by Roquemore [119] and Namazian [103], chemical reactions are seen to occur mostly within the shear layer between the jet and the recirculation bubble, and on the outer surfaces of the large-scale vortical structures for both cases. In addition, the reaction surfaces are seen to be strongly modulated by the large-scale structures as the eddies continue to grow within the recirculation region.

Comparing the reaction surfaces of the exothermic reactive flow presented in Figure 5.7 with the isothermal reactive case presented in Figure 5.8, the effects of the thermal energy on the large-scale entrainment and mixing can clearly be seen. Chemical reaction with heat release, while decreases the entrainment and mixing in the recirculation region close to the jet exit, does not alter the overall large-scale structures significantly. The large-scale dynamics observed in the isothermal reactive flow also appear in the exothermic reactive flow. The main difference between the two cases is mostly on the location and the magnitude of the instantaneous reaction within the recirculation region. For the isothermal reactive flow, reactions begin to take place immediately downstream of the jet exit, and the reaction surface between the jet and the recirculation bubble is almost parallel to the axis of the combustor. Fuel elements which are entrained into the jet shear layer and are moving radial upward along the outer surface of the recirculating air eddy cause reaction to take place along the jet shear layer as well as along the surface of the recirculating air eddy, as can clearly be seen in Figures 5.8a and b. For the exothermic reactive flow, the expanded jet shear layer pushes the air eddy away from the face of the bluff body. In this case, the reaction surface within the recirculation region becomes more angled relative to the axis of the combustor, resulting in combustion to take place further downstream of the jet exit. Otherwise, the large-scale entrainment and the mixing mechanisms of the two cases appear to be similar.

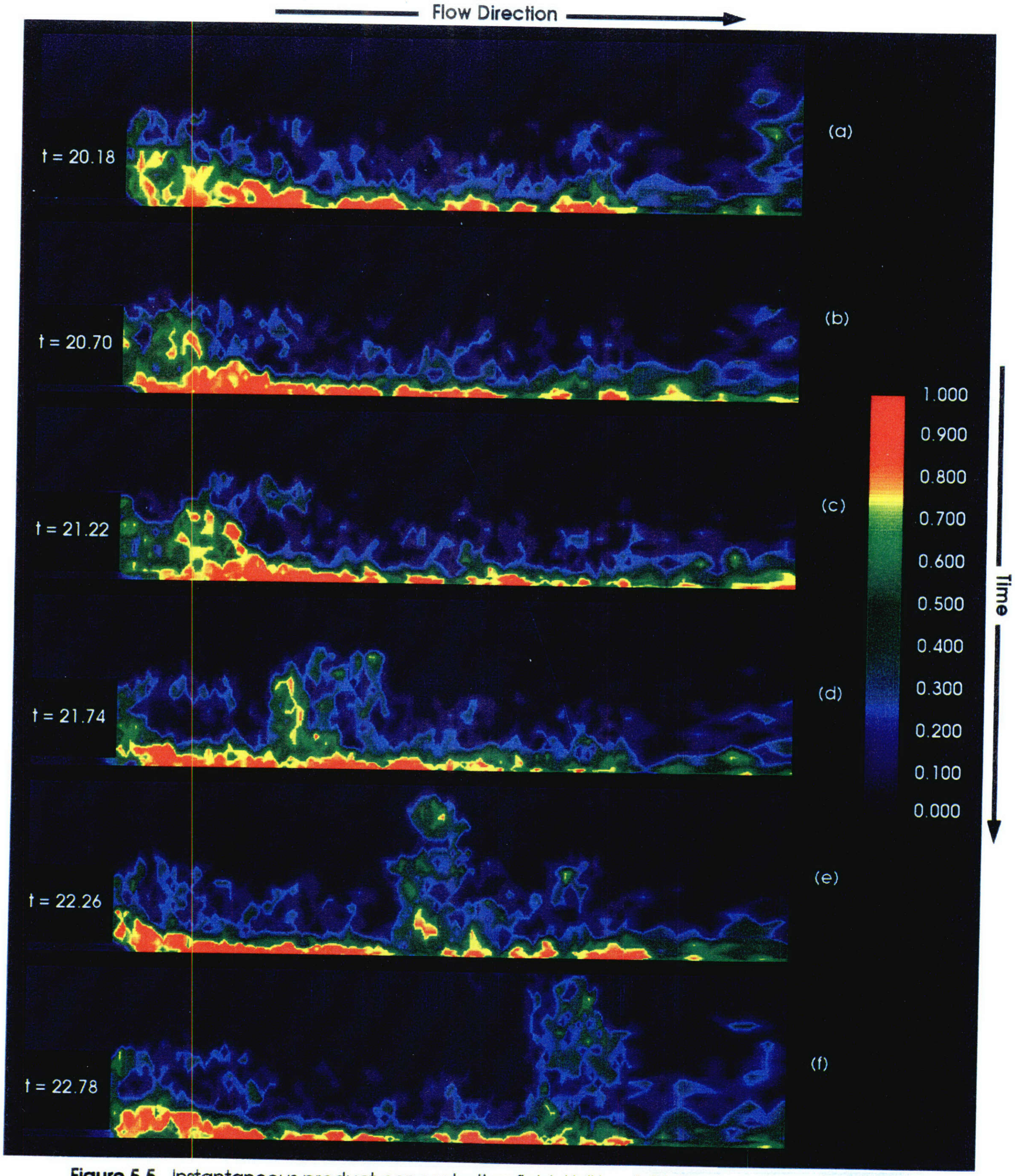

Figure 5.5 Instantaneous product concentration field. $U_j/U_a = 1.04$ (isothermal reactive flow).

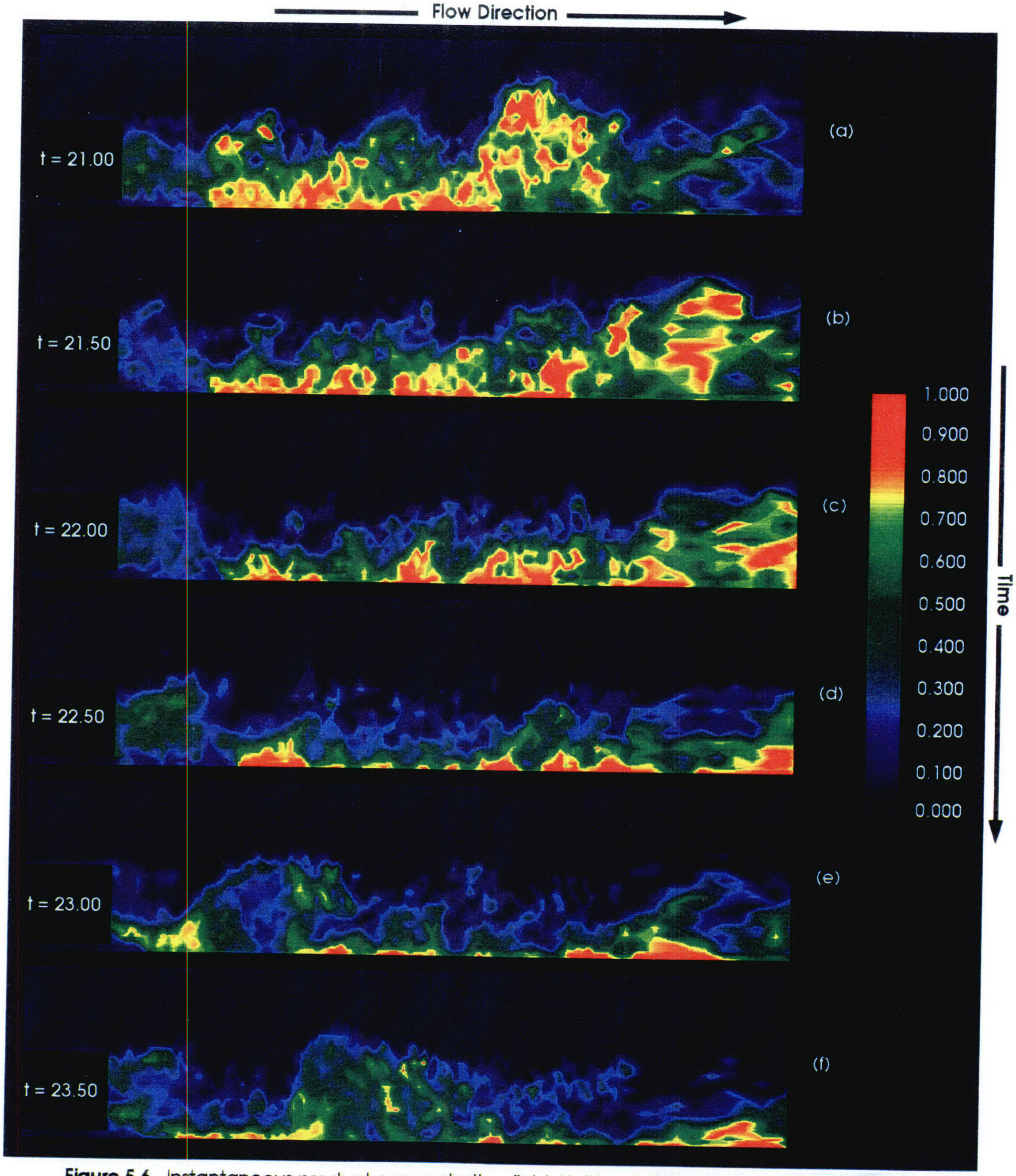

Figure 5.6 Instantaneous product concentration field. $U_j/U_a = 1.04$ (exothermic reactive flow).

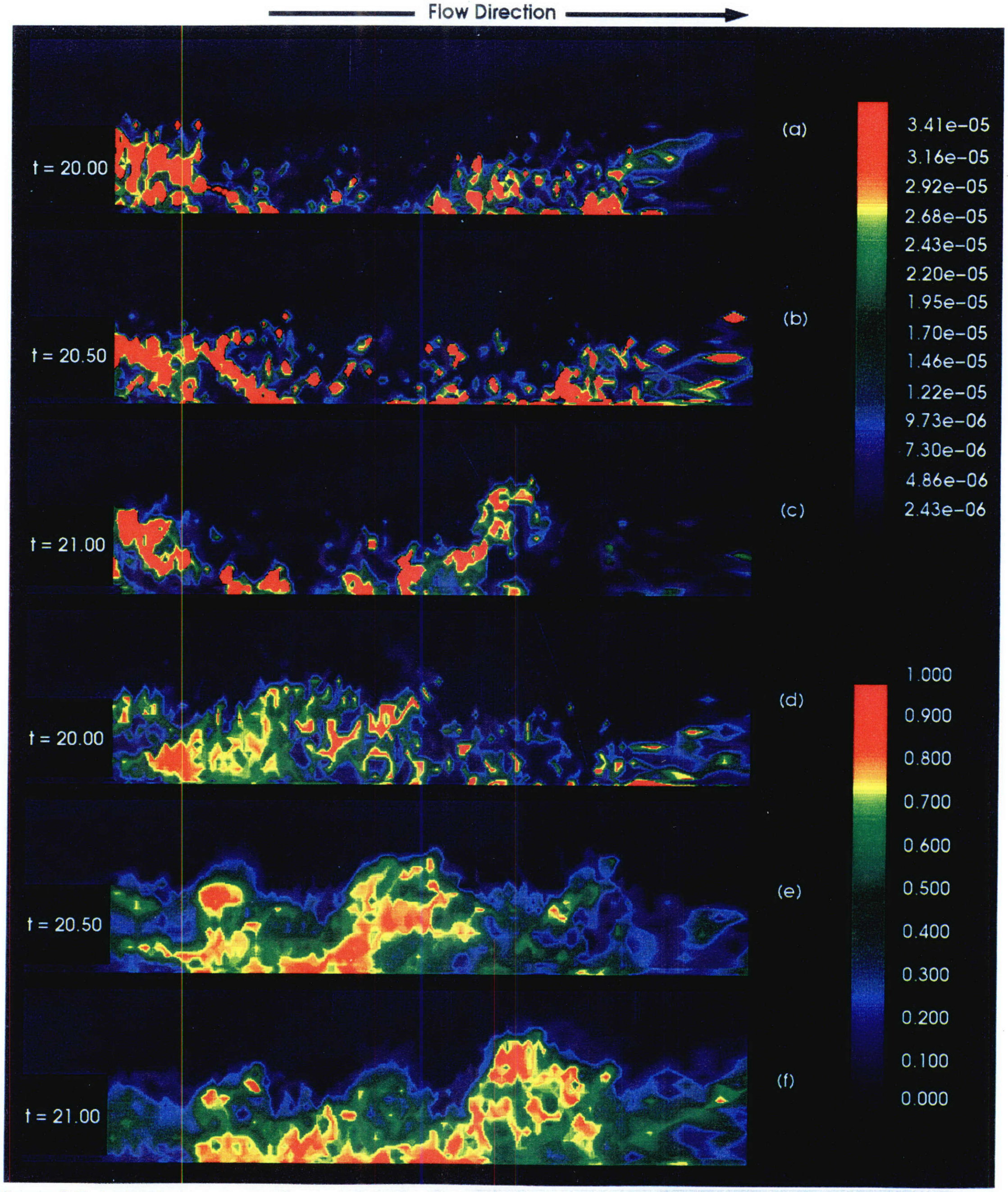

Figure 5.7 Instantaneous reaction zones in the flow field (a–c) and the corresponding product concentration field (d–f). $U_j/U_a = 1.04$ (exothermic reactive flow).

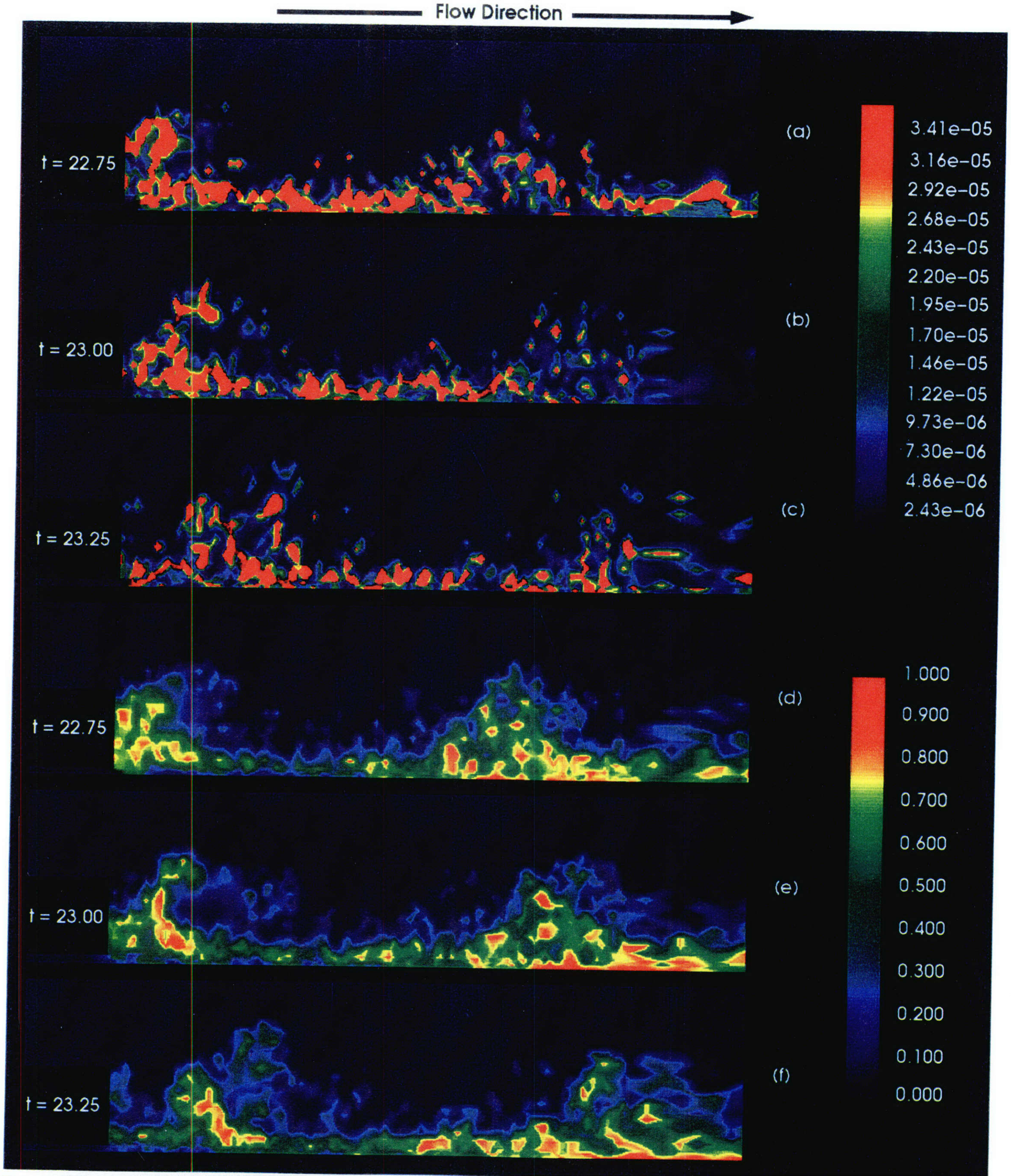

Figure 5.8 Instantaneous reaction zones in the flow field (a–c) and the corresponding product concentration field (d–f). $U_j/U_a = 1.04$ (isothermal reactive flow).

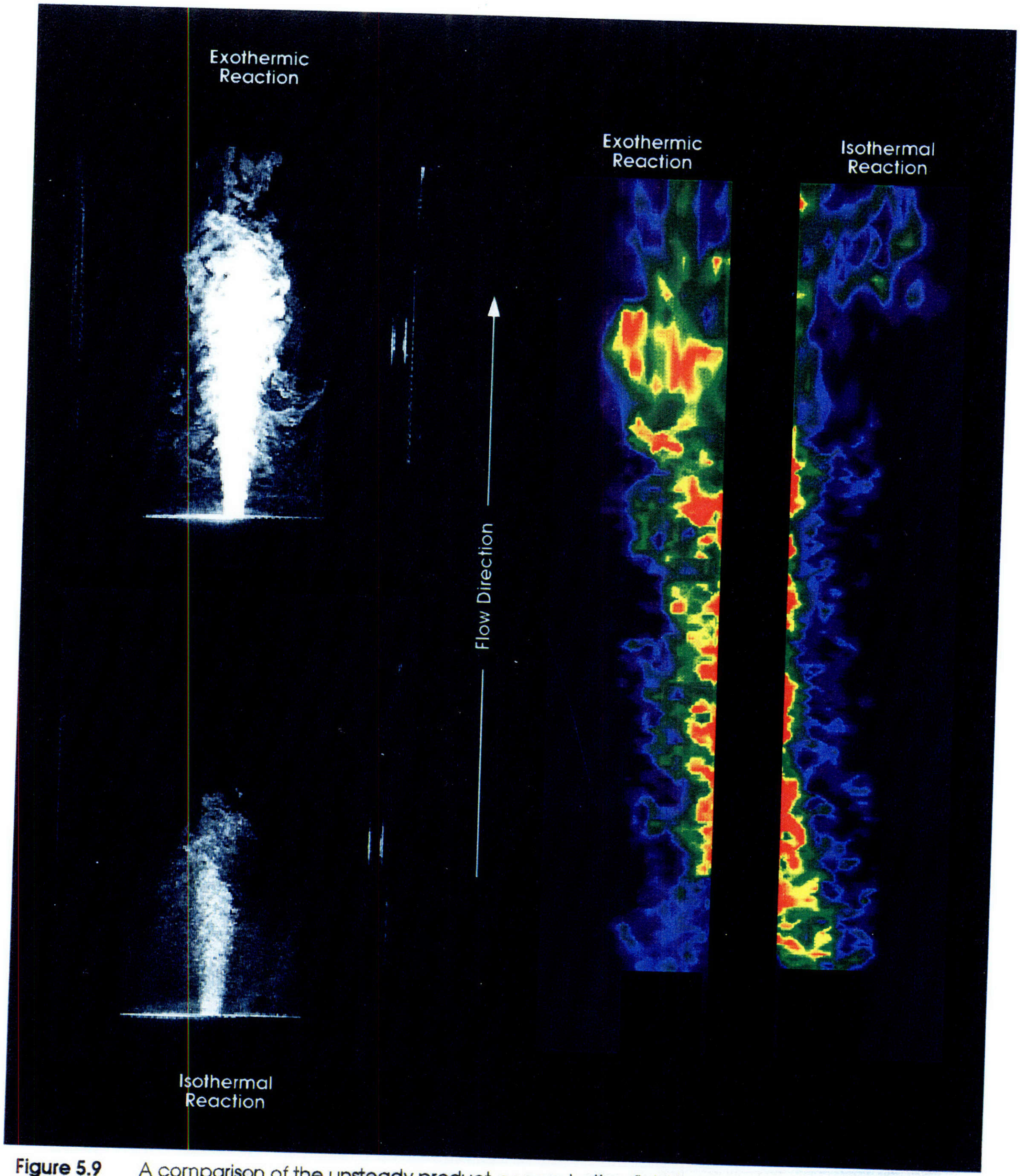

Figure 5.9 A comparison of the unsteady product concentration field between the isothermal and the exothermic reactive–flow calculation. The experimental Schlieren photographs on the left are from (103).

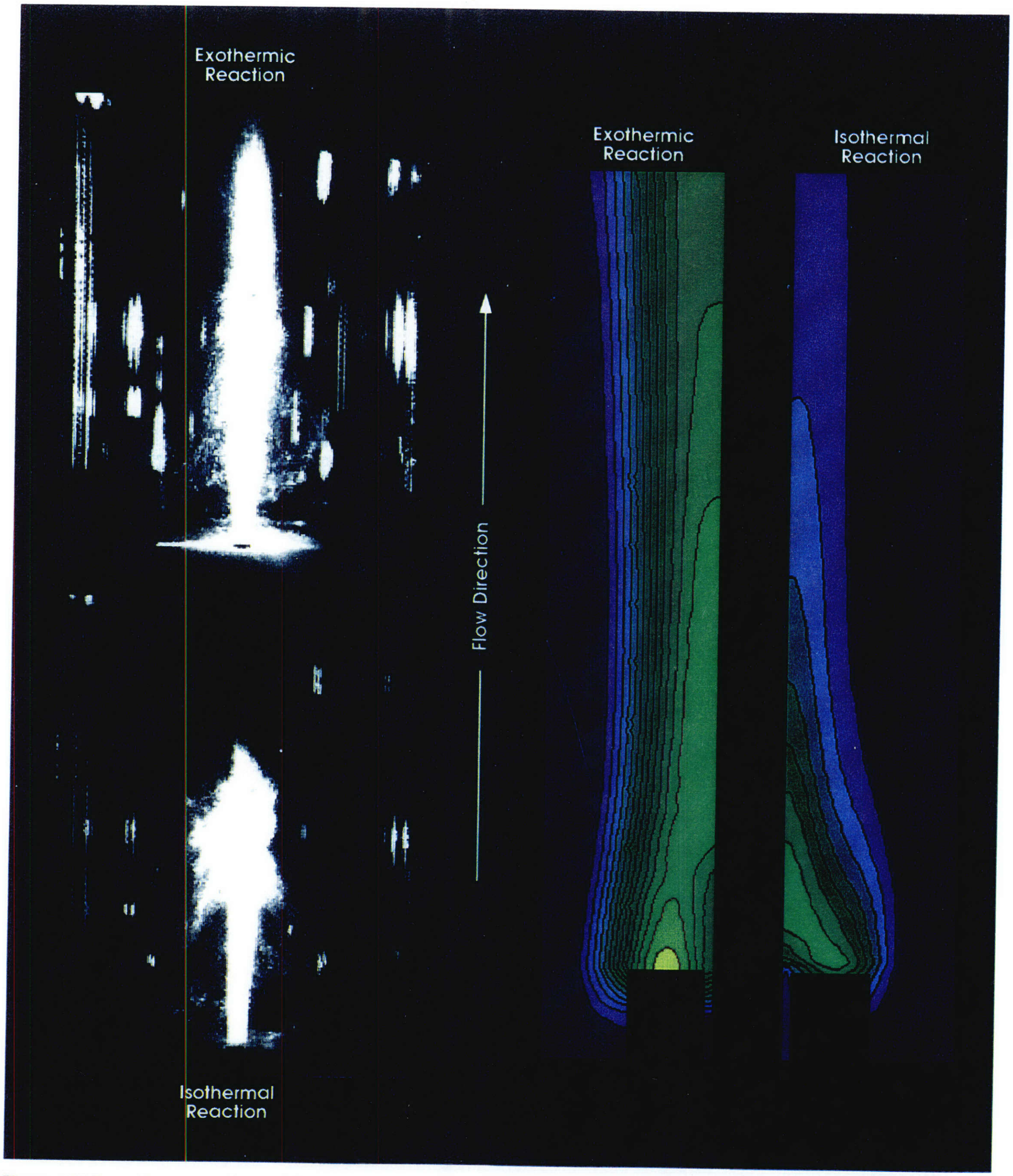

Figure 5.10 A comparison of the time–averaged product concentration field between the isothermal and the exothermic reactive–flow calculation. The experimental Schlieren photographs on the left are from (103).

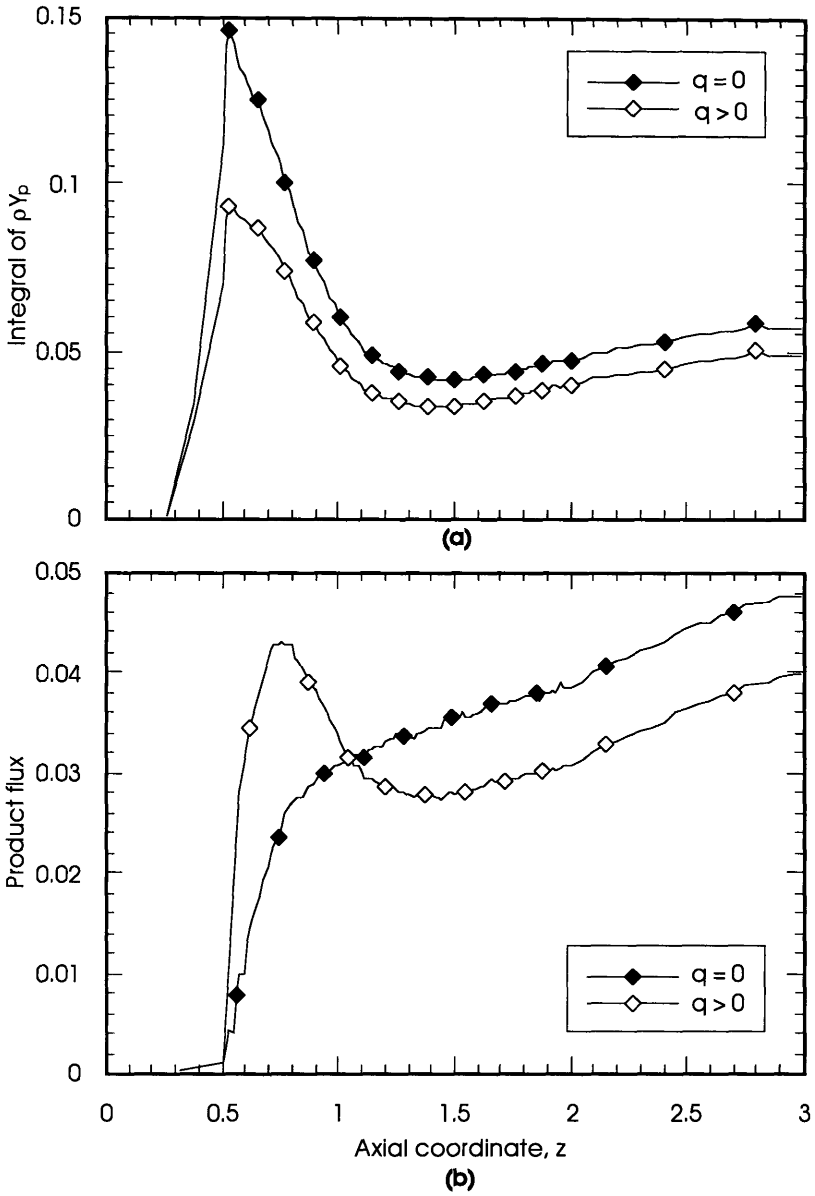

Figure 5.11 The integral of ρY_p and the product flux integrated across the combustor cross section as a function of the axial coordinate. **(a)** $\int_0^R (\rho Y_p 2\pi r)\,dr$. **(b)** $\int_0^R (\rho u Y_p 2\pi r)\,dr$.

From the isothermal reactive flow study presented in Chapter 4, it was observed that the spatial distribution of the unsteady fluctuation kinetic energy in the flow field is highly nonuniform, attaining maximum value in regions where the mean gradients are high; namely, in the shear layers along the central-jet boundary and along the boundary separating the recirculation bubble from the outer annular flow, as well as within the well-defined large-scale structures. The degree of the recirculation region instability was found to be directly related to the amount of fluctuation kinetic energy possessed by the eddies inside the recirculation region. Since unsteady fluctuation kinetic energy is usually associated with the momentum exchange due to large-scale transport, regions in the flow field with high level of unsteady fluctuation kinetic energy are usually the locations where intense mixing occurs. Thus, the investigation of the spatial distribution of the unsteady fluctuation kinetic energy, its production, redistribution, and dissipation rate provides another useful way to examine the effects of the thermal energy released from combustion on the large-scale motions, and to account for certain changes observed in the vorticity dynamics and the mixing field.

Two series of time frames showing the unsteady fluctuation kinetic energy field for the isothermal and the exothermic reactive flow are presented in Figures 5.12 and 5.13, respectively. From Figure 5.12, we see that most of the unsteady fluctuation kinetic energy in the isothermal reactive flow field is concentrated in the well-defined, large-scale vortical structures. Instability of the recirculation region starts as the large-scale eddies and the shear layers within the region begin to accumulate unsteady fluctuation kinetic energy. The magnitude of the unsteady fluctuation kinetic energy of the eddies continues to increase, and reaches a maximum value prior to the shedding of the composite structure from the recirculation region. After the ejection of the composite eddy from the recirculation region, the energy level within the region decreases substantially, and remains relatively low until the growth of the fuel eddy begins to affect the stability of the region again. Notice that the shed composite eddy remains coherent, and retains its unsteady fluctuation kinetic energy a large distance downstream of the recirculation region. Even after the interaction with the eddy on the upper wall boundary layer, the eddy is still highly distinguishable. Since the intensity of the unsteady fluctuation kinetic energy is directly related to the large-scale transport rate, the high level of unsteady fluctuation kinetic energy associated with these large-scale eddies implies that these eddies are efficient agents in terms of initiating mass and momentum exchanges among the fluid elements.

When the reaction is exothermic, the natural shedding dynamics of the recirculation region persist despite the less orderly and relatively incoherent of the large-scale structures within the recirculation region. However, Figure 5.13 clearly shows that a major effect of the thermal energy released from combustion on the flow dynamics is the suppression of the unsteady fluctuation kinetic energy of the large-scale structures. From Figure 5.13, we see that, very similar to the isothermal reactive case, instability of the recirculation region begins as the eddies within the region accumulate unsteady fluctuation kinetic energy. However, the kinetic energy acquired by the eddies within the recirculation region before the shedding is noticeably less in this case. The energy of the eddy being shed from the recirculation region is seen to dissipate very quickly, decreasing to a level which is almost undetectable at a distance less than two bluff-body diameters downstream of the recirculation region. This phenomenon can qualitatively be explained as follow. As the expansion velocity acts on the large-scale structure by spreading out its vorticity, the eddy becomes more diffuse and loses its ability to entrain irrotational fluid as well as to extract additional energy from the freestream. As the eddy continues to expand and becomes less distinguishable, the concentration of the unsteady fluctuation kinetic energy in the eddy is redistributed over a larger area. Therefore, the energy can be dissipated by molecular diffusion more quickly. Since lower level of fluctuation within an eddy implies lower large-scale transport rate, thus, thermal expansion decreases the ability of the large-scale structures to entrain fluid. As seen in Figure 5.13b, the unsteady fluctuation kinetic energy of the eddy shed from the recirculation region becomes almost undetectable at a distance just slightly greater than one bluff-body diameter, and disappears completely within two bluff-body diameters downstream of the recirculation region.

As discussed earlier, heat release did not affect the natural shedding frequencies of the flow significantly. A comparison of the differences between the power spectra of the isothermal and the exothermic reactive flow is provided by Figures 5.2 and 5.4. For the isothermal reactive flow, we see that the significant Strouhal numbers found in the flow domain included the well-known bluff-body shedding frequency, $S \sim 0.15$, and the frequency associated with the shedding of the composite eddy, $S \sim 0.06$. Also, notice that the dominant peaks in the isothermal reactive flow are very narrow and sharp. Examining the power spectra of the exothermic reactive flow, we see that the general trends of the power spectra are very similar. Differences, however, do exist between the two cases. The power spectra for the exothermic reactive flow are broader, the peaks are being spread out more and are less sharp as compared with those in the isothermal case. Furthermore, the frequency associated with the shedding of the composite structure from the recirculation region is slightly shifted toward 0.1. Suppression of certain high-frequency oscillations is also evident. This observation can be seen much clearer in Figures 5.14 and 5.15, where we compare the radial velocity fluctuations in the shear layer between the outer annular flow and the recirculation bubble and in the jet shear layer, respectively. From these figures, similar conclusion can be drawn. Heat release did not change the large-scale dynamics very significantly. Most of the large-scale coherent fluctuations observed in the isothermal reactive flow can also be seen in the exothermic reactive flow. The main difference being the relative amplitude of the different modes of fluctuation. In general, the maximum amplitude of the fluctuations is reduced for all frequencies and certain small-scale oscillations are suppressed. Lower radial velocity fluctuations implies less large-scale momentum transport in the radial direction. Thus, large-scale entrainment and mixing are both decreased in the exothermic reactive flow, a trend which has been observed in numerous experimental studies as well as in other numerical studies of two-dimensional exothermic reactive shear layer [55, 134]. From the information provided by these figures and the result of the unsteady fluctuation kinetic energy, we can conclude that heat release from chemical reaction decreases the large-scale entrainment and mixing, resulting from the more diffuse eddies which are less capable of entraining fluid from their surrounding.

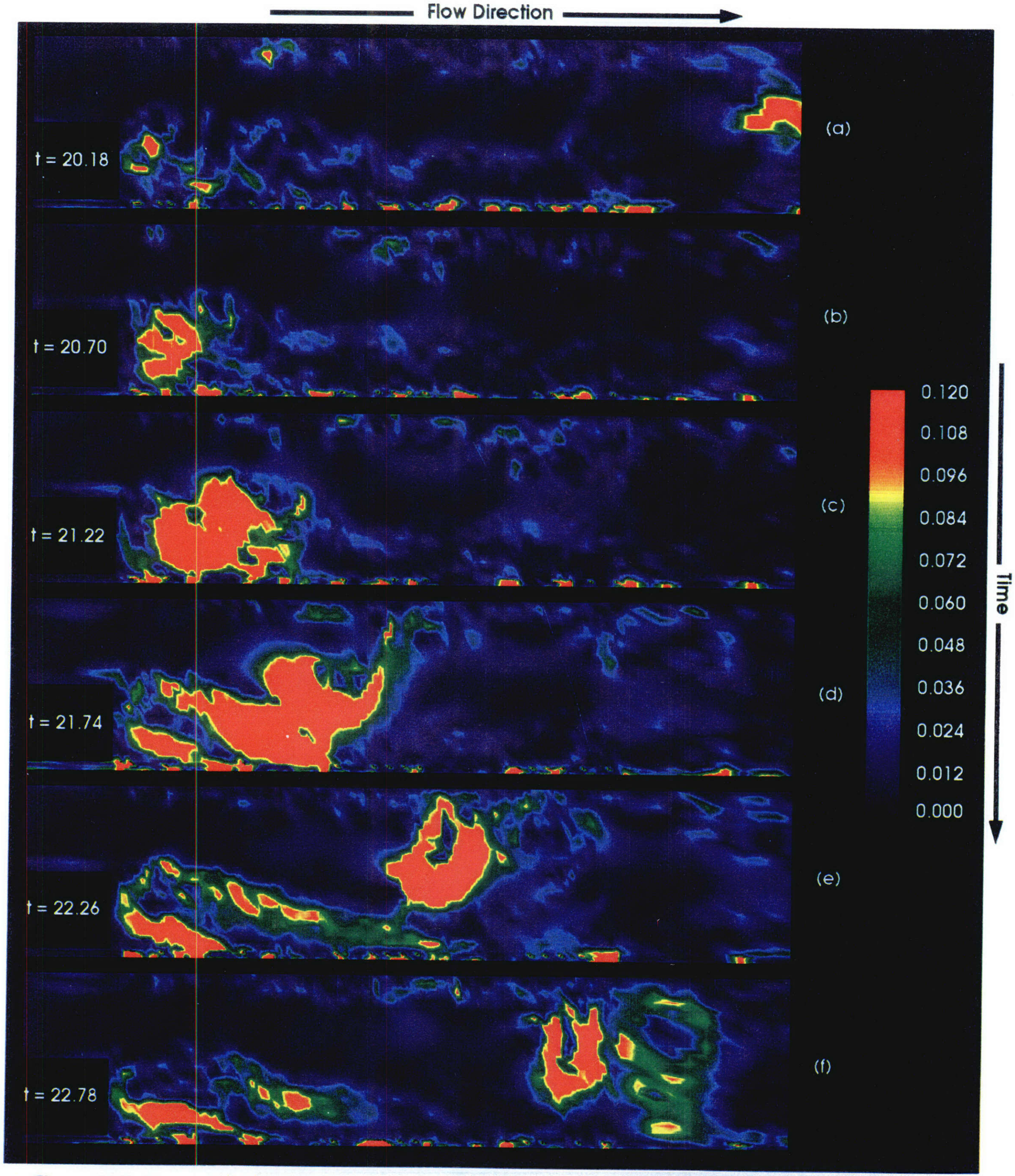

Figure 5.12 The unsteady fluctuation kinetic energy u'u'+v'v'. U_j/U_a = 1.04 (isothermal reactive flow).

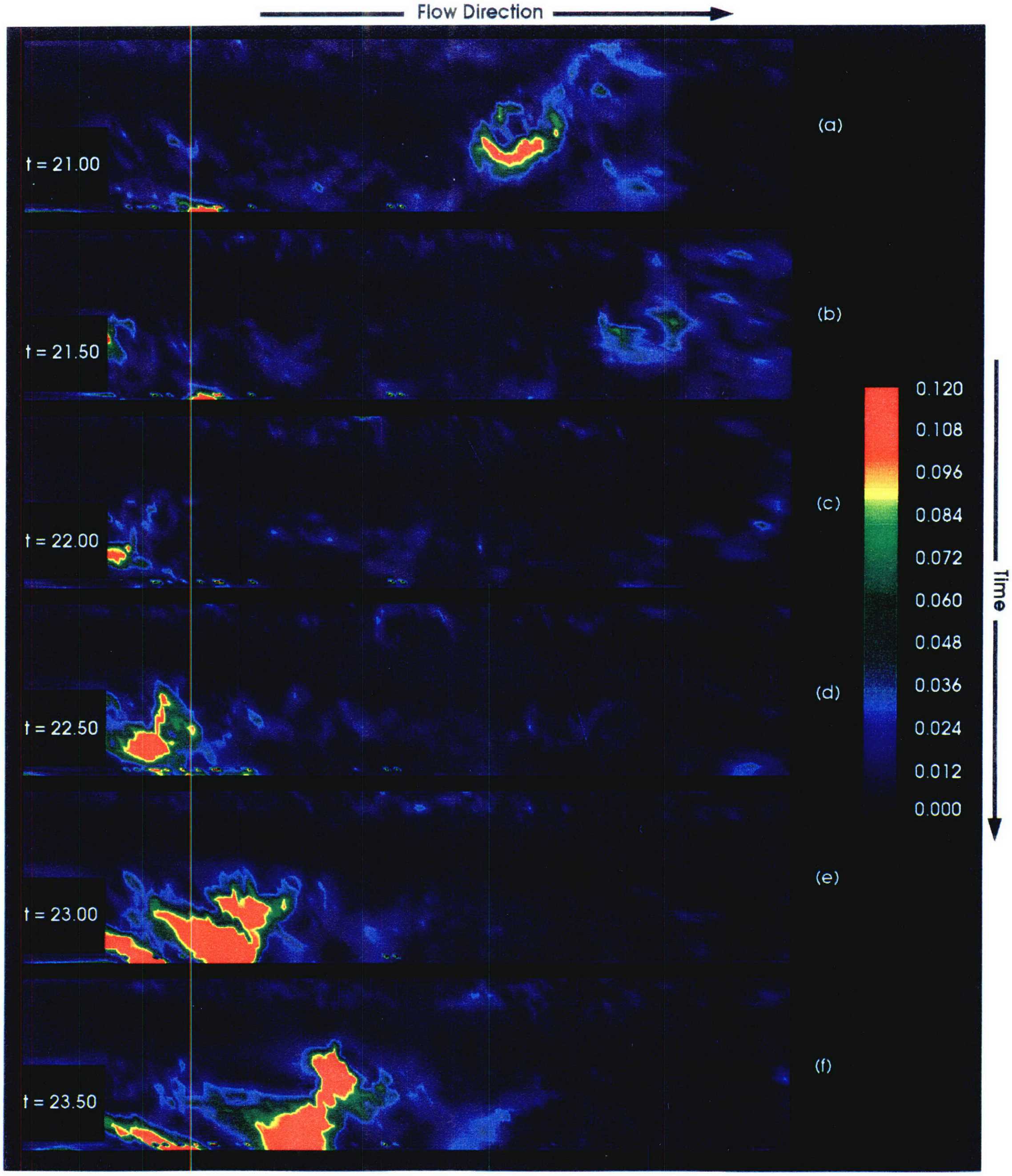

Figure 5.13 The unsteady fluctuation kinetic energy u'u'+v'v'. $U_j/U_a = 1.04$ (exothermic reactive flow).

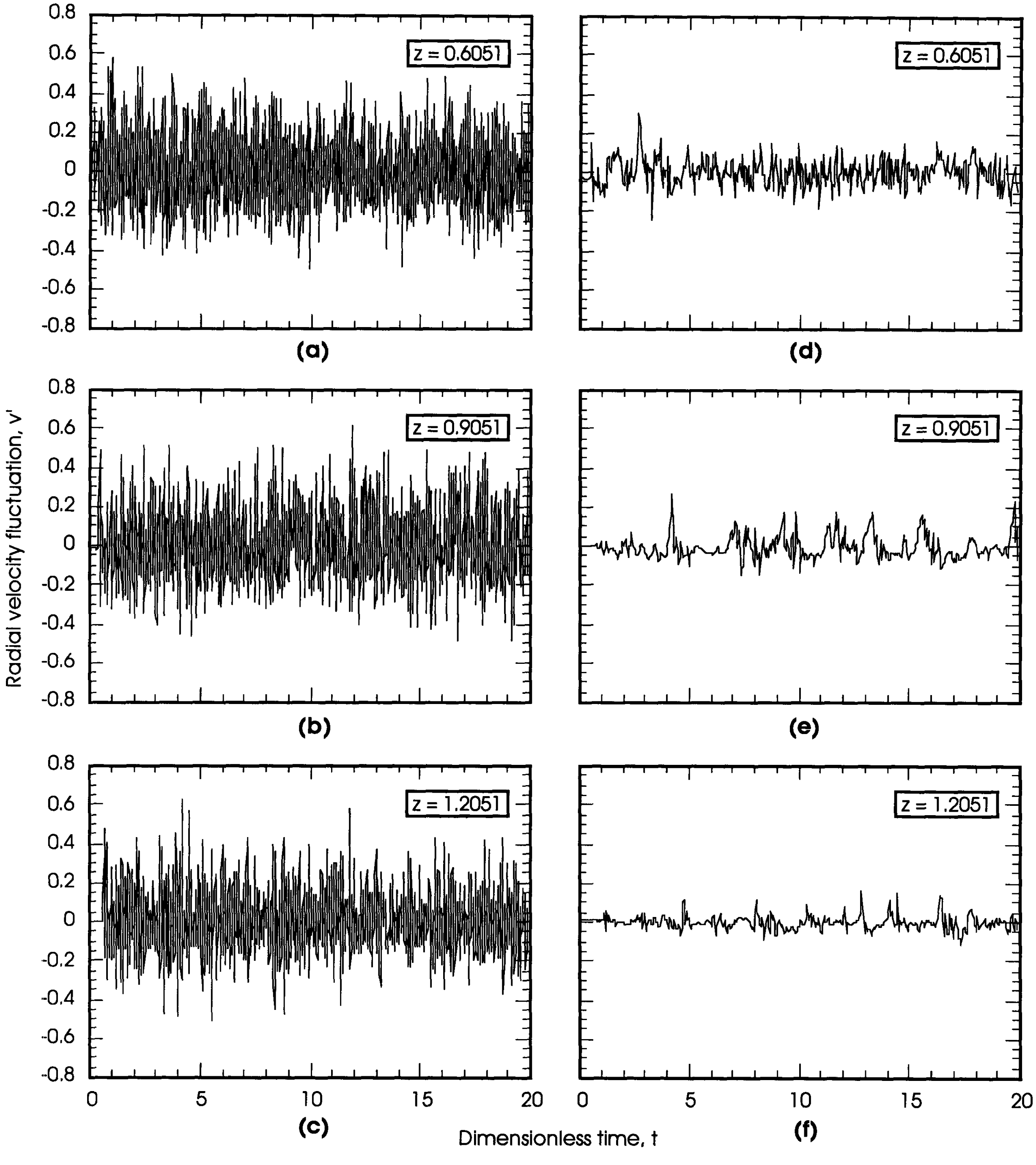

Figure 5.14 Comparisons of the radial velocity fluctuations between the isothermal (a-c) and exothermic (d-f) reactive flow. r = 0.027.

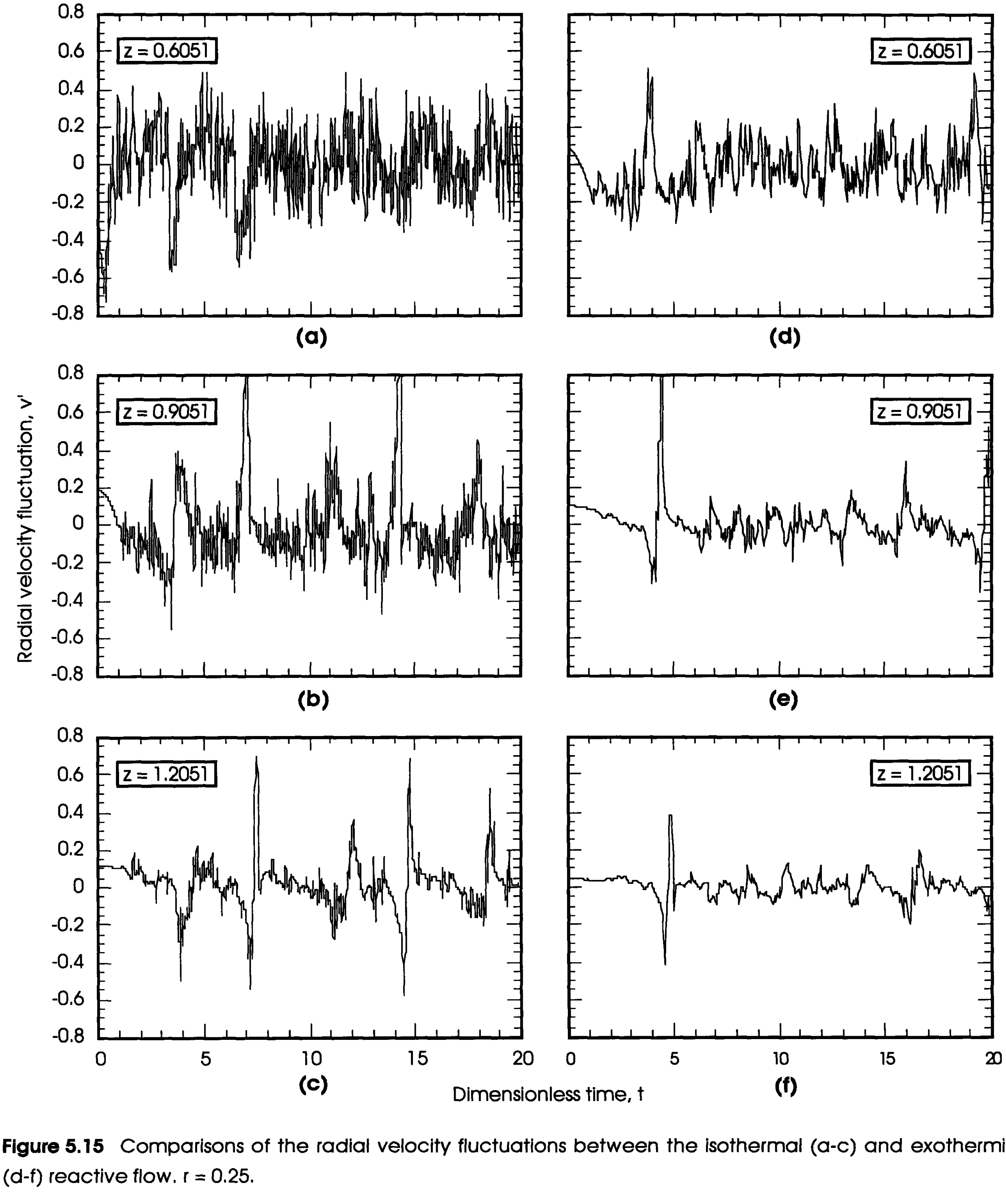

Figure 5.15 Comparisons of the radial velocity fluctuations between the isothermal (a-c) and exothermic (d-f) reactive flow. r = 0.25.

As seen in the isothermal reactive flow study presented in Chapter 4, the probability density functions (PDFs) of the velocity distributions are effective in terms of separating the large-scale dynamics from the more classical small-scale flow structures of high-Reynolds-number flows. From the isothermal study, it was found that the PDFs of the flow for all three velocity ratios studied did not deviate significantly from a Gaussian distribution except in regions where the local flow dynamics are dominated by large-scale activities. As discussed in the Introduction, this strong non-Gaussian behavior would significantly complicated the solution procedure using assumed probability density function methods. In the following, we will compare the PDFs between the isothermal and the exothermic reactive flow field in order to see the effect, if any, of heat release on the PDFs of the flow.

Figures 5.16-5.19 show the PDFs of u′ and v′ for the isothermal and the exothermic reactive flow field. Compare Figures 5.16 and 5.17, it is seen that the expansion velocity has very little impact on the PDF distribution. Within the jet shear layer, we see that the PDF of u′ becomes negatively skewed at the first station, and positively skewed at the last two stations. No significant changes can be detected at the upper shear layers between the two cases. Similarly, no significant changes can be detected between the two cases for the PDFs of v′. This observation can further be confirmed by examining Figure 5.20, where we show the comparisons of the skewness and Kurtosis between the two cases. From this figure, we see that, as observed from the PDF plots, the thermal energy did not change the structures of the main flow significantly (at least for the level of heat release chosen for this study). The variations of the skewness and Kurtosis for the case with heat release follow exactly the same trends as for the isothermal case, indicating that the most significant effect of heat release on the flow is the reduction of the unsteady fluctuations and the vorticity of the large-scale structures. All the significant global flow dynamics and the large-scale entrainment and mixing mechanisms occur in the isothermal case are also present when the reaction is exothermic, the main difference being the relative magnitude of the different events.

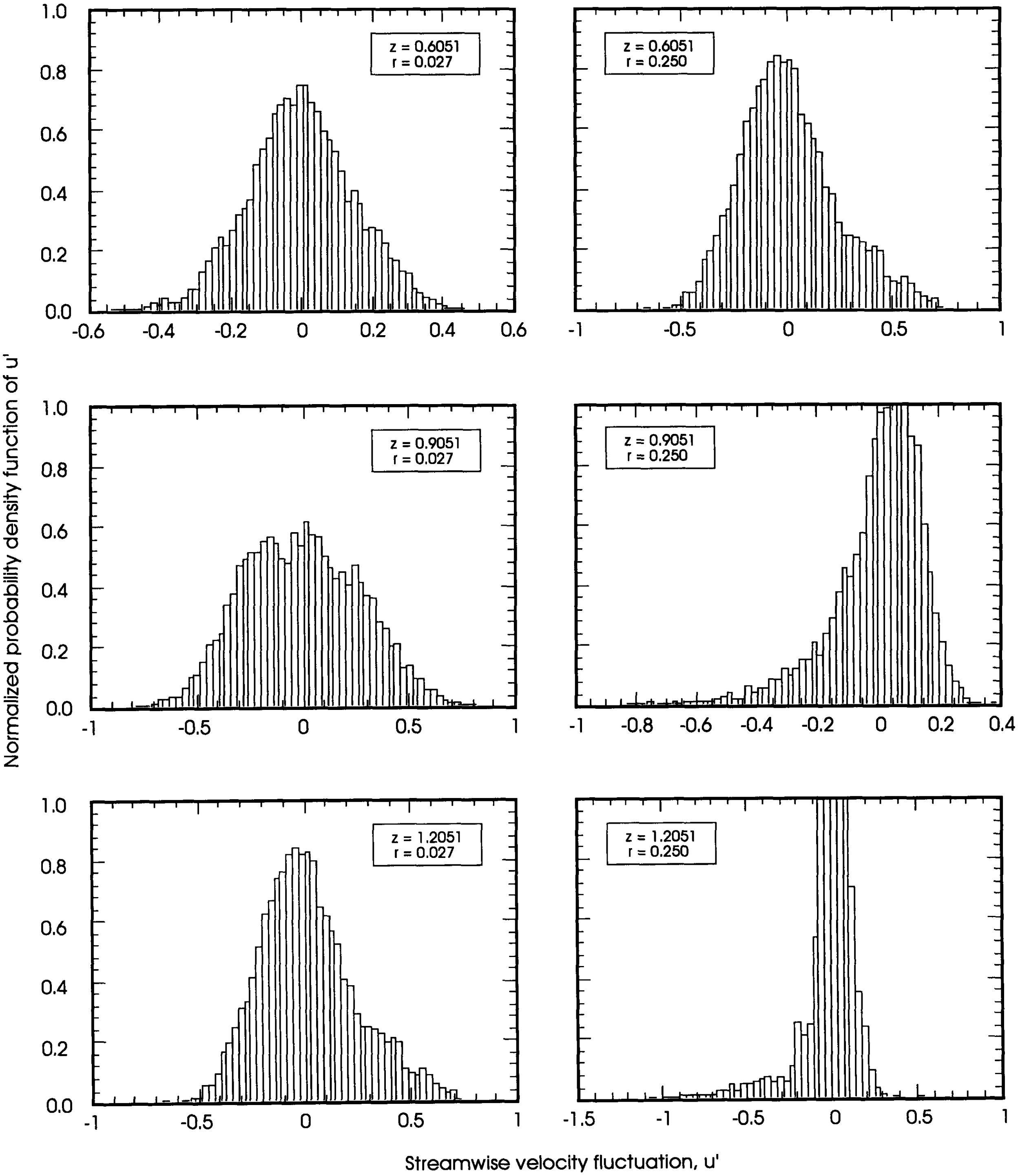

Figure 5.16 Normalized probability density function of u'. U_j / U_a = 1.04 (isothermal reactive flow).

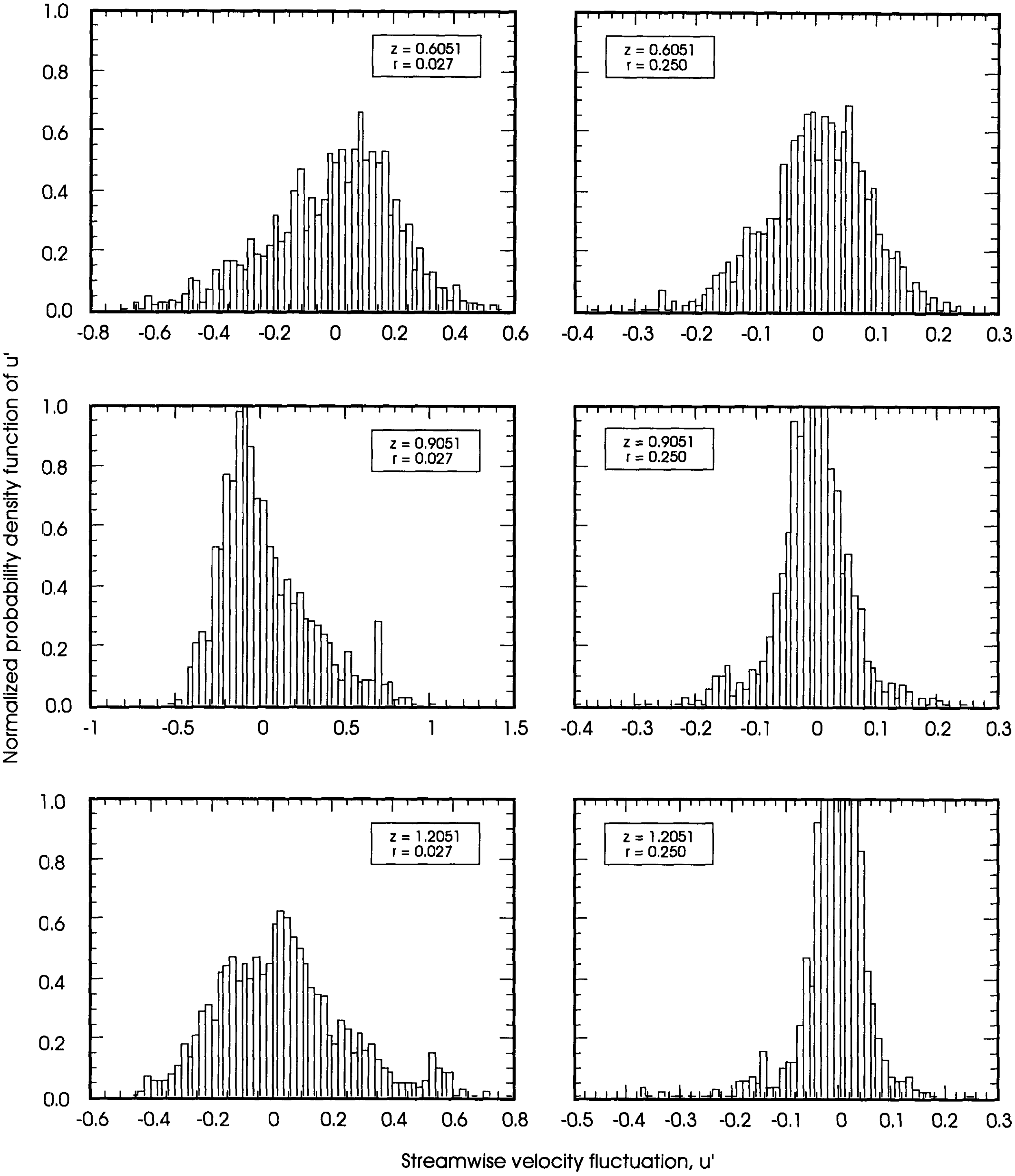

Figure 5.17 Normalized probability density function of u'. U_j / U_a = 1.04 (exothermic reactive flow).

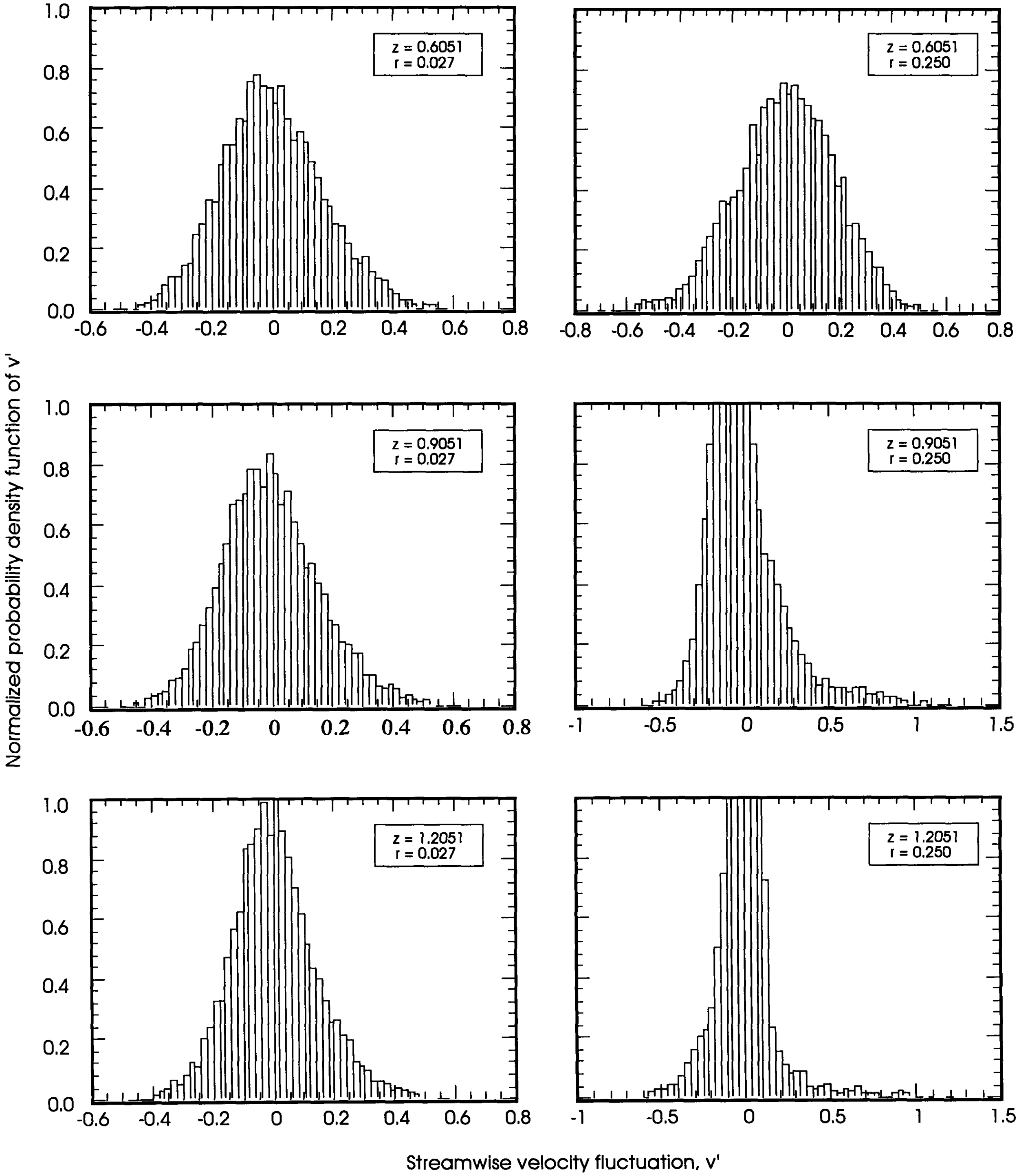

Figure 5.18 Normalized probability density function of v'. U_j / U_a = 1.04 (isothermal reactive flow).

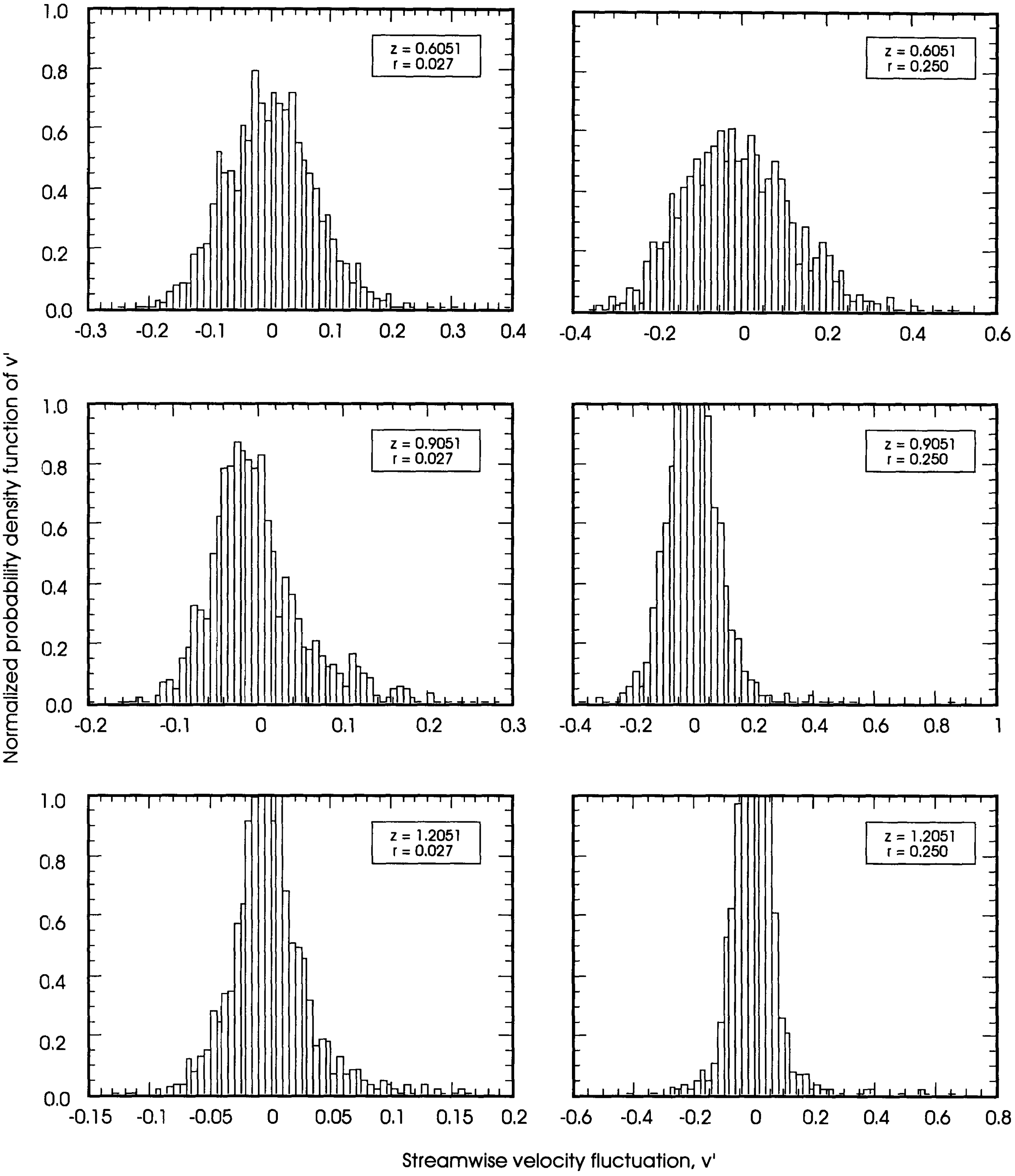

Figure 5.19 Normalized probability density function of v′. U_j/U_a = 1.04 (exothermic reactive flow).

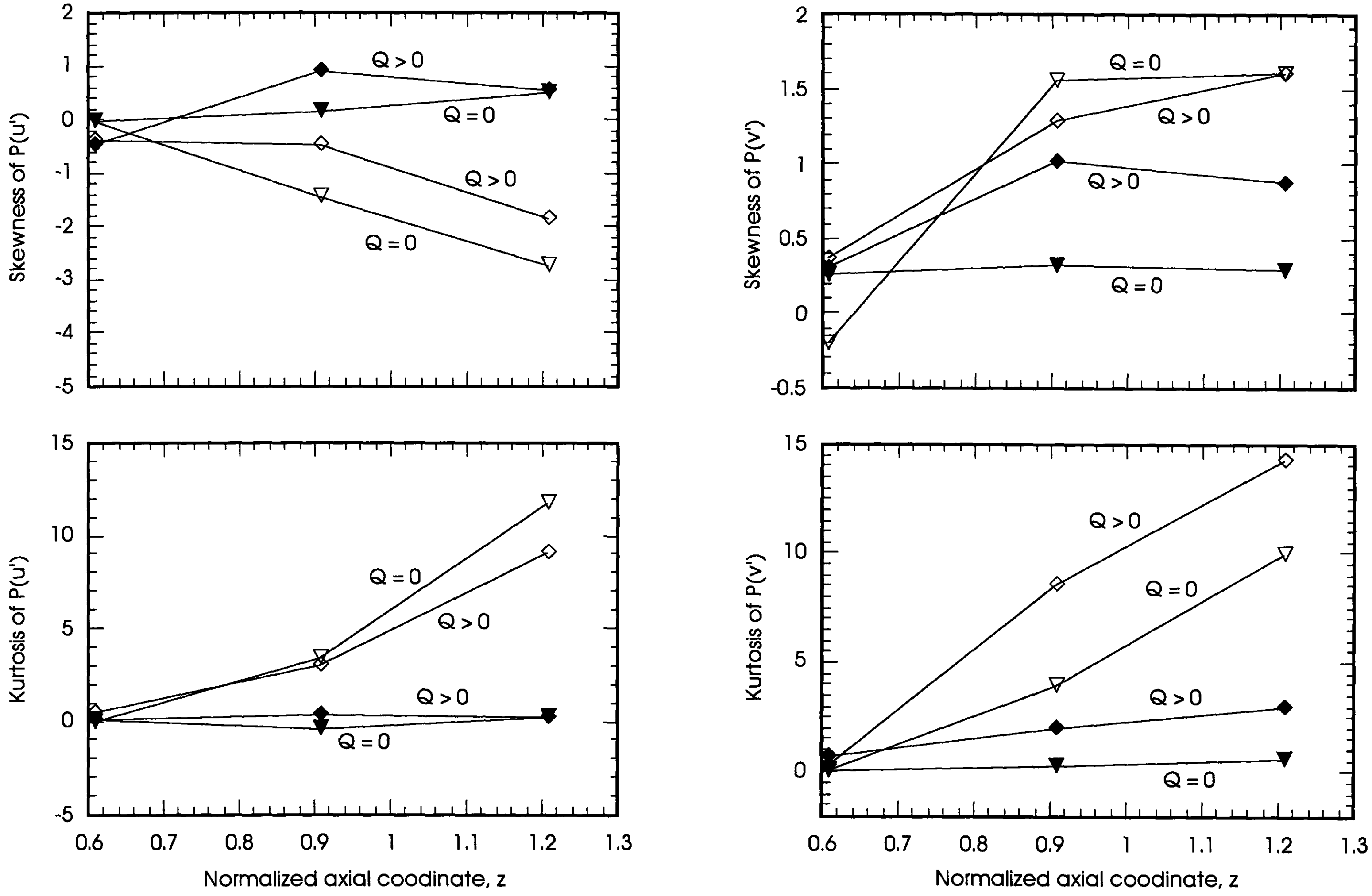

Figure 5.20 Comparisons of the kurtosis and skewness of the velocity probability density functions between the isothermal and the exothermic reactive flow. Filled symbols: r = 0.027, open symbols: r = 0.25.

5.2 CONCLUSIONS

Results of the exothermic reactive-flow simulation with low heat release discussed in this chapter have shown that, when heat release accompanies chemical reaction, volumetric expansion of the fluid induces an expansion velocity field which is superimposed on the rotational flow structures. As a result, the large-scale eddies appear more diffuse, their overall rotational rates decrease noticeably, and the entire structure of the recirculation region becomes more aligned with the streamwise coordinate. Stability of the recirculation region is not significantly dampened by the heat release. The large-scale coherent structures are still apparent in the exothermic-reactive flow field. The roll-up of the eddies, however, appear to be much less intense. The maximum amplitude of the eddies' vorticity, found mainly in the vortex cores, has decreased substantially. This phenomenon can be explained by the angular momentum consideration. Volumetric expansion of the fluid induces a local positive divergence $\nabla \cdot \mathbf{u}$ of the velocity field, as a consequence, the angular momentum of a rotating fluid element is redistributed over a larger area. Thus, the magnitude of its local rotational rate, hence the vorticity, must decrease in order to conserve angular momentum. In addition to reducing the maximum amplitude of the eddies' vorticity, heat release also decreases the unsteady fluctuation energy of these large-scale structures. This phenomenon can also be attributed to the expanding vortical structures in an exothermic reactive field. As an eddy expands and becomes less distinguishable, the concentration of the unsteady fluctuation kinetic energy is redistributed over a larger area and can decay much more quickly. Since unsteady fluctuation and large-scale transport are closely related, lower concentration of the unsteady fluctuation kinetic energy within these eddies, together with the reduced amplitude of the vorticity, implies that the ability of the large-scale structures to entrain fluid is substantially decreased in an exothermic reactive flow as compared to their counterparts in the isothermal reactive flow . Large-scale eddies are known to be responsible for most of the transport of momentum and mixing of the scalar quantities. Their structures and coherence have important repercussions with respect to mixing, reaction, and pollutant formation. The weaker large-scale vortices resulted from heat release implies that less large-scale entrainment and mixing, hence product formation, are possible in the near-wake region when the reaction is exothermic.

6. SUMMARY, CONCLUSIONS, AND SUGGESTIONS FOR FUTURE WORK

6.1 SUMMARY AND CONCLUSIONS

The axisymmetric vortex-scalar element method was developed and implemented to study the unsteady reactive flow in a two-stream, coaxial-jet, axisymmetric bluff-body combustor as a function of the inflow velocity (momentum) ratio. The vortex method is an adaptive Lagrangian numerical scheme in which the vorticity of the flow field is accurately discretized by a set of finite-area vortex elements with overlapping cores, and the positions of these elements are updated every time step according to the flow governing equations. The viscous splitting technique is used to decompose the vorticity transport equation into an advection and a diffusion component. Advection is expressed in terms of a set of coupled ordinary differential equations and is solved using a second-order predictor-corrector method; molecular diffusion is simulated stochastically by random-walking the vortex elements according to Gaussian statistics. Lagrangian scalar elements are also used to transport the scalar fields in order to maintain the grid-free, self-adaptive nature of the algorithm. Moreover, different sets of elements can be used to transport the scalar fields of the various species with different diffusivities. Thus, a wide disparity in diffusive length scales can be accommodated naturally without posing any particular difficulty. The scalar-element method solves the appropriate scalar transport equations describing the reactive field directly without making restrictive assumptions about the structure of the reaction zone. The method, as implemented in this study, is relatively simple and robust. It is capable of handling a variety of initial and complex boundary conditions and is not limited to simple flow domains. Using these numerical schemes, the underlying low-Mach-number flow dynamics within the combustor were investigated under the assumption of isothermal and exothermic reaction. In order to ease stability requirements in the numerical simulations, the low-Mach-number approximation was imposed on the governing equations to filter out the nonequilibrium influences of the acoustic waves in the flow. Chemical reaction in all the simulations was assumed to be described by a binary, single-step, irreversible equation with infinite-rate kinetics. Despite the simplicity of the model and the axisymmetric assumption, the simulations were able to capture most of the unsteady flow dynamics of the near-wake region as well as the large-scale entrainment and mixing.

The focus of the isothermal reactive-flow study was on the unsteady dynamics of the near-wake region downstream of the bluff body as a function of the inflow velocity ratio. The dynamics of the flow as well as the large-scale entrainment and mixing were studied under both steady and externally imposed sinusoidal inflow boundary conditions. The unsteady mixing process was investigated by assuming a fast second-order chemical reaction of the form $F + O \rightarrow P$ with negligible heat of reaction so that the dynamics of the large-scale entrainment and the global mixing field can be studied in a simpler environment, and a better understanding of the basic mixing mechanisms can be developed. In the simulations performed for the study, dilute fuel F and oxidizer O were added to the jet stream and the annular flow, respectively. Once inside the flow domain, the reactants were assumed to react instantaneously and irreversibly upon contact with one another to form products P. This simplified model leads to a diffusion-controlled reaction, and the total amount of products formed is directly proportional to the rate of consumption of the lean reactant F. In this case, the product concentration found within a sampling volume provides an approximation to the local instantaneous mixing. Despite the simplicity of the model, it is sufficiently accurate to describe the mixing process. The study has given important physical insight into the procedures by which the large-scale vortical structures entrain fluid in the near-wake region and, subsequently, enhance the overall mixing.

For the steady-inflow calculations, three cases with three different inflow velocity ratios, U_j/U_a = 0.62, 1.04, and 2.08, were performed for a combustor with diameter ratio D_a/D_b = 2.0. It was observed from the simulations that the complex flow structures in the near-wake region downstream of the bluff body is a dynamically unstable system involving two coexisting and coupled flow instabilities: the shear-layer instability and the recirculation-region instability. For the two lower inflow velocity ratios, the instability of the jet shear layer leads to the formation of organized fuel eddies within the recirculation region between the face of the bluff body and the recirculating air eddy. These fuel eddies interact vigorously with the air eddy as they grow in size; the interaction eventually leads to the merging and shedding of the composite structures from the recirculation region. This complicated unsteady flow dynamics of the near-wake region was found to be quasi-periodic, and all the events associated with a single period were observed to repeat more or less in every cycle. Since all the simulations were performed with steady inflow boundary condition, the unsteady interaction of the eddies and the shedding of the large composite structures from the recirculation region are the intrinsic flow dynamics of this confined bluff-body flow, and the corresponding shedding frequencies associated with these events are the characteristic frequencies of the flow system. To further characterize the shedding dynamics, the frequency spectra at selected locations in the flow field were obtained. From the power spectra, it was found that the dominant Strouhal number is approximately centered around 0.15, which is close to the well-known bluff-body shedding frequency at this Reynolds number. As one moves further downstream from the face of the bluff body, the dominant shedding frequency is seen to shift toward $O(0.06)$, which is the frequency associated with the shedding of the composite structures from the recirculation region.

The distribution of the unsteady fluctuation kinetic energy, $u'u' + v'v'$, in the flow field was found to be highly discrete and nonuniform, with most of the energy being concentrated in the well-defined, large-scale vortical structures and in the shear layers within the recirculation region. The velocity fluctuations exhibit strong non-Gaussian behaviors in the shear layer between the outer annular flow and the recirculation bubble, and between the recirculation bubble and the central jet. Instability of the recirculation region is initiated as the eddies within the region begin to accumulate fluctuation kinetic energy. The amplitude of the fluctuations reaches a maximum value prior to the shedding of the composite flow structures, and decays quickly after the eddies are shed from the recirculation region. The large composite eddies being ejected from the recirculation region retain their identities and the energy levels even at a large distance downstream of the recirculation zone.

The large-scale entrainment and the unsteady mixing in the near-wake region downstream of the bluff body were observed to be a strong function of the inflow velocity ratio. The overall characteristics of the mixing field are controlled by the large-scale eddies, especially in the recirculation region. When the momentum of the central jet is weak relative to the recirculating flow, a short, compact mixing zone confined mainly to the near-wake region with quasi-periodic shedding of large-scale reactive flow structures from the recirculation zone is observed. As the velocity ratio is increased, an intermittent pulsating and reacting jet, extending several bluff-body diameters downstream of the recirculation region, is noted in addition to the quasi-periodic shedding of reactive flow structure from the recirculation region. For the case $U_j/U_a = 2.08$, the recirculation region becomes relatively stable and the flow experiences less fluctuation and entrainment. In this case, shedding from the recirculation region is less frequent, and most of the jet fluid is confined to a narrow region close to the centerline where mixing and reaction are most intense.

Results from the forced-inflow study have shown that a preferred-mode coupling exists between the forced jet and the large-scale structures in the recirculation region. Time-averaged product concentration field indicates that the mixing length depends on the forcing frequency, as long as the pulse amplitude exceeds a minimum threshold to affect the stability of the shear layer near the jet exit. For the case $U_j/U_a = 2.08$, it was found that controlled excitation amplifies the inherent recirculation zone dynamics. As this amplification approaches the natural shedding frequency of the eddies, it causes instability in the otherwise stable recirculation region. This process produces interactions within the recirculation region similar to those occurring naturally in the two cases with lower velocity ratio. The most notable changes to the mixing field in the near-wake region was observed when the central jet was being forced at a dimensionless frequency based on the magnitude of the annular inflow velocity and the diameter of the bluff body of $O(0.06)$, with a forcing amplitude $A_f \geq 0.6$. Forcing at this frequency and amplitude destabilizes the jet shear layer near the exit. The process increases the local entrainment and mixing of the flow near the jet exit in two ways. Forcing enhances the growth of the jet shear layer by amplifying the vortex structures in the shear layer, causing it to roll up and to form a counterclockwise-rotating eddy. This eddy entrains most of the jet fluid entering the flow domain and interacts strongly with the recirculating air eddy. In addition, the unsteady energy added to the flow from forcing increases the unsteady fluctuation kinetic energy in the recirculation region. This process generates interaction among the large-scale flow structures within the recirculation region and eventually leads to the shedding of composite eddies from the region similar to the flow dynamics observed in the two cases with lower velocity ratio.

When the reaction is exothermic, volumetric expansion occurs within the recirculation region induces an expansion velocity field which is superimposed on the rotational vortical flow structures. As a consequence of this additional expansion velocity, the large-scale eddies within the exothermic reactive flow become more diffuse, their overall rotational rates decreased significantly. The entire structure of the recirculation region is noticeably elongated, with the major axis of the structure becomes more aligned with the streamwise coordinate. Compare to the isothermal reactive flow, we see that many of the characteristic global flow features observed in the isothermal flow are also present when the reaction is exothermic. The large eddies, although becoming more diffuse and less orderly, are still very much discernible within the recirculation region of the exothermic reactive flow. However, the maximum amplitude of the large-scale eddies' vorticity, found mainly in the vortex cores, has decreased substantially for the exothermic reactive flow.

Heat release in this bluff-body flow configuration did not significantly dampen the instability of the recirculation region as initially expected. This is due to the fact that the flow within the recirculation region is dominated by a highly unstable two-eddy dynamical system. In the isothermal reactive flow, instability of the recirculation region was initiated by the growth of the fuel eddy between the jet shear layer and the recirculating air eddy. These two eddies have opposite-sign vorticity and they interact vigorously with one another within the recirculation region. The interaction of these two eddies eventually leads to the shedding of the composite structure from the recirculation region, which has a Strouhal number of $O(0.06)$ associated with the shedding process. The same destabilizing mechanism is also observed in the recirculation region of the exothermic reactive flow. However, owing to the existence of a thicker jet shear layer within the recirculation region displacing the air eddy further downstream and the expansion velocity field, the instability of the composite structure was observed to occur sooner in the exothermic reactive flow, resulting in a slightly higher characteristic frequency associated with the shedding of the composite structure. This phenomenon is also reflected in the power spectra of the flow in the near-wake region.

The numerical simulations performed in this research have revealed much information about the inherently unsteady nature and the mixing pattern of this bluff-body flow. The main conclusions can be drawn from the study are

1) This bluff-body flow is inherently unsteady and the dynamics of the near-wake region are dominated by a highly unstable two-eddy system even with steady inflow boundary conditions. Simulating this flow using the time-averaged Navier-Stokes equations will most likely not be able to capture these important physics and is not recommended.

2) The presence of the strong periodic fluctuations within the recirculation region greatly enhance the entrainment and mixing in the near-wake region. The main effect of these unsteady fluctuations is to increase the rate of mixing between the fuel and the oxidizer in the recirculation region so that the length of the mixing zone can be reduced. Thus, it is desirable to have strong velocity fluctuations in the near-wake region. One way to accomplish this is to have a thick interface between the central jet and the annular flow. Further unsteady fluctuations can be induced

in the near-wake region by forcing the inflow velocity.

3) Mixing between the fuel and the oxidizer takes place in the shear layers as well as within the large-scale vortical structures. Initial entrainment and mixing between the fuel and the oxidizer is usually found within the shear layer located between the central jet and the recirculating air eddy. As the recirculation region becomes unstable, large-scale composite structures are ejected from the region quasi periodically. These large-scale vortices continue to entrain and to mix the two fluids as they are being convected downstream.

4) The release of thermal energy in the near-wake region of this bluff-body flow configuration did not significantly dampen the instability of the recirculation region. This is due to the fact that the flow within the recirculation region is dominated by a highly unstable two-eddy dynamical system. The large-scale entrainment and mixing mechanisms as observed in the isothermal reactive flow are also present when the reaction is exothermic. However, the differences in the flow dynamics between the two cases are significant enough to warrant the inclusion of the effects of the thermal energy on the flow dynamics if one wishes to capture the physics of the flow more accurately in a simulation.

6.2 SUGGESTIONS FOR FUTURE WORK

The conclusions discussed above do not answer all the questions and uncertainties which have been raised both in this study and by earlier researchers, and there is a need for further study on the unsteady dynamics of this confined bluff-body flow. The suggestions for future work fall into two categories. The first is a continuation of the work on the same flow configuration, and to develop a more robust numerical scheme which allows the inclusion of the baroclinic vorticity generation term and higher release rate of thermal energy in the solution procedure. The second is an extension of this work: to study a flow configuration which is widely used in practical combustion system by including a swirling velocity component in the jet or the annular flow or both.

REFERENCES

[1] Abramovich, G. N., *The Theory of Turbulent Jets*, translated by Scripta Technica, The M.I.T Press, Massachusetts Institute of Technology, Cambridge, MA, 1979.

[2] Anderson, C., and Greengard, A., "On Vortex Methods," Lawrence Berkeley Laboratory, University of California, Berkeley, LBL-16736, 1984.

[3] Anderson, D. A., Tannehill, J. C., and Pletcher, R. H., *Computational Fluid Mechanics and Heat Transfer*, Hemisphere Publishing Corporation, New York, 1984.

[4] Arvo, J. (editor), *Graphics Gems II*, Academic Press, New York, 1991.

[5] Barrere, M., and Williams, F. A., "Comparison of Combustion Instabilities Found in Various Type of Combustion Chambers," *Eleventh Symposium (International) on Combustion*, The Combustion Institute, Pittsburgh, PA, 1968, pp. 169-181.

[6] Barton, G., *Elements of Green's Functions and Propagation Potentials, Diffusion, and Waves*, Clarendon Press, Oxford, 1989.

[7] Batchelor, G. K., *An Introduction to Fluid Dynamics*, Cambridge University Press, Cambridge, 1990.

[8] Batchelor, G. K., *The Theory of Homogeneous Turbulence*, Cambridge University Press, Cambridge, 1990.

[9] Beale, J. T. and Majda, A., "Rates of Convergence for Viscous Splitting of the Navier-Stokes Equations," *Math. of Computation*, Vol. 37, No. 156, pp. 243-259, 1981.

[10] Beale, J. T. and Majda, A., "Vortex Methods II: Higher Order Accuracy in Two- and Three-Dimensions," *Math. of Computation*, Vol. 39, No. 159, pp. 28-52, 1982.

[11] Beér, J. M., and Chigier, N. A., *Combustion Aerodynamics*, John Wiley & Sons, New York, 1972.

[12] Bendat, J. S., and Piersol, A. G., *Random Data Analysis and Measurement Procedures*, 2nd ed., John Wiley & Sons, New York, 1986.

[13] Bird, B. R., Stewart, W. E., and Lightfoot, E. N., *Transport Phenomena*, John Wiley & Sons, 1960.

[14] Bradshaw, P., Cebeci, T., and Whitelaw, J. H., *Engineering Calculation Methods for Turbulent Flow*, Academic Press, New York, 1981.

[15] Bradshaw, P., *An Introduction to Turbulence and its Measurement*, Pergamon Press, New

York, 1985.

[16] Bremhorst, K., and Harch, W. H., "Near Field Velocity Measurements in a Fully Pulsed Subsonic Air Jet," *Turbulent Shear Flows I*, Springer-Verlag, Berlin, pp. 480-500, 1979.

[17] Chao, C. C., Orszag, S. A., and Shyy, W. (editors), *Recent Advances in Computational Fluid Dynamics*, Proceedings of the US/ROC (Taiwan) Joint Workshop on Recent Advances in Computational Fluid Dynamics, Springer-Verlag, New York, 1989.

[18] Cherry, N. J., Hillier, R., and Latour, M. E. M. P., "Unsteady Measurements in a Separated and Reattaching Flow," *J. Fluid Mech.*, 144, pp. 13-46, 1984.

[19] Chorin, A. J., "Numerical Study of Slightly Viscous Flow," *J. Fluid Mech.*, vol. 57, part 4, pp. 785-796, 1973.

[20] Chorin, A. J., and Marsden, J. E., *A Mathematical Introduction to Fluid Mechanics*, Springer-Verlag, New York, 1979.

[21] Cody, W. J., "Chebyshev Approximations for the Complete Elliptic Integrals K and E," *Math. of Computation*, vol. 19, pp. 105-112, 1965.

[22] Correa, S. M., "Prediction of an Axisymmetric Combusting Flow," *AIAA J.*, vol. 22, no. 11, pp. 1602-1608, 1984.

[23] Correa, S. M., and Gulati, "Measurements and Modeling of a Bluff-Body Stabilized Flame," *Combust. Flame* **89**, pp. 195-213, 1992.

[24] Crocco, L., "Theoretical Studies of Liquid Propellant Rocket Instability," *Tenth Symposium (International) on Combustion*, The Combustion Institute, Pittsburgh, PA, 1965, pp. 1101-1128.

[25] Crow, S. C., and Champagne, F. H., "Orderly Structure in Jet Turbulence," *J. Fluid Mech.*, 48:547-591, 1971.

[26] Cuvelier, C., Segal, A., and Van Steenhoven, A. A., *Finite Element Methods and Navier-Stokes Equations*, D. Reidel Publishing Company, P. O. Box 17, 3300 AA Dordrecht, Holland, 1988.

[27] Cullick, F. E. C., in *Combustion Instabilities in Liquid-Fuelled Propulsion Systems*, AGARD Conference Proceedings No. 450, 1988.

[28] Curtet, R. M., and Girard, J. P., "Visualization of a Pulsating Jet," *Proc. ASME Symp. Fluid Mech. Mixing*, Atlanta, GA, pp. 173-180, 1973.

[29] Daily, J. W., Pitz, R. W., Keller, J. O., Ellzey, J. L., and Shepherd, I. G., "The Structure and Dynamics of Reacting Two Stream Plane Mixing Layers," in *Experimental Measurements and Techniques in Turbulent Reactive and Non-Reactive Flows*, AMD-Vol. 66, pp. 175-209, edit-

ed by So, R. M. C., Whitelaw, and Lapp, M., presented at the winter annual meeting of The American Society of Mechanical Engineering, New Orleans, Louisiana, Dec. 9-14, 1984.

[30] Damköhler, G., *Jahrb. deut. Luftfartforsch.* 1939, p. 113; *Z. Elektrochem.* 1940, 46, p. 601. English translation, NACA Tech. Memo 1112, 1947.

[31] Davies, M. E., "A Comparison of the Wake Structure of a Stationary and Oscillating Bluff Body Using a Conditioned Averaging Technique," *J. Fluid Mech.*, Vol. 75, pp. 209-223, 1976.

[32] Davies, T. W., and Beér, J. M., "The Turbulence Characteristics of Annular Wake Flow," Heat and Mass Transfer in Flows With Separated Regions, International Seminar, Hercig-Novi, Yugoslavia, 1969.

[33] Davis, J. C., *Statistics and Data Analysis in Geology*, John Wiley & Sons, Inc. 1973.

[34] Drazin, P. G., and Reid, W. H., *Hydrodynamic Stability*, Cambridge University Press, Cambridge, 1981.

[35] Engquist, B., Luskin, M., and Majda, A. (editors), *Computational Fluid Dynamics and Reacting Gas Flows*, Springer-Verlag, New York, 1988.

[36] Favre-Marinet, M., and Binder, G., "Structure Des Jets Pulsants," *J. de Mecanique*, 18(2):355, 1979.

[37] Fettis, H. E., and Caslin, J. C., *Tables of Elliptic Integrals of the First, Second and Third Kind*, Aerospace Research Laboratories, Wright-Patterson Air Force Base, Ohio, 1964.

[38] Finlayson, B. A., *The Method of Weighted Residuals and Variational Principles with Application in Fluid Mechanics, Heat and Mass Transfer*, Academic Press, New York, 1972.

[39] Fristrom, R. M., and Westenberg, A. A., Flame Structure, McGraw-Hill, New York, 1965.

[40] Ghoniem, A. F., Chorin, A. J., and Oppenheim, A. K., "Numerical Modeling of Turbulent Flow in a Combustion Tunnel," *Phil. Trans. R. Soc. Lond.* A **304**, pp. 303-325, 1982.

[41] Ghoniem, A. F., "Dynamics of Flame Propagation in a Turbulent Field," *Lectures in Applied Mathematics*, vol. 22, 1985.

[42] Ghoniem, A. F., and Sherman, F. S., "Grid Free Simulation of Diffusion Using Random Walk Methods," *J. of Computational Physics*, **61**, pp. 1-37, 1985.

[43] Ghoniem, A. F., "Computational Methods in Turbulent Reacting Flow," *Lectures in Applied Mathematics*, vol. 24, 1986.

[44] Ghoniem, A. F., "Effect of Large Scale Structures on Turbulent Flame Propagation," *Combustion and Flame*, **64**, pp. 321-336, 1986.

[45] Ghoniem, A. F., and Cagnon, Y., "Vortex Simulation of Laminar Recirculating Flow," *J. of Computational Physics*, **68**, pp. 346-377, 1987.

[46] Ghoniem, A. F., and Ng, K. K., "Numerical Study of the Dynamics of a Forced Shear Layer," *Phys. Fluids*, vol. 30, no. 3, pp. 706-721, 1987.

[47] Ghoniem, A. F., and Givi, P., "Vortex-Scalar Element Calculations of a Diffusion Flame," **AIAA** paper 0225, 1987.

[48] Ghoniem, A. F., and Sethian, J. A., "Effect of Reynolds Number on the Structure of Recirculating Flow," *AIAA J.*, vol. 25, no. 1, pp. 168-170, 1987.

[49] Ghoniem, A. F., "Development and Application of Vortex Methods; A Review and Some Extensions," **AIAA** paper 3576, 1988.

[50] Ghoniem, A. F., and Givi, P., "Lagrangian Simulation of a Reacting Mixing Layer at Low Heat Release," *AIAA J.*, vol. 26, no. 6, pp. 690-697, 1988.

[51] Ghoniem, A. F., and Najm, H. N., "Numerical Simulation of the Coupling Between Vorticity and Pressure Oscillations in Combustion Instability," **AIAA** paper 2665, 1989.

[52] Ghoniem, A. F., and Martines, F. L., "Effect of Velocity Ratio on Bluffbody Flow Dynamics; Steady and Transitional Regimes," **AIAA** paper 0580, 1991.

[53] Ghoniem, A. F., Martines, F. L., Kelly, J., and Rotman, D. A., "The Dispersion of the Jet Fluid Due to the Large-Scale Motion in Bluffbody Flows," **AIAA** paper 1861, 1991.

[54] Givi, P., Ph.D. Thesis, Cargnegie-Mellon University, Pittsburgh, 1984.

[55] Givi, P., "Model-Free Turbulent Reactive Flows," *Prog. Energy Combust. Sci.*, Vol. 15, pp. 1-107, 1989.

[56] Glassman, I., *Combustion*, 2nd ed., Academic Press, Florida, 1987.

[57] Glassner, A. S. (editor), *Graphics Gems*, Academic Press, New York, 1990.

[58] Hald, O., "Convergence of Vortex Methods for Euler's Equations," **SIAM** *J. of Numer. Analysis*, Vol. 16, No. 5, PP. 726-755, 1979.

[59] Harrje, D. T., and Reardon, F. H., "Liquid Propellant Rocket Instability," NASA SP-194, 1972.

[60] Hayes, W. D., "The Vorticity Jump Across a Gasdynamic Discontinuity," *J. Fluid Mech.*, **2**, pp. 595-600.

[61] Haywood, J. B., *Internal Combustion Engine Fundamentals*, McGraw-Hill Book Company, 1988.

[62] Hegde, U. G., Reuter, D., Daniel, B. R., and Zinn, B. T., "Flame Driving of Longitudinal Instabilities in Dump Type Ramjet Combustors," **AIAA** paper 0371, 1986.

[63] Hinze, J. O., *Turbulence*, 2nd ed., McGraw-Hill, New York, 1987.

[64] Hirschfelder, J. O., Curtiss, C. F., and Bird, R. B., *Molecular Theory of Gases and Liquids*, John Wiley & Sons, New York, 1954.

[65] Hirt, C. W., and Nichols, B. D., "Volume of Fluid Method for the Dynamics of Free Boundaries," *J. of Computational Physics*, **39**, pp. 201-225, 1981.

[66] Howthorne, W. R., Wedell, D. S., and Hottel, H. C., *3rd Symp. Combust., Flames Expl. Phenomena*, p. 266, The Combustion Institute, Pittsburgh, 1949.

[67] Hussain, A. K. M. F., and Reynolds, W. C., "The Mechanics of an Organized Wave in Turbulent Shear Flow," *J. Fluid Mech.*, 41:241, 1970.

[68] Hussain, A. K. M. F., and Zaman, K. B. M. Q., "Vortex Pairing in a Circular Jet Under Controlled Excitation: Part 2. Coherent Structure Dynamics," *J. Fluid Mech.*, 101:493-544, 1980.

[69] Jones, W. P., and Whitelaw, J. H., "Calculation Methods for Reacting Turbulent Flows: A Review," *Combustion and Flame*, Vol. 48, pp. 1-26, 1982.

[70] Karamcheti, K., *Principles of Ideal-Fluid Aerodynamics*, Robert E. Krieger Publishing Company, Malabar, Florida, 1980.

[71] Kenworthy, J.S., "The Flow and Mixing in Double Concentric Jets," Ph.D. thesis, University of Sheffield, September 1971.

[72] Kimoto, K., Shiraishi, I., and Matsumoto, R., "Structure of Turbulent Jet Flames Stabilized in Annular Air Jet," *Combustion Science and Technology*, Vol. 25, pp. 31-41, 1981.

[73] Kiya, M., and Sasaki, K., "Structure of a Turbulent Separation Bubble," *J. Fluid Mech.*, 137, pp. 83-113, 1983.

[74] Knio, O., "Low Mach Number Simulation of Combustion in Closed Chambers," S.M. thesis, Department of Mechanical Engineering, Massachusetts Institute of Technology, Cambridge, MA, 1986.

[75] Koochesfahani, M. M., Dimotakis, P. E., and Broadwell, J. E., "Chemically Reacting Turbulent Shear Layers," **AIAA** paper 0475, 1983.

[76] Krishnan, A. "Numerical Study of Vorticity-Combustion Interaction in Shear Flow," Sc.D. thesis, Department of Mechanical Engineering, Massachusetts Institute of Technology, Cambridge, MA, 1989.

[77] Krishnamurthy, L., and Park, S. O., "Streamline Curvature Effects in Confined Isothermal Re-

circulating FlowFields Behind an Axisymmetric Bluff Body; Numerical Calculations with the $\kappa-\varepsilon$ Model," Fourth Shear Flow Symposium, Karlschruhe, Germany.

[78] Krishnamurthy, L., Wahrer, D. J., and Cochran, H. S., "Laser Diagnostic Development and Measurement and Modeling of Turbulent Flowfields of Jets and Wakes, Part II: Numerical Predictions of Isothermal Flowfields in a Ducted Centerbody Combustor," Air Force Wright Aeronautical Laboratories, Wright-Patterson Air Force Base, Ohio, AFWAL-TR-83-2044, 1983.

[79] Krishnamurthy, L., Wahrer, D. J., and Cochran, H. S., "Similarity Considerations of Isothermal Turbulent Recirculating Flowfields in Axisymmetric and Bluff-Body Wakes," **AIAA** paper 1203, 19th AIAA/SAE/ASME Joint Propulsion Conference, June 27-29, 1983, Seattle, WA.

[80] Kuo, K. K. *Principles of Combustion*, John Wiley & Sons, New York, 1986.

[81] Lamb, H., *Hydrodynamics*, 6th ed., Dover Publications, New York, 1945.

[82] Landau, L. D., "On the Theory of Slow Combustion," *J. Exp. Theor. Phys.* 14, p. 240, 1944.

[83] Landau, L. D., and Lifshitz, *Fluid Mechanics*, translated by Sykes, J. B. and Reid, W. H., Pergamon Press, Addison-Wesley Publishing Company, Inc., Reading, MA, 1959.

[84] Lefebvre, A. H., *Gas Turbine Combustion*, Hemisphere Publishing Corporation, New York, 1983.

[85] Li, X., and Tankin, R. S., "A Study of Cold and Combusting Flow Around Bluff-Body Combustors," *Combust. Sci. and Tech.*, vol. 00, 1986.

[86] Libby, P. A., and Williams, F. A. (editors), *Turbulent Reacting Flows*, Springer-Verlag, Berlin, 1980.

[87] Lightman, A. J., Richmond, R. D., Magill, P. D., Krishnamurthy, L., Roquemore, W. M., Bradley, R. P., Stutrud, J. S., and Reeves, C. M, "Velocity Measurements in a Bluff-body Diffusion Flame," **AIAA** paper 1544, 1980.

[88] Lin, C. C., *The Theory of Hydrodynamic Stability*, Cambridge University Press, Cambridge, 1966.

[89] Long, M. B., and Chu, B. T., "Mixing Mechanism and Structure of an Axisymmetric Turbulent Mixing Layer," *AIAA J.*, vol. 19, no. 9, pp. 1158-1163, 1981.

[90] Longwell, J. P., Frost, E. E., and Weiss, M. A., "Flame Stability in Bluff Body Recirculation Zones," *Industrial and Engineering Chemistry*, vol. 45, No. 8, pp. 1629-1633, 1953.

[91] Luu, V. and Ghoniem, A. F., "Simulation of the Reacting Field in an Axisymmetric Bluff-Body Combustor Using the Vortex-Scalar Element Method-An Isothermal, Fast-Chemistry Model," **AIAA** paper 0808, 1995.

[92] Majda, A. and Sethian, J., "The Derivation and Numerical Solution of Equations for Zero Mach Number Combustion," *Combustion Sci. and Tech.*, 42, pp. 185-205.

[93] Martins, L. F., "Vortex Computations of Axisymmetric High Reynolds Number Flows in Complex Domains," Ph.D. thesis, Department of Mechanical Engineering, Massachusetts Institute of Technology, Cambridge, MA, 1990.

[94] Martins, L. F., and Ghoniem, A. F., "Simulation of the Non-Reacting Flow in a Bluff-Body Burner; Effect of the Diameter Ratio," *J. of Fluids Engineering*, Vol. 115, 1993.

[95] McMurtry, P. A., Riley, J. J., and Metcalfe, R. W., "Effects of Heat Release on the Large-Scale Structure in Turbulent Mixing Layers," *J. Fluid Mech.*, 1989, vol. 199, pp. 297-332.

[96] Memering, J. N., and Krishnamurthy, L., "Reynolds-Averaged, Isothermal Predictions of the Vortex-Center Characteristics in Axisymmetric, Turbulent Recirculation Zones," **AIAA** paper 1365, AIAA/SAE/ASME 2oth Joint Propulsion Conference, June 11-13, 1984, Cincinati, OH.

[97] Menon, S., and Jou, W. H., "Large-Eddy Simulations of Combustion Instability in an Axisymmetric Ramjet Combustor," **AIAA** paper 0267, 1990.

[98] Metghalchi, M., and Keck, J. C., "Laminar Burning Velocity of Propane-Air Mixtures at High Temperature and Pressure," *Combustion and Flame*, **38**, vol. 2, pp. 143-154, 1980.

[99] Michalke, A., "On the Spatially Growing Disturbances in an Inviscid Shear Layer," *J. Fluid Mech.*, 23(3):521-544, 1965.

[100] Najm, H. N. and Ghoniem, A. F., "Numerical Simulation of the Convective Instability in a Dump," **AIAA**-87-1874, **AIAA/SAE/ASME/ASEE** 23rd Joint Propulsion conference, 1987.

[101] Najm, H. N., "Numerical Investigation of the Instability of Premixed Dump Combustors," Ph.D. thesis, Department of Mechanical Engineering, Massachusetts Institute of Technology, Cambridge, MA, 1989.

[102] Nakamura, Y., Leonard, A., and Spalart, P., "Vortex Simulation of an Inviscid Shear Layer," **AIAA/ASME** 3rd Joint Thermophysics, Fluids, Plasma and Heat Transfer Conf., **AIAA**-82-0948, St. Louis, MO, 1982.

[103] Namazian, M., "Velocity and Concentration Data in Bluff-Body Flows," private communications.

[104] Noh, W. T., and Woodward, P., "SLIC (Simple Line Interface Calculation)," *Proc. 5th Int. Conf. Numer. Math. Fluid Mechanics*, pp. 330-339, Springer-Verlag, Berlin, 1976.

[105] Oppenheim, A. V., and Schafer, R. W., *Digital Signal Processing*, Prentice-Hall, Inc., Englewood Cliffs, New Jersey, 1975.

[106] Oran, E. S., and Boris, J. P., *Numerical Simulation of Reactive Flow*, Elsevier Science Publish-

ing Co., New York, 1987.

[107] Owen, F. K., and Johnson, D. A., "Measurements of Unsteady Vortex Flow Fields," **AIAA** paper 78-18, 1978.

[108] Parikh, P. G., and Moffat, R. J., "Mixing Improvement in a Resonantly Pulsed, Confined Jet," *Proc. ASME Fluid Mech. Comb. Sys.*, pp. 251-256, 1981.

[109] Parker, R., and Welsh, M. C., "Effects of Sound on Flow Separation From Blunt Flat Plates," *Int. J. Heat & Fluid Flow*, 4, no. 2, 1983.

[110] Pao, Y. C., *A First Course in Finite Element Analysis*, Allyn and Bacon, Inc., Newton, MA, 1986.

[111] Perlman, M., "On the Accuracy of Vortex Methods," *J. of Computational Physics*, **59**, pp. 200-223, 1985.

[112] Perry, A. F., and Watmuff, J. H., "The Phase-Averaged Large-Scale Structures in Three-Dimensional Turbulent Wakes," *J. Fluid Mech.*, Vol. 103, pp. 33-51, 1981.

[113] Petersen, R. A., and Samet, R. A., "On the Preferred Mode of Jet Instability," *J. Fluid Mech.*, 194:153-173, 1988.

[114] Pope, S. B., *Prog. Energy Combust. Sci.*, **11**, 119, 1985.

[115] Putnam, A. A., *Combustion-Driven Oscillations in Industry*, Elsevier, Amsterdam, 1971.

[116] Proakis, J. G., and Manolakis, D. G., *Introduction to Digital Signal Processing*, Macmillian Publishing Company, New York, 1988.

[117] Roquemore, W. M., Britton, R. L., and Sandhu, S. S., "Investigation of the Dynamic Behavior of a Bluff Body Diffusion Flame Using Flame Emission," **AIAA** paper 0178, 1982.

[118] Roquemore, W. M., Bradley, R. P., Stutrud, J. S., Reeves, C. M., Obringer, C. A., and Britton, R. L., "Utilization of Laser Diagnostics to Evaluate Combustion Models," AGARD-CP-353, pp. 1-36, 1983.

[119] Roquemore, W. M., Bradley, R. P., Stutrud, J. S., Reeves, C. M., and Britton, R. L., "Influence of the Vortex Shedding Process on a Bluff-Body Diffusion Flame," **AIAA** paper 0335, 1983.

[120] Roquemore, W. M., Tankin, R. S., Chiu, H. H., and Lottes, S. A., "The Role of Vortex Shedding in a Bluff-Body Combustor," in *Experimental Measurements and Techniques in Turbulent Reactive and Non-Reactive Flows*, AMD-Vol. 66, pp. 159-174, edited by So, R. M. C., Whitelaw, and Lapp, M., presented at the winter annual meeting of The American Society of Mechanical Engineering, New Orleans, Louisiana, Dec. 9-14, 1984.

[121] Roshko, A., "On the Development of Turbulent Wakes from Vortex Streets," NACA Rep. 1191, 1954.

[122] Saffman, P. G., *Vortex Dynamics*, Cambridge University Press, 1992.

[123] Sample, J. W., and Lilley, D. G., "Chemically Reacting Axisymmetric Flowfield Prediction," **AIAA** paper 0364, 1984.

[124] Sarohia, V., and Bernal, L. P., "Entrainment and Mixing in Pulsatile Jets," *Third Symp. Turb. Shear Flows*, Univ. of Calif., Davis, CA, 11.30-11.35, 1981.

[125] Schlichting, H., *Boundary-Layer Theory*, 7th ed., translated by Kestin, J., McGraw-Hill, New York, 1979.

[126] Scott, J. N., and Hankey, Jr., W. L., "Numerical Simulation of Cold Flow in an Axisymmetric Centerbody Combustor," **AIAA** paper 1741, 1983.

[127] Segerlind, L. J., *Applied Finite Element Analysis*, John Wiley & Sons, New York, 1976.

[128] Sethian, J. A., "Turbulent Combustion in Open and Closed Vessels," *J. of Computational Physics*, **54**, pp. 425-456, 3, 1985.

[129] Sherman, F. S., *Viscous flow*, McGraw-Hill, New York, 1990.

[130] Sivashinsky, G. I., "On a Distorted Flame Front as a Hydrodynamic Discontinuity," *Acta Astronautica*, 6, pp. 631-645, 1979.

[131] Smith, I. M., *Programming the Finite Element method with Application to Geomechanics*, John Wiley & Sons, New York, 1982.

[132] Smooke, M. D. (editor), *Reduced Kinetic Mechanisms and Asymptotic Approxis for Methane-Air Flames*, Lecture Notes in Physics 384, Springer-Verlag.

[133] Sobolev, S. L., *Partial Differential Equations of Mathematical Physics*, Addison-Wesley Publishing Company, Reading, Massachusetts, 1964

[134] Soteriou, M., "Numerical Study of Turbulent Combustion in a Shear Layer," Ph.D. thesis, Department of Mechanical Engineering, Massachusetts Institute of Technology, Cambridge, MA, 1993.

[135] Starr, V. P., Physics of Negative Viscosity Phenomena, McGraw-Hill, New York, 1968.

[136] Strehlow, R. A., *Combustion Fundamentals*, McGraw-Hill, New York, 1984.

[137] Sturgess, G. J., and Syed, S. A., "Widely-Spaced Co-Axial Jet, Diffusion-Flame Combustor: Isothermal Flow Calculations Using the Two-Equation Turbulence Model," **AIAA** paper 0113, 1982.

[138] Sturgess, G. J., and Syed, S. A., "Multi-Species Isothermal Flow Calculations of Widely-Spaced Co-Axial Jets in a Confined Sudden Expansion, with the Central Jet Dominant,"